UNIVERSITÀ DEGLI STUDI DI PADOVA

DIPARTIMENTO DI INGEGNERIA INDUSTRIALE
CORSO DI LAUREA MAGISTRALE IN INGEGNERIA CHIMICA E DEI PROCESSI INDUSTRIALI

Tesi di Laurea Magistrale in
Ingegneria Chimica e dei Processi Industriali

DEVELOPMENT OF MICROFLUIDIC PLATFORMS FOR ENZYMATIC REACTIONS: EFFECTS OF FLUID DYNAMICS AND REACTOR SURFACE ON REACTION RATE

Relatore: Dott. Ing. Nicola Elvassore

Laureanda: SILVIA GALVANIN

ANNO ACCADEMICO 2013/2014

Riassunto

Introduzione e scopo dello studio Le ammine otticamente pure sono composti chimici di alto valore. Sono utilizzate per la sintesi di numerosi farmaci e come principi attivi nell'industria farmaceutica e agrochimica. La loro sintesi può avvenire tramite processi chimici tradizionali; i due principali processi sono la cristallizzazione con acidi carbossilici chirali e la riduzione enantioselettiva del doppio legame $C-N$ presente nelle immine. Tuttavia, la sintesi chimica di ammine otticamente pure rimane problematica per la bassa resa globale del processo: sono infatti necessarie molteplici reazioni in serie per produrre ammine ad elevata purezza in un'unica forma enantiomerica. Un'alternativa è rappresentata dalla possibilità di preparare ammine otticamente pure per via biocatalitica, per produrre il prodotto desiderato in maniera estremamente selettiva; questa possibilità si sta rendendo sempre più fattibile in seguito ai recenti sviluppi nella disponibilità di biocatalizzatori, tecniche per migliorare la loro stabilità e l'intrinseca alta selettività e attività catalitica degli enzimi. Tra le vie biocatalitiche, la sintesi asimmetrica catalizzata dall'enzima $\omega-$Transaminasi rappresenta il futuro per la sintesi di ammine chirali pure dal momento che l'enzima $\omega-$Transaminasi presenta una alta stereoselettività.

Per rendere possibile l'utilizzo di biocatalizzatori è necessario conoscere la loro cinetica di reazione, nonchè i loro parametri cinetici, per valutare la loro efficienza e per il dimensionamento del reattore. Data l'applicabilità industriale della produzione di ammine otticamente pure catalizzata dall'enzima $\omega-$Transaminasi, il meccanismo cinetico di $\omega-$Transaminasi è noto; tuttavia, è studiato solo per soluzioni diluite in sistemi batch. Recentemente, l'attenzione dei ricercatori si è spostata da reattori batch a sistemi spazialmente limitati (microreattori), dove è possibile ricreare un ambiente ristretto e affollato tipico delle cellule degli esseri viventi, luogo naturale di azione degli enzimi.

Da qui nasce lo scopo di questo studio: analizzare sperimentalmente l'attività dell'enzima $\omega-$Transaminasi in un microreattore e confrontarla con l'attività dello stesso in un sistema batch. I due reattori differiscono per il regime fluidodinamico e la scala; l'effetto di questi parametri è studiato sperimentalmente per $\omega-$Transaminasi, insieme all'effetto del rapporto superficie/volume del microreattore. L'esistenza di fenomeni fisici di superficie quali l'adsorbimento dell'enzima alle pareti del microreattore (oltre alla ritenzione idrodinamica dovuta al regime di flusso laminare) è analizzata sperimentalmente con l'enzima glucosio ossidasi. Infine, l'ipotesi dell'adsorbimento è verificata attraverso simulazioni CFD.

Materiali e metodi Le reazioni chimiche oggetto della parte sperimentale di questa attività di tesi sono la transaminazione catalizzata dall'enzima $\omega-$Transaminasi e l'ossidazione del glucosio catalizzata dall'enzima glucosio ossidasi. L'attività enzimatica e i parametri cinetici dell'enzima $\omega-$Transaminasi sono stati misurati in piattaforme microfluidiche e in un sistema batch. Inoltre, la velocità di reazione è stata misurata in microreattori con diverso rapporto superficie/volume. Questo è stato fatto allo scopo di determinare la dipendenza della reazione enzimatica studiata dalle condizioni fluidodinamiche del reattore, dalla scala del reattore e dal rapporto superficie/volume del microreattore.

Gli esperimenti condotti con l'enzima glucosio ossidasi sono stati effettuati per analizzare la presenza di adsorbimento dell'enzima sulla superficie interna del microreattore e/o la ritenzione idrodinamica dello stesso all'interno del microcanale. La reazione catalizzata dall'enzima glucosio ossidasi in microreattori è stata studiata anche attraverso simulazioni CFD, che includono un modello di adsorbimento dell'enzima.

Risultati e discussione Gli esperimenti condotti con l'enzima $\omega-$Transaminasi hanno mostrato che l'attività dell'enzima nel microreattore è significativamente più alta rispetto all'attività dello stesso nel sistema batch. Ciò mostra che la scala e la fluidodinamica del reattore influenzano la velocità di reazione dell'enzima. Anche la determinazione dei parametri cinetici ha mostrato che la reazione è più rapida nel microreattore rispetto al sistema batch. Inoltre, la velocità di reazione dell'enzima $\omega-$Transaminasi è risultata più alta in microreattori con un più alto rapporto superficie/volume.

Gli esperimenti effettuati con l'enzima glucosio ossidasi hanno mostrato la presenza di adsorbimento dell'enzima sulle pareti del reattore, la quale è stata qualitativamente verificata con simulazioni CFD che includono un modello di adsorbimento. La sola ritenzione idrodinamica, infatti, non è riuscita a spiegare le evidenze sperimentali.

Conclusione È stato trovato che sia la fluidodinamica del reattore sia il rapporto superficie/volume del microreattore hanno influenza sulla cinetica di reazione dell'enzima $\omega-$Transaminasi. La presenza di un fenomeno superficiale quale l'adsorbimento dell'enzima è stata verificata sperimentalmente con l'enzima glucosio ossidasi; infine, le simulazioni CFD che includono il modello di adsorbimento dell'enzima glucosio ossidasi alle pareti del microreattore verificano l'ipotesi che l'adsorbimento dell'enzima abbia luogo nei microreattori.

Questi risultati sperimentali aprono la strada alla possibilità di utilizzare piattaforme microfluidiche per la transaminazione con l'enzima $\omega-$Transaminasi, e, probabilmente, per altre reazioni enzimatiche. $\omega-$Transaminasi presenta infatti una attività molto maggiore in reattori confinati con regime di flusso laminare rispetto ai tradizionali reattori batch a parità di condizioni operative; inoltre, ha luogo un adsorbimento del biocatalizzatore sulle superfici per l'elevato rapporto superficie/volume dei microreattori. Tale adsorbimento può essere potenziato con una funzionalizzazione delle superfici. Ciò determina una ulteriore maggiore attività dell'enzima in microreattori rispetto a un sistema diluito batch.

Summary

Enantiomerically pure chiral amines are valuable chemical compounds. They can be produced by traditional chemical routes, for example by crystallization with chiral carboxylic acids and enantioselective reduction of C = N bonds. However, their chemical synthesis remains a challenge. The possibility of preparing chiral amines using biocatalytic routes is becoming more attractive as a result of recent developments in biocatalyst availability, techniques for improving biocatalyst stability and the proper high selectivity and catalytic activity of enzyme catalysis (Turner and Truppo, 2010). Among biocatalytic routes, asymmetric synthesis with $\omega-$transaminase ($\omega-$TAm) represents the future for the synthesis of optically pure active amines since $\omega -$ TAm display high stereoselectivity (Tufvesson et al., 2011).

The kinetic mechanism of $\omega -$ TAm is well studied in diluted solutions in batch systems. In recent years, researchers have moved their interest towards space-confined systems, which can well mimic the confined and crowded environment in living systems. This is why the enzymatic reaction catalysed by $\omega -$ TAm is studied in a microreactor in order to test how an enzymatic reaction performs in a space-confined system.

The reactions used in this work are transamination catalysed by $\omega-$TAm and oxidation of glucose catalysed by glucose oxidase (GOx). Activity, kinetic parameters and reaction rate in reactors with a different surface-area-to-volume ratio (SA:V) have been measured for the enzyme $\omega-$TAm, in order to determine the dependence of enzymatic reaction kinetics on scale and geometry of the reactor. The investigation of the presence of adsorption of the enzyme on the walls and/or hydrodynamic retention of the enzyme has been investigated through *ad hoc* experiments with the enzyme GOx. The reaction catalysed by GOx has also been studied through CFD simulations, including a model for adsorption, to verify the experimental results.

It has been found that reactor scale and geometry have an influence on the reaction kinetics of the enzyme $\omega-$TAm, and that the CFD simulation including an adsorption model verify the hypothesis that enzyme adsorption to the reactor walls occurs.

Contents

Chapter 3 - Methods 47

List of Figures

List of Tables

Introduction

A vast majority of drugs are amines or contain functional groups derived from amines, and an increasing number of these molecules are chiral and nonracemic. Thus, there is the need for efficient methods for the preparation of enantiomerically pure chiral amines. However, their chemical synthesis remains a challenge. The possibility of preparing chiral amines using biocatalytic routes is becoming more attractive as a result of recent developments in biocatalyst availability, techniques for improving biocatalyst stability and proper high selectivity and catalytic activity of enzyme catalysis. Among biocatalytic routes, asymmetric synthesis with the enzyme $\omega-$Transaminase represents the future for the synthesis of optically pure active amines.

For the effective implementation of a biocatalyst in a process, detailed knowledge about its reaction kinetics is essential, in order to provide an insight into the biocatalyst performance and effectiveness. The kinetic mechanism of the enzyme $\omega-$Transaminase is well studied in diluted solutions in batch systems. However, in recent years, researchers have moved their interest towards space-confined systems, which can well mimic the confined and crowded environment in living systems. Since enzymes are actually catalysts in such environment in biological cells, it is expected that the recreation of their natural environment will enhance their catalytic activity compared to a diluted batch system. Nevertheless, the quantification of the change of enzyme activity from a batch system to a microreactor is not known yet.

The aim of this work is the experimental investigation of the kinetics of the enzyme $\omega-$Transaminase in microfluidic platforms, in order to test how this enzymatic reaction performs in a space-confined system compared to a batch system, in relation to the fluid dynamics and the scale of the reactor. The effect of the surface-area-to-volume ratio of the microreactor on the reaction rate is also studied experimentally. In addition, the presence of other physical phenomena related to the surface is investigated experimentally by analysing the reaction rate of the enzyme glucose oxidase. The physical modeling of the system is done using Computational Fluid Dynamics (CFD), since the flow in microreactors is laminar and a local and accurate description of the physics of the system can be achieved. CFD is suggested as an important supporting tool to develop processes at microscale, gain knowledge of the reaction kinetics and collect data for process development and scale-up.

The structure of the thesis is as follows. The first Chapter contains the theoretical background; it explains the uses of chiral amines and the chemical routes for their production. Then, it focuses on biocatalytic routes for the production of chiral amines, outlining asymmetric synthesis with $\omega-$Transaminase as the most promising biocatalytic route. One Section of the Chapter thoroughly describes the kinetics and the kinetic model of $\omega-$Transaminase, followed by a literature review regarding the current investigations of enzyme kinetics in microreactors. At the end, it describes the kinetics of the enzyme glucose oxidase and general concepts about on line measurement in microfluidic platforms.

The second Chapter gives a thorough description of the material used in the experimental work; the Chapter is structured into two Sections: the first one describes the material used for the experiments with $\omega-$Transaminase, and the second one explains the one used for the enzyme glucose oxidase, as well as the software used for the CFD simulations.

The third Chapter describes the experimental and simulation methods; the first part of the Chapter is about the experimental methods used for the enzyme $\omega-$Transaminase, and the second one describes the experimental and simulation methods used for the enzyme glucose oxidase.

The fourth Chapter presents the results obtained from the experimental work with the enzyme $\omega-$Transaminase; they are followed by the experimental results obtained with the enzyme glucose oxidase. The Chapter is concluded by the main results of the CFD simulations.

The fifth Chapter contains the analysis and discussion of the results presented in the previous Chapter. It discusses the results of the experiments with the enzyme $\omega-$Transaminase and it compares them with the available literature, The Conclusion Chapter presents a summary of this work and, specially, of its results and outlines the future work.

Chapter 1

Theoretical background

This Chapther describes the main uses of chiral amines and the mostly used chemical and biochemical routes to produce them. Since transamination with the enzyme ω-Transaminase is the most promising strategy among biocatalytic routes, the reaction kinetics and mechanism of ω-Transaminase are described. The behaviour of the enzyme is qualitatively compared in batch reactors and in microreactors. The Chapter concludes with the description of the kinetics of the enzyme glucose oxidase, used to investigate the behaviour of enzymes in microfluidic platforms.

1.1 Chiral amines

Enantiomerically pure chiral amines are powerful pharmacophores for defining new pharmaceutical drugs due to their highly valuable functionalized molecular structure and intrinsic ability for hydrogen bonding (Nugent and El-Shazly, 2010; Turner and Truppo, 2010). Their wide range of applications includes intermediates for the synthesis of drugs as well as Active Pharmaceutical Ingredients (APIs) and agrochemical active ingredients, for which both a high degree of purity and large quantities of the compounds are required, resolving agents for separation of enantiomers via diastereomeric salt formation and ligands for the asymmetric synthesis using either transition metal catalyst or organocatalysis (Breuer et al., 2004; Turner and Truppo, 2010). Some examples of pharmaceutical drugs containing chiral amines are shown in Figure 1.1, in order to prove the broad range of applications of chiral amines in the products of pharmaceutical industry.

(a) Codeine, pain relief (Johnson Matthey)

(b) Lariam, malaria (Roche)

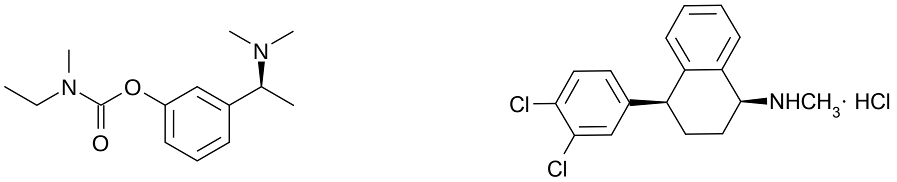

(c) Rivastigmine, Alzheimer´s (Novartis)

(d) Zoloft/Sertraline, depression (Pfeizer)

Figure 1.1 *Examples of non-amino acid based chiral amine pharmaceutical drugs. Adapted from Nugent and El-Shazly (2010).*

It is estimated that the total revenue from sales in the pharmaceutical and agrochemical industries for the year 2000 was more than 20 billion of Euro. Optically active intermediates used as chemical building blocks, auxiliaries, or advanced intermediates accounted for 15% of this market, and it is expected that this fraction will increase continuously, since the demand in the pharmaceutical industry for optically active intermediates increases at about 10% annually (while other special intermediates are increasing at about 7– 8% annually) (Breuer et al., 2004). Looking specifically only into the amines market (which is part of the market of all optically active compounds such as alcohols, carboxylic acids, amino acids and epoxides), it will grow 5% over the next decade according to BASF (Stanton, 2014).

The introduction of enantiopure active substances is also enforced through the strict regulations of the US Food and Drug Administration (FDA) and European Committee for Proprietary Medicinal Products, the authorities responsible for the registration of new active compounds. They require the complete characterization of the physiological action of each enantiomer of a pharmaceutical product and increasingly demand the targeted synthesis of one stereoisomer (Breuer et al., 2004).

Therefore, both economical reasons and regulatory issues have driven the development of new technologies and their implementation in large-scale industrial processes in order to open up new perspectives and economically more attractive methods for the production of active compounds in large amounts with high optical purity, which was limited before (Breuer et al., 2004).

1.2 Synthesis of chiral amines

Despite the need for and continued interest in enantiomerically pure chiral amines, their synthesis remains a challenge because of the introduction of nitrogen into a commodity chemical or an advanced intermediate via an operationally simple, preferably one-step, procedure, allowing high chemo-, regio-, distereo-, and enantiocontrol (Nugent and El-Shazly, 2010). The chemical industry has primarily relied upon established chemical routes for the synthesis of enantiomerically pure chiral amines, but it is now turning more and more to biocatalytic and biotechnological fermentation processes (Breuer et al., 2004). The possibility of preparing chiral amines using biocatalytic routes is becoming more attractive as a result of recent developments in biocatalyst availability, techniques for improving biocatalyst stability and the proper high selectivity and catalytic activity of enzyme catalysis (Turner and Truppo, 2010).

1.2.1 Chemical routes

The two mostly used chemical routes for the production of enantiomerically pure chiral amines are crystallization with chiral carboxylic acids and enantioselective reduction of $C = N$ bonds. These two routes are described below in this Section.

1.2.1.1 Crystallization with chiral carboxylic acids

The crystallization of diastereomeric salts of chiral carboxylic acids with racemic amines is the most widely used technique in industry; this method allows the isolation of (S) or (R) chiral amines as well as (S) or (R) carboxylic acids on an industrial scale (Breuer et al., 2004; Neto, 2013). The process is based on the transformation of enantiomers into diastereomers by addition of a resolving agent, since pairs of diastereomers have different chemical and physical properties thus they can be separated by conventional separation

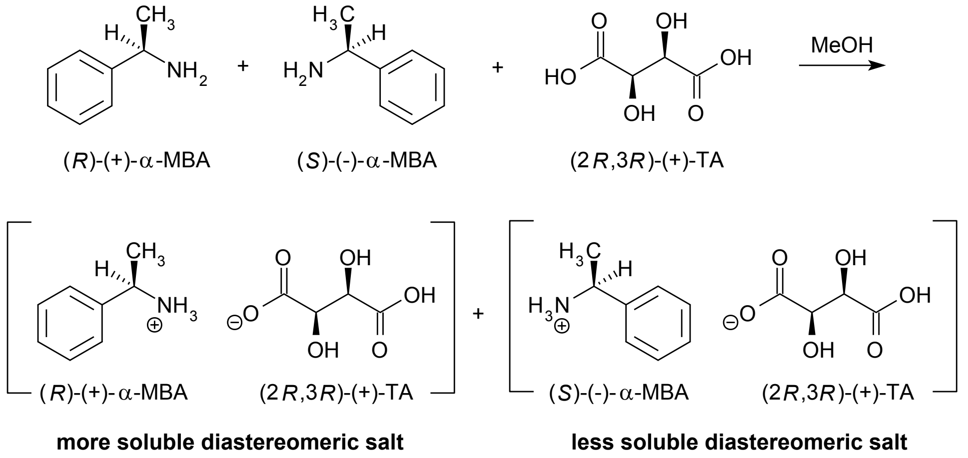

(a) Diastereomeric salts formation from racemic α−Methylbenzylamine (α-MBA) and enantiomerically pure $(2R,3R)-(+)-$Tartaric acid ($(2R,3R)-(+)-$TA).

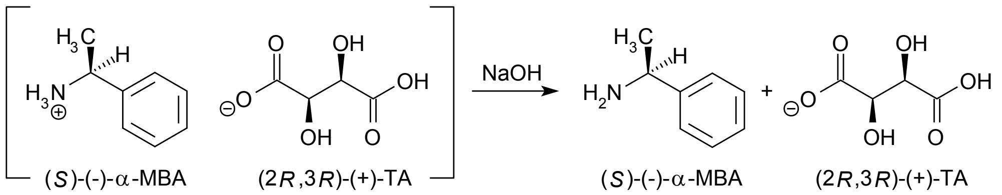

(b) Recover of the product from the less soluble $(S)-(-)-\alpha-$Methylbenzylamine $(2R,3R)-$Tartaric acid ($(S)-(-)-\alpha-$MBA $(2R,3R)-$TA) diastereomeric salt.

Figure 1.2 *Racemate resolution of α-Methylbenzylamine ($\alpha-$MBA) through fractional distillation. Adapted from Ault (1965).*

methods such as crystallization (while enantiomers have identical chemical and physical properties except for their ability to rotate plane-polarized light and their separation is not possible). In the case of amines, an enantiomerically pure carboxylic acid (the resolving agent) is added to a racemic mixture of amines and a pair of diastereomeric salts is formed (the equilibrium of the reaction is in favour of the products since it is an acid-base reaction). Depending on the difference in the chemical and physical properties of the diastereomers, a suitable separation method is to be selected. Usually, the different solubility of the diastereomers in a certain solvent is exploited: the less soluble enantiomer is separated and, by addition of proper solvents, the remaining carboxylic acid is removed (Breuer et al., 2004).

For instance, racemic $\alpha-$Methylbenzylamine ($\alpha-$MBA) reacts with enantiomerically pure $(2R,3R)-(+)-$Tartaric acid ($(2R,3R)-(+)-$TA) to form diastereomeric salts which can be separated by selective crystallization from methanol, since the $(R)-(+)-\alpha-$MBA $(2R,3R)-$TA complex is more soluble in methanol than $(S)-(-)-$

$\alpha-$MBA $(2R,3R)-$TA complex (Figure 1.2a). The isolated salt $((S)-(-)-\alpha-$MBA $(2R,3R)-$TA) will be converted to the optically active free base by treatment with sodium hydroxide in order to isolate the product $(S)-\alpha-$MBA (Figure 1.2b) (Ault, 1965).

The main drawbacks of this method are related to the screening and the selection of suitable resolving agents for the amine, which can require a long time, and the limit of 50 % of yield that is possible to achieve.

1.2.1.2 Enantioselective reduction of C=N bonds

Optically active amines can be chemically produced by reduction of a C - N double bond from a prochiral precursor (a molecule that can be converted from achiral to chiral in a single step). This is the case of a prochiral imines that can undergo enantioselective reduction of their $C=N$ bond. The whole process is shown in Figure 1.3: an imine, in particular a secondary ketimine, is first reduced forming a chiral compound, and after the auxiliary group X (phenyl, substituted phenyl, sulfonyl, benzyl, alkoxy, aryl, alkyl or amino group) of the prochiral precursor is cleaved giving the desired chiral amine. The auxiliary group X is added to the imine in order to N-activate it.

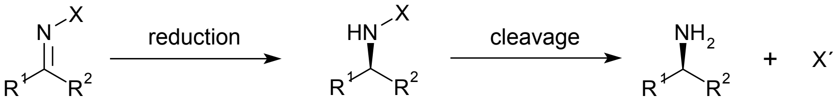

Figure 1.3 *Reduction and cleavage of a prochiral precursor with a C - N double bond and auxiliary group X for the enantioselective synthesis of an amine.*

The main strategies for targeting the desired enantiomerically pure product are the use of transition metal-mediated homogeneous catalysis and organocatalytic methods, as well as different chiral homogeneous catalysts in combination with molecular hydrogen (Breuer et al., 2004; Nugent and El-Shazly, 2010). Homogeneous catalysis has been replacing the more common use of heterogeneous catalysts such as palladium, rhodium and nichel Raney (Breuer et al., 2004; Nugent and El-Shazly, 2010).

The major challenges are related to the preparation of the prochiral precursor, the screening effort for the selection of a reducing agent, the subsequent cleavage of the auxiliary group to give the free amine and the use of precious metals, which increase the cost of the process (Neto, 2013).

1.2.2 Biocatalytic routes

An alternative method to produce enantiomerically pure chiral amines makes use of biocatalysis to selectively yield the target product from a wide range of substrates. Biocatalytic processes have developed as an environmentally friendly alternative to chemical processes, operating under mild conditions and avoiding the need for highly flammable metal-organic reagents and contamination from heavy metal (Höhne and Bornscheuer, 2009).

Three general approaches have been developed for the preparation of enantiomerically pure chiral amines (Turner and Truppo, 2010):

1. kinetic resolution (KR) of racemic amines
2. dynamic kinetic resolution (DKR) and deracemization of racemic amines
3. asymmetric synthesis (AS) of pure chiral amines.

1.2.2.1 Kinetic resolution of racemic amines

Kinetic resolution (KR) is a mean for separating two enantiomers in a racemic mixture due to the different chemical reactivity of the enantiomers in the racemate with a chiral catalyst or reagent. Thus, the reaction rate of the enantiomers are different (enantioselective reaction), resulting in a continuous rise of the enantiomeric excess[1] (*ee*) of the less reactive enantiomer as the reaction proceeds, reaching theoretically 100 % (Kagan and Fiaud, 1988). Although this approach is efficient in terms of producing highly enantiomerically pure compounds, its maximum theoretical yield is limited to 50 %.

The use of enzymes as catalysts for the KR of racemic organic substances is of interest because enzymes can catalyze a great variety of organic reactions with high efficiency operating under mild conditions (for both temperature and pH) preserving the integrity of functional groups of the substrate. Among the six main groups of enzymes, hydrolases and oxido-reductases have been so far the most frequently used in kinetic resolution

---

[1] The enantiomeric excess is defined as the difference of the amounts of the two enantiomers over the amount of both enantiomers, i.e.

$$ee = \frac{R-S}{R+S} \cdot 100$$

(Kagan and Fiaud, 1988).

Hydrolytic enzymes Hydrolytic enzymes have been used for the KR of racemic alcohols and carboxylic acids, and in recent years they have been applied to resolution of racemic amines as well. Most of the reported examples are performed under low water conditions, with *Candida antarctica* lipase B (CAL-B) as the most commonly employed hydolase (Figure 1.4). An example of large-scale application of lipase-catalyzed resolution of amines is the process performed at BASF, which has a production capacity larger than 3000 ton per year of a wide variety of enantiomerically pure aryl and alkyl amines (Turner and Truppo, 2010).

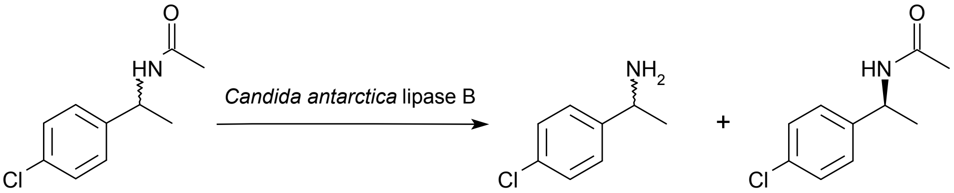

***Figure 1.4** Lipase-catalyzed resolution of racemic (+/-)-N-1-4-chlorophenylethylacetamide. Adapted from Turner and Truppo (2010).*

Besides lipases, proteases, amidases and acylases have also been tested; while lipases and proteases are typically commercially available, amidases and acylases need to be separated from microorganisms.

Transaminases Transaminases (TAm), in the form of ω−Transaminases (ω – TAm)[2], have developed as an alternative methodology for KR of racemic amines. ω – TAm have the unique feature that they can be employed also for AS, as will be discussed in § 1.2.2.3 on page 14 (Turner and Truppo, 2010). ω – TAm are pyridoxal-5′-phosphate (PLP) dependent enzymes that catalyse the transfer of an amine group to a carbonyl compound, i.e. the amine group acceptor, such as a ketone, aldehyde or a keto acid. As an example, Celgene developed a process on a 2.5 m^3 scale for the KR of several different aliphatic and aromatic amines using propionaldehyde as the amine group acceptor (Figure 1.5) (Breuer et al., 2004; Nugent and El-Shazly, 2010).

---

[2] ω – TAm are able to accept aliphatic ketones and amines as their substrates, not only keto acids and amino acids, whereas another type of TA, α – TAm, require the presence of the carboxylic acid group in the α position to the keto or amine functionality and hence allow only the formation of α-amino acids (Cassimjee, 2012; Höhne and Bornscheuer, 2009).

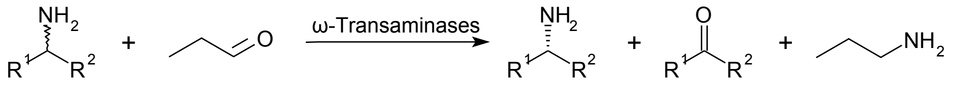

Figure 1.5 *Kinetic resolution with $\omega-$Transaminases and propionaldehyde as the amine group acceptor. Adapted from Turner and Truppo (2010).*

The main advantages of using $\omega-$TAm are the high enantioselectivity for (*S*) enantiomers and the low cost of the amine donor compounds. On the other hand, the lack of (*R*)-selective enzymes hinders the applicability of $\omega-$TAm, together with relatively low product concentration achievable (as it is expected for aqueous reaction system with hydrophobic compounds), inhibition of caused by both the amine product and the ketone substrate (Turner and Truppo, 2010).

1.2.2.2 Dynamic kinetic resolution and racemization of racemic amines

The resolution of racemates is a very important industrial approach in the synthesis of enantiomerically pure compounds; however, KR has the limitation of having a maximum theoretical yield of 50 %. Dynamic kinetic resolution (DKR) represents the evolution of KR since it has the goal to achieve higher yields with the same enantiomeric purity; DKR combines the resolution step of KR with an *in situ* racemisation of the unreactive enantiomer, allowing the conversion of all of the substrate into a single product isomer with a 100 % theoretical yield (Figure 1.6).

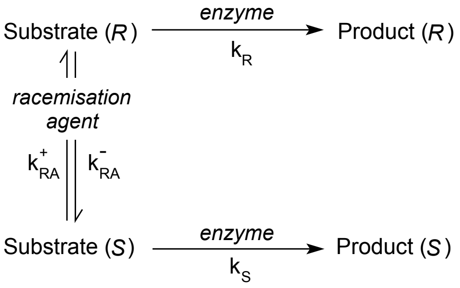

Figure 1.6 *Reaction scheme for dynamic kinetic resolution. For each reaction, the catalyst is written in italics. k_R, k_S, k^+_{RA} and k^-_{RA} are the kinetic constants of each reaction. Adapted from El Gihani and Williams (1999).*

The racemisation of the substrate must occur more rapidly than the resolution, so as not to become the rate determining step of DKR, i.e. $k^{+}_{\mathrm{RA}} > k_{\mathrm{R}}$ (El Gihani and Williams, 1999). The racemisation of the unreactive enantiomer is achieved with a chemocatalyst (a racemisation agent RA) under the reaction conditions of the biocatalyst, which is responsible for the kinetic resolution step. The main issues of DKR are finding conditions under which the biocatalyst and the chemocatalyst can function efficiently together and the chemocatalyst itself, which has to catalyse the selective racemisation of the substrate but not of the product. Several types of enzymes can be used for DKR, and most of them are the same that can be used of KR.

Hydrolytic enzymes Hydrolytic enzymes can be used for DKR as they are used in KR since the resolution reaction is the same in both processes; in this case lipases such as CAL-B are used together with a chemocatalyst such as palladium, ruthenium or iridium. Typical values for the *ee* are above 99 %, and the range of the yields is from 60 to 99 %, yet overcoming the limitation of the yield of KR (Turner and Truppo, 2010).

Amine oxidases Monoamine oxidase N (MAO-N) from *Aspergillus niger* catalyses the enantioselective oxidation of one enantiomer of a racemic mixture to the corresponding imine. A chemical reducing agent is added to the reaction in order to reduce the imine back to the racemic amine, preventing imine hydrolysis. The racemic amine can then undergo another enantioselective oxidation to the imine. The whole process is shown in Figure 1.7.

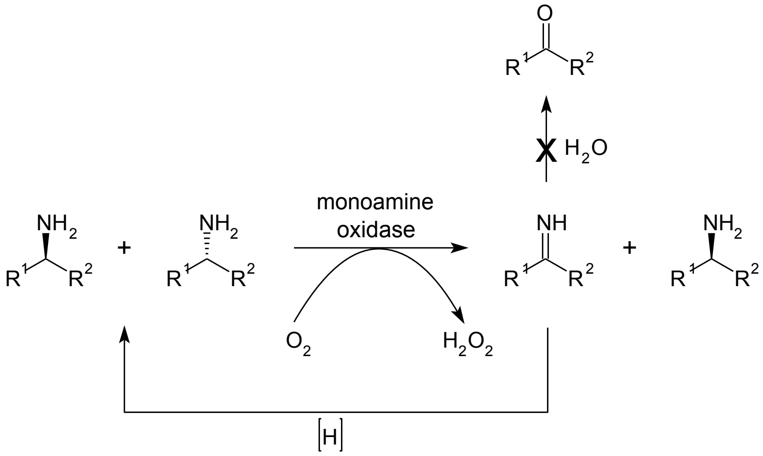

Figure 1.7 Dynamic kinetic resolution of racemic amines using monoamine oxidases. Adapted from Neto (2013).

If the enzyme is highly enantioselective, the theoretical yield and the *ee* of one enantiomer of the amine will both be 100 %. In order to make this method applicable to a wide range of substrates, monoamine oxidases with a broad substrate specificity and high enantioselectivity need to be identified (Turner and Truppo, 2010).

1.2.2.3 Asymmetric synthesis

In asymmetric synthesis (AS) enzymes are used to yield exclusively the enantiomer of interest with a theoretical yield of 100 %, thus both targets, i.e. high enantiomeric purity of the product and high process yield, are achieved in the approach of AS; this is why AS is continuously attracting interest. Chiral amines can be produced by AS using imine reductases, amine dehydrogenases and $\omega-$TAm. The first option is the less explored one, while the last one is the most promising, since presently it offers the unique possibility to synthesize optically active amines directly from ketones with a theoretically quantitative yield (Höhne and Bornscheuer, 2009).

Imine reductases Enantiomerically pure amines can be produced by reduction of imines with imine reductases. The enzyme is not extensively studied yet, thus further investigations are required to render its use versatile for organic synthesis (Höhne and Bornscheuer, 2009). An example of its application, which gave moderate yield and 99 % of *ee* is shown in Figure 1.8 (Höhne and Bornscheuer, 2009).

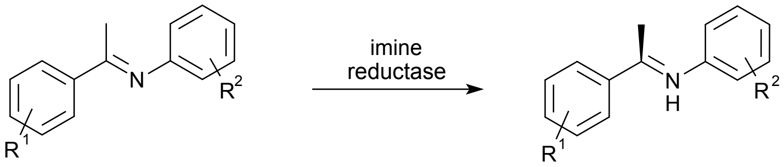

Figure 1.8 Asymmetric synthesis with imine reductases. Adapted from Höhne and Bornscheuer (2009).

Amine dehydrogenases Amine dehydrogenases oxidize amines to ketones and ammonia, in presence of a redox co-factor used as electron acceptors, such as copper proteins or artificial redox mediators. Recycle of the co-factor is required for the feasibility of the process, thus only NADH-dependent enzymes are of interest since in this case a recycle and a regeneration of the co-factor is possible (for example reduction of formate with formate dehydrogenase) (Höhne and Bornscheuer, 2009). However, the use of NADH-dependent enzymes is limited by the expense of the co-factor. So far, there is only one

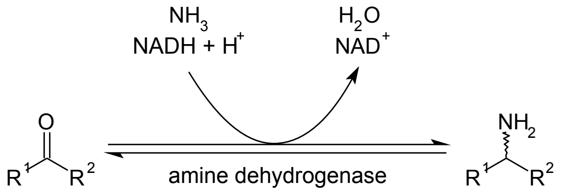

Figure 1.9 Asymmetric synthesis with amine dehydrogenases. Adapted from Höhne and Bornscheuer (2009).

known amine dehydrogenases (purified from *Streptomyces virginiae*) that accepts NADH as a co-factor; this enzyme can convert a very broad range of substrates, with the limitation of low enantioselectivity (Höhne and Bornscheuer, 2009). The reaction is shown in Figure 1.9.

Transaminases The use of TAm in the form of $\omega - \text{TAm}$ for AS is the most promising strategy, since the enzyme is well studied and it avoids the problem of the co-factor recycle and regeneration even though, as explained in § 1.2.2.1 on page 10, $\omega - \text{TAm}$ requires the addition of a different co-factor, i.e. PLP, to act as a shuttle for the transfer of the amine group. TAm catalyze the transfer of an amine group from an amine donor, usually an amino acid or a simple amine, to a prochiral acceptor ketone, yielding a chiral amine as well as a co-product ketone or alpha-keto acid, as shown in Figure 1.10.

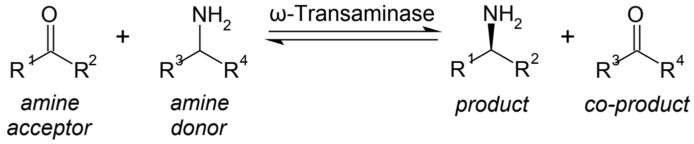

Figure 1.10 Asymmetric synthesis with transaminases.

$\omega - \text{TAm}$ are suitable catalysts due to their high stereoselectivity and ability to operate under environmentally mild reaction conditions. Therefore, nowadays, AS with $\omega - \text{TAm}$ represents the future for the synthesis of optically pure active amines (in spite of some challenges that will be addressed in § 1.3.3 on page 21) (Tufvesson et al., 2011).

Since it is so attractive, this process has been investigated from two complementary points of view. On the one hand, the enzyme itself has been studied, focusing on its reaction mechanism, inhibition, reaction conditions and kinetics, in order to achieve high enzyme activity. On the other hand, process engineering and separation techniques have been applied to AS with $\omega-$TAm in order to render this technology applicable for processes at large scale, which are required to be efficient, economic and green. In this work, the focus is on the enzyme kinetics, which is studied both in batch reactors and in micro-systems.

1.3 Reaction kinetics of $\omega-$TAm

Detailed knowledge about the reaction kinetics of a biocatalyst is essential for its effective implementation in a process. Additionally, the determination of the kinetic parameters (such as the Michaelis-Menten constant, the maximum reaction rate and the inhibition constants) provides an insight into the biocatalyst performance and effectiveness. The kinetic parameters can be used to derive the reaction equilibrium, which is essential in defining appropriate process operating strategies. Furthermore, the quantification of the parameters is useful as a guidance for biocatalyst improvement (Al-Haque, 2012). Specially in the case of transamination, which is strongly limited by substrate and product inhibition and unfavorable reaction equilibrium, the determination of the kinetic model and its parameters is essential for predicting the behaviour of the reaction under different process conditions.

1.3.1 Reaction mechanism

Transaminases requires the co-factor PLP to transfer the amino group from the amine donor to the amine acceptor; during the transamination, PLP alternates between its aldehyde form, i.e. PLP, and its amine form, pyridoxamine-5-phosphate (PMP). The transfer of the amino group can be performed either as kinetic resolution of racemic amines (§ 1.2.2.1 on page 10) or as asymmetric synthesis from a prochiral ketone (§ 1.2.2.3 on page 14).

The enzyme is known to follow the Ping-Pong bi-bi mechanism, a mechanism for molti-substrate enzymes (Figure 1.11). The first part of the mechanism consists of the binding of the amine donor (species A in Figure 1.11a) to the enzyme E (and the co-factor PLP) and the subsequent formation and release of the co-product P from the "altered" structure of the enzyme E´; thus, the co-product is released before that the second

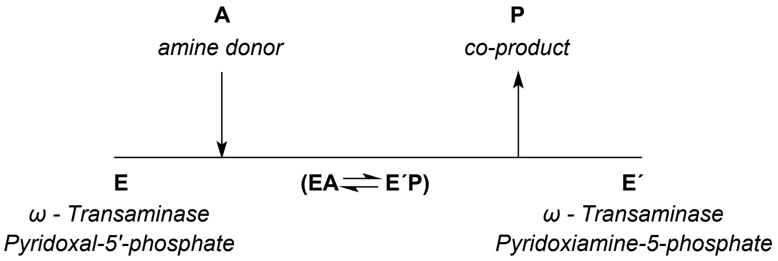

(a) Release of the co-product from the binding of the amine donor to the complex of the enzyme and the co-factor.

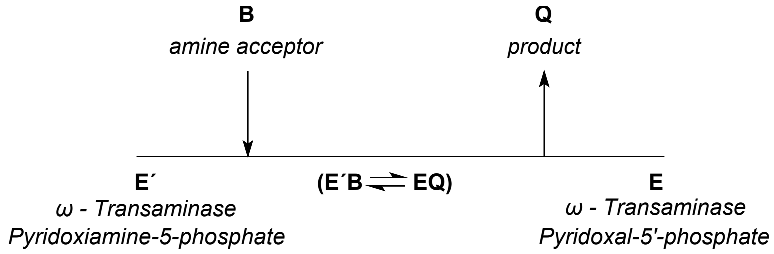

(b) Release of the product from the binding of the amine acceptor to the complex of the enzyme and the co-factor.

Figure 1.11 *Ping-Pong bi-bi mechanism in the Cleland notation for the enzyme $\omega-$ Transaminase.*

substrate, i.e. the amine acceptor B, is bound to the enzyme (Figure 1.11b), giving the product Q, which is the desired product, and restoring the enzyme back to its original form.

1.3.2 Kinetic model

Based on the general reaction mechanism explained in §1.3.1, the kinetic model can be formulated as

$$v = v_{\mathrm{Q}} = -v_{\mathrm{A}} = \frac{c_{\mathrm{E0}} k^{\mathrm{r}}_{\mathrm{cat}} k^{\mathrm{f}}_{\mathrm{cat}} \left(\gamma c_{\mathrm{A}} c_{\mathrm{B}} - \lambda \frac{c_{\mathrm{P}} c_{\mathrm{Q}}}{K_{\mathrm{EQ}}} \right) \left(1 + \frac{c_{\mathrm{I}}}{K^{\mathrm{I}}_{\mathrm{Si}}} \right)}{k^{\mathrm{r}}_{\mathrm{cat}} K^{\mathrm{B}}_{\mathrm{M}} c_{\mathrm{A}} \gamma + k^{\mathrm{r}}_{\mathrm{cat}} K^{\mathrm{A}}_{\mathrm{M}} c_{\mathrm{B}} \gamma + \frac{k^{\mathrm{f}}_{\mathrm{cat}} K^{\mathrm{Q}}_{\mathrm{M}}}{K_{\mathrm{EQ}}} c_{\mathrm{P}} \lambda + \frac{k^{\mathrm{f}}_{\mathrm{cat}} K^{\mathrm{P}}_{\mathrm{M}}}{K_{\mathrm{EQ}}} c_{\mathrm{Q}} \lambda} \cdot$$

$$\cdot \frac{1}{k^{\mathrm{r}}_{\mathrm{cat}} c_{\mathrm{A}} c_{\mathrm{B}} \gamma + \frac{k^{\mathrm{f}}_{\mathrm{cat}} K^{\mathrm{Q}}_{\mathrm{M}}}{K^{\mathrm{A}}_{\mathrm{i}} K_{\mathrm{EQ}}} c_{\mathrm{A}} c_{\mathrm{P}} \gamma \lambda + \frac{k^{\mathrm{f}}_{\mathrm{cat}}}{K_{\mathrm{EQ}}} c_{\mathrm{P}} c_{\mathrm{Q}} \lambda + \frac{k^{\mathrm{r}}_{\mathrm{cat}} K^{\mathrm{A}}_{\mathrm{M}}}{K^{\mathrm{Q}}_{\mathrm{i}}} c_{\mathrm{B}} c_{\mathrm{Q}} \gamma \lambda} \tag{1.1}$$

where c_{A} (mM), c_{B} (mM), c_{P} (mM), c_{Q} (mM) and c_{I} (mM) are the concentration of species A, B, P, Q and inhibitory compounds, respectively (species as in Figure 1.11), c_{E0} ($\mathrm{g \cdot l^{-1}}$) is the initial concentration of the enzyme, $k_{\mathrm{cat}}^{\mathrm{f}}$ ($\mathrm{min^{-1}}$) and $k_{\mathrm{cat}}^{\mathrm{r}}$ ($\mathrm{min^{-1}}$) are the turnover rates of the forward and reverse reaction, $K_{\mathrm{Si}}^{\mathrm{I}}$ (mM) is the substrate uncompetitive inhibition constant, $K_{\mathrm{i}}^{\mathrm{A}}$ (mM) and $K_{\mathrm{i}}^{\mathrm{Q}}$ (mM) are the competitive inhibition constants, $K_{\mathrm{M}}^{\mathrm{A}}$ (mM), $K_{\mathrm{M}}^{\mathrm{B}}$ (mM), $K_{\mathrm{M}}^{\mathrm{P}}$ (mM) and $K_{\mathrm{M}}^{\mathrm{Q}}$ (mM) are the Michealis-Menten constants for each species (Al-Haque et al., 2012). K_{EQ} is the chemical equilibrium constant and it can be expressed with a constitutive equation using the Haldane relation

$$K_{\mathrm{EQ}} = \left(\frac{k_{\mathrm{cat}}^{\mathrm{f}}}{k_{\mathrm{cat}}^{\mathrm{r}}}\right) \frac{K_{\mathrm{M}}^{\mathrm{P}} K_{\mathrm{M}}^{\mathrm{Q}}}{K_{\mathrm{M}}^{\mathrm{A}} K_{\mathrm{M}}^{\mathrm{B}}} \tag{1.2}$$

γ and λ are the binary indicators for the direction of the reaction, being the former the indicator for the forward reaction and the latter the indicator for the reverse reaction. They can be used to decompose the model to simpler ones which are valid only for initial reaction rate, i.e. when product concentration and the reversibility of the reaction are negligible. Thus, by considering $\gamma = 1$, $\lambda = 0$ the initial rate of the forward reaction is obtained ($-r_{\mathrm{A}} = r_{\mathrm{Q}}$), while $\gamma = 0$ and $\lambda = 1$ give the initial rate of the reverse reaction ($r_{\mathrm{A}} = -r_{\mathrm{Q}}$). The rate at equilibrium corresponds to the combination $\gamma = \lambda = 1$.

From now on, in order to consider a particular example of a transamination, the reaction in Figure 1.12 will be used.

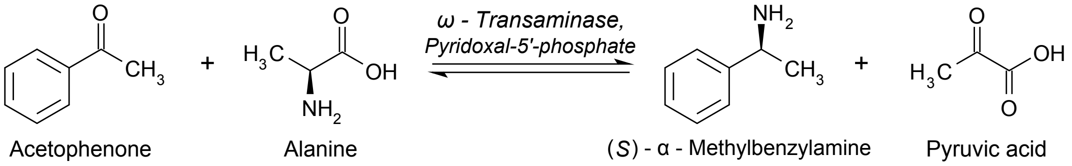

Figure 1.12 *Transamination catalysed by $\omega-$Transaminase with the co-factor Pyridoxal-5'-phosphate, for the production of $(S)-\alpha-$Methylbenzylamine and pyruvic acid using acetophenone as the amine acceptor and alanine as the amine donor.*

The reaction has $(S) - \alpha -$ MBA as the enantiomerically pure chiral amine, pyruvic acid (PYR) as the co-product, acetophenone (APH) as the amine acceptor and alanine (ALA) as the amine donor.

The kinetic model of the rate equation is derived based on the King-Altman method (Figure 1.13) Al-Haque et al. (2012). The kinetic model that will be presented is adapted from (Al-Haque et al., 2012), where the model is written for the same type of reaction but with another amine donor (2-propylamine instead of ALA), that leads to the formation of another co-product (acetone instead of PYR).

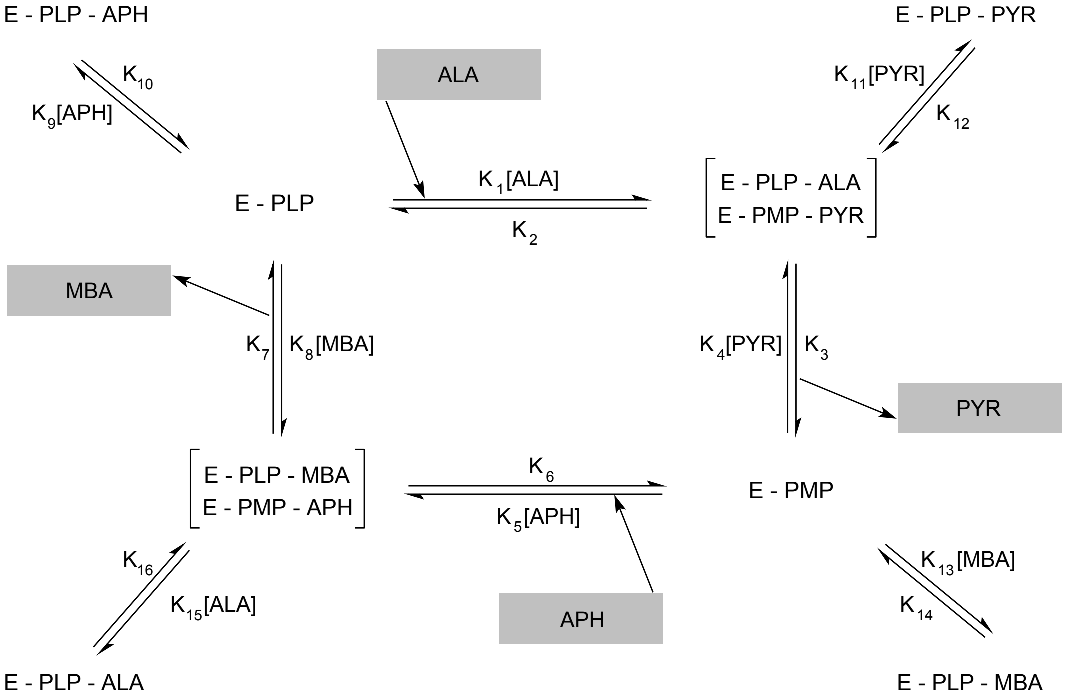

Figure 1.13 *King-Altman representation of the ω−Transaminase reaction mechanism. Substrates and products that have to be bound or released in order to from the desired product are shaded in light grey. (ALA = alanine, APH = acetophenone, E = ω−Transaminase,* K_i *= kinetic constant of the reaction i, MBA = Methylbenzylamine, PLP = pyridoxal-5'-phosphate, PMP = pyridoxiamine-5-phosphate, PYR = pyruvic acid). Adapted from Al-Haque et al. (2012).*

The mechanism includes the formation of four nonproductive complexes ($\mathrm{E-PLP-APH}$, $\mathrm{E-PMP-ALA}$, $\mathrm{E-PMP-MBA}$ and $\mathrm{E-PLP-PYR}$). The complete rate equation is

$$v = v_{\mathrm{MBA}} = -v_{\mathrm{APH}} =$$

$$= \frac{c_{\mathrm{E0}} k^{\mathrm{r}}_{\mathrm{cat}} k^{\mathrm{f}}_{\mathrm{cat}} \left(\gamma c_{\mathrm{ALA}} c_{\mathrm{APH}} - \lambda \frac{c_{\mathrm{PYR}} c_{\mathrm{MBA}}}{K_{\mathrm{EQ}}} \right)}{k^{\mathrm{r}}_{\mathrm{cat}} K^{\mathrm{APH}}_{\mathrm{M}} c_{\mathrm{ALA}} \gamma \left(1 + \frac{c_{\mathrm{ALA}}}{K^{\mathrm{ALA}}_{\mathrm{Si}}} + \lambda \frac{c_{\mathrm{MBA}}}{K^{\mathrm{MBA}}_{\mathrm{Si}}}\right) + k^{\mathrm{r}}_{\mathrm{cat}} K^{\mathrm{ALA}}_{\mathrm{M}} c_{\mathrm{APH}} \gamma \left(1 + \frac{c_{\mathrm{APH}}}{K^{\mathrm{APH}}_{\mathrm{Si}}} + \lambda \frac{c_{\mathrm{PYR}}}{K^{\mathrm{PYR}}_{\mathrm{Si}}}\right)} \cdot$$

$$\cdot \frac{1}{k^{\mathrm{f}}_{\mathrm{cat}} \frac{K^{\mathrm{MBA}}_{\mathrm{M}} c_{\mathrm{PYR}}}{K_{\mathrm{EQ}}} \lambda \left(1 + \frac{c_{\mathrm{APH}}}{K^{\mathrm{APH}}_{\mathrm{Si}}} + \gamma \frac{c_{\mathrm{PYR}}}{K^{\mathrm{PYR}}_{\mathrm{Si}}}\right) + k^{\mathrm{f}}_{\mathrm{cat}} \frac{K^{\mathrm{PYR}}_{\mathrm{M}} c_{\mathrm{MBA}}}{K_{\mathrm{EQ}}} \lambda \left(1 + \frac{c_{\mathrm{MBA}}}{K^{\mathrm{MBA}}_{\mathrm{Si}}} + \gamma \frac{c_{\mathrm{ALA}}}{K^{\mathrm{ALA}}_{\mathrm{Si}}}\right)} \cdot$$

$$\cdot \frac{1}{k^{\mathrm{r}}_{\mathrm{cat}} c_{\mathrm{ALA}} c_{\mathrm{APH}} \gamma + k^{\mathrm{f}}_{\mathrm{cat}} \frac{K^{\mathrm{MBA}}_{\mathrm{M}} c_{\mathrm{ALA}} c_{\mathrm{PYR}}}{K_{\mathrm{EQ}} K^{\mathrm{ALA}}_{i}} \gamma\lambda + k^{\mathrm{f}}_{\mathrm{cat}} \frac{c_{\mathrm{PYR}} c_{\mathrm{MBA}}}{K_{\mathrm{EQ}}} \lambda + k^{\mathrm{r}}_{\mathrm{cat}} \frac{K^{\mathrm{ALA}}_{\mathrm{M}} c_{\mathrm{APH}} c_{\mathrm{MBA}}}{K^{\mathrm{MBA}}_{i}} \gamma\lambda} \tag{1.3}$$

where c_{APH} (mM), c_{ALA} (mM), c_{PYR} (mM), c_{MBA} (mM) and c_{E0} (g/l) are the concentration of each species, $K^{\mathrm{APH}}_{\mathrm{M}}$ (mM), $K^{\mathrm{ALA}}_{\mathrm{M}}$ (mM), $K^{\mathrm{PYR}}_{\mathrm{M}}$ (mM) and $K^{\mathrm{MBA}}_{\mathrm{M}}$ (mM) are the Michaelis-Menten constant for each component, $K^{\mathrm{APH}}_{\mathrm{Si}}$ (mM) and $K^{\mathrm{ALA}}_{\mathrm{Si}}$ (mM) are the inhibition constant in the forward direction and $K^{\mathrm{MBA}}_{\mathrm{Si}}$ (mM) and $K^{\mathrm{PYR}}_{\mathrm{Si}}$ (mM) in the reverse direction, and K^{ALA}_{i} (mM) and K^{MBA}_{i} (mM) are the competitive inhibition constants. As it can be seen from the equation, the reaction is influenced by inhibition of the substrate APH and the the product MBA, as well as having unfavourable reaction equilibrium.

If only the initial reaction rate of the forward reaction is considered, the effects of product concentration can be neglected, thus equation (1.3) is simplified into

$$v = v_{\mathrm{MBA}} = -v_{\mathrm{APH}} = \frac{c_{\mathrm{E0}} K^{\mathrm{f}}_{\mathrm{cat}} c_{\mathrm{ALA}} c_{\mathrm{APH}}}{K^{\mathrm{APH}}_{\mathrm{M}} c_{\mathrm{ALA}} \left(1 + \frac{c_{\mathrm{ALA}}}{K^{\mathrm{ALA}}_{\mathrm{Si}}}\right) + K^{\mathrm{ALA}}_{\mathrm{M}} c_{\mathrm{APH}} \left(1 + \frac{c_{\mathrm{APH}}}{K^{\mathrm{APH}}_{\mathrm{Si}}}\right) + c_{\mathrm{ALA}} c_{\mathrm{APH}}} \tag{1.4}$$

substituting $\gamma = 1$ and $\lambda = 0$. Similarly, the initial rate of the reverse reaction is obtained from equation (1.3)

$$v = -v_{\mathrm{MBA}} = v_{\mathrm{APH}} = \frac{c_{\mathrm{E0}} K_{\mathrm{cat}}^{\mathrm{r}} c_{\mathrm{PYR}} c_{\mathrm{MBA}}}{K_{\mathrm{M}}^{\mathrm{MBA}} c_{\mathrm{PYR}} \left(1 + \frac{c_{\mathrm{APH}}}{K_{\mathrm{Si}}^{\mathrm{APH}}}\right) + K_{\mathrm{M}}^{\mathrm{PYR}} c_{\mathrm{MBA}} \left(1 + \frac{c_{\mathrm{MBA}}}{K_{\mathrm{Si}}^{\mathrm{MBA}}}\right) + c_{\mathrm{PYR}} c_{\mathrm{MBA}}} \tag{1.5}$$

substituting $\gamma = 0$ and $\lambda = 1$.

1.3.3 Limitations

The major challenges related to the use of $\omega - \mathrm{TAm}$ for AS are the unfavourable thermodynamic equilibrium and substrate and product inhibition.

1.3.3.1 Unfavourable thermodynamic equilibrium

The maximum reaction rate for the forward reaction is much higher than that for the reverse direction, i.e. the equilibrium is on the side of APH and ALA and not on the side of the products $(S) - \alpha - \mathrm{MBA}$ and PYR: the equilibrium constant of the transamination reaction represented in Figure 1.12 is reported to be $8.81 \cdot 10^{-4}$ (Shin and Kim, 1998). Thus, the equilibrium needs to be shifted to the product side using several process strategies, such as product or co-product removal and/or addition of excess of amine donor (Tufvesson et al., 2011).

1.3.3.2 Substrate and product inhibition

Inhibition is a common phenomena in enzymatic reaction and it is a particular issue for $\omega - \mathrm{TAm}$ because of the Ping-Pong bi-bi mechanism of the enzyme. When an enzyme operates with this mechanism, inhibition is more likely than in a simple enzymatic reaction as

$$\mathrm{E} + \mathrm{S} \rightleftharpoons \mathrm{ES} \rightarrow \mathrm{E} + \mathrm{P} \tag{1.6}$$

because in the Ping-Pong bi-bi mechanism the enzyme forms two complexes, and two substrates and two products are involved in the reaction. Thus, the possibility of a compound to bind to the “wrong” form of the enzyme are increased compared to a simple reaction. Several inhibition mechanisms have been formulated by Höhne and Bornscheuer

(2009); Shin and Kim (1998, 2002) depending on the type of complexes (i.e. the binding of a species with a certain form of the enzyme) that are included in the kinetic model. In this case, the inhibitions included in the model proposed by Al-Haque et al. (2012) are described.

Regarding substrate inhibition, in this model (Figure 1.13) it is considered that, due to the similarity of the two forms of the enzyme $\mathrm{E-PLP}$ and $\mathrm{E-PMP}$, it is likely that $\mathrm{E-PMP}$ can accommodate ALA instead of APH, and $\mathrm{E-PLP}$ can bind APH instead of ALA, forming the abortive dead-end complexes $\mathrm{E-PLP-APH}$ and $\mathrm{E-PLP-ALA}$. However, the two substrates do not inhibit the enzyme to the same extent since the inhibitory effect of ALA is less strong than the one of APH (Koszelewski et al., 2010; Neto, 2013). The inhibition given by the substrates is known as competitive inhibition[3]. The competitive inhibitory action of the substrates is included in the kinetic model as can be seen in equation (1.3), and more clearly in equation (1.4).

In a similar fashion, products exhibit competitive inhibition and it occurs because one the products interacts with the wrong form of the enzyme; $(S)-\alpha-\mathrm{MBA}$ gives the strongest product inhibition, which is due to the formation of the Michaelis complex between the enzyme bound to PMP ($\mathrm{E-PMP}$) and molecules of $(S)-\alpha-\mathrm{MBA}$, which

---

[3] Inhibition occurs in enzyme kinetics when a compound binds reversibly to the enzyme, slowing down the reaction rate. There are three types of inhibition which affects the enzyme kinetics, and therefore their contribution is inserted into the kinetic expression by modifying the general Michaelis-Menten expression:

1. competitive: the inhibitor competes with the substrate to bind the enzyme, occupying the active site and forming a complex with the enzyme; in this way the substrate cannot bind to the enzyme. It results in an apparent decrease in the affinity of the enzyme for the substrate, without reducing the enzyme maximum velocity. The reaction rate becomes

$$\frac{1}{v}=\frac{K_M}{V_{max}}\frac{1}{c_A}\left(1+\frac{c_I}{K_i}\right)+\frac{1}{V_{max}}$$

2. uncompetitive: the inhibitor binds to the enzyme on a site that is different from the site where the substrate binds to the enzyme. This results in an apparent increase in affinity of the enzyme for the substrate and in a decrease of the maximum velocity due to unproductive substrate binding. The reaction rate becomes

$$\frac{1}{v}=\frac{K_M}{V_{max}}\frac{1}{c_A}+\frac{1}{V_{max}}\left(1+\frac{c_I}{K_i}\right)$$

3. non-competitive: the inhibitor binds to the enzyme, either to the free enzyme or to a complex, on a site which is not the active one. Thus, the substrate can still bind but the enzyme is inactivated. It results in an apparent decrease of the maximum velocity and an apparent increase of the affinity of the enzyme for the substrate. The reaction rate becomes

$$\frac{1}{v}=\frac{K_M}{V_{max}}\frac{1}{c_A}\left(1+\frac{c_I}{K_i}\right)+\frac{1}{V_{max}}\left(1+\frac{c_I}{K_i}\right)$$

cannot undergo further reaction (Koszelewski et al., 2010; Neto, 2013).

Without addressing the inhibition problem, large-scale processes at industrially relevant substrate and product concentrations are impossible.

1.4 Kinetic dependence on geometry, scale and conditions

Up to now, enzyme kinetics have been investigated in very diluted solutions in batch mode. In recent years, researchers have moved their interest towards space-confined systems, which can well mimic the confined and crowded environment in living systems Wang et al. (2013). Enzymes are actually catalysts in such environment in biological cells, thus the investigation of enzyme activity in micro- or nanoreactor should help in explanation and understanding of chemical processes in life activities Wang et al. (2013). At the same time, this study could pave the way for industrial application of microreactors for enzymatic reaction, once that it is proved that enzyme catalysis is more efficient in microsystems than in industrial scale reactors.

1.4.1 Enzyme catalysis in microreactors

The microchannel environment differs greatly from that of a batch-wise system because of the constrained environment and for the laminar nature of the fluid flow (Reynolds number is far below 2000 in a microchannel). In a batch reactor, interactions between enzyme and reactants take place isotropically, while in the microchannel the interactions are non-isotropic because of the laminar flow conditions. Consequently, reactivity in a microchannel with laminar flow may differ from that of a batch system. Thus, microreactors might be used as chemical-reactivity regulating devices by changing the flow rate. This advantage might be exploited specially for enzymatic reactions, since they allow low substrate consumption and efficient reactions through a high surface-area-to-volume ratio (SA:V) m^{-1} (Yamashita et al., 2009).

Enzyme assays in space confinement (i.e. micro- and nanoreactor) include heterogeneous and homogeneous reaction systems. In a heterogeneous system, enzymes are usually immobilized on nanostructured materials or on microchannel walls. For nanostructures, mesoporous or layered materials are used to immobilize enzymes; this confined environment mimicks the environment in living organisms because it is constrained and narrow (Wang et al., 2013; Yamashita et al., 2009). However, even though the size of the cavities is comparable to the size of biomolecules, mass diffusion into the pores is unfavourable. Thus, in this case enzyme activity is not properly evaluated since it is limited by mass transfer. For microchannels, enzymes are immobilized directly on the walls of the channel, allowing ease of enzyme recycling and enhanced enzyme concentrations. However, reduced enzyme activity is usually observed due to possible changes in the enzyme conformation and steric hindrance of the enzyme active sites. Taking into account these limitations related to heterogeneous catalysis, the focus of the research has been moved in favour of homogeneous catalysis. It is expected that homogeneous enzyme reaction systems may provide a better understanding of enzyme catalysis in space confinement.

So far, several studies have been performed on homogeneous enzymatic reaction in microreactors (Wang et al., 2013; Yamashita et al., 2009). In microsystems, enzyme assays are always conducted in continuous flow mode; the operation mode clearly marks the difference with traditional enzyme assays done in batch mode.

Recently, Yamashita et al. (2009) studied non-immobilized enzyme reaction kinetics in a microchannel at laminar flow (in particular they studied the hydrolysis by trypsin); the results show that reaction rates for non-immobilized enzyme in the microchannel are higher than the batch-wise enzymatic reactions. Moreover, in microchannels K_M, the Michaelis-Menten constant[4], is always smaller than the one measured in batch conditions (Yamashita et al., 2009). According to Yamashita et al. (2009), the lower value of K_M is due to an efficient complex formation between enzyme and substrate in the microchannel.

---

[4] The Michaelis-Menten kinetics is defined as

$$v = k_{cat} c_{\mathrm{E0}} \frac{c_{\mathrm{S}}}{K_M + c_{\mathrm{S}}} = V_{max} \frac{c_{\mathrm{S}}}{K_M + c_{\mathrm{S}}} \tag{1.7}$$

where k_{cat} is turnover number, c_{S} is substrate concentration, K_M is Michaelis-Menten constant and V_{max} is maximum reaction rate. The Michaelis-Menten constant K_{M} is defined as the substrate concentration at which the reaction rate is half of the maximum reaction rate. K_M is an inverse measure of the affinity of the substrate for the enzyme: small K_M values indicate that low substrate concentrations are required to reach half of the maximum reaction rate, meaning that substrate and enzyme have high affinity. On the contrary, high K_M values indicate that low affinity exists between substrate and enzyme since high substrate concentrations are required in order to reach half of the reaction rate. The value of K_M depends on both the enzyme and the substrate, as well as conditions such as temperature and pH.

Similar results have been achieved by Wang et al. (2013), which studied the reaction rate of glucose oxidase. They observed that K_M for non-immobilized enzyme in a nanochannel was three times smaller than in bulk systems, indicating a higher affinity of substrate and enzyme a space confined environment. They calculated also the turnover number k_{cat}[5], which was found to be more than two times higher in the microfluidics than in bulk conditions. Overall, the smaller value of K_M and the higher value of k_{cat} in microfluidics suggest that the activity of the enzyme increases in space confinement.

According to Wang et al. (2013), a faster reaction rate in a confined environment is due to two reasons. The first one is that a nanochannel is a very narrow crowded environment that mimics the operating conditions of an enzyme in living systems, which are very different from the diluted solutions normally used in batch reactors. Actually, the crowded environment acts on the protein chain by reducing the available conformational space that enzymes can occupy, increasing the folding stability of the protein. This means that the nanochannel stabilizes the enzyme molecules because it shifts the conformational equilibrium of the enzyme chain from the unfolded state to the native state. Secondly, the laminar flow can provide an ideal interface for a homogeneous enzyme reaction due to fast diffusion and mixing that is possible to achieve in a nanochannel.

In conclusion, from the available literature, it can be concluded that enzyme kinetics acts differently in the microchannel compared to a normal batch reactor, giving higher reaction rates in a space-confined environment than in a diluted solution. This is due to the interaction between the spatial conformation of the enzyme (i.e. the enzyme ternary structure) and the nanochannel, and the laminar flow, which creates a stratified flow.

One aspect that has not been considered so far is the possible existence of interactions between the enzyme and the walls of the microchannel. It is known that in a nano- or microchannel the SA:V is much higher than in a batch reactor; thus, the presence of the walls may have influence on the reaction rate, giving either hydrodynamic retention or adsorption of the enzyme to the walls or both. These two phenomena, separately or a combination of the two, are considered the possible explanation for the higher reaction rate observed in the microchannel. The need for an additional hypothesis arises from an

---

[5] The turnover number k_{cat} in equation (1.7) is the maximum number of substrate molecules converted to product per enzyme molecule per unit of time.

experimental evidence that cannot be explained only with the theories proposed in the current literature. The topic of this thesis is the discussion and the verification of the proposed physical phenomena, in order to determine if they can explain the experimental data. The physical modeling of the system is done using Computational Fluid Dynamics (CFD), since the flow in microreactors is laminar and a local and accurate description of the physics of the system can be achieved. CFD is suggested as an important supporting tool to develop processes at microscale, gain knowledge of the reaction kinetics and collect data for process development and scale-up (Bodla et al., 2013).

1.4.2 Computational Fluid Dynamics

Computational Fluid Dynamics is a branch of fluid mechanics that uses numerical methods and algorithms to solve and analyze problems that involve fluid flow, chemical reaction, heat and mass transfer and many other phenomena. The fundamental equation that is solved is the Navier-Stokes equation

$$\rho \frac{D\mathbf{v}}{Dt} = -\nabla \mathbf{p} + \mu \nabla^2 \mathbf{v} + \rho \mathbf{g} \tag{1.8}$$

where ρ ($\mathrm{kg \cdot m^{-3}}$) is the fluid density, t (s) is time, μ (Pa s) is dynamic viscosity, $\mathbf{v}$ ($\mathrm{m \cdot s^{-1}}$) is the vector of velocity components, $\mathbf{p}$ (Pa) is the vector of pressure and $\mathbf{g}$ ($\mathrm{m \cdot s^{-2}}$)is the vector of gravity components. Navier-Stokes equation expresses the conservation of momentum for a fluid with constant density and viscosity and describes the velocity field. In this way, a numerical description in space and/or time of the complete flow field is achieved. The solution of the Navier-Stokes equation is often coupled with the solution of the equation of continuity for each species

$$\rho \frac{Dw_A}{Dt} = \rho D_{AB} \nabla^2 w_A + r_A \tag{1.9}$$

where w_A is the mass fraction of component A, D_{AB} ($\mathrm{m^2 s^{-1}}$) is the diffusion coefficient of the species A in the species B and r_A ($\mathrm{kg \cdot m^{-3} \cdot s^{-1}}$) is the mass rate of production of species A per unit of volume by homogeneous chemical reaction. An expression for r_A has to be provided as well. This equation describes the transport of mass in the system and it is a local form of the conservation law of mass. If in the system heat transfer is also present, the equation of energy

$$\rho\hat{C}_p\frac{DT}{Dt} = k\nabla^2 T + \mu\Phi_v \tag{1.10}$$

is also solved, where $\hat{C}_p$ ($\mathrm{J \cdot K^{-1} \cdot kg^{-3}}$) is the heat capacity per unit of mass, T (K) is temperature, k ($\mathrm{W \cdot m^{-1} \cdot K^{-1}}$) is the thermal conductivity coefficient and Φ_v ($\mathrm{s^{-2}}$) is the viscous dissipation function. However, in enzymatic reactions in microsystems heat transfer is not an issue, therefore in this work the energy balance is not included in the simulations.

The focus of this work is on the velocity field and on the distribution of the species in the microchannel, in order to investigate the relation between kinetics and mass transfer for transaminase and other enzymatic reactions; this is why equation (1.8) and equation (1.9) are to be solved. CFD is a powerful tool in this type of analysis because it solves the above mentioned equations numerically (the analytical solution of the Navier-Stokes equation and of the continuity equation is possible only for very simple geometries and for laminar flow). Nowadays, several software are available for the solution of the fluid dynamics equations, such as ANSYS CFX, Fluent, CFD++ and Comsol. In this work ANSYS CFX 15 is used.

1.4.2.1 How CFD works

Computational methods are used to solve equation (1.8) and equation (1.9), which are partial differential equations. However, these methods can only manipulate discrete numerical values, thus the solution cannot be produced directly from partial differential equations. Consequently, partial differential equations have to be transformed into discrete equations by numerical discretization: each term of a partial differential equation is converted into a discrete quantity that a numerical solver can handle. The major techniques used for discretization are the finite difference method, the finite element method and the finite volume method. ANSYS CFX uses a finite volume method (FVM), a common approach used in CFD codes; it has an advantage in solution speed and memory usage, especially for large problems, compared to other discretization methods such as finite element method.

Numerical discretization is not the only type of discretization to be required, but discretization of the spatial domain is also needed (mesh, structured or unstructured). Thus, the fluid domain is divided into small non-overlapping control volumes over which the set of algebraic equations resulting from the numerical discretization (i.e. mass and momentum conservation) are solved. Using the FVM, the computational node lies at the center of the control volume while the mesh defines only the boundaries of the control volume. The advantage of FVM is that the integral conservation is satisfied exactly over the control volume.

The next step is the solution of the discrete numerical equations in each control volume to obtain a set of numerical values for each variable throughout the fluid domain. The discrete equations in the equation set are solved simultaneously using iterative methods in which a guess is taken for the solution and more accurate guesses are produced as long as the iteration procedure continues. The iterations stop when all variables are obeyed in all cells to a specified tolerance and the change in the variable from one iteration to the next one becomes negligible.

1.4.3 Online measurement

Currently, kinetic data are collected either under steady-state conditions in flow or by generating time-series data in batch (Moore and Jensen, 2014). Batch experiments are considered to be more suitable for the generation of kinetic data since from a single batch experiment many data at different time can be collected. However, continuous flow experiments (specially in microreactors) have advantages over batch systems in terms of mixing times, temperature control and reactants usage. They also allow to perform sequential experiments without intermediate cleaning steps (Moore and Jensen, 2014). Therefore, microfluidic technology has many potential inherent advantages that might be exploited. The drawbacks of performing experiments in microreactors are related to the practical execution of the experiment and the sampling procedure; they both require a long time and a long preparation of materials, as it will be explained in § 3.1.2.2 on page 49. Finally, the analysis of the samples, which is done *ex situ* by High Performance Liquid Chromatography (HPLC), is also a time consuming activity (as an example, the analysis of one sample in the HPLC in this case requires more than 5 minutes); after the analysis, data of the samples have to be collected and treated manually one by one. These practical aspects are tedious and they may hinder the application of microfluidic technology. Thus, in order to take advantage of the use of microreactors, there is the need to overcome the practical limitations of conducting experiments in microreactors. Continuous online measurements may represent the solution.

With continuous online measurement, flow experiments in microreactors can generate time-series data by a continuous variation of the flow rate, yet achieving different residence times in the microreactor. This analysis is possible because an ideal batch reactor and an ideal plug flow reactor have a very similar behaviour: the two ideal reactors have exactly the same kinetics equation, i.e. they will give the same conversion as function of conditions and time for any reaction, since time in batch reactor is equivalent to residence time in a plug flow reactor (Moore and Jensen, 2014). Thus, with online measurement of continuous flow in a microreactor, it is possible to obtain the same type of measures that are done in a batch reactor. Additionally, advantages of working with microreactors are exploited, as well as the fact that a completely automatic measuring procedure is used, thus the uncertainty and the experimental variability are reduced. In this way, experimental results from online measurements of a continuous flow will be more accurate than the one obtained from batch experiments.

1.4.3.1 Application of online measurement to transaminase reaction

In the case of transamination, online measurement can be performed with two different strategies: the first one consists in the direct connection of the outlet of the reactor to an UV detector, which measures continuously the light absorbance of the fluid in order to determine the concentration of $\alpha-\mathrm{MBA}$ and APH. This approach avoids the manual sampling procedure and the delay and waiting time due to *ex situ* analysis by HPLC. The second one consists in cascade or sequential enzymatic reactions, which is done by adding two different enzymes in the reactor; the first enzyme is $\omega-\mathrm{TAm}$, which is the catalyst for the transaminase reaction

$$\mathrm{APH}+\mathrm{ALA} \overset{\omega-\mathrm{TAm}}{\rightleftharpoons} \alpha-\mathrm{MBA}+\mathrm{PYR} \tag{1.11}$$

and the second enzyme is MAO-N (see § 1.2.2.2 on page 12), which catalyses the oxidative deamination of $\alpha-\mathrm{MBA}$

$$\alpha-\mathrm{MBA}+\mathrm{O_2}+\mathrm{H_2O} \overset{\mathrm{MAO-N}}{\rightleftharpoons} \mathrm{APH}+\mathrm{NH_3}+\mathrm{H_2O_2} \tag{1.12}$$

This second reaction can be monitored by measuring continuously the concentration of oxygen with an oxygen sensor. The variation of oxygen concentration is related to the variation of the concentration of $\alpha-\mathrm{MBA}$, thus the amount of $\alpha-\mathrm{MBA}$ produced from the first reaction can be estimated. This method is very attractive, specially for the easiness and the speed of data acquisition. However, the main issues are related to the characteristics of the second enzyme in the cascade: it has to have a very fast reaction rate and it has to be very selective towards of $\alpha-\mathrm{MBA}$, and the amount of oxygen should not limit the reaction rate, nor the amount of $\alpha-\mathrm{MBA}$ that can be oxidized. So far, the enzyme MAO-N does not display the desired characteristics, yet it cannot be used for this purpose. Two additional problems arise from the second reaction: firstly, APH is produced, yet more substrate will be present for the transamination reaction, causing either inhibition of the enzyme or increase of the reaction rate; secondly, the presence of $\mathrm{H_2O_2}$ may damage the enzyme $\omega-\mathrm{TAm}$. This problem could be overcome by adding an enzyme such as catalase, which rapidly converts $\mathrm{H_2O_2}$ into $\mathrm{O_2}$ and water. However, the release of oxygen interferes with oxygen consumption due to amine oxidation, thus variation of oxygen concentration cannot be directly related to variation of $\alpha-\mathrm{MBA}$ concentration (O'Reilly et al., 2014). Therefore, more investigation is required in order to find a more suitable enzyme or to engineer MAO-N in order to make it usable for this application.

In this project, none of the two outlined strategies could be used, the first one because of lack of the proper equipment and the second one because it requires further development before its applicability. However, the possibility of collecting online measurements is not discarded, considering the availability of an oxygen sensor and microchannel with sensor spots. This sensor allows the rapid collection of accurate experimental data relative to different points in the microchannel and not only at the outlet. The use of this instrument fits perfectly with the aim of this work, which is the investigation of kinetics in a microsystem. With the data collected from the sensor and the parallel CFD modeling of the system, a thorough understanding of the physical phenomena taking place can be achieved.

In order to be able to exploit the potentiality of this instrument, the focus is shifted from transaminase reaction to oxidation of glucose with the enzyme glucose oxidase (GOx), considering it as a tool to unravel the mechanism of enzymatic reactions in microreactors.

1.4.4 Oxygen sensor

Oxygen depletion by GOx for glucose oxidation (as it will be presented in § 1.5.1 on the next page) can be monitored with a fluorescence sensor for oxygen. As a sensing method, fluorescence has attracted special attention because it is highly sensitive, versatile, noninvasive and of low toxicity. Moreover, the sensor does not need to be in physical contact with the medium during measurement. It has a very fast response and wide spatial resolution, that can go from the macroscale to the nanoscale, overcoming the limitations of electrochemical sensors, which are difficult to miniaturize and limited to discrete points (Baleizão et al., 2008). A drawback of fluorescence-based oxygen sensors is the interference of temperature on the behaviour of the sensor; this problem can be solved by using a second sensor to measure the temperature, yet account for the contribution of temperature. In the case of enzymatic reaction in microchannels, temperature variation is not an issue since the temperature is constant. On the contrary, it is important to have a sensor with a fast response and high sensitivity; in this way it can be used to detect a compound or a variable with high precision at a very small scale.

The oxygen sensor is formed of two parts: the first one is a probe and the other one is a sensor spot located at a specific position in a microchannel. The probe (made of optical fiber) is used to generate a red light beam ($\lambda = 620$ nm) and to measure the luminescence lifetime of the luminescent compound located in the sensor spot. The luminescent compound is a red sensitive dye excited by the red light beam; the dye shows an oxygen dependent luminescence in the near infrared (NIR) (because oxygen as a triplet molecule easily quenches the fluorescence of luminescent compounds). More specifically, the red sensitive dye displays high NIR emissions at low oxygen concentration and low NIR emissions at high oxygen concentration. From the detection of NIR emissions, the decay times of the luminescent compound is obtained; from the decay time, oxygen concentration can be calculated from the two-sites model Stern-Volmer implicit equation

$$\frac{\tau}{\tau_0} = \frac{f_1}{1 + K_{\mathrm{SV}}^1 c_{\mathrm{O}_2}} + \frac{f_2}{1 + K_{\mathrm{SV}}^2 c_{\mathrm{O}_2}} \tag{1.13}$$

where τ (s) is the fluorescence lifetime, τ_0 (s) is the fluorescence lifetime is absence of oxygen, K_{SV}^1 $(\mathrm{l \cdot g^{-1}})$ and K_{SV}^2 $(\mathrm{l \cdot g^{-1}})$ are the Stern-Volmer constants for each component of the sensor and f_1 and f_2 are the fractions of the total emission for each component (with $f_1 + f_2 = 1$). The two-sites model represents as evolution of the standard Stern-Volmer model and it takes into account the possibility that molecules of the sensor are distributed to two different microenvironments with different oxygen permeability (known as non-ideal quenching) (Baleizão et al., 2008). The calculation of oxygen concentration from equation (1.13) can be done after the calibration of the sensor, which is performed after measuring τ_0 and decay times of known oxygen concentrations.

1.5 Kinetics of glucose oxidase

1.5.1 Reaction mechanism

The enzyme GOx from *Aspergillus niger* is a homodimeric glycoprotein. Each subunit carries one molecule of non-covalently bound co-enzyme Flavin Adenine Dinucleotide (FAD), which acts as the redox carrier in the catalytic action of the enzyme Leskovac et al. (2005). GOx catalyses the oxidation of $\beta - \mathrm{D} - \mathrm{glucose}$ (GLU) by molecular oxygen to $\mathrm{D} - \mathrm{glucono} - 1,5 - \mathrm{lactone}$ (LAC) (Figure 1.14a), which subsequently hydrolyses spontaneously (i.e. without enzyme catalysis) to gluconic acid (Figure 1.14b). The overall reaction is represented in Figure 1.14.

The enzyme obeys a Ping-Pong bi-bi kinetic mechanism, as $\omega - \mathrm{TAm}$ (Figure 1.15) (Leskovac et al., 2005; Wohlfahrt et al., 2004): the first step consists in the binding of a $\beta - \mathrm{D} - \mathrm{glucose}$ molecule to the enzyme (which contains the co-enzyme FAD); the co-enzyme is reduced to $\mathrm{FADH_2}$ and the product $\mathrm{D} - \mathrm{glucono} - 1,5 - \mathrm{lactone}$ is released from the complex. This first part of the reaction corresponds to the reductive part of the overall reaction, because the co-factor is reduced (Figure 1.15a). The second part of the reaction (Figure 1.15b) corresponds to the re-oxidation of the co-factor after the binding of a molecule of oxygen to the enzyme and the release of H_2O_2.

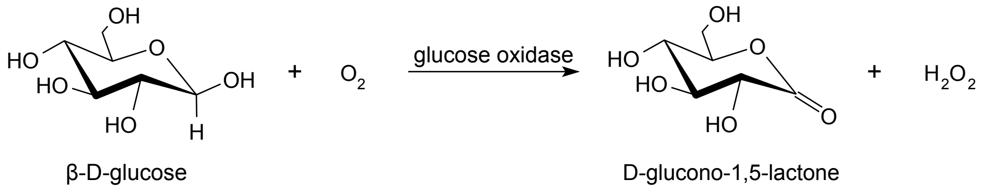

(a) Oxidation of $\beta-\mathrm{D}-$glucose catalysed by glucose oxidase.

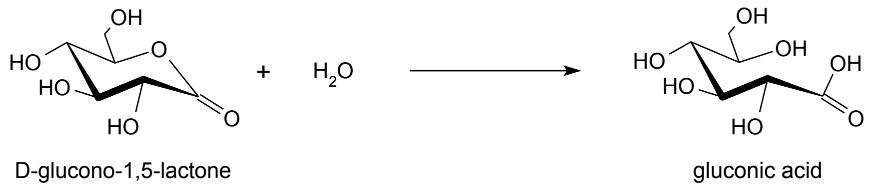

(b) Hydrolysis of D − glucono − 1,5 − lactone to gluconic acid.

Figure 1.14 *Oxidation* $\beta-\mathrm{D}-$glucose *catalysed by glucose oxidase and subsequent hydrolysis of* D − glucono − 1,5 − lactone.

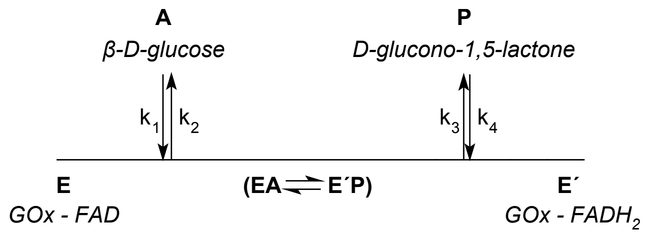

(a) Reductive half reaction: release of the co-product *D − glucono* − 1,5 − *lactone* from the binding of the substrate β − *D* − *glucose* to the complex GOx - FAD.

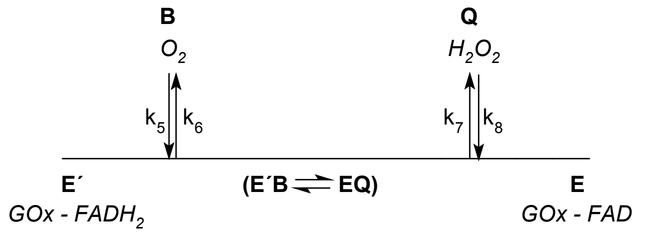

(b) Oxidative half reaction: release of the product H_2O_2 from the binding of the substrate O_2 to the complex GOx - $FADH_2$.

Figure 1.15 *Ping-Pong bi-bi mechanism in the Cleland notation for the enzyme glucose oxidase (FAD = Flavin Adenine Dinucleotide,* $FADH_2$ *= reduced form of Flavin Adenine Dinucleotide, GOx = glucose oxidase,* k_i *= kinetic constant of the reaction i).*

1.5.2 Kinetic model

According to the literature (Leskovac et al., 2005; van Stroe-Biezen et al., 1994) the reaction rate for GOx is expressed as

$$v = -v_{\mathrm{O_2}} = c_{\mathrm{E0}} k_{cat} \frac{c_{\mathrm{GLU}} c_{\mathrm{O_2}}}{K_{\mathrm{M}}^{\mathrm{O_2}} c_{\mathrm{GLU}} + K_{\mathrm{M}}^{\mathrm{GLU}} c_{\mathrm{O_2}} + c_{\mathrm{GLU}} c_{\mathrm{O_2}}} = v_{max} \frac{c_{\mathrm{GLU}} c_{\mathrm{O_2}}}{K_{\mathrm{M}}^{\mathrm{O_2}} c_{\mathrm{GLU}} + K_{\mathrm{M}}^{\mathrm{GLU}} c_{\mathrm{O_2}} + c_{\mathrm{GLU}} c_{\mathrm{O_2}}} \tag{1.14}$$

where the kinetics constants can be related to the rate constants of each step in the Ping-Pong bi-bi mechanism in Figure 1.15 by the expressions

$$k_{cat} = \frac{k_3 k_7}{k_3 + k_7} \tag{1.15}$$

$$K_{\mathrm{M}}^{\mathrm{GLU}} = \frac{k_{cat}}{k_1} \frac{k_2 + k_3}{k_3} \tag{1.16}$$

$$K_{\mathrm{M}}^{\mathrm{O_2}} = \frac{k_{cat}}{k_5} \frac{k_6 + k_7}{k_7} \tag{1.17}$$

If all reactions in the Ping-Pong bi-bi mechanism are nearly irreversible, which is the case when glucose and oxygen are the substrates of the enzyme,

$$k_2 \approx k_4 \approx k_6 \approx k_8 \approx 0 \tag{1.18}$$

then equation (1.16) and equation (1.17) are reduced to

$$K_{\mathrm{M}}^{\mathrm{GLU}} = \frac{k_{cat}}{k_1} \tag{1.19}$$

$$K_{\mathrm{M}}^{\mathrm{O_2}} = \frac{k_{cat}}{k_5} \tag{1.20}$$

respectively. Under the assumption expressed by equation (1.18), the bimolecular rate constants $k_{cat}/K_{\mathrm{M}}^{\mathrm{GLU}}$ and $k_{cat}/K_{\mathrm{M}}^{\mathrm{O_2}}$, which describes all steps beginning with interaction of enzyme and substrate, become respectively k_1 and k_5. This means that the enzyme interaction with each substrate is entirely determined by the rate of irreversible binding of that substrate (Leskovac et al., 2005).

1.6 Adsorption

Adsorption of the enzyme to the wall of the microreactor is tested as a possible explanation for the higher reaction rate of enzymatic reaction in microsystem. The other theories suggested in the literature and reviewed in §1.4.1 cannot explain the fact that, if a series of measurements (for example measurement of product concentration at the outlet of the microreactor) is repeated in the same conditions, in each replicate a higher product concentration is measured. In this Section the theory about adsorption is briefly reviewed and the most relevant literature about protein adsorption on glass and plastic surfaces in presented.

1.6.1 Physical phenomena

Adsorption is the adhesion of chemical species from a gas, liquid, or dissolved solid to a surface. This process creates a film of the adsorbed molecules on the surface of the solid.

Molecules can attach to surfaces because of two different types of interaction: van der Waals forces and chemical bonds.

The former is characterized by long range and weak interactions. The energy released when a particle is adsorbed is of the same order of magnitude as the enthalpy of condensation; such small energies (in the range of 20 $\mathrm{kJ \cdot mol^{-1}}$) can be absorbed as vibration of the lattice and dissipated as thermal motion. A molecule will gradually lose its energy and adsorb to the surface. A small change in enthalpy is insufficient to lead to bond breaking, thus the adsorbed molecules retain their identity, although they might be distorted by the presence of the surface. This type of adsorption is called physical adsorption (abbreviated as physisorption) (Atkins and De Paula, 2010).

In the latter, particles stick to the surface by forming a chemical bond (usually a covalent bond), having an enthalpy of 200 $\mathrm{kJ \cdot mol^{-1}}$; they tend to find sites that maximise their coordination number with the substrate. The distance between the surface and the closest adsorbate atom is shorter than physical adsorption. This phenomena is called chemical adsorption (or chemisorption) (Atkins and De Paula, 2010).

1.6.2 Protein adsorption on glass

Proteins (and enzymes) are interfacially active molecules that tend to accumulate spontaneously at interfaces. Experimental evidences of protein adsorption on glass surfaces are given by Bull (1956) and Suelter and DeLuca (1983). They describe from a qualitative point of view the adsorption on glass of bovine serum albumin and creatine kinase, respectively.

Proteins show the propensity to adsorb to surfaces due to nature of the side chains present on the protein external surface. The amino acids forming the protein backbone have different characteristics: some are apolar, and they are most likely in the protein globule, whereas others are polar and charged and they are found on the outside protein surface. A strong, long-ranged electrostatic attraction between a charged adsorbent and oppositely charged amino acid side chain will lead to a significant free energy change favouring the adsorption process (Hlady et al., 1999).

Another possibility is that the structural stability of proteins is affected by surfaces; if a protein has a marginal structural stability, this can modify its interfacial activity. However, in the vicinity of the walls, the stability and the compactness of the protein may be enhanced because the walls can "compete" for the same interactions that are formed between parts of the chain, which are the ones that make the protein unstable. Thus, the surface decreases the total free energy of the protein make it more stable (Hlady et al., 1999).

A quantitative description of adsorption is obtained by measuring adsorption isotherm, adsorption and desorption kinetics, conformation of adsorbed proteins, number and character of protein segments in contact with the surface and the thickness of adsorbed protein layer. Experiments have to be designed in order to identify the mechanism and the value of the parameters of the system.

1.6.3 Langmuir isotherm

Adsorption is usually described through isotherms, which relate the number of adsorbed molecules on the adsorbent surface as a function of partial pressure of the adsorbed species or concentration (if the adsorbed species is a liquid) at constant temperature.

The simplest model for an adsorption isotherm, namely Langmuir isotherm, is based on three assumptions:

1. adsorption is limited to a monolayer coverage;
2. all sites are equivalent and the surface is uniform;
3. the binding ability of a molecule at a given site is independent of the occupation of neighbouring sites.

During an adsorption process, two phenomena, i.e. adsorption of free molecules and desorption of adsorbed molecules, are in dynamic equilibrium. The phenomena is frequently described in terms of the variable θ, the fractional coverage of the surface, which is defined as

$$\theta = \frac{c_i^*}{c^*} \tag{1.21}$$

where c_i^* ($\mathrm{kg \cdot m^{-2}}$) is the concentration of the adsorbed species i on the surface and c^* ($\mathrm{kg \cdot m^{-2}}$) is the concentration of available adsorption sites.

The rate of change of θ due to adsorption is expressed as

$$\frac{d\theta}{dt} = k_{ads} c_i c^* \left(1 - \theta\right) \tag{1.22}$$

where k_{ads} ($\mathrm{m^5 \cdot kg^{-2} \cdot s^{-1}}$) is the rate constant for adsorption. The expression means that adsorption is proportional to the concentration of the species that is adsorbed and the concentration of vacant sites.

The rate of change of θ due to desorption is expressed as

$$\frac{d\theta}{dt} = -k_{des} c^* \theta \tag{1.23}$$

where k_{des} ($\mathrm{m^2 \cdot kg^{-1} \cdot s^{-1}}$) is the rate constant for desorption. Rate of desorption is proportional to the concentration of adsorbed species.

At equilibrium, the absolute value of the rate of adsorption and desorption are equal, i.e.

$$k_{ads} c_i c^* \left(1 - \theta\right) = k_{des} c^* \theta \tag{1.24}$$

and solving for θ gives

$$\theta = \frac{Kc_i}{1 + Kc_i} \tag{1.25}$$

where K is the ratio of k_{ads} to k_{des}.

Chapter 2

Material

In this Chapter, chemicals and equipment that are used for all experiments and CFD software are described. The Chapter is divided into two parts: the first one is about materials used for $\omega-$TAm experiments, the second one for materials used for GOx experiment and simulations.

2.1 Transamination

In this Section all chemicals, enzyme, stock solutions and equipment used for the experiments with $\omega-$TAm are described.

2.1.1 *Chemicals, enzyme and stock solutions*

Technical-grade reagents were purchased and used without further purification. $(S)-\alpha-$Methylbenzylamine ($\alpha-$MBA) and Hydrochloric acid (HCl) were procured from Merck Schuchardt (Hohenbrunn, Germany), while Acetophenone (APH), Pyridoxal-5´-phosphate monohydrate (PLP), Sodium pyruvate, Sodium hydroxide (NaOH), Sodium phosphate monobasic monohydrate ($NaH_2PO_4 \cdot H_2O$) and Sodium phosphate dibasic (Na_2HPO_4) were procured from Sigma-Aldrich (St. Louis, MO, USA). The enzyme $\omega-$TAm, with commercial name ATA-50, was purchased from c-LEcta (Leipzig, Germany) as lyophilized powder; the specific activity of the enzyme commercial preparation was 3.46 U/mg.

Pure reagents and the enzyme were used to prepare the following solutions:

- a phosphate buffer, which was prepared by solubilizing Na_2HPO_4 and $NaH_2PO_4 \cdot H_2O$ in distilled water in order to have a total concentration of 20 mM; the pH of the solution was adjusted to the desired value, i.e. 8, by adding NaOH and/or HCl;
- 1 mM solution of PLP, which was prepared by solubilization of the PLP in the phosphate buffer; the solution was stored in the fridge and wrapped in aluminium foil since PLP is light sensitive;
- 1 M solution of PYR, which was prepared by dissolving Sodium pyruvate in the buffer;
- a solution containing $(S)-\alpha-$MBA, PYR and PLP, which was prepared by solubilizing the desired amount of $(S)-\alpha-$MBA, then adding the desired volume of the PYR solution and PLP solution in the buffer; the pH of the solution was adjusted to 8 by adding HCl since $(S)-\alpha-$MBA increases the value of the pH;
- a solution containing 0.1 mg/ml of ATA-50 in phospate buffer.

2.1.2 Syringe pumps

In order to perform the experiments in continuous flow in microreactors, a modular digital pump, Cavro XL 3000 from Cavro Scientific Instruments Inc was used. The pump is a stepper motor driven syringe pump and it is controlled from the software Cavro Fusion V3.3. Two syringes with a stroke volume of 50 μl each were used in parallel.

2.1.3 Batch system

When the experiments were run in a batch mode, a thermoshaker was used to heat and stir the content of the vials (Model 11, HLC Biotech, Bovenden, Germany). In the thermoshaker vials of 4 ml of volume were placed.

2.1.4 Microreactors

Two different types of microreactors were used: a meander microreactor of 400 μm height and 200 μm width and a set of straight microchannels with rectangular cross section.

2.1.4.1 Meander microreactor of 400 μm height and 200 μm width

The geometry of the meander microreactor of 400 μm height and 200 μm width (iX-factory, Dortmund, Germany) is shown in Figure 2.1. The channel is made of glass and it had two inlets and one outlet. It has a total volume of 24.08 μl: the volume of the two inlet branches is 1.38 μl, so the volume available for the reaction is 22.70 μl. The microchip with the meander channel is placed in a microplate holder, in order to connect the channel to the inlet and outlet microtubes.

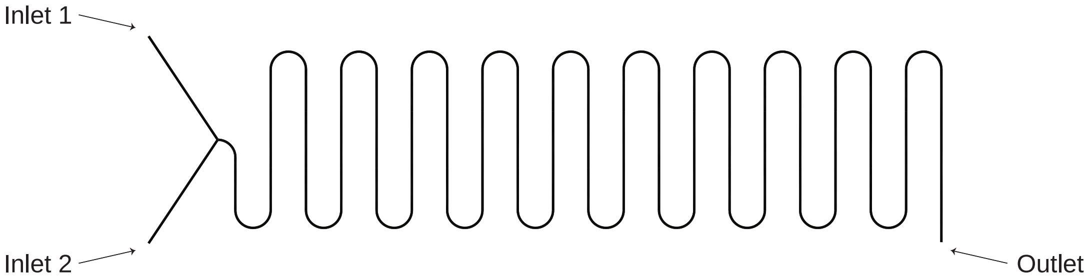

Figure 2.1 *Geometry of the meander microreactor of 400 μm height and 200 μm width.*

2.1.4.2 Reactors with different surface-area-to-volume ratio

Reactors with different geometrical dimensions were built manually. The bottom of the reactor was made of a glass microscope slide, while the top surface was made with a stainless steel plate. On the metal plate, two holes were drilled for placing the inlet and outlet tubes. In between the top and bottom surfaces a piece of double-sided tape was placed, thus the sides of the reactor were delimited by tape. The geometry of the channel was drawn in the tape with a CO_2 laser and then the tape was glued to the metal plate and to the glass slide (in this order). The reactors had the shape of a parallelepiped, with constant length and volume, while the height and the width changed in order to keep the total volume constant. The height of tape was 140 μm. Several layers of tape were glued on top of each other in order to increase the height of the reactor. The geometrical dimensions, the volume, the surface and the surface-area-to-volume ratio (SA:V) of the reactors are presented in Table 2.1. The modification of the cross-sectional areas in all structures due to the change in geometric dimensions is shown in Figure 2.2.

Table 2.1 *Geometrical dimensions of the microreactor.*

Configuration	Number of layers of tape	Height (μm)	Width (mm)	Length (mm)
α	1	140	2.60	60
β	2	280	1.30	60
γ	3	420	0.87	60
δ	4	560	0.65	60
ε	5	700	0.52	60

Configuration	Volume (μl)	Surface (mm^2)	SA:V (mm^{-1})
α	21.87	329.17	15.05
β	21.87	189.78	8.68
γ	21.87	154.52	7.07
δ	21.87	145.29	6.64
ε	21.87	146.47	6.70

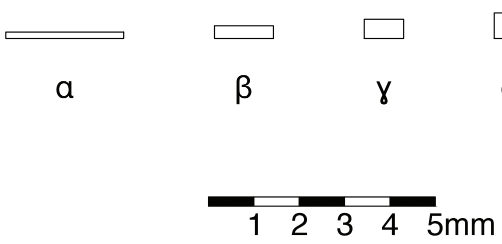

Figure 2.2 *Cross-sectional area of microreactors with different surface-area-to-volume ratio.*

2.1.5 HPLC

Samples were analyzed *ex situ* with a reversed-phase chromatography on an Ultimate 3000 HPLC (Dionex, Sunnyvale, CA, USA) equipped with a UV detector and a photodiode array detector. The column was a Gemini® 3 μm NX-C18 110 Å, 100 x 2.0 mm (Phenomenex, Torrance, CA, USA), with a stationary phase made of a fully porous (pore size of 110 Å) organo-silane material incorporating ethylene bridges. The mobile phase was a solvent formed by 35 % of acetonitrile and 65 % of a solution of Milli-Q water and NaOH at pH 11.

2.2 Oxidation

In this Section all chemicals, enzyme, stock solutions and equipment used for the experiments with GOx are detailed.

2.2.1 Chemicals, enzyme and stock solutions

Technical-grade chemicals were purchased and used without further purification. Potassium phosphate dibasic (K_2HPO_4), Potassium phosphate monobasic (KH_2PO_4) and $\beta - D -$ glucose (GLU) were purchased from Sigma-Aldrich (St. Louis, MO, USA). The protein bovine serum albumin (BSA) was procured from Sigma-Aldrich (St. Louis, MO, USA) in form of a lyophilized powder. The enzyme GOx, with commercial name Gluzyme® Mono 10.000 BG, was purchased from Novozymes (Bagsværd, Denmark). The preparation is a mix of yellowish/grey, free-flowing, non-dusting, agglomerated granulate, with an average particle size of 150 μm within the range of 50-212 μm. The preparation contains a non-standardized catalase side activity. The preparation is standardized using a special wheat flour with a narrow particle size distribution. According to the supplier, the activity of the preparation is 10 000 GODU/mg, where 1 GODU (glucose oxidase unit) is the amount of enzyme that produces 1 μmol of hydrogen peroxide per minute under standard conditions (Novozymes, 2002).

The reagents, the enzyme and the protein were used to prepare the following solutions:

- a buffer solution, which was prepared by solubilizing K_2HPO_4 and KH_2PO_4 in distilled water in order to have total concentration of 200 mM and pH 7;
- 0.2 g/l solution of BSA, which was prepared by solubilizing BSA in buffer;

- 0.2 g/l solution of GOx, which was prepared by solubilizing GOx in buffer; the solution was then placed in a centrifuge at 7200 rpm for 5 minutes for separating the particles that are contained in the commercial preparation; the supernatant is then used as the enzyme solution;
- 50 mM solution of GLU, which was prepared by solubilizing GLU in buffer.

2.2.2 Syringe pumps

The same syringe pumps that were used for the experiments with the enzyme $\omega-\mathrm{TAm}$ were used in the experiments with GOx (§2.1.2). For some experiments two syringes with a stroke volume of 250 μl each were used in parallel, instead of the strokes with a volume of 50 μl.

2.2.3 Meander microreactor of 200 μm height and 100 μm width with sensor spots

The geometry of the meander microreactor of 200 μm height and 100 μm width (iX-factory, Dortmund, Germany) is shown in Figure 2.3. The channel has two inlets and one outlet. It has a total volume of 10.52 μl: the volume of the two inlet branches is 0.44 μl, so the volume available for the reaction is 10.08 μl. The channel is made of glass. As shown in Figure 2.3, along the channel seven sensor spots are located; they contain a luminescent compound, i.e. a red sensitive dye with an oxygen dependent luminescence in the near infrared. The shape of a sensor spot is shown in Figure 2.4. They are 7 μm higher than the height of the channel, they have a width of 1 mm and a length of 3.5 mm. The microchip with the meander channel is placed in a microplate holder, in order to connect the channel to the inlet and outlet microtubes, as well as placing the probes in correspondence to the sensor spots.

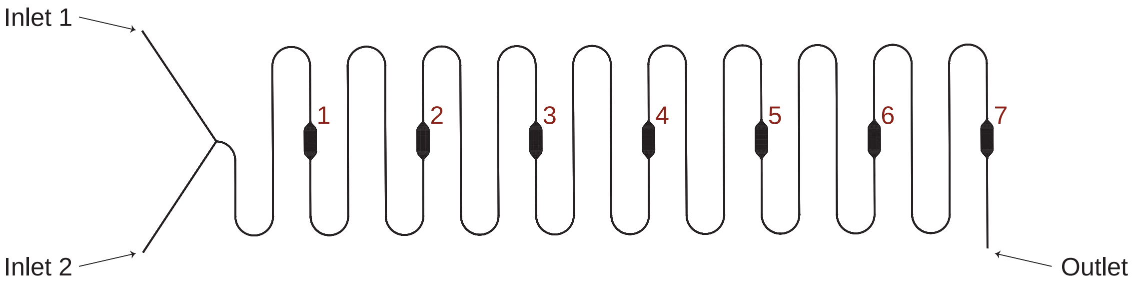

Figure 2.3 *Geometry of the meander microreactor of 200 μm height and 100 μm width. The red numbers indicate the sensor spots.*

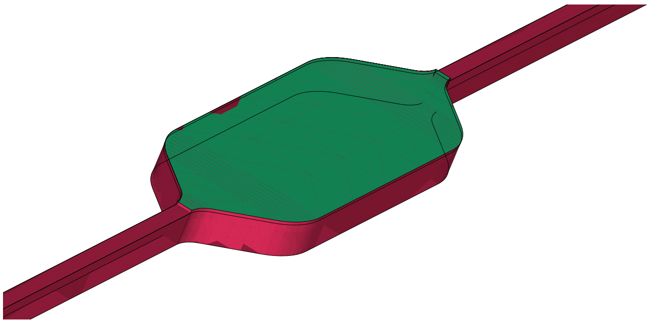

Figure 2.4 *Sensor spot of the meander microreactor of 200 μm height and 100 μm width.*

2.2.4 Oxygen meter

Oxygen concentration was measured by the fiber-optic oxygen meter “Firesting O_2” from Pyro Science (Aachen, Germany). The oxygen meter had four channels, i.e. 4 measurements could be collected simultaneously. The oxygen meter was formed by optical fibers and a reader: the optical fibers generated the red light beams and detected the near infrared emissions from the luminescent dye of the sensor spots. The intensity of the emissions was detected and sent to the reader. The reader collected the signals, and transmitted them as input data to the software “Pyro Oxygen Logger” which first calculated the decay times and, by equation (1.13), converted them into oxygen partial pressure.

2.2.5 CFD simulation

For CFD simulations, the software ANSYS 15.0 was used. For drawing the geometry and for doing the mesh of the domains, the software ANSYS ICEM was used. For setting the simulations, the software ANSYS CFX - Pre 15.0 was used. ANSYS CFX - SolverManager 15.0 was used for the numerical solution of the system and ANSYS CFD - Post 15.0 for result visualization and analysis.

Chapter 3

Methods

In this Chapter, experimental methods and the models and solver parameters used in the CFD simulations are described. The Chapter is divided into two parts: the first one is about experimental methods for $\omega-$transaminase ($\omega-$TAm) experiments, the second one includes experimental methods for glucose oxidase (GOx) experiment and parameters and models used in the simulations.

3.1 Transamination

In this Section all experimental methods used for the experiments with $\omega-$TAm are detailed.

3.1.1 Analytical method

The compounds $(S)-\alpha-$MBA and APH were separated in the column of the HPLC at a mobile phase flow rate of 450 ml/min at 30 °C; their absorbance peaks were quantified at wavelength of 244 nm for APH and 265 nm for $(S)-\alpha-$MBA at retention times of 1.8 min and 1.4 minutes, respectively. The injection volume of the samples was 10 μl. The quantitative analysis was performed from peak areas by external standard calibration with the software Chromeleon™ 6.8 Chromatography Data System. The calibration curves for $(S)-\alpha-$MBA and APH were built with the following procedure: two solutions at known concentrations, one with phosphate buffer and $(S)-\alpha-$MBA and another one with phosphate buffer and APH, were prepared. Three samples of each solution were taken and analyzed with the HPLC; the injection volume of the sample into the column was varied (from 0.1 μl to 10 μl for $(S)-\alpha-\mathrm{MBA}$ and from 0.05 μl to 1.7 μl for APH) in order to build the calibration curve in the desired range of concentration (Appendix A on page 129).

3.1.2 Activity measurement

One unit of enzyme activity U is defined as the amount of enzyme which catalyzes the formation of one μmol of APH per liter in one minute by the reaction in Figure 3.1 at 40 mM of $(S)-\alpha-\mathrm{MBA}$, 40 mM of PYR, 0.1 mM of PLP at 30 °C and pH 8, at $\omega-\mathrm{TAm}$ concentration of 0.05 g/l. Activity was measured for the reaction performed in the batch system described in §2.1.3 and in the meander channel described in §2.1.4.1; the initial forward reaction rate was measured by analyzing APH produced.

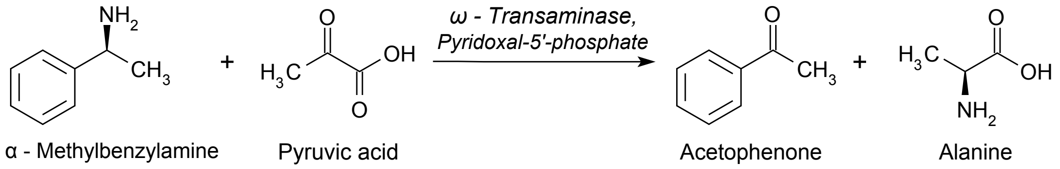

Figure 3.1 *Reaction performed for activity measurement of the enzyme preparation ATA-50, at 40 mM of* $(S)-\alpha-$*Methylbenzylamine, 40 mM of pyruvic acid, 0.1 mM of pyridoxal-5'-phosphate at 30 °C and pH 8.*

3.1.2.1 Batch system

1.5 ml of a solution at pH 8 containing 80 mM of $(S)-\alpha-\mathrm{MBA}$, 80 mM of PYR, 0.2 mM of PLP and the buffer was injected into a 4 ml glass vial placed in a thermoshaker at 30 °C with orbital agitation of 400 rpm. After that the solution had been heated to 30 °C, the reaction was started by adding 1.5 ml of a solution containing 0.1 mM of enzyme in buffer. Considering the injection time of the enzyme as time zero, samples were taken after 1, 2, 4, 6, 10 and 60 minutes. Samples were taken by injecting 100 μl of the reacting mixture in a HPLC vial containing 900 μl of 1 M NaOH, in order to stop the reaction. The sample corresponding to time zero was prepared by adding 50 μl of the solution with the enzyme and 50 μl of the solution with $(S)-\alpha-\mathrm{MBA}$ (in this order) to 900 μl of 1

M NaOH. The activity was determined considering the reaction rate during the first four minutes of the reaction, as an average of two experiments each done in quadruplicate.

3.1.2.2 Microchannel

The experimental set up consisted of the meander microreactor (described in § 2.1.4.1 on page 41) with each inlet connected to one syringe of the pump by polytetrafluoroethylene (PTFE) tubings. One syringe pumped the solution at pH 8 with 80 mM of $(S)-\alpha-\mathrm{MBA}$, 80 mM of PYR, 0.2 mM of PLP and the buffer and the other one pumped the solution containing 0.1 mM of enzyme in buffer. The outlet of the system is collected in a HPLC vial by a PTFE tubing. The microreactor, placed inside the microplate holder, was placed on the ceramic heating plate of a magnetic stirrer, with the temperature set at 30 °C. The microplate holder was wrapped in aluminium foil in order to prevent heat dispersion from the top and the sides of the microchannel. The experimental set up is shown in Figure 3.2.

The experiment, performed under continuous flow conditions, consisted of measuring the product concentration at the outlet for different residence times (0.454 min, 1.067 min, 2.595 min and 3.632 min) for the determination of enzyme activity; in order to change the residence time in the reactor, the flow rate was changed by modifying the speed of the plungers.

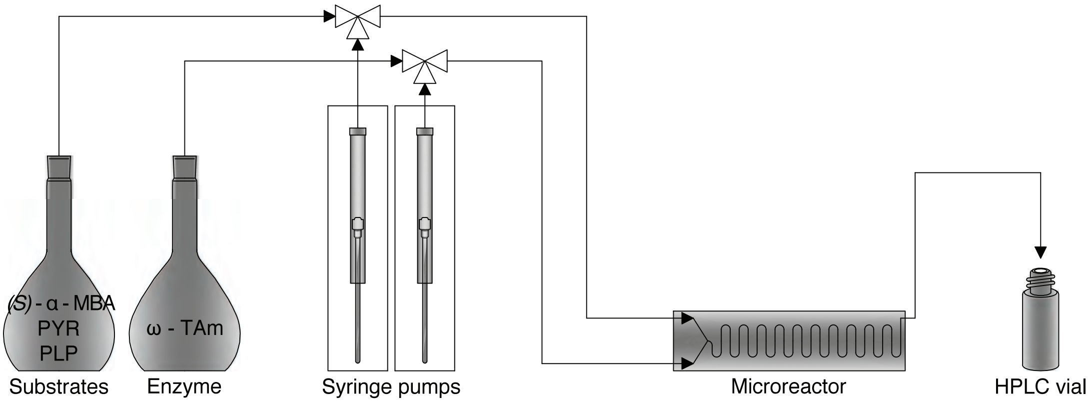

Figure 3.2 *Experimental set-up for activity measurement in the microreactor (PLP = pyridoxal-5'-phosphate, PYR = pyruvic acid, $(S)-\alpha-$MBA = $(S)-\alpha-$Methylbenzylamine, $\omega-$TAm = $\omega-$Transaminase).*

During the entire experiment, the two plungers of the two syringes were moving upward and downward with the same speed for both syringes and they were starting and terminating their movement simultaneously, yet the same flow rate was given by both syringes. The system was primed by flushing the pumps, tubing and the reactor 7 times in order to reach steady state condition and remove all air bubbles. This procedure was repeated before taking the first sample every time that the flow rate was changed. The sampling procedure in this experiment consisted of collecting the outlet from the reactor in a vial containing 900 μl of 1 M NaOH; the sample was collected continuously in the same vial from when the plungers began to move upward until when they finished their movement upward, thus the volume of the sample collected in each vial was 100 μl. Five samples were collected per each flow rate. The sample corresponding to time zero was prepared by adding 50 μl of the solution with $(S)-\alpha-\mathrm{MBA}$ to a vial containing 50 μl of the solution with the enzyme and to 900 μl of 1 M NaOH. The activity was determined considering the reaction rate for the initial 3.632 minutes of the reaction, as an average of three experiments each done in quintuplicate.

3.1.3 Determination of apparent kinetic parameters $K_{M,app}^{MBA}$, $V_{max,app}^{MBA}$, $K_{M,app}^{PYR}$ and $V_{max,app}^{PYR}$

A set of experiments was designed for the determination of the kinetic parameters K_M and V_{max} for the forward reaction in Figure 3.1. Since the reaction has two substrates, apparent kinetic parameters were estimated by varying the concentration of one substrate at a time, while keeping the other constant. In particular, $K_{M,app}^{\mathrm{MBA}}$ and $V_{max,app}^{\mathrm{MBA}}$ were estimated by varying $(S)-\alpha-\mathrm{MBA}$ concentration and keeping constant PYR concentration (§3.1.3.1), and $K_{M,app}^{\mathrm{PYR}}$ and $V_{max,app}^{\mathrm{PYR}}$ were measured by changing PYR concentration at constant $(S)-\alpha-\mathrm{MBA}$ concentration (§3.1.3.2).

The experiments were performed both in the batch system presented in § 2.1.3 on page 40 and in the meander reactor described in § 2.1.4.1 on page 41.

3.1.3.1 Variable $(S)-\alpha-\mathrm{MBA}$ concentration, constant pyruvate concentration

Apparent kinetic parameters for $(S)-\alpha-\mathrm{MBA}$ were determined by keeping PYR concentration constant at 80 mM and varying $(S)-\alpha-\mathrm{MBA}$ concentration. The concentration of $(S)-\alpha-\mathrm{MBA}$ varies from values below K_M to values at saturation conditions, while the concentration of PYR is at saturation conditions (for the design of this experiment, an indication for the value of K_M was taken from Shin and Kim (1998)). The concentrations of $(S)-\alpha-\text{MBA}$, PYR and PLP in the different solutions used for the kinetic parameter estimation are detailed in Table 3.1. The same solutions were used for the determination of $K_{M,app}^{\text{MBA}}$ and $V_{max,app}^{\text{MBA}}$ in the batch system and in the microreactor.

Table 3.1 *Concentration of the solutions used for the determination of apparent kinetic parameters for $(S)-\alpha-$Methylbenzylamine.*

Solution	c_{MBA} (mM)	c_{PYR} (mM)	c_{PLP} (mM)
A	1	80	0.2
B	4	80	0.2
C	10	80	0.2
D	20	80	0.2
E	120	80	0.2
F	200	80	0.2

Batch system Initial reaction rate measurements were performed for a series of reacting mixtures prepared from a 2 folds dilution of each solution presented in Table 3.1. The experimental set up and the way of performing the experiments were the same as presented in § 3.1.2.1 on page 48. Samples were taken at time 0, 1, 2, 4, 6 and 10 minutes. For each solution, the initial reaction rate was calculated for the first four minutes of reaction as an average of triplicate measurements.

Microreactor The experimental set up, the sampling procedure and the way of performing the experiment were the same that are presented in § 3.1.2.2 on page 49. Initial reaction rate measurements were obtained for each of the solutions presented in Table 3.1, which were used to feed the microreactor. The initial reaction rate was calculated for each solution as an average of a triplicate. Initial reaction rate was calculated for the initial 3.632 minutes of the reaction. Only for the solutions A and B the initial reaction rate was determined for the first 2.595 minutes.

3.1.3.2 Variable pyruvate concentration, constant $(S)-\alpha-\mathrm{MBA}$ concentration

Apparent kinetic parameters for PYR were determined by keeping $(S)-\alpha-\mathrm{MBA}$ concentration constant at 80 mM and varying PYR concentration. The concentration of PYR varies from values below K_M to values at saturation conditions, while the concentration of $(S)-\alpha-\mathrm{MBA}$ is at saturation conditions (for the design of this experiment, an indication for the value of K_M was taken from Shin and Kim (1998)). The concentrations of $(S)-\alpha-\mathrm{MBA}$, PYR and PLP in the different solutions used for the kinetic parameter estimation are detailed in Table 3.2. The same solutions were used for the determination of $K_{M,app}^{\mathrm{PYR}}$ and $V_{max,app}^{\mathrm{PYR}}$ in the batch system and in the microreactor.

Table 3.2 *Concentration of the solutions used for the determination of apparent kinetic parameters for pyruvate.*

Solution	c_{MBA} (mM)	c_{PYR} (mM)	c_{PLP} (mM)
L	80	10	0.2
M	80	20	0.2
N	80	30	0.2
O	80	160	0.2
P	80	200	0.2
Q	80	400	0.2

Batch system Initial reaction rate measurements were performed for a series of reacting mixtures prepared from a 2 folds dilution of each solution presented in Table 3.2. The experimental set up and the way of performing the experiments were the same as presented in § 3.1.2.1 on page 48. Samples were taken at time 0, 1, 2, 4, 6 and 10 minutes. For each solution, the initial reaction rate was calculated for the first four minutes of reaction as an average of triplicate measurements.

Microreactor The experimental set up, the sampling procedure and the way of performing the experiment were the same that are presented in § 3.1.2.2 on page 49. Initial reaction rate measurements were obtained for each of the solutions presented in Table

3.2, which were used to feed the microreactor. The initial reaction rate was calculated for each solution as an average of a triplicate. Initial reaction rate was calculated for the initial 3.632 minutes of the reaction. Only for the solutions L and M the initial reaction rate was determined for the first 2.595 minutes.

3.1.4 Reaction rate in microreactors with different surface-area-to-volume ratio

The reaction in Figure 3.1 was performed in the set of microreactors described in § 2.1.4.2 on page 41. The experiment consisted in comparing APH concentration at the outlet of the microreactor in the different microreactors. The experimental set-up is shown in Figure 3.3. The set-up and the conditions were the same for all the reactors in the set; the only difference was the microreactor, i.e. the geometrical dimensions, which determine different SA:V. The reactant solution contained 80 mM of $(S) - \alpha - \text{MBA}$, 80 mM of PYR and 0.2 mM of PLP in buffer. The enzyme solution contained $\omega - \text{TAm}$ in the concentration of 0.1 g/l. The reaction was performed at 30 °C and pH 8, thus the conditions were the same as for the activity determination. The total flow rate was 0.146 μl/s in all microreactors, and, since they all have the same volume, the residence time was 2.5 minutes. As shown in Figure 3.3, the reactant mixture and the enzyme solution were mixed before the inlet of the microreactor in a microtube with internal diameter of 0.17 mm.

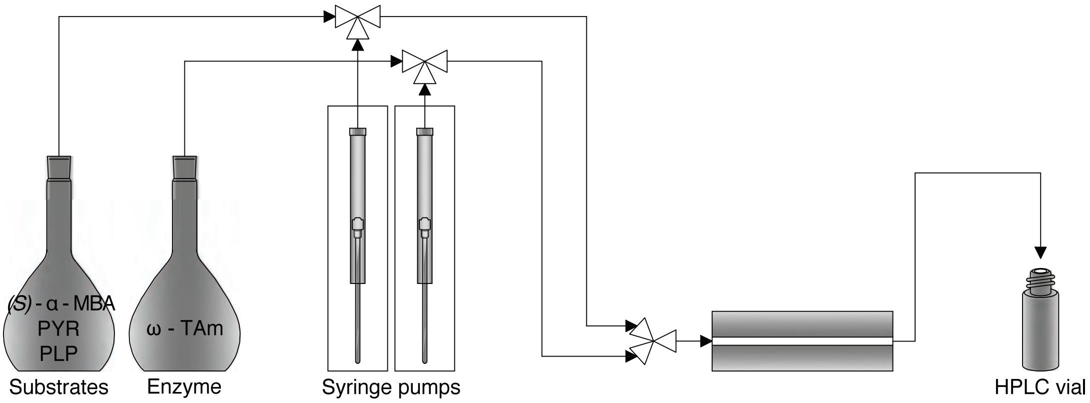

Figure 3.3 *Experimental set-up for the measurement of acetophenone concentration at the outlet of the microreactor in the structures with different surface-area-to-volume ratio (PLP = pyridoxal-5'-phosphate, PYR = pyruvic acid, $(S) - \alpha - MBA$ = $(S) - \alpha - Methylbenzylamine$, $\omega - TAm$ = $\omega - Transaminase$).*

The length of the tube was decided for having all compounds completely mixed at the outlet of the tube (which corresponds to the inlet of the microreactor); this was ensured by a CFD simulation, which was used to test the mixing of the compounds in the microtube (Appendix B on page 133). The sampling procedure was the same as the one explained in §3.1.2.2. The experiment was performed in each microreactor four times, thus the experimental results are given as an average of quadruplicate.

3.2 Oxidation

In this Section the experimental methods referred to GOx are presented. In the last part of the Section, models and solver parameters used in the CFD simulations are detailed.

3.2.1 Experimental set-up

The experimental set-up is similar to the one shown in Figure 3.2, with the only difference that in this set of experiments the substrate solution contained GLU and the enzyme solution contained GOx. All experiments are run in the microreactor with the sensor spots shown in Figure 2.3 on page 45. The four sensor probes were placed in the first, second, fourth and sixth sensor spots. The concentration of GLU solution was 50 mM in all experiments and oxygen was at saturation concentration at ambient temperature in all solutions (concentration of 0.258 mM).

3.2.2 Calibration of the oxygen meter

The oxygen meter needed to be calibrated before being used. The calibration requires the measurement of two known oxygen concentrations, which corresponds to 100 % and 0 % of saturation of oxygen in water. 100 % saturation was measured while flushing in the microreactor the solution of GLU, while 0 % saturation was measured by creating anoxic conditions in the microreactor (after feeding simultaneously GOx and GLU in the reactor, the flow was stopped and the reaction was let to run until completion, which corresponded to total depletion of oxygen).

3.2.3 Continuous feed of glucose and glucose oxidase

The reactor was fed with GOx solution from one inlet and with GLU solution from the other one. Two experiments were performed with the same procedure, in order to test the influence of enzyme concentration on the reaction rate. The concentrations of the two GOx solutions were 0.2 g/l and 0.05 g/l. After flushing the system 11 times at a total high flow rate of 2.5 μl/s (1.25 μl/s from each inlet), the system was not fed for some time, until the detected oxygen concentration was approximately zero in all measuring points in the microchannel. Then, the microreactor was fed continuously from both inlets at a total flow rate of 0.250 μl/s. The dependence on the total flow rate was also tested by feeding the reactant and the enzyme at a total flow rate of 1.25 μl/s. At the end of the experiment the system was flushed 22 times with water.

A similar experiment with GOx solution at concentration of 0.05 g/l at total flow rate of 0.313 μl/s was also done using the syringes with stroke volume of 250 μl each. Before performing this experiment the microreactor was cleaned by flushing several times distilled water and then ethanol in order to completely eliminate GOx activity. After cleaning with ethanol, the microreactor was flushed with water and then flushed three times at a fast flow rate with GOx and GLU. Then, GOx and GLU were fed at the same time from the two inlets.

3.2.4 Continuous feed of glucose and glucose oxidase after feeding bovine serum albumin

The subsequent experiments consisted in performing the same experiment as described in §3.2.3, after putting in the system another protein, bovine serum albumin (BSA). The purpose of this experiment was to saturate the available sites of the microreactor internal surface, if any, with BSA. Thus, the system was first flushed 11 times with a solution of BSA at a concentration of 0.2 g/l at a total flow rate of 2.5 μl/s, and then BSA solution was fed to the reactor at a very slow flow rate (0.125 μ/l) from one inlet at a time for 80 minutes. After this, BSA was left inside the microreactor for 20 minutes in no-flow conditions. It was assumed that all BSA that could adsorb to the surfaces was adsorbed after this. At this moment the inlet microtubes were disconnected from the microreactor in order to fill the microtube and syringe volumes with GOx and GLU solutions without flushing through the microreactor. After this, the inlet tubes were connected again to the reactor inlets and the microreactor was fed at a total flow rate of 0.25 μl/s. The behaviour of the system was also tested at a total flow rate of 1.25 μl/s. The same procedure was done for the two enzyme concentrations of 0.2 g/l and 0.05 g/l.

3.2.5 Continuous feed of glucose and glucose oxidase mixed with bovine serum albumin

The procedure that was followed in this experiment was the same as the one explained in §3.2.3. The only difference is in the composition of the enzyme solution, which contained 0.05 g/l of GOx and 0.2 g/l of BSA.

3.2.6 Alternate flow of glucose oxidase and glucose

In the experiment here described GOx and GLU were not fed at the same time, as it was done in all other experiments. In this case GOx at a concentration of 0.2 g/l was first fed to the microreactor from one inlet for 24 seconds at a flow rate of 2.08 μl/s. Immediately after having fed GOx, only GLU was fed from the other inlet at the same flow rate for the same number of seconds. The sequence of alternate flows was repeated four times, in order to check if there were differences between the replicates.

3.2.7 Flow of glucose and stop flow after continuous feed of glucose and glucose oxidase

For this experiment the syringes with stroke volume of 250 μl each were used. Before performing the experiment the microreactor was flushed with ethanol to remove residual GOx activity. Then, ethanol was removed by flushing the microreactor with water. The microreactor was fed simultaneously with GOx solution at concentration of 0.05 g/l and GLU, at a total flow rate of 0.313 μl/s for around 1 hour and 50 minutes. After it, only GLU was fed from one inlet at a flow rate or 0.313 μl/s for 800 seconds. Then the flow was stopped in order to give time to the reaction to continue in the microchannel. After a long time, GLU was fed again in the same way, and then the flow was stopped.

3.2.8 Flow of glucose and stop flow after continuous feed of glucose, glucose oxidase and bovine serum albumin

This experiment was a variation of the previous one because the experimental procedure was the same. The only difference was represented by the composition of the GOx solution, which contained GOx at a concentration of 0.05 g/ and BSA at a concentration of 0.15 g/l.

3.2.9 CFD simulations

CFD simulations were performed to simulate the fluid dynamics and the reaction of the enzyme GOx in the microreactor. The simulations were also used to test if experimental data could be explained by a monolayer adsorption model of the enzyme to the walls of the microchannel.

Setting the fluid dynamics simulations involved several sequential steps, and for each step a specific software (or product of a software) was used:

1. the geometry (physical bounds) of the system were defined (software: SolidWorks or ANSYS ICEM);
2. the volume occupied by the fluid was divided into discrete elements (i.e. mesh, uniform or non-uniform) (software: ANSYS ICEM);
3. the physical models are defined as well as boundary and/or initial conditions (software: ANSYS CFX - Pre);
4. the options for the numerical solver are chosen (software: ANSYS CFX - Pre and ANSYS CFX - SolverManager);
5. the result are visualized and analyzed (software: ANSYS CFD - Post).

In the next paragraphs more details about each each step are given.

3.2.9.1 Geometry definition

The geometry of the meander channel in Figure 2.3 was drawn in ANSYS ICEM from a drawing of the geometry. The geometry represented the real geometric shape of the system, including the shape of the sensor spots.

3.2.9.2 Mesh of the physical domain

The physical domain was meshed in ANSYS ICEM with a hexahedral mesh, in order to have more reliable results than with tetrahedral mesh. More specifically, the mesh was a non-uniform rectangular mesh because a finer mesh was used near the walls of the system (Figure 3.4a). The quality of the mesh was very high because more than 91 % of the elements had angles between 81 ° and 90 ° and the remaining 9 % was in the range between 45 ° and 81 °. The total number of elements in the domain was around 362,900. The mesh on the sensor spots is shown in Figure 3.4b.

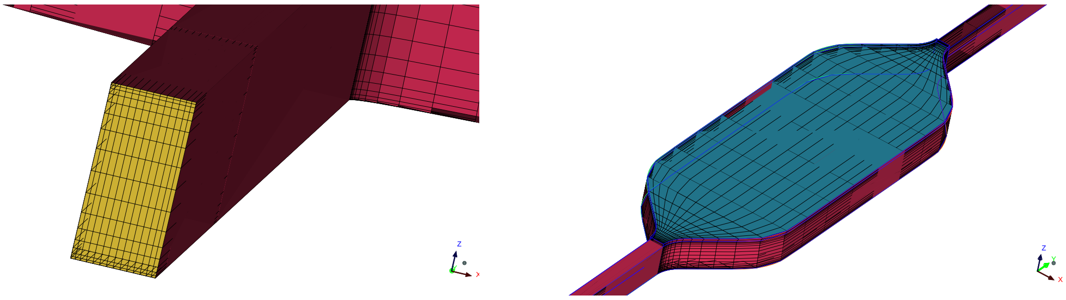

(a) Mesh on the cross-sectional area. ***(b)*** Mesh on the sensor spot.

Figure 3.4 *Examples of the mesh of the domain.*

3.2.9.3 Boundary and/or initial conditions and physical models definitions

The complete definition of the physics of the system was done in ANSYS CFX - PRE. First of all, the general characteristics of the system were defined: the fluid flow was defined as laminar, heat transfer was not modeled, the effect of gravity was neglected and the pressure of the system was fixed at atmospheric pressure. The additional chemical compounds were inserted in the domain and defined in terms of diffusion coefficients. The diffusion coefficients of the compounds present in the system are detailed in Table 3.3.

Table 3.3 *Diffusion coefficients of the compounds present in the system.*

Compound	**Diffusion coefficient** $\left(\mathrm{m}^2 \cdot \mathrm{s}^{-1}\right)$
Glucose oxidase	$2.0 \cdot 10^{-11}$
Adsorbed glucose oxidase	$1.0 \cdot 10^{-15}$
$\beta - \mathrm{D} -$ glucose	$6.9 \cdot 10^{-10}$
D − glucono − 1,5 − lactone	$1.0 \cdot 10^{-9}$
Hydrogen peroxide	$2.1 \cdot 10^{-9}$
Oxygen	$2.1 \cdot 10^{-9}$

Boundary conditions As far as boundary conditions are concerned, the mass flow was defined for each inlet as well as the composition of the inlet flow. The outlet was defined as an opening, in order to allow the possibility of having back flows and not forcing the system to have an outlet flow.

Reaction rate model The reaction was defined in the volume of the meander channel according to equation

$$v = c_{\mathrm{E}} k_{cat} \frac{c_{\mathrm{GLU}} c_{\mathrm{O_2}}}{K_{\mathrm{M}}^{\mathrm{O_2}} c_{\mathrm{GLU}} + K_{\mathrm{M}}^{\mathrm{GLU}} c_{\mathrm{O_2}} + c_{\mathrm{GLU}} c_{\mathrm{O_2}}} \tag{3.1}$$

with the parameters in Table 3.4. A model for the reaction rate of the enzyme catalase, included in the enzyme preparation, is not included since the amount of catalase in the preparation is not known. Moreover, an experiment has been done to measure catalase activity (GOx solution was mixed with a solution of H_2O_2) and no significant increase in oxygen concentration was observed.

Table 3.4 Parameters used in the kinetic model of glucose oxidase (van Stroe-Biezen et al., 1994).

Parameter	Value
k_{cat}	$200\ \mathrm{mol \cdot kg^{-1} \cdot min^{-1}}$
K_M^{GLU}	$70\ \mathrm{mol \cdot m^{-3}}$
$K_M^{\mathrm{O_2}}$	$0.8\ \mathrm{mol \cdot m^{-3}}$

When the adsorption model is implemented in the system, the expression of the reaction rate in equation (3.1) is modified into

$$r = \left(c_{\mathrm{E}} + \frac{c_{\mathrm{E}}^*}{\delta} \right) k_{cat} \frac{c_{\mathrm{GLU}} c_{\mathrm{O_2}}}{K_{\mathrm{M}}^{\mathrm{O_2}} c_{\mathrm{GLU}} + K_{\mathrm{M}}^{\mathrm{GLU}} c_{\mathrm{O_2}} + c_{\mathrm{GLU}} c_{\mathrm{O_2}}} \tag{3.2}$$

where δ (m), the diffusional length, is defined as

$$\delta = 2\sqrt{t \cdot D_{\mathrm{E}^*}} \tag{3.3}$$

where D_{E^*} ($\mathrm{m^2 \cdot s^{-1}}$) is the diffusion coefficient of the immobilized enzyme.

Adsorption model It is considered that the adsorption takes place on the walls of the microreactor, therefore the walls are modeled in the simulation as a 2 - D boundary source for the concentration of the free and immobilized enzyme. The rate of adsorption is defined as

$$r_{ads} = k_{ads} c_{\mathrm{E}} \left(c^* - c_{\mathrm{E}}^* \right) \tag{3.4}$$

and the rate of desorption is expressed by

$$r_{des} = k_{des} c_{\mathrm{E}}^* \tag{3.5}$$

The concentration of the free enzyme will be determined by the difference of the two rates, since it is increased by desorption and decreased by adsorption

$$c_{\mathrm{E}} = r_{des} - r_{ads} \tag{3.6}$$

The concentration of the immobilized enzyme increases because of adsorption and decreases by desorption times the reciprocal of SA:V

$$c_{\mathrm{E}}^{*} = \left(r_{ads} - r_{des}\right)\frac{V}{S} \tag{3.7}$$

where V is the volume of the reactor and S is the surface of the walls of the reactor.

Several simulations are performed with different values of the parameters k_{ads}, k_{des} and c^{*}. The values of the parameters are given in Table 3.5.

Table 3.5 *Parameters used in the different adsorption models.*

Relative speed of the different adsorption kinetics	$\mathbf{k_{ads}}$ $\left(\mathbf{m^5 \cdot kg^{-1} \cdot s^{-1}}\right)$	$\mathbf{k_{des}}$ $\left(\mathbf{kg \cdot s^{-1}}\right)$	$\mathbf{c^{*}}$ $\left(\mathbf{kg \cdot m^{-2}}\right)$
very slow	$1 \cdot 10^{-10}$	$1 \cdot 10^{-12}$	$5 \cdot 10^{-7}$
slow	$1 \cdot 10^{-8}$	$1 \cdot 10^{-12}$	$5 \cdot 10^{-5}$
fast	$1 \cdot 10^{-4}$	$1 \cdot 10^{-5}$	$5 \cdot 10^{-7}$

The adsorption model (from equation (3.4) to equation (3.7)) has been formulated and tested in a simple geometry before adding it into the simulations of the meander channel. The geometry and the results of the performed simulations are shown in Appendix E on page 167.

Initialization When transient simulations were run, the system initialization was done either by putting zero for all the variables (velocity components and concentrations of all compounds) if the simulation was just started or by using the values calculated by previous simulations for the solution of the new domain.

3.2.9.4 Numerical solver for transient simulations

The selected advection scheme was high resolution and the transient scheme was second order backward Euler. The maximum number of iterations per loop was set to 50 and the convergence criteria at Root Mean Square (RMS) of the residuals of $1 \cdot 10^{-4}$. The solver was always at double precision.

3.2.9.5 Results analysis and visualization

Data analysis was done in ANSYS CFD - Post. The mass balance was always checked, as well as the velocity profiles. Streamlines, contour plots and volume renderings were used to analyse the system. When the concentration of one species was monitored at one specific point, the concentration was calculated as the surface weighted average concentration.

Chapter 4

Results

In this Chapter the experimental results are presented. The Chapter is divided into two Sections: in §4.1 the results regarding $\omega-$TAm are presented and in §4.2 the results regarding GOx experiments and CFD simulations are shown.

4.1 Transamination

In this Section the results obtained from the experiments with $\omega-$TAm are presented.

4.1.1 Activity determination

$\omega-\mathrm{TAm}$ activity is calculated from initial reaction rate measurements, which is obtained by measuring the variation over time of the concentration of a reactant ($(S)-\alpha-\mathrm{MBA}$) and of a product (APH). Due to the poor precision of the measurements of $(S)-\alpha-\mathrm{MBA}$ concentration, activity could not be determined in terms of substrate depletion but in terms of product synthesis. The experimental data of $(S)-\alpha-\mathrm{MBA}$ are presented in Appendix C on page 137.

4.1.1.1 Batch system

$\omega-\mathrm{TAm}$ activity was measured in the batch system with the method described in § 3.1.2.1 on page 48 at the standard activity conditions defined in § 3.1.2 on page 48. The experimental data of the two experiments, each done in quadruplicate, are presented in Table 4.1

and Table 4.2 for APH, as well as mean values and standard deviations at each time (the corresponding data for $(S)-\alpha-\mathrm{MBA}$ are presented in § C.1 on page 137). In the same tables, the slopes and the corresponding coefficients of determination are presented. This is because, when initial reaction rate is measured, linear variation of concentration over time is expected. Therefore, simple linear regression is used to fit a straight line through the set of experimental data in such a way that it makes the sum of squared residuals of the model (i.e. the vertical distances between the points of the data set and the fitted line) as small as possible. Since it is intended to measure initial reaction rate, only the data points in within the first four minutes of reaction are included in the initial reaction rate estimation. The slope of the straight line corresponds to the activity of the enzyme because it indicates the variation of concentration of a compound over time. The evolution of the mean concentration values of APH in both sets are graphically shown in Figure 4.1.

Table 4.1 *Variation of the concentration of acetophenone over time in the batch system for activity measurement (first measurement set).*

Time (min)	c_{APH} (1) **(mM)**	c_{APH} (2) **(mM)**	c_{APH} (3) **(mM)**	c_{APH} (4) **(mM)**	**Mean (mM)**	**SD (mM)**
0	0.029	0.026	0.028	0.028	0.028	0.001
1	0.126	0.137	0.140	0.138	0.135	0.007
2	0.288	0.288	0.261	0.237	0.268	0.024
4	0.434	0.439	0.444	0.449	0.441	0.007
6	0.616	0.631	0.675	0.662	0.646	0.027
10	0.996	1.041	1.112	1.058	1.052	0.048
60	4.992	4.963	5.051	5.069	5.019	0.050
Slope (mM/min)	0.103	0.104	0.104	0.105	0.104	0.001
R^2	0.974	0.978	0.996	1.000	0.992	

Table 4.2 *Variation of the concentration of acetophenone over time in the batch system for activity measurement (second measurement set).*

Time (min)	c_{APH} (1) **(mM)**	c_{APH} (2) **(mM)**	c_{APH} (3) **(mM)**	c_{APH} (4) **(mM)**	**Mean (mM)**	**SD (mM)**
0	0.031	0.027	0.027	0.029	0.028	0.002
1	0.164	0.168	0.282	0.164	0.194	0.058
2	0.277	0.368	0.521	0.294	0.365	0.111
4	0.571	0.557	0.663	0.531	0.580	0.057
6	0.831	0.796	0.889	0.793	0.827	0.045
10	0.240	1.208	1.249	1.288	0.996	0.505
60	2.686	5.694	5.676	5.616	4.918	1.488
Slope (mM/min)	0.135	0.134	0.156	0.125	0.137	0.013
R^2	0.997	0.975	0.908	0.999	0.985	

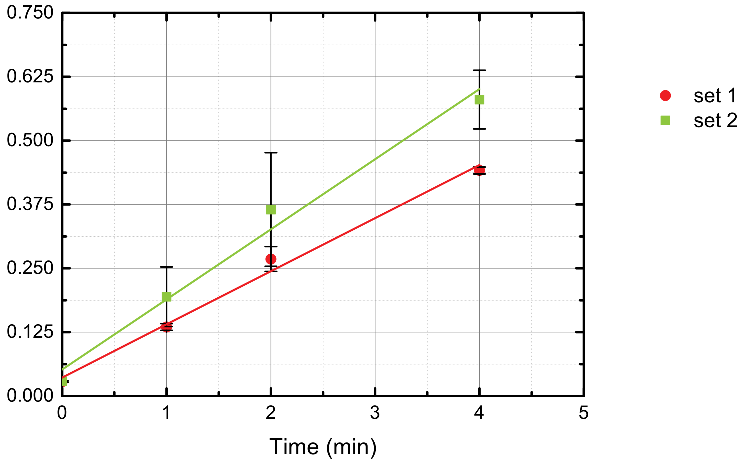

Figure 4.1 *Variation of acetophenone concentration over time in the batch system for activity measurement. The graph shows only the measurements from time 0 to 4 minute. The measurements have been done in activity conditions, i.e. 40 mM of $(S)-\alpha-$Methylbenzylamine, 40 mM of pyruvic acid, 0.1 mM of pyridoxal-5'-phosphate, 0.05 g/l of enzyme $\omega-$Transaminase at 30 ℃ and pH 8.*

Enzyme activities of the two experimental sets are summarized in Table 4.3; the activity of each experimental set is calculated as average of quadruplicates and the activity in the batch system is calculated as mean of the measured activities in the two experiments. The specific activity is calculated by dividing the activity by the amount of enzyme injected in the vial.

Table 4.3 *$\omega-$Transaminase activity in the batch system. The measurements have been done in activity conditions, i.e. 40 mM of $(S)-\alpha-$Methylbenzylamine, 40 mM of pyruvic acid, 0.1 mM of pyridoxal-5'-phosphate, 0.05 g/l of enzyme $\omega-$Transaminase at 30 ℃ and pH 8.*

	Experimental set 1	**Experimental set 2**	**Mean**
Activity (U)	104.01	137.33	120.67
Specific activity (U/mg)	666.75	847.72	757.24

The activity of $\omega-$TAm in the batch system is 120.67 U and the specific activity is 757.24 U/mg.

4.1.1.2 Microreactor

$\omega-$TAm activity was measured in the microreactor with the method described in § 3.1.2.2 on page 49, at the standard activity conditions defined in § 3.1.2 on page 48. The procedure for calculating enzyme activity is the same as for the activity measurement in the batch system. In this case the initial reaction rate, i.e. activity, is measured in within the first 3.632 minutes of reaction. The experimental data of the three experiments, each done in quintuplicate, are presented in Table 4.4, Table 4.5 and Table 4.6 for APH, as well as mean values, standard deviations, slopes and determination coefficients. Experimental data for $(S)-\alpha-$MBA are presented in § C.2 on page 139.

Table 4.4 *Variation of concentration of acetophenone over time in the microreactor for activity measurement (first measurement set).*

Time (**min**)	c_{APH} (1) (**mM**)	c_{APH} (2) (**mM**)	c_{APH} (3) (**mM**)	c_{APH} (4) (**mM**)	c_{APH} (5) (**mM**)	**Mean** (**mM**)	**SD** (**mM**)
0	0.047	0.088	0.027	0.032	n.a.	0.048	0.027
0.454	0.093	0.102	0.112	0.120	0.128	0.111	0.014
1.067	0.248	0.287	0.294	0.293	0.306	0.285	0.022
2.595	0.612	0.755	0.736	0.771	0.770	0.729	0.067
3.632	0.919	1.069	1.066	1.075	1.086	1.043	0.070
Slope (mM/min)	0.244	0.284	0.290	0.294	0.302	0.270	0.023
R^2	0.993	0.989	0.998	0.998	1.000	0.992	

Table 4.5 *Variation of concentration of acetophenone over time in the microreactor for activity measurement (second measurement set).*

Time (**min**)	c_{APH} (1) (**mM**)	c_{APH} (2) (**mM**)	c_{APH} (3) (**mM**)	c_{APH} (4) (**mM**)	c_{APH} (5) (**mM**)	**Mean** (**mM**)	**SD** (**mM**)
0	0.028	0.027	0.027	0.029	0.028	0.028	0.001
0.454	0.097	0.152	0.134	0.144	0.163	0.138	0.025
1.067	0.178	0.264	0.310	0.337	0.370	0.292	0.075
2.595	0.777	0.939	0.953	1.010	1.016	0.939	0.097
3.632	1.174	1.403	1.435	1.494	1.485	1.398	0.131
Slope (mM/min)	0.326	0.385	0.393	0.410	0.405	0.357	0.037
R^2	0.978	0.987	0.991	0.993	0.997	0.984	

Table 4.6 *Variation of concentration of acetophenone over time in the microreactor for activity measurement (third measurement set).*

Time **(min)**	c_{APH} (1) (mM)	c_{APH} (2) (mM)	c_{APH} (3) (mM)	c_{APH} (4) (mM)	c_{APH} (5) (mM)	**Mean** **(mM)**	**SD** **(mM)**
0	0.025	0.026	0.026	0.025	0.027	0.026	0.001
0.454	0.094	0.113	0.128	0.161	0.174	0.134	0.033
1.067	0.291	0.327	0.320	0.340	0.358	0.327	0.025
2.595	0.721	0.841	0.879	0.914	0.898	0.850	0.077
3.632	1.067	1.210	1.188	1.315	1.309	1.218	0.102
Slope (mM/min)	0.291	0.332	0.330	0.358	0.352	0.323	0.028
R^2	0.996	0.997	0.997	0.998	0.998	0.997	

The evolution of the mean concentration values of APH concentration in all sets are graphically shown in Figure 4.2.

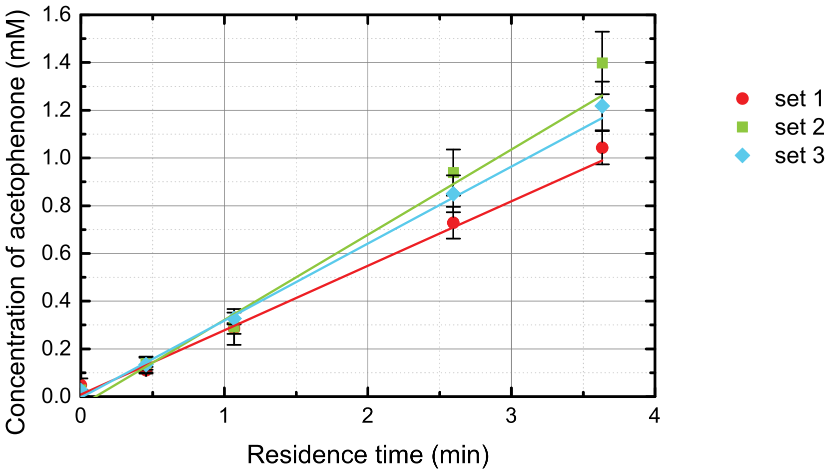

Figure 4.2 *Variation of acetophenone concentration over time in the microreactor for activity measurement. The measurements have been done in activity conditions, i.e. 40 mM of* (S) $-\alpha-$*Methylbenzylamine, 40 mM of pyruvic acid, 0.1 mM of pyridoxal-5'-phosphate, 0.05 g/l of enzyme* $\omega-$*Transaminase at 30 °C and pH 8.*

Enzyme activities calculated from the three experimental sets are summarized in Table 4.7; the activity of each experimental set is calculated as average of the quintuplicates in the set and the activity in the microreactor is calculated as mean of the measured activities in the three experiments. The specific activity is calculated by dividing the activity by the total amount of $\omega-$TAm fed in the microreactor.

Table 4.7 *$\omega-$Transaminase activity in the microreactor. The measurements have been done in activity conditions, i.e. 40 mM of $(S)-\alpha-$Methylbenzylamine, 40 mM of pyruvic acid, 0.1 mM of pyridoxal-5'-phosphate, 0.05 g/l of enzyme $\omega-$Transaminase at 30 ℃ and pH 8.*

	Experimental set 1	**Experimental set 2**	**Experimental set 3**	**Mean**
Activity (U)	270.06	357.261	322.71	316.68
Specific activity (U/mg)	51,934.94	66,159.37	62,059.87	60,051.39

The activity of $\omega-$TAm in the microreactor is 316.68 U and the specific activity is 60051.39 U/mg.

4.1.2 Determination of apparent kinetic parameters

The set of experiments presented in § 3.1.3 on page 50 was designed for the determination of the apparent kinetic parameters $K_{M,app}^{\mathrm{MBA}}$, $V_{max,app}^{\mathrm{MBA}}$, $K_{M,app}^{\mathrm{PYR}}$ and $V_{max,app}^{\mathrm{PYR}}$ in the batch system and in the microreactor for the forward reaction in Figure 3.1. Transamination is a bisubstrate reaction and the determination of K_M and V_{max} for each substrate (and not of the apparent kinetic parameters) would have required a large number of experiments, each of them done to evaluate the reaction rate at different relative concentrations of the two substrates according to the scheme in Figure 4.3 (Purich, 2010).

$$\begin{array}{ccccc}
\mathrm{C_A^1/C_B^1} & \mathrm{C_A^2/C_B^1} & \color{red}{\mathrm{C_A^3/C_B^1}} & \cdots & \mathrm{C_A^n/C_B^1} \\
\mathrm{C_A^1/C_B^2} & \mathrm{C_A^2/C_B^2} & \color{red}{\mathrm{C_A^3/C_B^2}} & \cdots & \mathrm{C_A^n/C_B^2} \\
\color{red}{\mathrm{C_A^1/C_B^3}} & \color{red}{\mathrm{C_A^2/C_B^3}} & \color{red}{\mathrm{C_A^3/C_B^3}} & \color{red}{\cdots} & \color{red}{\mathrm{C_A^n/C_B^3}} \\
\vdots & \vdots & \color{red}{\vdots} & \ddots & \vdots \\
\mathrm{C_A^1/C_B^m} & \mathrm{C_A^2/C_B^m} & \color{red}{\mathrm{C_A^3/C_B^m}} & \cdots & \mathrm{C_A^n/C_B^m}
\end{array}$$

Figure 4.3 *Scheme for the design of experiment for kinetic parameter estimation for a bisubstrate enzyme. The red colour indicates the subset of experiments that were performed in this project.*

Along the rows, the concentration of substrate B is maintained constant, while the concentration of substrate A is changed; along the columns it is exactly the opposite. The determination of apparent kinetic parameters corresponds to the sub-set of experiments indicated with the red colour in Figure 4.3. This means that the reaction rate was only evaluated for each substrate at constant (and only one) concentration of the other substrate.

For the determination of the kinetic parameters, it is assumed that the initial reaction rate can be represented by a Michaelis-Menten kinetic model, even though in reality it is known that the kinetic model is much more complex. In fact, the determination of the kinetic parameters is only aimed at investigating the different behaviour of the enzymatic reaction in a batch system and in a microreactor.

The determination of the kinetic parameters was done by rearranging Michaelis-Menten equation (which defines a hyperbolic relation between initial substrate concentration and initial reaction rate)

$$v = \frac{V_{max} c_S}{K_M + c_S} \tag{4.1}$$

into the linear relation

$$\frac{c_S}{v} = \frac{1}{V_{max}} c_S + \frac{K_M}{V_{max}} \tag{4.2}$$

between c_S/v and c_S, which is known as Hanes-Woolf relation. Experimental data were plotted in the semi-reciprocal plot c_S/v versus c_S (Hanes-Woolf plot) and they were fitted to a straight line; according to equation (4.2), V_{max} corresponds to the reciprocal of the slope and K_M can be calculated by multiplying the intercept by V_{max}.

The apparent kinetic parameters were calculated in this way for $(S)-\alpha-\mathrm{MBA}$ (at constant PYR concentration) and for PYR (at constant $(S)-\alpha-\mathrm{MBA}$ concentration) in the batch system and in the microreactor.

4.1.2.1 Variable $(S)-\alpha-\mathrm{MBA}$ concentration, constant pyruvate concentration

In order to evaluate $K_{M,app}^{\mathrm{MBA}}$ and $V_{max,app}^{\mathrm{MBA}}$, the reaction rate of the forward reaction in Figure 3.1 was evaluated at different compositions of the reaction mixture; the mixture had constant PYR concentration (40 mM), which had to be at saturation conditions in order to avoid limitation of the reaction rate. The range of concentration of $(S)-\alpha-\mathrm{MBA}$ was decided based on K_M measured by Shin and Kim (1998), since $(S)-\alpha-\mathrm{MBA}$ concentration has to range from concentrations below K_M to concentrations higher than K_M for a proper $K_{M,app}$ evaluation.

Batch system The initial reaction rate was measured in the batch system at different $(S)-\alpha-\mathrm{MBA}$ concentrations; the data are shown in Table 4.8. The reagent mixture composition corresponds to a two folds dilution of the solutions described in Table 3.1 on page 51, since half of the reaction volume is filled with the enzyme solution. The reaction rate corresponding to the activity determination was also included in the set of data. The experimental data that are used to calculate the initial reaction rate are presented in Appendix D.1.1 on page 141.

Table 4.8 *Initial reaction rate at different $(S)-\alpha-$Methylbenzylamine concentrations in the batch system.*

Reagent mixture	c_{MBA} (mM)	v $\left(\text{mM}\cdot\text{min}^{-1}\right)$
A.1	0.376	0.050
B.1	1.726	0.100
C.1	4.771	0.118
D.1	9.014	0.131
Activity mixture	40.000	0.121
E.1	57.459	0.128
F.1	100.526	0.118

c_{MBA} and the ratio of c_{MBA} to v were plotted in the Hanes-Woolf plot for the determination of $K_{M,app}^{\text{MBA}}$ and $V_{max,app}^{\text{MBA}}$ (Figure 4.4). Simple linear regression was used to fit a straight line, corresponding to equation (4.2), to the set of data points. The equation resulting from the linear regression is

$$\frac{c_{\text{MBA}}}{v} = 8.348 \cdot c_{\text{MBA}} + 2.578 \tag{4.3}$$

with a determination coefficient of 0.9981. The kinetic parameters were calculated from the slope and intercept as $K_{M,app}^{\text{MBA}} = 0.31$ mM and $V_{max,app}^{\text{MBA}} = 0.12\ \text{mM}\cdot\text{min}^{-1}$.

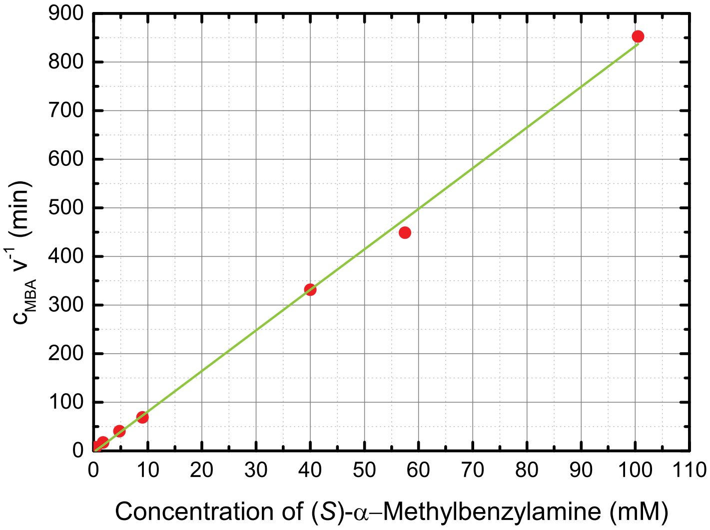

Figure 4.4 *Hanes-Woolf plot for the determination of $K_{M,app}^{MBA}$ and $V_{max,app}^{MBA}$ at 40 mM of pyruvic acid and variable $(S)-\alpha-$Methylbenzylamine concentration in the batch system. The straight line is obtained by simple linear regression. The y-axis indicates the ratio of the concentration of $(S)-\alpha-$Methylbenzylamine to the initial reaction rate.*

Microreactor The initial reaction rate was measured in the microreactor at different $(S)-\alpha-\mathrm{MBA}$ concentrations; the data are shown in Table 4.9. The reagent mixture composition corresponds to a two folds dilution of the solutions described in Table 3.1 on page 51, since the reagent mixture corresponded to half of the total feed of the microreactor. For the microreactor, the reaction rate measured in the activity determination experiment is not included in the data set. The experimental data that are used to calculate the initial reaction rate are presented in Appendix D.1.2 on page 148.

Table 4.9 *Initial reaction rate at different $(S)-\alpha-$Methylbenzylamine concentrations in the microreactor.*

Reagent mixture	**c_{MBA} (mM)**	**v $\left(\mathrm{mM}\cdot\mathrm{min}^{-1}\right)$**
A.1	0.393	0.059
B.1	1.742	0.148
C.1	4.859	0.183
D.1	9.200	0.234
E.1	60.941	0.486
F.1	101.629	0.609

c_{MBA} and the ratio of c_{MBA} to v were plotted in the Hanes-Woolf plot for the determination of $K_{M,app}^{\mathrm{MBA}}$ and $V_{max,app}^{\mathrm{MBA}}$ in the microreactor (Figure 4.5). Simple linear regression was used to fit a straight line, corresponding to equation (4.2), to the set of data points. The equation resulting from the linear regression is

$$\frac{c_{\mathrm{MBA}}}{v} = 1.573 \cdot c_{\mathrm{MBA}} + 15.878 \tag{4.4}$$

with a determination coefficient of 0.9776. The kinetic parameters were calculated from the slope and intercept as $K_{M,app}^{\mathrm{MBA}} = 10.10$ mM and $V_{max,app}^{\mathrm{MBA}} = 0.64\ \mathrm{mM} \cdot \mathrm{min}^{-1}$.

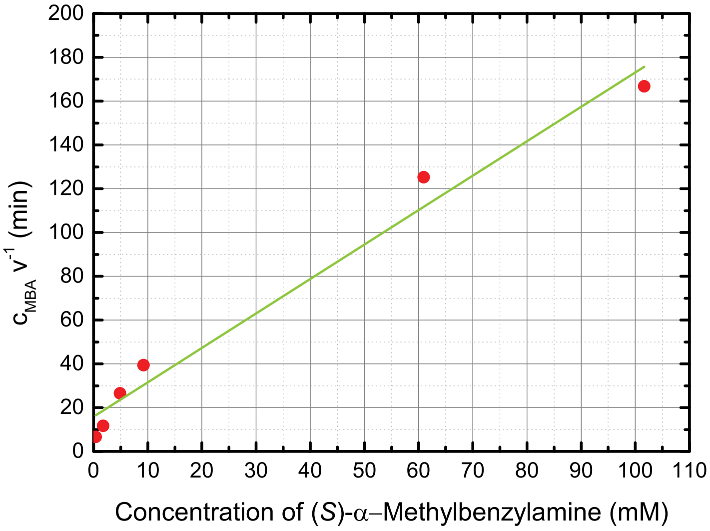

Figure 4.5 *Hanes-Woolf plot for the determination of $K_{M,app}^{\mathrm{MBA}}$ and $V_{max,app}^{\mathrm{MBA}}$ at 40 mM of pyruvic acid and variable $(S)-\alpha-$Methylbenzylamine concentration in the microsystem. The straight line is obtained by simple linear regression. The y-axis indicates the ratio of the concentration of $(S)-\alpha-$Methylbenzylamine to the initial reaction rate.*

In Table 4.10 $K_{M,app}^{\mathrm{MBA}}$ and $V_{max,app}^{\mathrm{MBA}}$ for the batch system and the microreactor are summarized. The catalytic efficiency of the enzyme is also calculated; the efficiency η ($\mathrm{mg}^{-1} \cdot \mathrm{min}^{-1}$) is defined as

$$\eta = \frac{k_{cat}}{K_M} = \frac{V_{max}}{m_{\mathrm{E}} K_M} \tag{4.5}$$

where m_{E} (mg) is the mass of enzyme used for the reaction.

Table 4.10 *Apparent kinetic parameters for* $(S)-\alpha-$*Methylbenzylamine.*

	$K_{M,app}^{MBA}$ (mM)	$V_{max,app}^{MBA}$ $(mM \cdot min^{-1})$	η^{MBA} $(mg^{-1} \cdot min^{-1})$
Batch system	0.31	0.12	2.49
Microreactor	10.10	0.64	12.11

4.1.2.2 Variable pyruvate concentration, constant $(S)-\alpha-$MBA concentration

The same procedure was used to evaluate $K_{M,app}^{\mathrm{PYR}}$ and $V_{max,app}^{\mathrm{PYR}}$ for the forward reaction in Figure 3.1. In this case all reagent mixtures had constant $(S)-\alpha-$MBA concentration of 40 mM, which corresponds to saturation conditions. The range of concentration of PYR was decided based on K_M measured by Shin and Kim (1998), since PYR concentration has to range from concentrations below K_M to concentrations higher than K_M for a proper $K_{M,app}$ evaluation.

Batch system Measurements of initial reaction rate in the batch system at different PYR concentrations are shown in Table 4.11. The reagent mixture composition corresponds to a two folds dilution of the solutions described in Table 3.1 on page 51. The set of data includes also the reaction rate determined in activity conditions. The experimental data that are used to calculate the initial reaction rate are presented in Appendix D.2.1 on page 154.

Table 4.11 *Initial reaction rate at different pyruvic acid concentrations in the batch system.*

Reacting mixture	**c_{PYR} (mM)**	**v $\left(\mathrm{mM} \cdot \mathrm{min}^{-1}\right)$**
L.1	5	0.087
M.1	10	0.107
N.1	15	0.112
O.1	40	0.121
Activity mixture	80	0.148
P.1	100	0.145
Q.1	200	0.127

c_{PYR} and the ratio of c_{PYR} to v are plotted in the Hanes-Woolf plot for the determination of $K_{M,app}^{\mathrm{PYR}}$ and $V_{max,app}^{\mathrm{PYR}}$ (Figure 4.6). Simple linear regression is used to fit a straight line, corresponding to equation (4.2), to the set of data points. The equation resulting from the linear regression is

$$\frac{c_{\mathrm{PYR}}}{v} = 7.577 \cdot c_{\mathrm{PYR}} + 0.655 \tag{4.6}$$

with a determination coefficient of 0.9918. The kinetic parameters are calculated from the slope and intercept as $K_{M,app}^{\mathrm{PYR}} = 0.09$ mM and $V_{max,app}^{\mathrm{PYR}} = 0.13\ \mathrm{mM} \cdot \mathrm{min}^{-1}$.

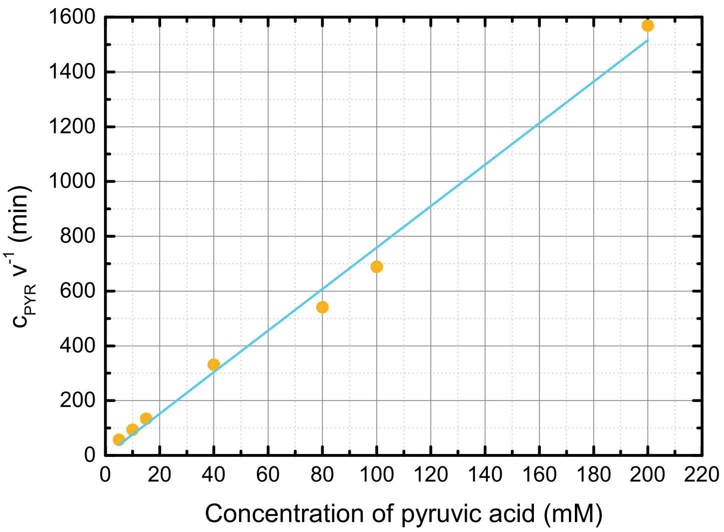

Figure 4.6 *Hanes-Woolf plot for the determination of $K^{PYR}_{M,app}$ and $V^{PYR}_{max,app}$ at 40 mM of $(S)-\alpha-$Methylbenzylamine and variable pyruvic acid concentration in the batch system. The straight line is obtained by simple linear regression. The y-axis indicates the ratio of the concentration of pyruvic acid to the initial reaction rate.*

Microreactor Data of initial reaction rate in the microreactor at different PYR concentrations are shown in Table 4.12. The reagent mixture composition corresponds to a two folds dilution of the solutions described in Table 3.1 on page 51. For the microreactor, the reaction rate measured in the activity determination experiment is not included in the data set. The experimental data that are used to calculate the initial reaction rate are presented in Appendix D.2.2 on page 161.

Table 4.12 *Initial reaction rate at different pyruvic acid concentrations in the microreactor.*

Reacting mixture	c_{PYR} (mM)	v $\left(\mathrm{mM} \cdot \mathrm{min}^{-1}\right)$
L.1	5	0.167
M.1	10	0.217
N.1	15	0.365
O.1	80	0.449
P.1	100	0.644
Q.1	200	0.606

$K^{PYR}_{M,app}$ and $V^{PYR}_{max,app}$ in the microreactor were determined from the Hanes-Woolf plot in Figure 4.7. Simple linear regression was used to fit a straight line, corresponding to equation (4.2), to the set of data points. The equation of the straight line resulted to be

$$\frac{c_{\mathrm{PYR}}}{v} = 1.520 \cdot c_{\mathrm{PYR}} + 26.257 \tag{4.7}$$

with a determination coefficient of 0.9772. The kinetic parameters were calculated from the slope and intercept as $K_{M,app}^{\mathrm{PYR}} = 17.28$ mM and $V_{max,app}^{\mathrm{PYR}} = 0.66\ \mathrm{mM} \cdot \mathrm{min}^{-1}$.

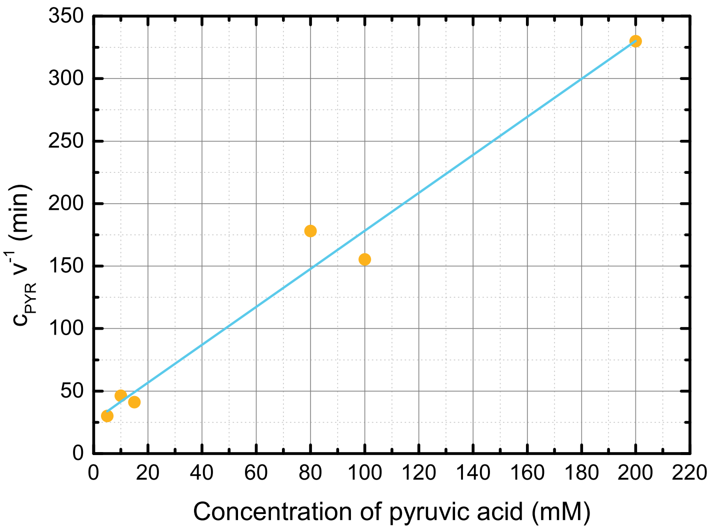

Figure 4.7 *Hanes-Woolf plot for the determination of $K_{M,app}^{\mathrm{PYR}}$ and $V_{max,app}^{\mathrm{PYR}}$ at 40 mM of $(S)-\alpha-$Methylbenzylamine and variable pyruvic acid concentration in the microsystem. The straight line is obtained by simple linear regression. The y-axis indicates the ratio of the concentration of pyruvic acid to the initial reaction rate.*

In Table 4.13 $K_{M,app}^{\mathrm{PYR}}$, $V_{max,app}^{\mathrm{PYR}}$ and efficiency for the batch system and the microreactor are compared .

Table 4.13 *Apparent kinetic parameters for pyruvic acid.*

	$K_{M,app}^{\mathrm{PYR}}$ (mM)	$V_{max,app}^{\mathrm{PYR}}$ $(\mathrm{mM} \cdot \mathrm{min}^{-1})$	η^{PYR} $(\mathrm{mg}^{-1} \cdot \mathrm{min}^{-1})$
Batch system	0.09	0.13	9.79
Microreactor	17.28	0.66	7.32

4.1.3 Reaction rate in microreactors with different SA:V

The dependence of the enzymatic kinetics in microreactors differing only for SA:V was tested performing the reaction in Figure 3.1. In Figure 4.8 the variation of the SA:V vs. the height of the microreactor is represented. The structures that were used for the experiment are the ones listed in Table 2.1 on page 42.

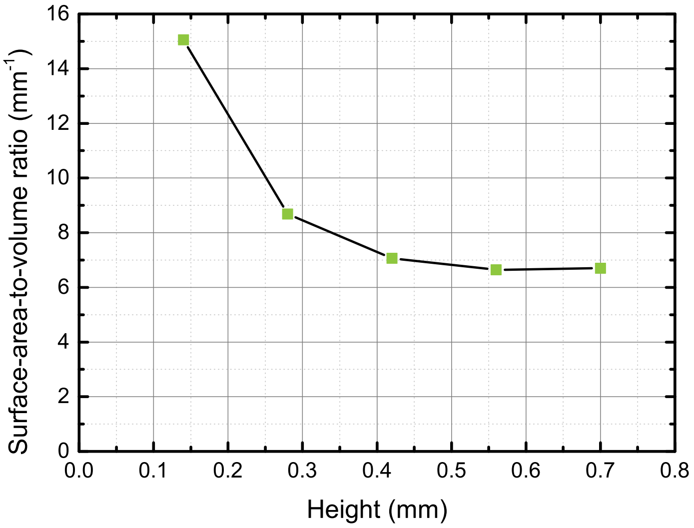

Figure 4.8 *Variation of the surface-area-to-volume ratio with the height of the microreactors, at constant length and volume of the microreactors.*

The experiment was performed at the conditions explained in § 3.1.4 on page 53. The outlet concentration of APH measured in each microreactor, which has a specific SA:V, is represented in Figure 4.9. Thus, the concentration of product increases with the increase of SA:V.

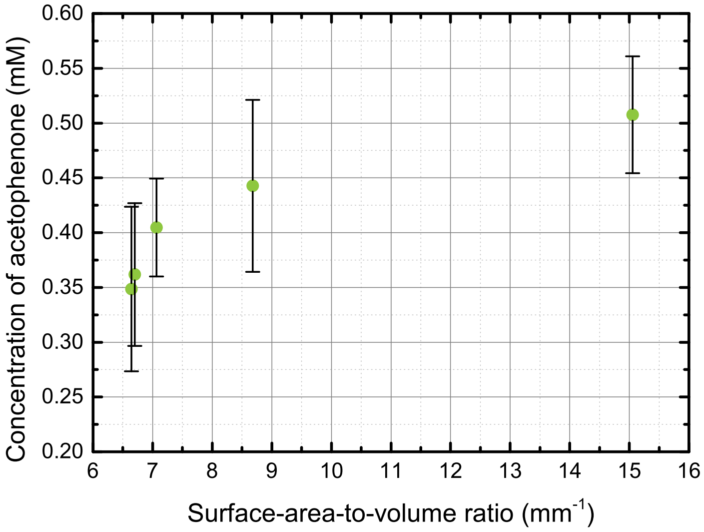

Figure 4.9 *Variation of the concentration of acetophenone at the outlet of the microreactors with different surface-area-to-volume ratio. For all microreactors, the residence time was 2.5 minute.*

This experiment shows that enzymatic kinetics is a SA:V related phenomena, and it could be exploited in the design of microreactors in order to enhance the productivity of enzymatic reactions in microreactors.

4.2 Oxidation

The experimental results regarding GOx are presented in this Section, followed by the presentation of the results of the CFD simulations of the system.

4.2.1 Experimental results

4.2.1.1 Continuous feed of glucose and glucose oxidase

In this Section the experimental results regarding the experiment with continuous flow of GOx and GLU are presented. The Section is divided into two parts: the first part contains the results using GOx solution of concentration of 0.2 $\mathrm{g \cdot l^{-1}}$, the second one is about the results with GOx solution of concentration 0.05 $\mathrm{g \cdot l^{-1}}$. Each solution is used for two experiments at a different flow rate.

Glucose oxidase concentration of 0.2 g $\cdot$ l^{-1} In Figure 4.10 and Figure 4.11 the oxygen profiles relative to the experiment with GOx solution with concentration 0.2 g/l explained in §3.2.3 are shown. Figure 4.10 is relative to a total flow rate of 0.25 μl/s, while Figure 4.11 is referred to a total flow rate of 1.25 μl/s. Note that the these two sets of data are taken sequentially, without flushing the reactor in between. All measurements belong to the same data set, this is why the time axis does not start from zero in each graph. The oxygen profiles relative to the entire experiment are shown in § F.1.1 on page 177.

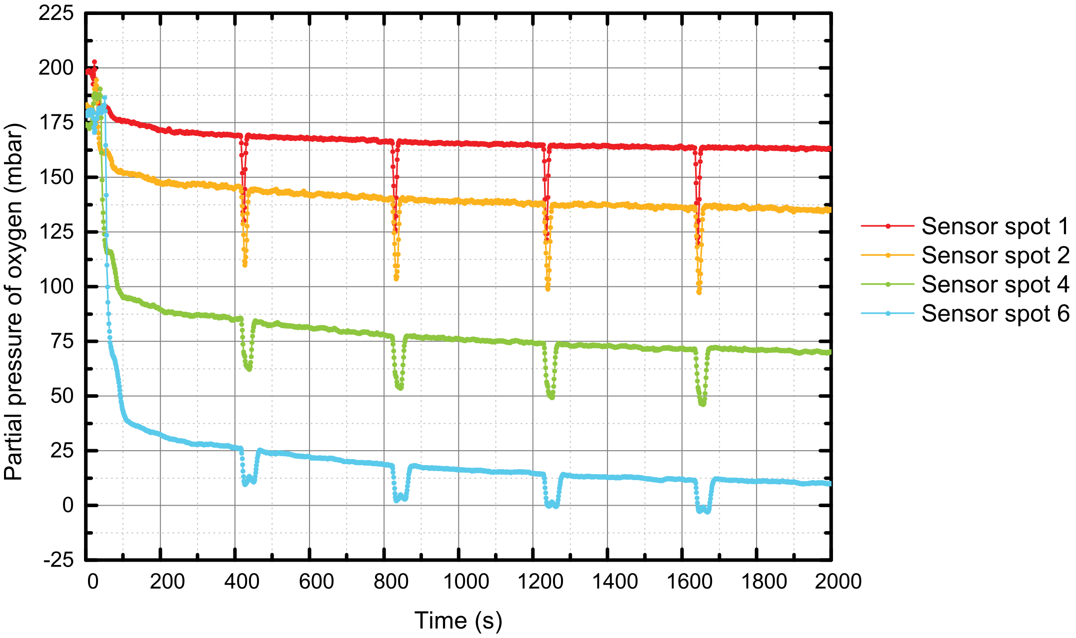

Figure 4.10 *Profiles of oxygen partial pressure over time in the sensor spots 1, 2, 4 and 6 at a total flow rate of 0.025 μl$\cdot$s^{-1} at a concentration of glucose oxidase solution of 0.2* g $\cdot$ l^{-1}.

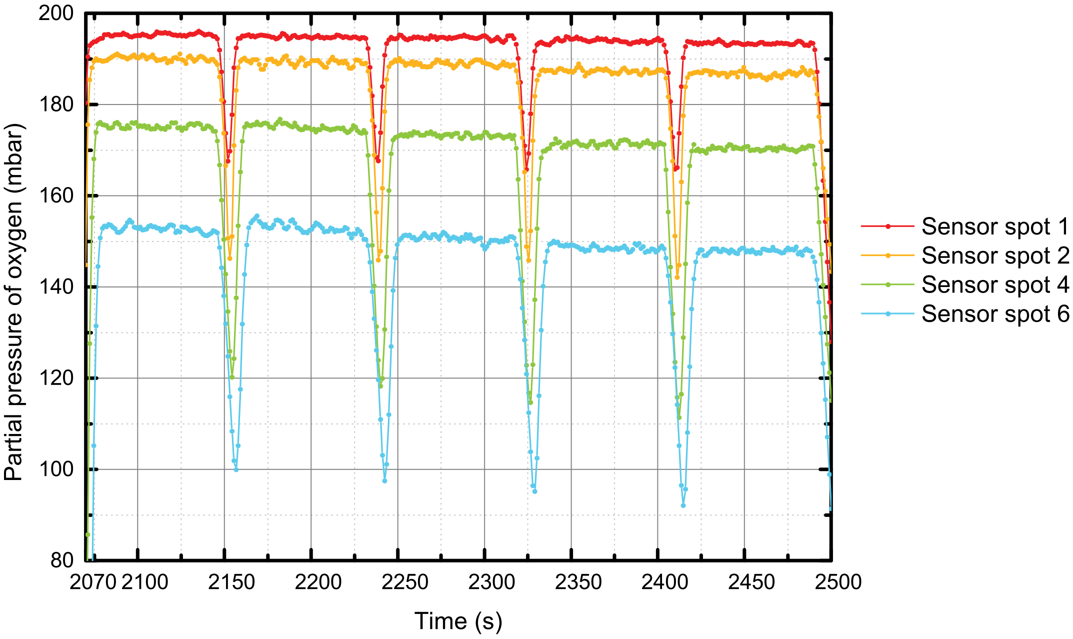

Figure 4.11 *Profiles of oxygen partial pressure over time in the sensor spots 1, 2, 4 and 6 at a total flow rate of 1.25* $\mu l \cdot s^{-1}$ *at a concentration of glucose oxidase solution of 0.2* $g \cdot l^{-1}$.

Glucose oxidase concentration of 0.05 $\mathbf{g \cdot l^{-1}}$ In Figure 4.12 and Figure 4.13 the oxygen profiles relative to the experiment with GOx solution with concentration 0.05 g/l explained in §3.2.3 are shown. Figure 4.12 is relative to a total flow rate of 0.25 μl/s, while Figure 4.13 is referred to a total flow rate of 1.25 μl/s. These two sets of data are taken sequentially, without flushing the reactor in between. The time axis does not start from zero in each graph because all measurements belong to the same data set. The oxygen profiles relative to the entire experiment are shown in § F.1.2 on page 178.

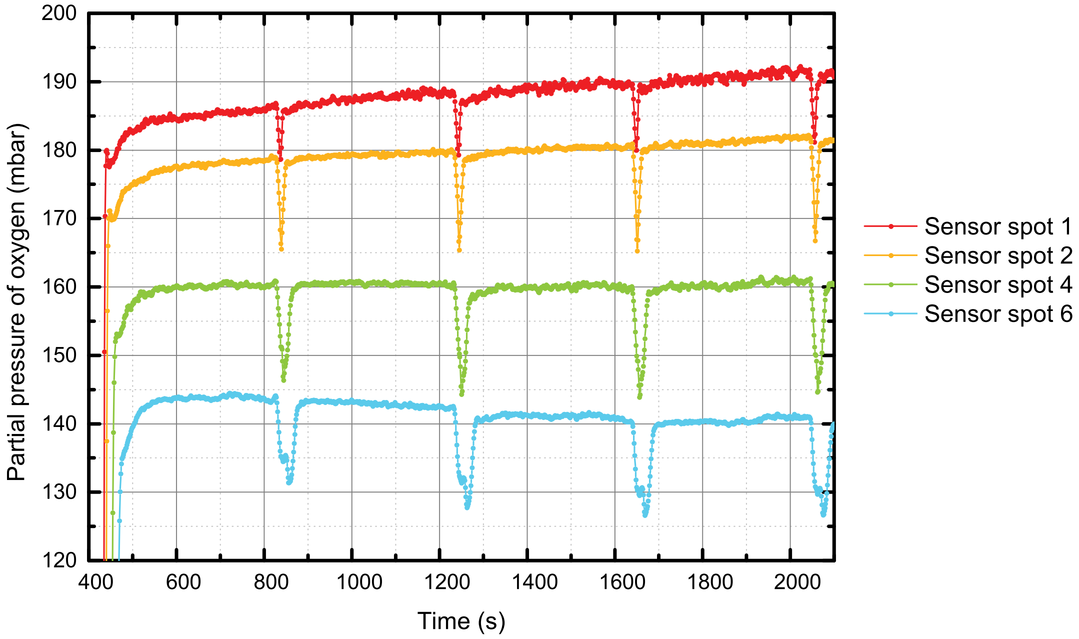

Figure 4.12 *Profiles of oxygen partial pressure over time in the sensor spots 1, 2, 4 and 6 at a total flow rate of 0.25* μ*l*·s^{-1} *at a concentration of glucose oxidase solution of 0.05* g · l^{-1}*.*

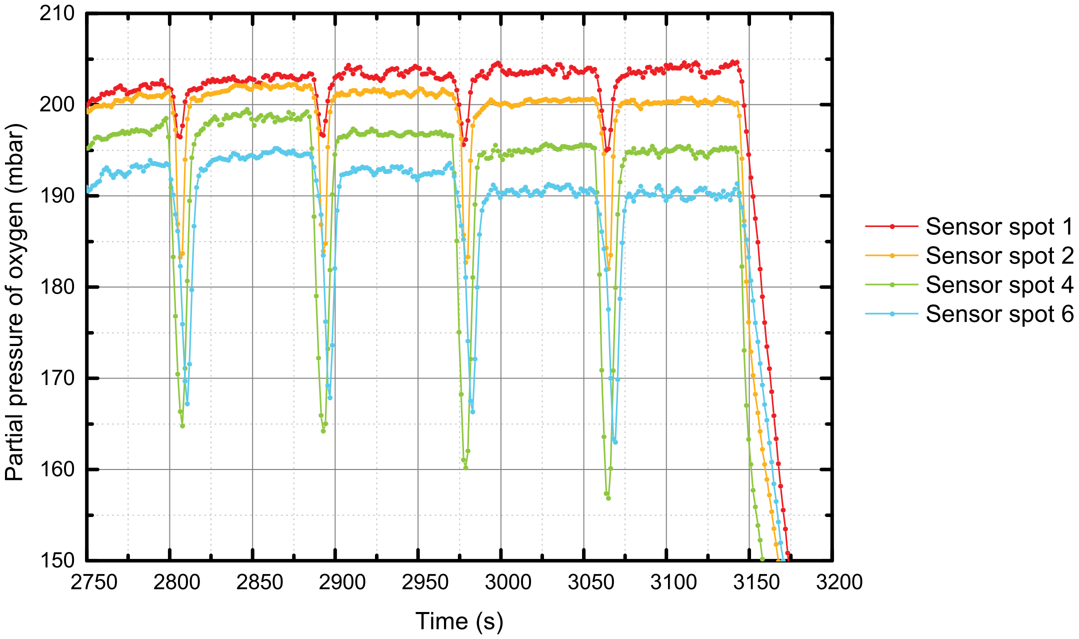

Figure 4.13 *Profiles of oxygen partial pressure over time in the sensor spots 1, 2, 4 and 6 at a total flow rate of 1.25* μ*l*·s^{-1} *at a concentration of glucose oxidase solution of 0.05* g · l^{-1}*.*

In Figure 4.14 the oxygen profiles relative to the experiment with GOx solution with concentration 0.05 g/l at a flow rate of 0.313 μl/s explained in §3.2.3 are shown. In this case the syringes with a stroke volume of 250 μl each were used. The full oxygen profiles are shown in § F.1.2 on page 178.

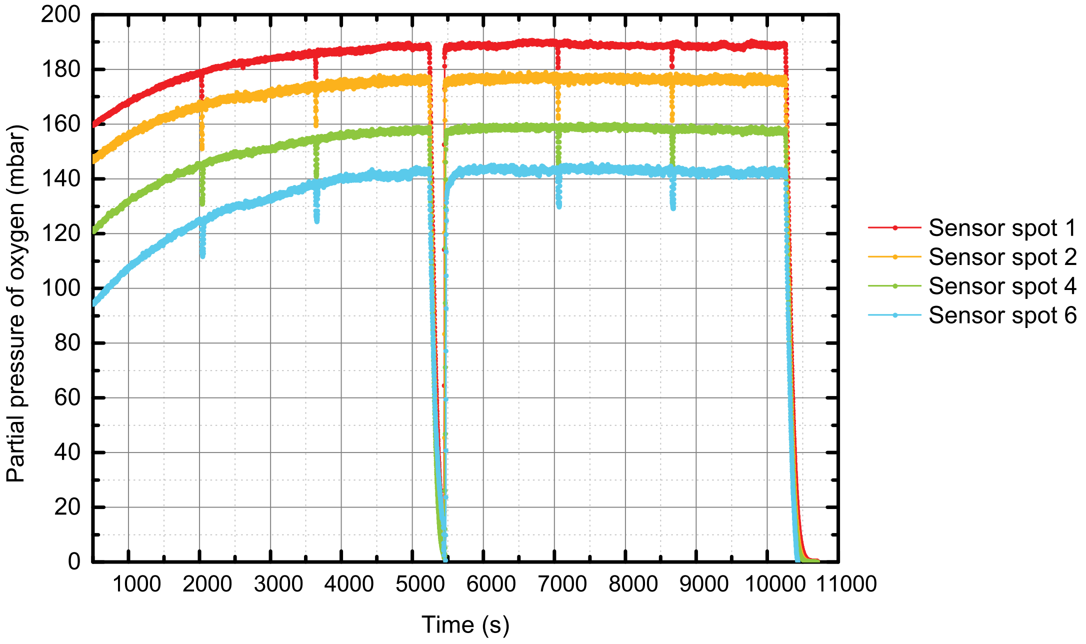

Figure 4.14 *Profiles of oxygen partial pressure over time in the sensor spots 1, 2, 4 and 6 at a total flow rate of 0.313* $\mu l \cdot s^{-1}$ *at a concentration of glucose oxidase solution of 0.05* $g \cdot l^{-1}$.

4.2.1.2 Continuous feed of glucose and glucose oxidase after feeding bovine serum albumin

In this Section the experimental results regarding the experiment with continuous flow of GOx and GLU after the feed of BSA are presented. The Section is divided into two parts: the first part shows the results obtained with GOx solution of concentration of 0.2 $g \cdot l^{-1}$, the second one is about the results with GOx solution of concentration 0.05 $g \cdot l^{-1}$. In each part the results obtained at two different flow rates are presented.

Glucose oxidase concentration of 0.2 $\mathbf{g \cdot l^{-1}}$ In Figure 4.15 and Figure 4.16 the oxygen profiles relative to the experiment with GOx solution with concentration 0.2 g/l explained in §3.2.4 are shown. Figure 4.10 is relative to a total flow rate of 0.25 μl/s, while Figure 4.11 is referred to a total flow rate of 1.25 μl/s. The Figures show only the oxygen profiles at the specified flow rates; the previous part of the experiment, i.e. when BSA was fed to the system, is shown in the graph that represents the measurements for the entire experiment (in § F.2.1 on page 179). The data sets of Figure 4.15 and Figure 4.16 are taken sequentially, without flushing the reactor in between.

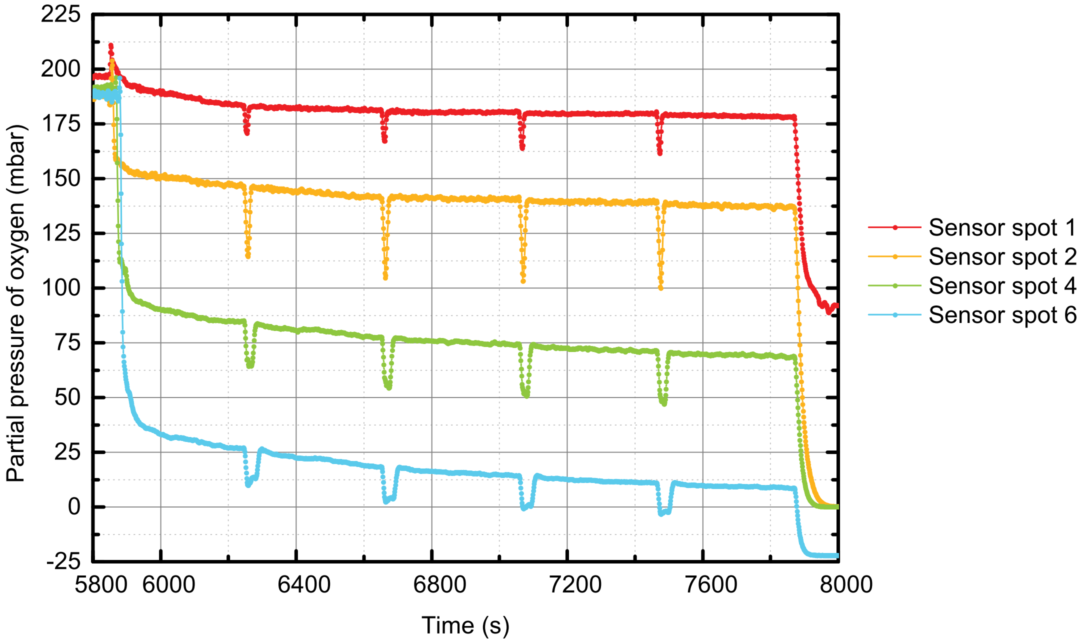

Figure 4.15 *Profiles of oxygen partial pressure over time in the sensor spots 1, 2, 4 and 6 at a total flow rate of 0.25* $\mu l{\cdot}\mathrm{s}^{-1}$ *at a concentration of glucose oxidase solution of 0.2* $\mathrm{g}\cdot\mathrm{l}^{-1}$*, after having fed only bovine serum albumin.*

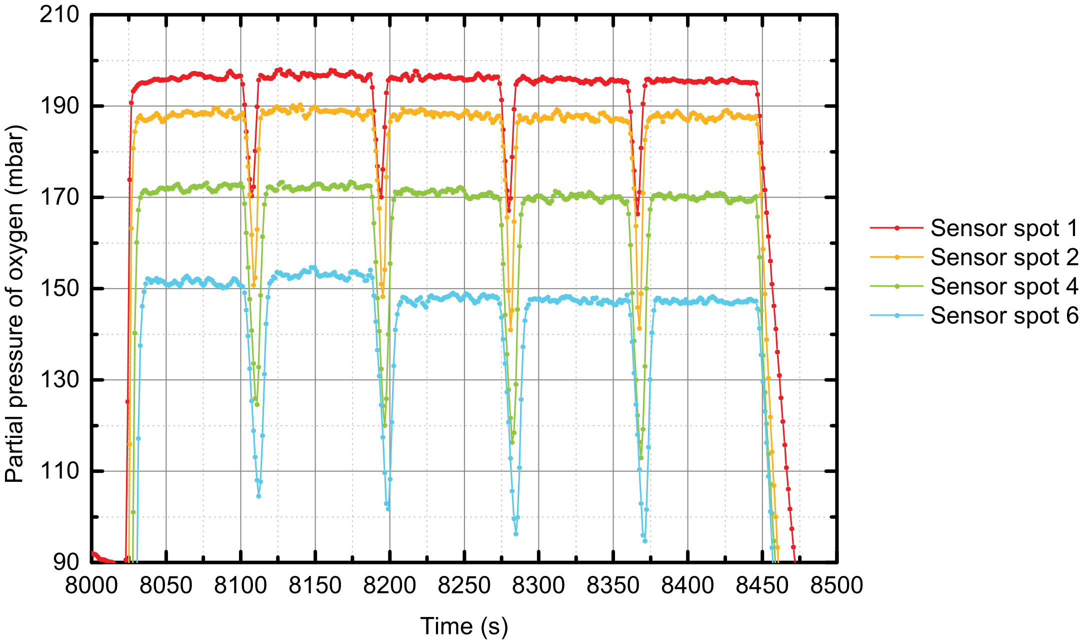

Figure 4.16 *Profiles of oxygen partial pressure over time in the sensor spots 1, 2, 4 and 6 at a total flow rate of 1.25* $\mu l{\cdot}\mathrm{s}^{-1}$ *at a concentration of glucose oxidase solution of 0.2* $\mathrm{g}\cdot\mathrm{l}^{-1}$*, after having fed only bovine serum albumin.*

Glucose oxidase concentration of 0.05 g · l^{-1} In Figure 4.17 and Figure 4.18 the oxygen profiles relative to the experiment with GOx solution with concentration 0.05 g/l explained in §3.2.4 are shown. Figure 4.17 is relative to a total flow rate of 0.25 μl/s, while Figure 4.18 is referred to a total flow rate of 1.25 μl/s. In the graph in § F.2.2 on page 180 the oxygen profiles relative to the entire experiment, including the initial feed of BSA, are shown.

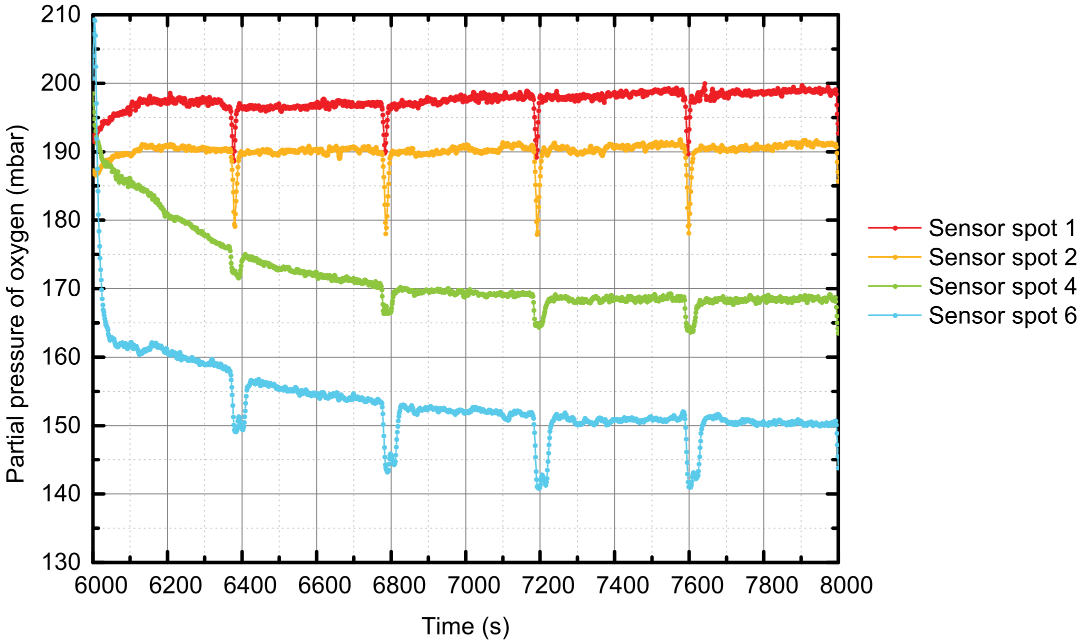

Figure 4.17 Profiles of oxygen partial pressure over time in the sensor spots 1, 2, 4 and 6 at a total flow rate of 0.25 μl·s^{-1} at a concentration of glucose oxidase solution of 0.05 g · l^{-1}, after having fed only bovine serum albumin.

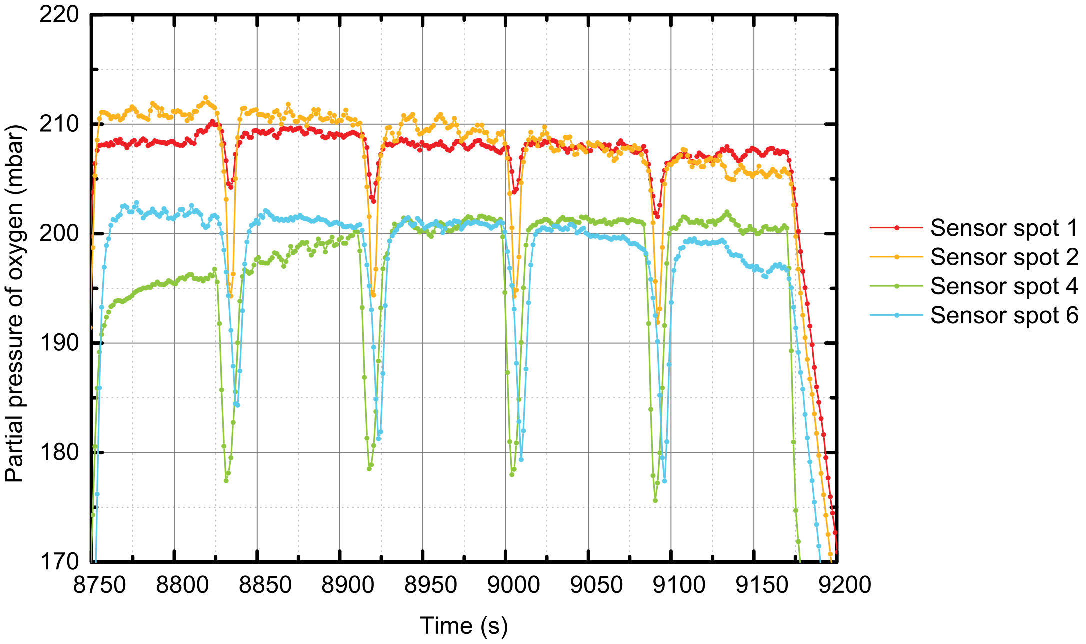

Figure 4.18 *Profiles of oxygen partial pressure over time in the sensor spots 1, 2, 4 and 6 at a total flow rate of 1.25* $\mu l \cdot s^{-1}$ *at a concentration of glucose oxidase solution of 0.05* $g \cdot l^{-1}$*, after having fed only bovine serum albumin.*

4.2.1.3 Continuous feed of glucose and glucose oxidase mixed with bovine serum albumin

In Figure 4.19 and in Figure 4.20 the oxygen profiles relative to the simultaneous feed of GLU and GOx, containing also 0.15 g/l of BSA are shown. Figure 4.19 shows the profiles at a total flow rate of 0.25 μl/s, while Figure 4.20 shows the profiles at a total flow rate of 1.25 μl/s. The profiles relative to the entire experiment, from which these two data set are extracted, are shown in the plot in § F.3 on page 181.

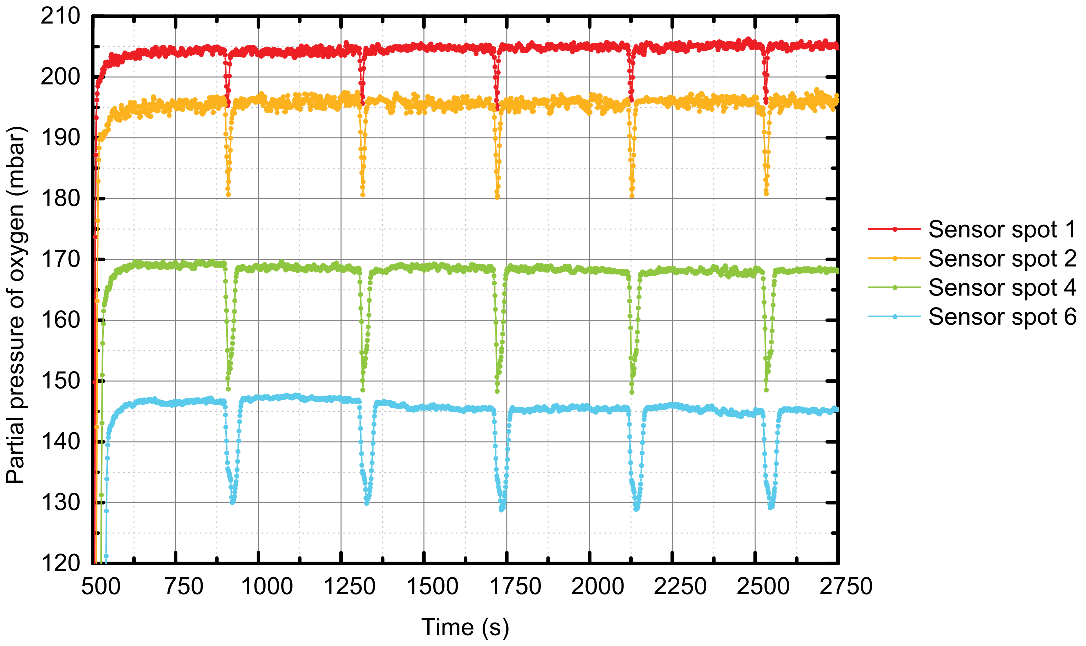

Figure 4.19 *Profiles of oxygen partial pressure over time in the sensor spots 1, 2, 4 and 6 at a total flow rate of 0.25* $\mu l \cdot s^{-1}$ *at a concentration of glucose oxidase solution of 0.05* $g \cdot l^{-1}$. *Glucose oxidase solution contains 0.15* $g \cdot l^{-1}$ *of bovine serum albumin.*

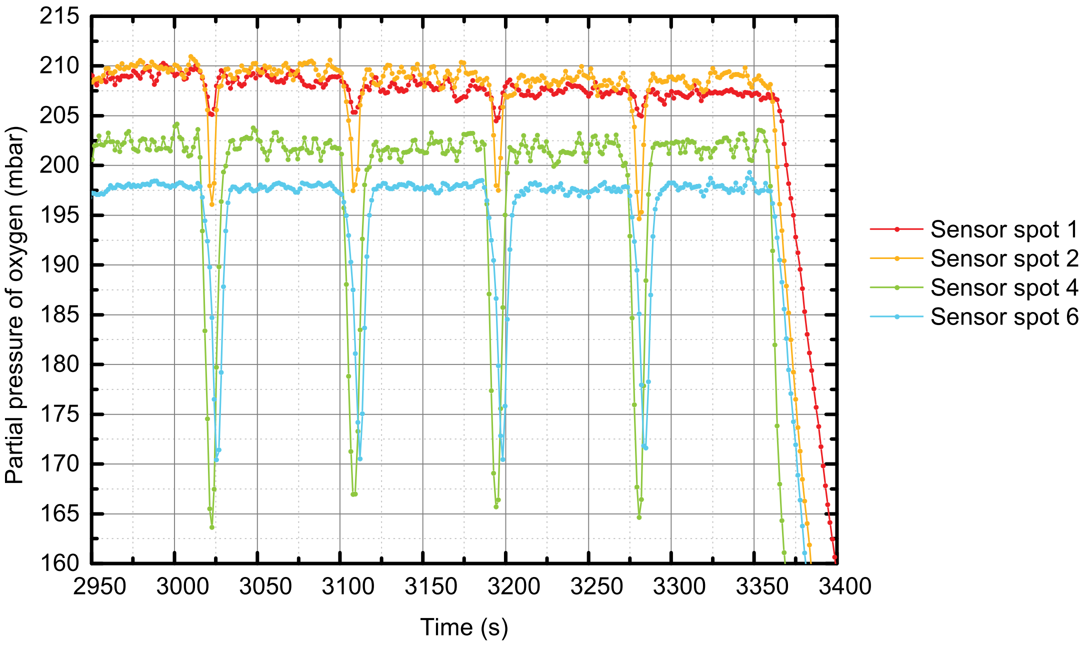

Figure 4.20 *Profiles of oxygen partial pressure over time in the sensor spots 1, 2, 4 and 6 at a total flow rate of 1.25* $\mu l \cdot s^{-1}$ *at a concentration of glucose oxidase solution of 0.05* $g \cdot l^{-1}$. *Glucose oxidase solution contains 0.15* $g \cdot l^{-1}$ *of bovine serum albumin.*

4.2.1.4 Alternate flow of glucose oxidase and glucose

In Figure 4.21 the oxygen profiles relative to the experiment explained in §3.2.6 are shown. The upward part of the profile corresponds to the feed of GOx, while the downward part is relative to the feed of GLU. The alternate flow is done for a total of four times.

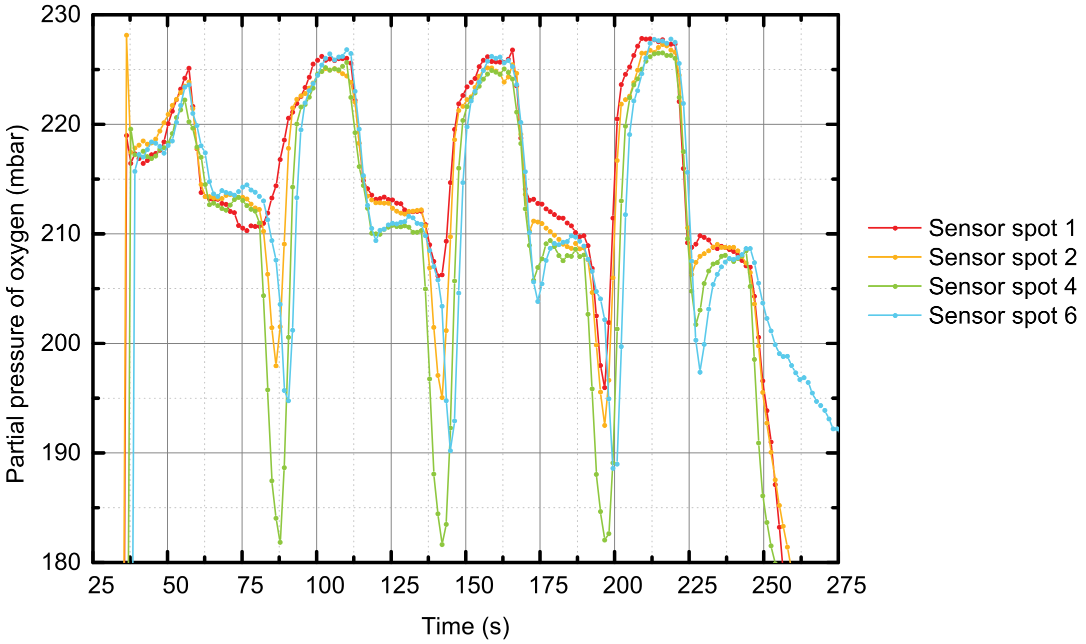

Figure 4.21 *Profiles of oxygen partial pressure over time in the sensor spots 1, 2, 4 and 6 with flow of glucose oxidase followed by flow of glucose. The sequence is repeated four times.*

4.2.1.5 Flow of glucose and stop flow after continuous feed of glucose and glucose oxidase

In this Section the experimental results relative to the experiment presented in §3.2.7 are presented. In Figure 4.22 the oxygen profiles relative to the feed of GLU and the subsequent stop flow condition (repeated two times) are shown. The previous part of the experiment (where GLU and GOx are fed simultaneously) is shown in the plot representing the entire experiment in § F.6 on page 184.

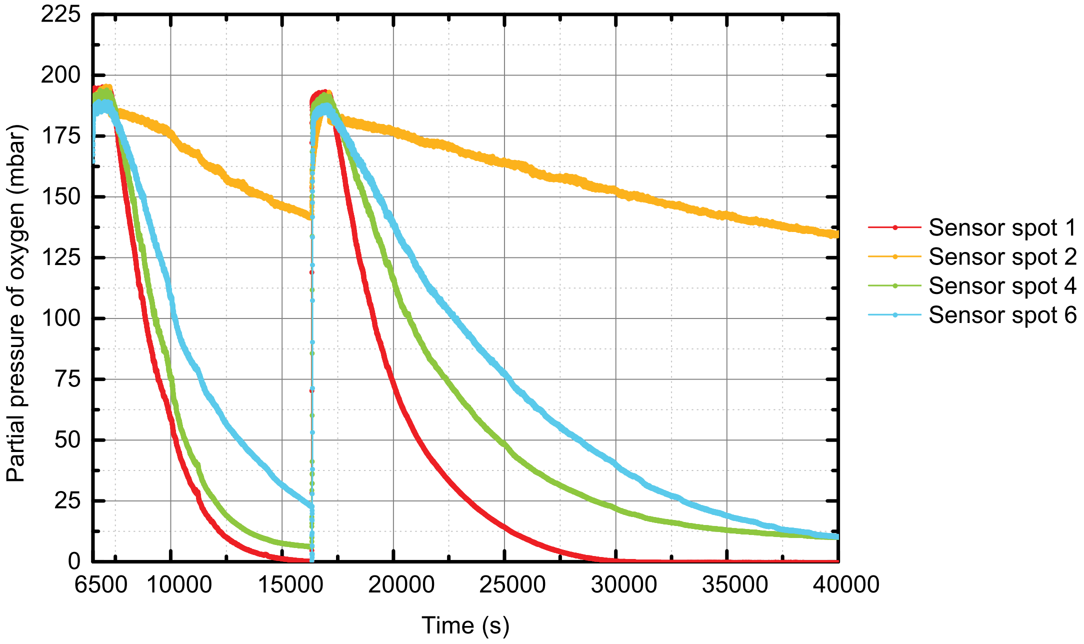

Figure 4.22 *Profiles of oxygen partial pressure over time in the sensor spots 1, 2, 4 and 6 with flow of glucose followed by a stop flow condition. The flow of glucose is repeated two times. Before feeding only glucose, the system is fed with glucose and glucose oxidase.*

4.2.1.6 Flow of glucose and stop flow after continuous feed of glucose, glucose oxidase and bovine serum albumin

In this Section the experimental results relative to the experiment presented in §3.2.8 are presented. In Figure 4.22 the oxygen profiles relative to the feed of GLU and the subsequent stop flow condition (repeated two times) are shown. The previous part of the experiment (where GLU, GOx and BSA are fed simultaneously) is shown in the plot representing the entire experiment in § F.6 on page 184.

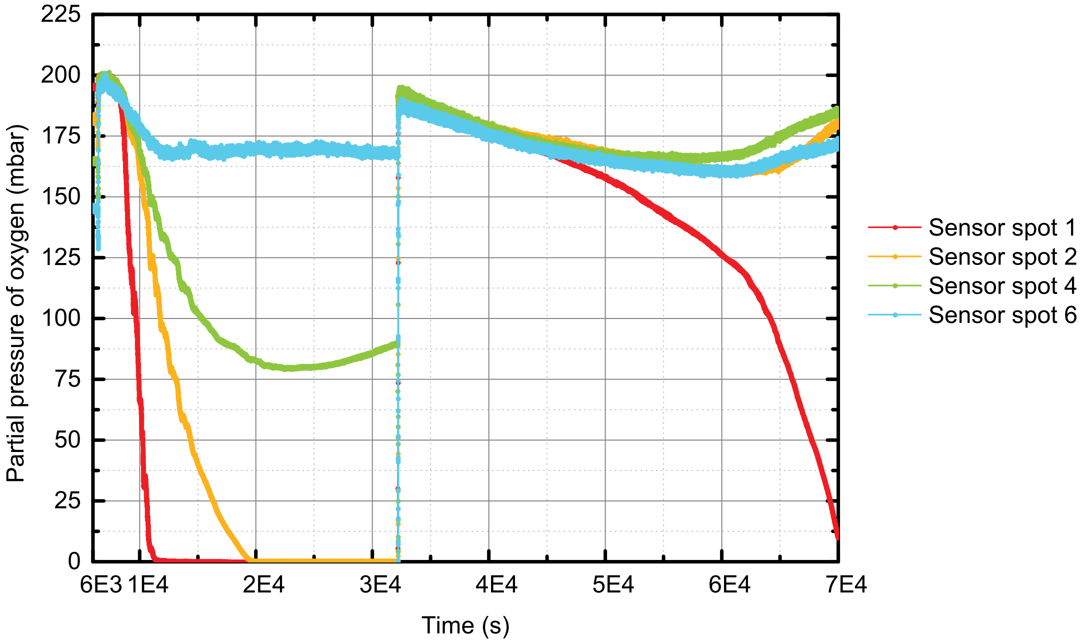

Figure 4.23 *Profiles of oxygen partial pressure over time in the sensor spots 1, 2, 4 and 6 with flow of glucose followed by a stop flow condition. The flow of glucose is repeated two times. Before feeding only glucose, the system is fed with glucose, glucose oxidase and bovine serum albumin.*

4.2.2 CFD simulation results

In this Section the results obtained from CFD simulations are presented.

4.2.2.1 Without adsorption

In Figure 4.24, the profiles of oxygen partial pressure obtained from the CFD simulation without including adsorption are presented. The oxygen partial pressure is calculated from the surface average concentration of oxygen, by calculating the surface average concentration by the Henry´s constant for oxygen in water (769.23 $\mathrm{l \cdot atm \cdot mol^{-1}}$). The results are obtained from a transient simulation, with a total flow rate of 0.25 μl/s.

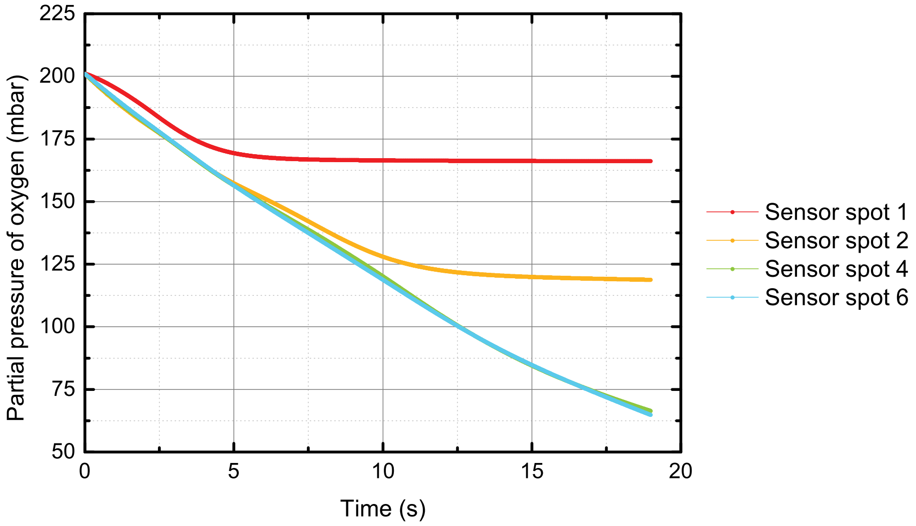

Figure 4.24 *Oxygen partial pressure on sensor spot 1, 2, 4 and 6 for the simulation without adsorption.*

4.2.2.2 With very slow adsorption kinetics

When an adsorption model with a very slow kinetics is added, the profiles of oxygen partial pressure are modified as shown in Figure 4.25. The kinetic constants for this model are $k_{ads} = 10^{-10}\,\mathrm{m}^5 \cdot \mathrm{kg}^{-1} \cdot \mathrm{s}^{-1}$, $k_{des} = 10^{-12}\,\mathrm{kg} \cdot \mathrm{s}^{-1}$ and $c^* = 5 \cdot 10^{-7}\,\mathrm{kg} \cdot \mathrm{m}^{-2}$. The profiles correspond to a total flow rate of 0.25 μl/s.

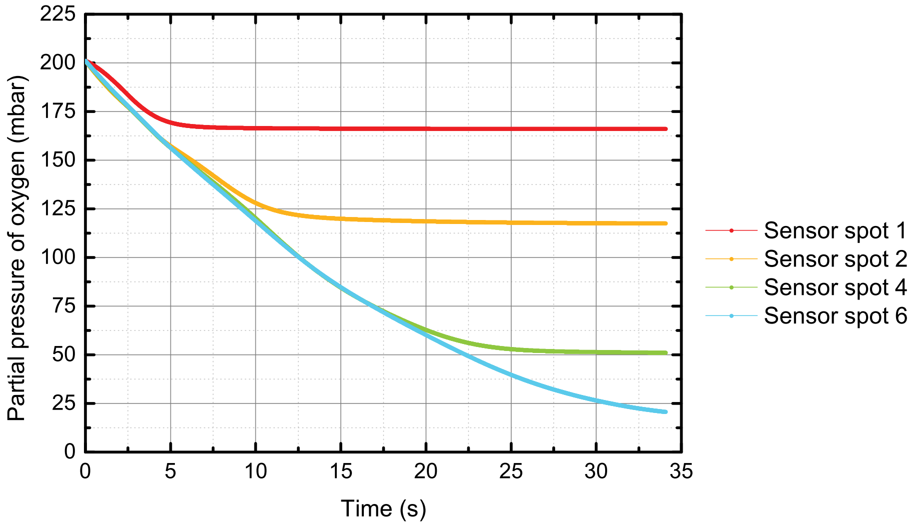

Figure 4.25 *Oxygen partial pressure on sensor spot 1, 2, 4 and 6 for the simulation with very slow adsorption kinetics ($k_{ads} = 10^{-10}\,\mathrm{m}^5 \cdot \mathrm{kg}^{-1} \cdot \mathrm{s}^{-1}$, $k_{des} = 10^{-12}\,\mathrm{kg} \cdot \mathrm{s}^{-1}$ and $c^* = 5 \cdot 10^{-7}\,\mathrm{kg} \cdot \mathrm{m}^{-2}$).*

In Figure 4.26 the profile over time of the concentration of the enzyme adsorbed on the microreactor walls is represented.

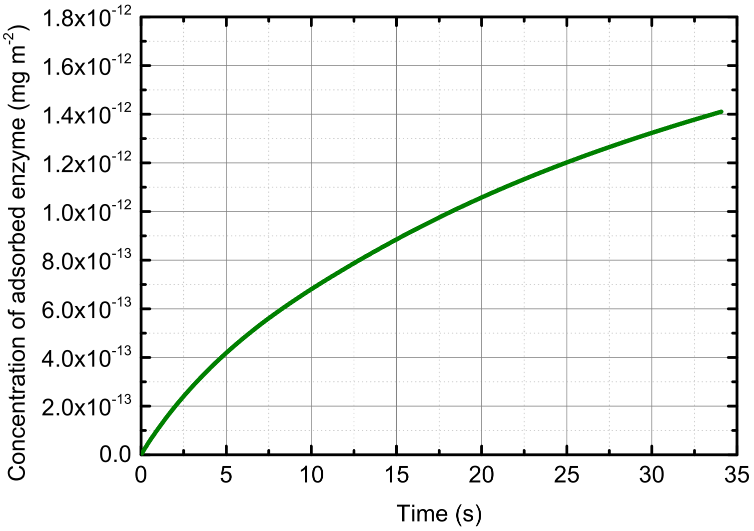

Figure 4.26 *Enzyme concentration on the microreactor walls for the simulation with very slow adsorption kinetics ($k_{ads} = 10^{-10}\,\mathrm{m}^5 \cdot \mathrm{kg}^{-1} \cdot \mathrm{s}^{-1}$, $k_{des} = 10^{-12}\,\mathrm{kg} \cdot \mathrm{s}^{-1}$ and $c^* = 5 \cdot 10^{-7}\,\mathrm{kg} \cdot \mathrm{m}^{-2}$).*

4.2.2.3 With slow adsorption kinetics

When an adsorption model with a slow kinetics is added, the profiles of oxygen partial pressure are modified as shown in Figure 4.27. The kinetic constants for this model are $k_{ads} = 10^{-8}\,\mathrm{m}^5 \cdot \mathrm{kg}^{-1} \cdot \mathrm{s}^{-1}$, $k_{des} = 10^{-12}\,\mathrm{kg} \cdot \mathrm{s}^{-1}$ and $c^* = 5 \cdot 10^{-5}\,\mathrm{kg} \cdot \mathrm{m}^{-2}$. The profiles are obtained with a total flow rate of 0.25 μl/s.

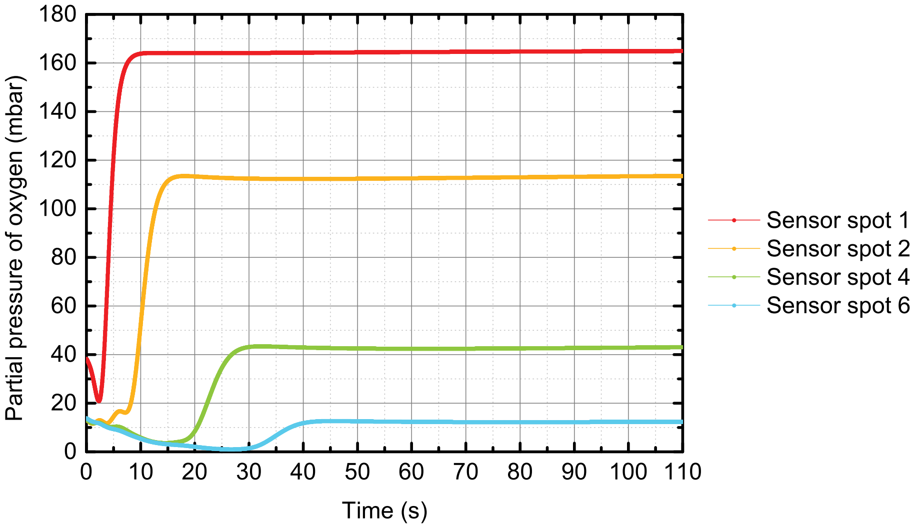

Figure 4.27 *Oxygen partial pressure on sensor spot 1, 2, 4 and 6 for the simulation with slow adsorption kinetics ($k_{ads} = 10^{-8}\,\mathrm{m}^5 \cdot \mathrm{kg}^{-1} \cdot \mathrm{s}^{-1}$, $k_{des} = 10^{-12}\,\mathrm{kg} \cdot \mathrm{s}^{-1}$ and $c^* = 5 \cdot 10^{-5}\,\mathrm{kg} \cdot \mathrm{m}^{-2}$).*

4.2.2.4 With fast adsorption kinetics

The profiles of oxygen partial pressure with fast adsorption kinetics are shown in Figure 4.28. The kinetic constants for this model are $k_{ads} = 10^{-4}\,\mathrm{m}^5 \cdot \mathrm{kg}^{-1} \cdot \mathrm{s}^{-1}$, $k_{des} = 10^{-5}\,\mathrm{kg} \cdot \mathrm{s}^{-1}$ and $c^* = 5 \cdot 10^{-7}\,\mathrm{kg} \cdot \mathrm{m}^{-2}$. The total flow rate is 0.25 μl/s.

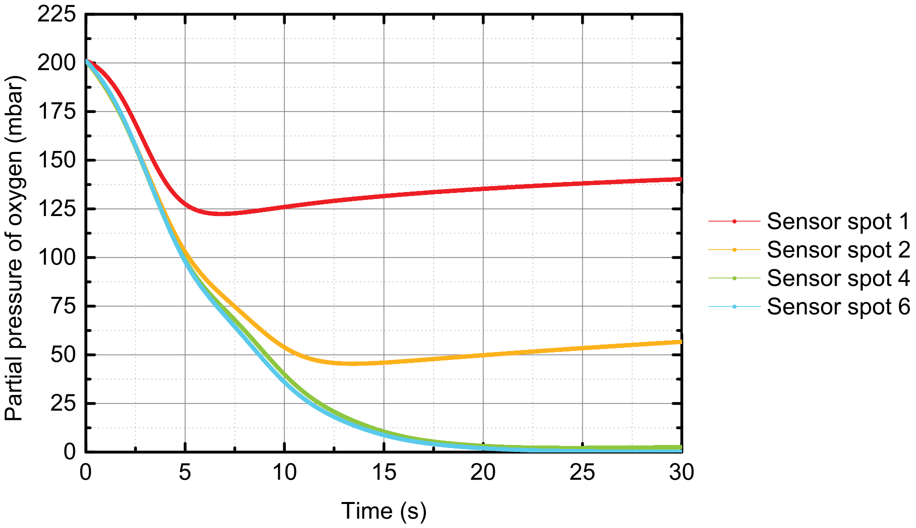

Figure 4.28 *Oxygen partial pressure on sensor spot 1, 2, 4 and 6 for the simulation with fast adsorption kinetics ($k_{ads} = 10^{-4}\,\mathrm{m}^5 \cdot \mathrm{kg}^{-1} \cdot \mathrm{s}^{-1}$, $k_{des} = 10^{-5}\,\mathrm{kg} \cdot \mathrm{s}^{-1}$ and $c^* = 5 \cdot 10^{-7}\,\mathrm{kg} \cdot \mathrm{m}^{-2}$).*

In Figure 4.29 the profile of enzyme concentration on the walls of the microreactor over time is shown.

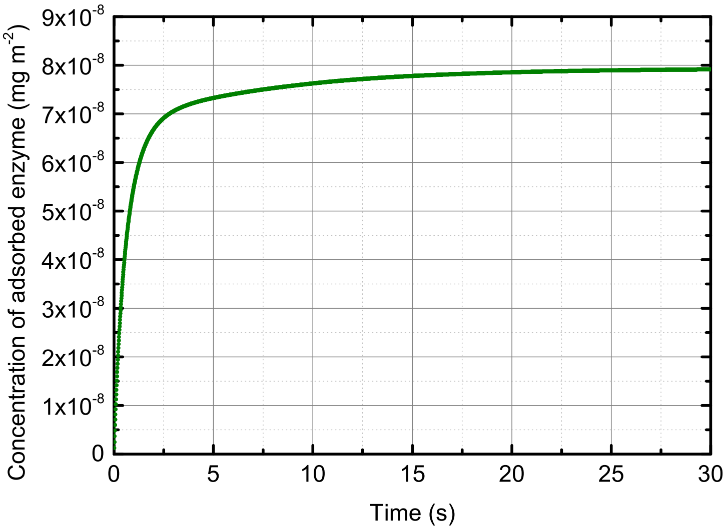

Figure 4.29 *Enzyme concentration on the microreactor walls for the simulation with fast adsorption kinetics ($k_{ads} = 10^{-4}\,\mathrm{m}^5 \cdot \mathrm{kg}^{-1} \cdot \mathrm{s}^{-1}$, $k_{des} = 10^{-5}\,\mathrm{kg} \cdot \mathrm{s}^{-1}$ and $c^* = 5 \cdot 10^{-7}\,\mathrm{kg} \cdot \mathrm{m}^{-2}$).*

In Figure 4.30 the contour plot representing the concentration of the adsorbed enzyme on the walls of the microreactor is shown. The plot is referred to time interval 31 seconds.

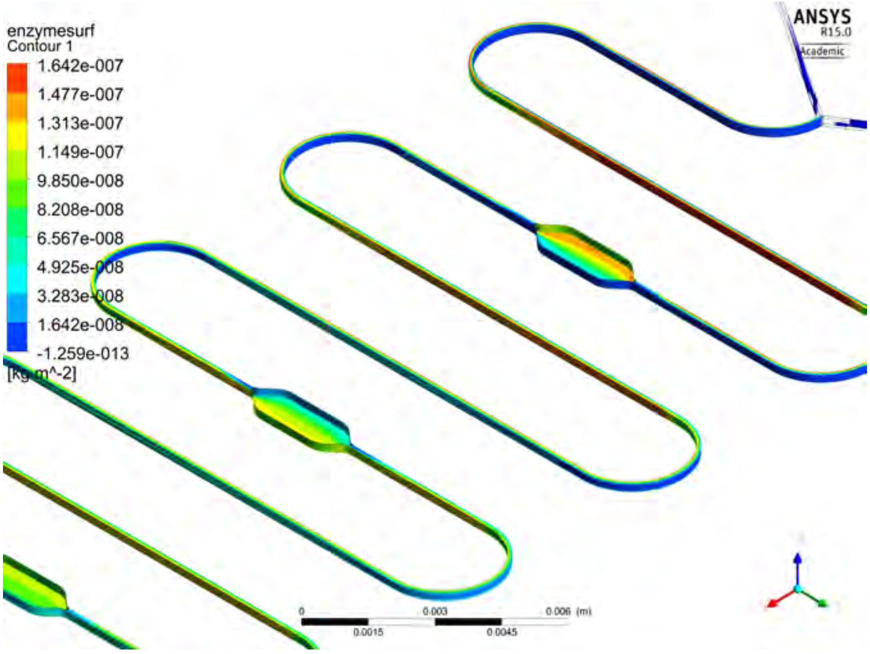

Figure 4.30 *Contour plot representing the concentration of the enzyme adsorbed on the walls of the first part of the microchannel.*

In Figure 4.31b and in Figure 4.31a the contour plots representing the concentration of the adsorbed enzyme on the walls of the first and second sensor spots are shown. The plots are referred to the same time interval (31 seconds).

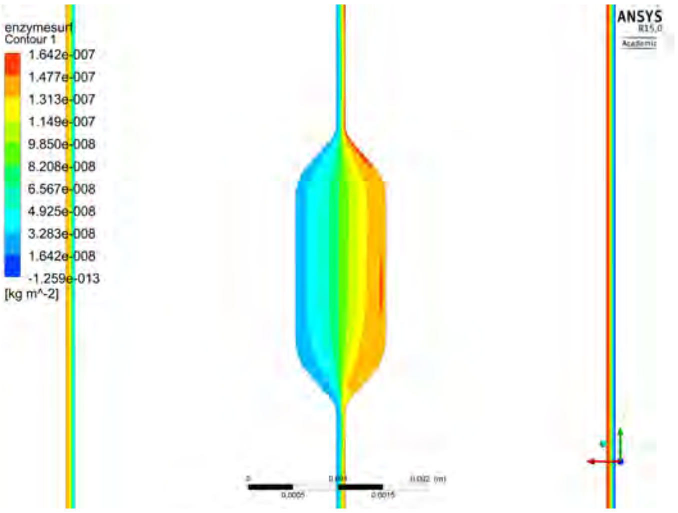

(a) Contour plot representing the concentration of the adsorbed glucose oxidase on the walls of the first sensor spot.

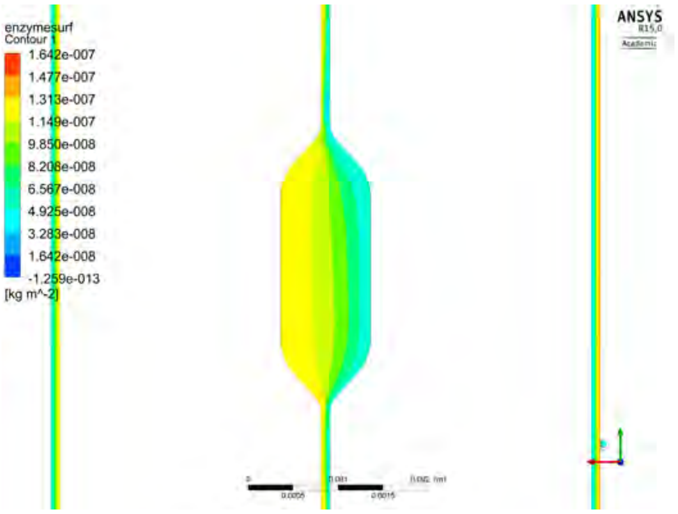

(b) Contour plot representing the concentration of the adsorbed glucose oxidase on the walls of the second sensor spot.

Figure 4.31 *Contour plots of the concentration of the adsorbed glucose oxidase on the walls of the first and second sensor spots at the same time interval (31 seconds).*

Chapter 5

Discussion

This Chapter contains the discussion of the results presented in Chapter 4, it is divided into two parts: transamination (§5.1) and oxidation (§5.2).

5.1 Transamination

This Section contains the discussion of the experimental results obtained for $\omega-$TAm: activity, apparent kinetic parameters and kinetics in shapes with a different SA:V. Before, a brief discussion on the accuracy of the measurements is given.

5.1.1 Accuracy and precision of measurements

First, the very poor quality of the measurements of concentration of $(S)-\alpha-$MBA is caused by the shallow slope of the standard curve (Appendix A on page 129); this is due to low sensitivity of absorbance of $(S)-\alpha-$MBA to concentration differences. Consequently, small errors in the determination of the peak areas corresponds to large errors in the estimation of the concentration of the compound. On the contrary, APH shows a very steep slope of the standard curve, therefore small errors in the determination of the peak areas are not amplified in the conversion from areas to concentration.

Second, measurements of APH concentration have good precision and accuracy; in particular, it is observed a higher quality of the measurements in the batch system than in the microreactor. This is due to the sampling procedure in the microreactor, which should be improved in order to obtain more accurate data. The set-up for samples collection consisted in connecting the outlet of the microreactor to a microtube; the end of the microtube was immersed in the NaOH contained in the HPLC vial. The end of the microtube was left inside NaOH until two strokes of the syringes were completely empty. While the syringes were refilled, the end of the tube was removed from the HPLC vial and placed immediately inside a new vial for collecting the subsequent sample. The inherent inaccuracy of this procedure was due to the surface close to the outlet being “dirty” from the previous sample, meaning that probably not exactly 100 μl were put inside the vial. Thus, the dilution of the sample was not absolutely precise and, consequently, its concentration.

Higher precision would be obtained by other sampling methods. Two examples are: discontinuous sampling and on-line measurement. The former consists in stopping the flow after collecting each sample, in order to give time to the operator to clean the surface of the microtube before placing it in the subsequent vial. This procedure implies that before taking each sample, the microchannel has to be flushed in order to reach steady state in the reactor. The latter would be a great advantage in terms of accuracy and speed.

5.1.2 Activity

Activity was determined in the batch system and in the microreactor exactly at the same conditions of initial substrate concentration, enzyme concentration, temperature and pH. The activity for both systems is also referred approximately to the same time interval from the beginning of the reaction (4 minutes for the reaction in the batch system and 3.632 minutes for the reaction in the microreactor) (§ 3.1.2 on page 48). The constancy of all conditions is essential for the comparison of the activity in the two systems.

The activity and the specific activity in batch system and microreactor are summarized in Table 5.1.

Table 5.1 *$\omega-$Transaminase activity and specific activity in the batch system and in the microreactor.*

	Activity (U)	**Specific activity (U/mg)**
Batch system	120.67	757.24
Microreactor	316.68	60,051.39

The activity in the microsystem is found to be much higher than in the batch system (Table 5.1). Precisely, the activity in the microreactor is 2.62 times the activity in the batch system and even a higher difference is noted for the specific activity, which in the microreactor is 79.3 times the activity of ω−TAm in the batch system.

This result is in agreement with other experimental results presented in the current literature such as in Wang et al. (2013); Yamashita et al. (2009). However, in principle it is expected that reaction rates are faster in a completely stirred reactor than in a system where there is fluid segregation. In fact in a microreactor the flow is laminar and it is expected that the mass transfer could be a limiting factor for a chemical reaction (if the reaction rate is faster than the mass transfer rate). Moreover, in the batch reactor the enzyme ω−TAm is distributed in the whole volume because the content of the vial is completely mixed. Thus, theoretically, all molecules of enzyme have molecules of substrate in the volume of fluid around them. ω−TAm can bind substrate molecules and catalyse the reaction.

Instead, in the microreactor, ω−TAm is introduced in the channel from one inlet and the substrates from the other one. The two streams flow one on the side of the other one for a long path in the meander channel (the length depends on the flow rate) before being mixed because of diffusion and the presence of the turns in the structure of the channel. In fact, the curves in structure of the channel improve the mixing of the inlet streams. Therefore, at least in the first part of the channel, only the molecules of enzyme that are close to the interface of the two streams can catalyse the conversion of substrates into products. Further down in the microchannel, more molecules of enzyme can catalyse the reaction because the substrates have diffused into the enzyme and viceversa. From this analysis it is noted that the reaction does not take place in the entire volume of the microreactor. On the contrary, in the batch reactor the reaction takes place all over the reactor volume (the part filled with fluid).

In conclusion, the experiment shows that the activity of the enzyme is higher in the microsystem than in the batch system. A possible explanation for the observed faster reaction rate in the microreactor than in the batch system is that the enzyme has a different reaction mechanism depending on the shape or on the scale of the reactor. It could also be possible that the enzyme has always the same reaction mechanism, but the parameters in the kinetic model are different because of the different conditions in the different reactor configurations. In this work, it was assumed that the enzyme displays the same kinetic mechanism in both systems since the purpose of this work was not the determination of the kinetic model and no proof for the alteration of the mechanism was found in the literature. Therefore the subsequent step was the determination of the apparent kinetic parameters for both substrates.

5.1.3 Apparent kinetic parameters

It is known that the kinetic mechanism and, consequently, the expression of the reaction rate for $\omega-$TAm are very complex (§ 1.3.2 on page 17). In addition, the determination of all kinetic parameters for the reaction rate in equation (1.3) requires the execution of 52 experiments (Al-Haque et al., 2012). Due to time limitations, it was not possible to perform all these experiments. Therefore, the model was reduced to a simple Michaelis-Menten kinetic model, being aware that Michaelis-Menten kinetic model will be able to predict only some aspects of the very complex behaviour of the enzyme $\omega-$TAm and not, for example, product and substrate inhibition. However, the parameters will give a qualitative estimation of the behaviour of $\omega-$TAm in the batch system and in the microreactor. Moreover, they will allow a comparison of the two systems because the parameters were determined in both under the same hypothesis.

The determination of the apparent kinetic parameters $K_{M,app}^{\text{MBA}}$, $V_{max,app}^{\text{MBA}}$, $K_{M,app}^{\text{PYR}}$ and $V_{max,app}^{\text{PYR}}$ was obtained by the linearization of the Michaelis-Menten equation into the linear form known as Hanes-Woolf relation (equation (4.2)). This linearization form is the best among all linearization forms of Michaelis-Menten (Lineweaver-Burk, Eadie-Hofstee and Hanes-Woolf) because it has smaller and more consistent errors across the plot, i.e. in the entire range of concentration.

In order to achieve a good estimation of the apparent kinetic parameters, the reaction rate should be measured in a wide range of concentration of the substrate. Substrate concentration should vary from values below and above the value of K_M, including substrate saturation concentration. In this way, the complete profile of the variation of the reaction rate vs. substrate concentration can be described. Consequently, the determined parameters are representative of the kinetics of the enzyme in the entire range of substrate concentration, at the constant concentration of the other substrate.

Therefore, the reaction rate is plotted vs. the concentration of the substrate in order to check if these conditions are satisfied. It can be seen from Figure 5.1 that the range of concentration of $(S)-\alpha-$MBA for the batch reactor is wide enough to describe the entire profile of the reaction rate curve, from the very steep increase of the reaction rate at low $(S)-\alpha-$MBA concentration to saturation concentration. It is also observed that the reaction rate decreases at high $(S)-\alpha-$MBA concentration, indicating that high $(S)-\alpha-$MBA concentration may have an inhibitory effect on $\omega-$TAm because it reduces the reaction rate.

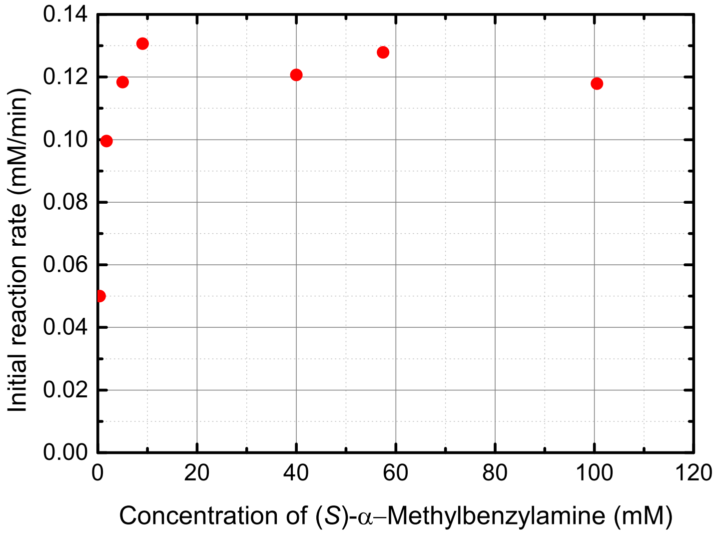

Figure 5.1 *Initial reaction rate vs. concentration of* $(S)-\alpha-$*Methylbenzylamine at constant pyruvic acid concentration in the batch system.*

On the contrary, the same range of concentration of $(S)-\alpha-$MBA is not wide enough for the determination of the complete profile of the reaction rate in the microsystem (Figure 5.2). From this Figure conclusion can be taken: either the enzyme in the microsystem reaches saturation concentrations at very high substrate concentration, without suffering from inhibitory effects from $(S)-\alpha-$MBA, or the kinetic model is completely different from Michaelis-Menten kinetics (whereas, from Figure 5.1 it seems that Michaelis-Menten could fit quite well the data of the batch system). In order to determine which one of these two hypotheses is correct more experiments are required: it would be necessary to determine the reaction rate at concentration of $(S)-\alpha-$MBA higher than 100 mM. In this project it is considered that $\omega-$TAm follows a Michaelis-Menten kinetic model and that the profile shown in Figure 5.1 corresponds to the part of the profile before reaching the saturation.

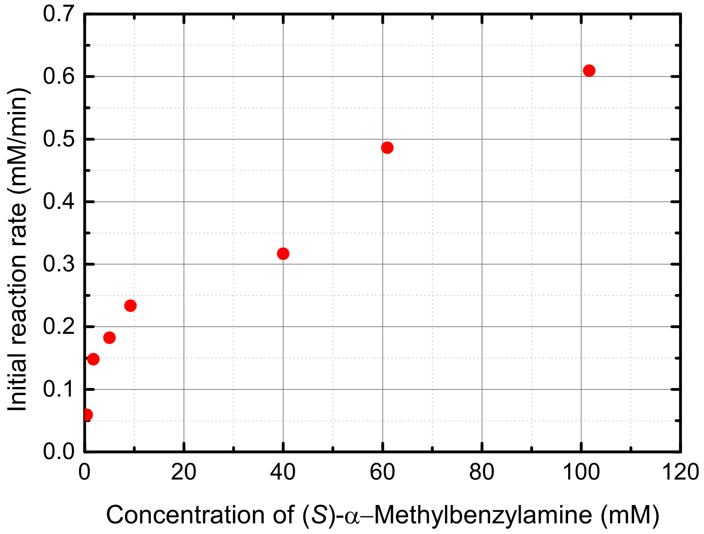

Figure 5.2 *Initial reaction rate vs. concentration of $(S)-\alpha-$Methylbenzylamine at constant pyruvic acid concentration in the microreactor.*

Very similar considerations can be done for the variation of the reaction rate vs. PYR concentration at constant $(S)-\alpha-$MBA concentration. In Figure 5.3 it is observed that in the batch system the reaction rate has a steep increase at low PYR concentration, and it reaches an almost constant reaction rate at high PYR concentration. However, more measurements would be necessary to determine precisely the maximum reaction rate in these conditions and the saturation concentration of PYR.

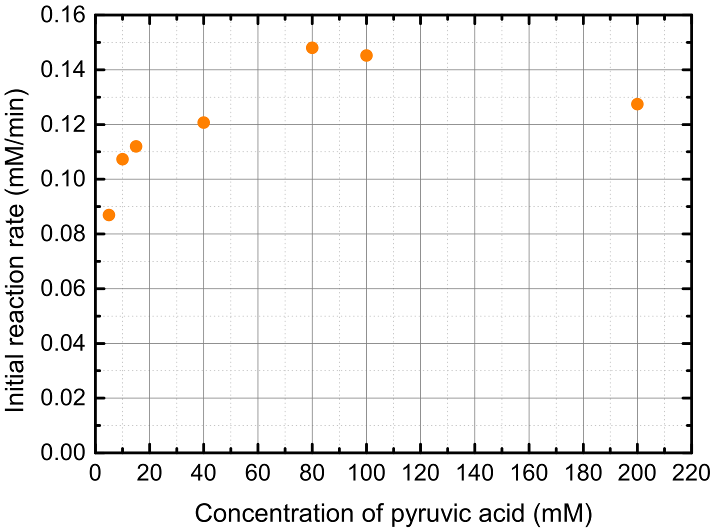

Figure 5.3 *Initial reaction rate vs. concentration of pyruvic acid at constant* (S) $-$ $\alpha-$*Methylbenzylamine concentration in the batch system.*

On the other hand, for the microreactor, a clear trend of the data point cannot be easily determined from Figure 5.4, due to the poor consistency of the measurements. If the data at 15 mM and 100 mM of PYR concentration are discarded, it seems that the reaction rate keeps increasing as long as PYR concentration increases, reaching maybe a maximum for PYR concentrations above 200 mM.

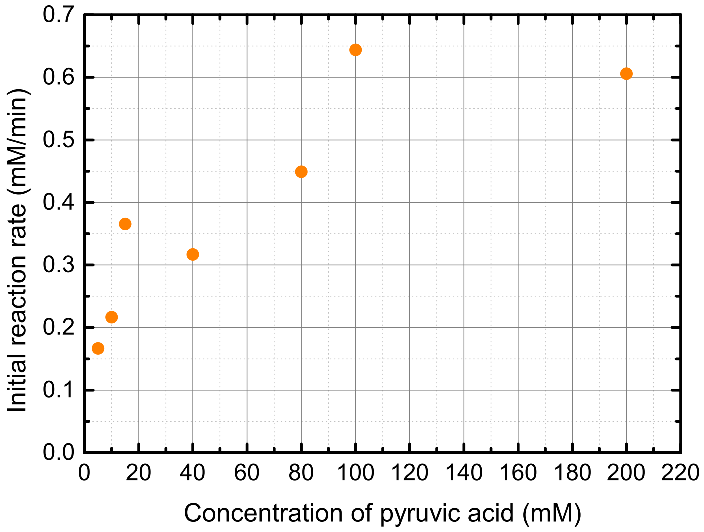

Figure 5.4 *Initial reaction rate vs. concentration of pyruvic acid at constant* (S) $-$ $\alpha-$*Methylbenzylamine concentration in the microreactor.*

From the analysis of the plots in Figure 5.1, Figure 5.2, Figure 5.3 and Figure 5.4 it is possible to conclude that the kinetic parameter determination will be more accurate for the batch system than for the microreactor. It is also observed and confirmed what was already known from the experiment of activity determination: the kinetics of $\omega-$TAm in the microsystem differs from the kinetics in the batch system. It is not possible to establish from the performed experiments if the enzyme has a different mechanism or if the mechanism is the same but the parameters are different. In this project it is assumed that the mechanism is the same, yet the expression of the reaction rate is the same, and the parameters are fit to each system.

In Table 4.10 and in Table 4.13 all the determined apparent kinetic parameters are summarized.

It is observed that for both $(S)-\alpha-\mathrm{MBA}$ and PYR, K_M values are lower in the batch reactor than in the microreactor. A low K_M value indicates easiness of binding of the enzyme to the substrate, thus it seems that the formation of the Michaelis-Menten complex is more favoured in the batch reactor than in the microreactor. This is maybe due to the fact that the batch reactor is a completely stirred system, thus it may be easier for $\omega-$TAm to bind to substrate molecules. It is also noticed that in the batch system $K_{M,app}^{\mathrm{MBA}}$ is higher than $K_{M,app}^{\mathrm{PYR}}$; this experimental result is as expected because it is known that the enzyme has more affinity with PYR than with $(S)-\alpha-\mathrm{MBA}$.

However, for the microreactor the relation is exactly the opposite. This is may be due to the not so high accuracy of the data of the reaction rate in the microsystem, which may give an error in the parameter estimation. It could also be due to the fact that the reaction rate in the microsystem was not measured in a sufficiently wide range of substrate concentration. Therefore, the determined K_M values are not the same that would be found if the set of data point would have included measurements of reaction rate at substrate saturation conditions.

The higher value of K_M in the microreactor than in the batch system is not in agreement with the experimental data obtained by Wang et al. (2013) and Yamashita et al. (2009). They state that K_M in the microreactor is smaller than in the microsystem, meaning that the formation of Michaelis-Menten complex is more favourable in the microsystem.

Regarding V_{max}, it is observed that it is always higher in the microreactor than in the batch system (Table 4.10 and in Table 4.13). More specifically, both $V_{max,app}^{\mathrm{MBA}}$ and $V_{max,app}^{\mathrm{PYR}}$

are five times higher in the microsystem than in the batch reactor. This confirms the fact that the reaction rate in microreactors is faster than in batch systems, if operational conditions allow to run the reaction at a rate close to V_{max}. The values of $V_{max,app}^{\mathrm{MBA}}$ and $V_{max,app}^{\mathrm{PYR}}$ for both systems are very similar. Wang et al. (2013) and Yamashita et al. (2009) also state that k_{cat} (which is related to V_{max} by the relation $V_{max} = k_{cat} \cdot c_{\mathrm{E0}}$) is higher in the microsystem. The measured reaction rates do not seem to stabilize at a maximum value at high substrate concentration in the microsystem (Figure 5.2 and 5.4); thus, it may be that the real value of V_{max} is even higher than the determined one, unless $\omega-$TAm will display inhibition at higher substrate concentrations.

The efficiency of $\omega-$TAm is a more global indicator for the action of the enzyme than K_M and V_{max} individually. This is due to the fact that η includes both affinity (K_M) and catalytic ability (V_{max} or k_{cat}), thus it is useful for comparing different enzymes against each other, or the same enzyme with different substrates. It indicates how good an enzyme is at catalysing a reaction at low substrate concentration. For $\omega-$TAm, it is noted in Table 4.10 and in Table 4.13 that the enzyme is more efficient at low PYR concentration than at low $(S)-\alpha-$MBA concentration in the batch system, while it is the opposite for $\omega-$TAm in the microreactor. It is observed that the efficiency with respect to $(S)-\alpha-$MBA is higher in the microsystem than in the batch reactor, meaning that more molecules of product are produced per unit of time per molecule of enzyme. The efficiency with respect to PYR has similar values in both systems, and it is a bit higher in the batch than in the microsystem.

The saturation curves showing the dependence of the reaction rate on $(S)-\alpha-$MBA concentration and PYR concentration are shown respectively in Figure 5.5 and in Figure 5.6.

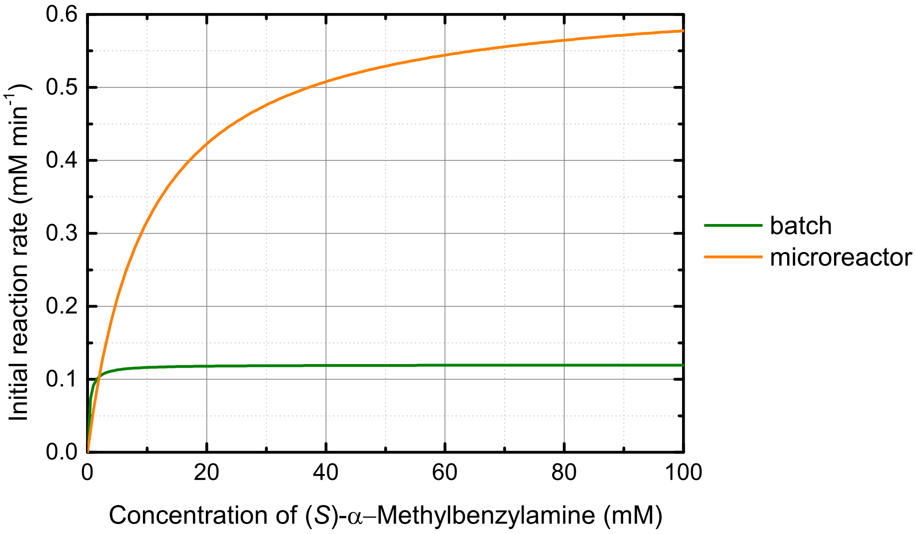

Figure 5.5 *Saturation curve for $\omega-$Transaminase at constant pyruvic acid concentration, showing the dependence of the reaction rate on $(S)-\alpha-$Methylbenzylamine concentration.*

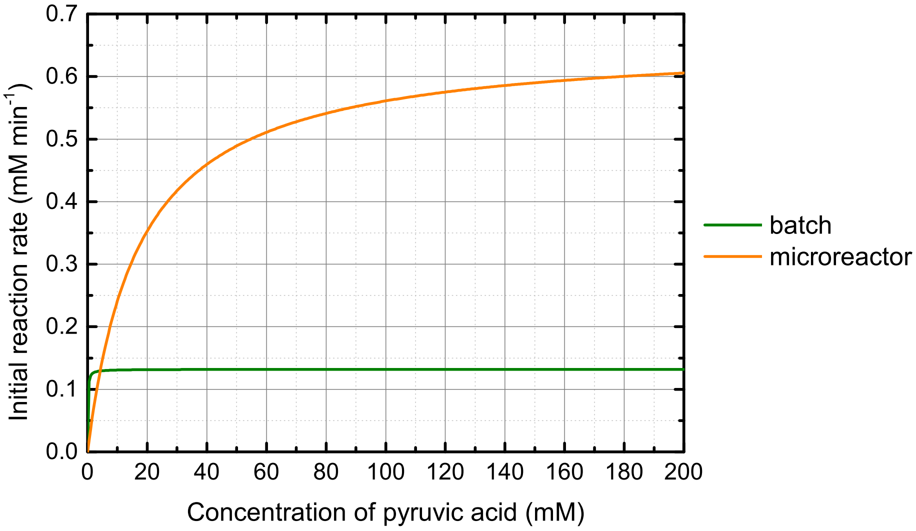

Figure 5.6 *Saturation curve for $\omega-$Transaminase at constant $(S)-\alpha-$Methylbenzylamine concentration, showing the dependence of the reaction rate on pyruvic acid concentration.*

The curves are obtained by inserting in Michaelis-Menten kinetic equation (equation (1.7)) the parameters in Table 4.10 and in Table 4.13; a saturation curve is drawn for the batch system and another curve is drawn for the microreactor. From Figure 5.5 and Figure 5.6 it is observed that the reaction rate in the microreactor is faster than the reaction rate in the batch system at substrate concentration above the concentration corresponding to the intersection of the two curves. This concentration is below 5 mM for $(S)-\alpha-$MBA (Figure 5.5) at PYR concentration of 40 mM and around 5 mM for PYR (Figure 5.6) at $(S)-\alpha-$MBA concentration of 40 mM. Note that the determined kinetic parameters are apparent, which means that they are determined at constant concentration of one of the substrate. Thus, the parameters are valid at this fixed concentration of the substrate (which is PYR when $(S)-\alpha-$MBA concentration is varying and $(S)-\alpha-$MBA when PYR concentration is changing).

It can be concluded that the reaction rate in the microreactor is higher than in the batch system in the operational range of concentration of the substrates. This is justified by the fact that enzymatic reaction are always performed at a substrate concentration that allows to run the reaction at a reaction rate close to V_{max} since it is intended to perform the reaction at the fastest reaction rate. Secondly, it is avoided to run the reaction in proximity of the very steep profile of the reaction rate at low substrate concentration, in order to avoid the drop in the reaction rate as long as the substrate is depleted.

In conclusion, from the determination of the kinetic parameters, it is confirmed that the reaction rate in the microreactor is faster than in the batch reactor in a broad range of substrate concentration. No conclusions can be taken regarding the kinetic mechanism of the enzyme in the two systems. However, it can be concluded that, if the same simple model is used, i.e. Michaelis-Menten, the parameters that describe the reaction are not the same. Therefore, it might be expected that the catalytic action of an enzyme depends on the scale of the reactor, or on the fluid conditions inside the reactor.

5.1.4 Effect of SA:V

The experimental results from the previous experiment confirmed the hypothesis that the enzyme has at least different kinetic parameters in a batch system than in a microreactor, if not a different kinetic model. However, this does not seem to be the only aspect that marks the difference between enzymatic reactions in microreactors and in batch systems. In fact another aspect is observed from the experimental data by looking at the trend displayed by the replicates. As an example, data from the third measurement set in the microreactor for activity determination (Table 4.6 on page 68) are used, but the same trend between replicates is observed in all measurement sets. The trend can be observed in all Tables presented in § D.1.2 on page 148 and in § D.2.2 on page 161, by noting the increase in the concentration of APH with the replicate number at the same flow rate. In Figure 5.7, the concentration of APH at different residence times in all five replicates of the measurement set is shown. The straight lines obtained by linear regression of the points belonging to the same replicate are also shown.

As explained in § 3.1.2.2 on page 49, the way of collecting the replicates was as follows: microtubings, syringes and microreactor were flushed 7 times with ω−TAm and the substrate solution and, after, all samples corresponding to the same flow rate were collected one after the other one. Then, the system was flushed other 7 times and all samples corresponding to another flow rate were collected one after the other one, and so on. Then, the activity was evaluated for the set of first samples collected at each flow rate (replicate 1), and for the set of second samples collected at each flow rate (replicate 2), and so on. From Figure 5.7, it is observed that the slope of the straight line calculated for the first replicate is the smallest one, and, in more general terms, the slope increases from the first replicate to the fifth replicate. Thus, it seems that the reaction rate depends on the number of times that the enzyme and the substrate mixture had flowed in the microreactor.

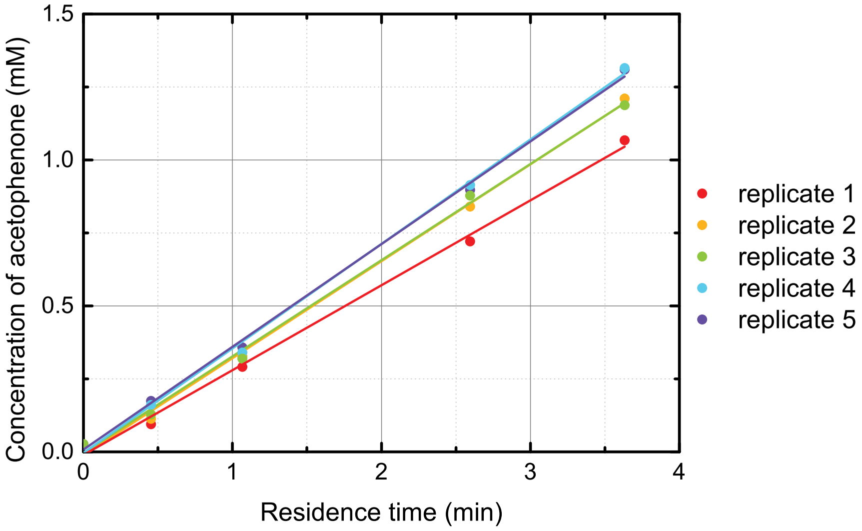

Figure 5.7 *Concentration of acetophenone at the outlet of the microreactor at activity conditions at different residence times for the 5 replicates belonging to the third measurement set of activity determination. In the graph each line represents the straight line obtained by linear regression of the 5 points belonging to the same replicate.*

The trend displayed by the replicates is also shown in Figure 5.8, where the concentration of APH is plotted vs. the replicate number.

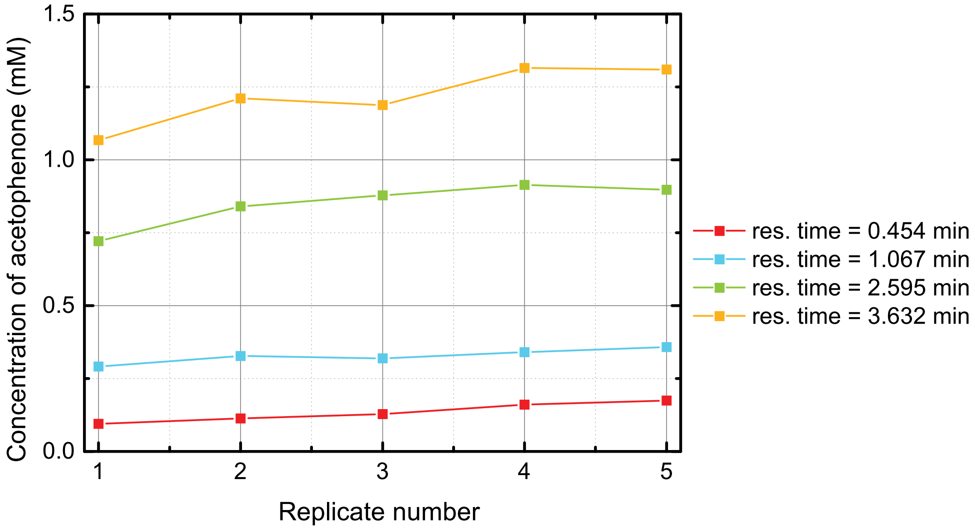

Figure 5.8 *Concentration of acetophenone vs. replicate number at different residence times (res. time) in the microreactor, for the 5 replicates belonging to the third measurement set of activity determination.*

It can be seen that the concentration increases with the replicate number at the same residence time. The increase in the concentration is higher at high residence time (low flow rate) than at low residence time (high flow rate). Since the operating conditions are the same for all replicates, if more APH is produced it should be related to the presence of more enzyme, which catalyses the conversion of more substrate into product. Higher product concentration is obtained after that the substrate mixture and the enzyme solution have flowed more times in the reactor; thus, there is the possibility that the enzyme accumulates inside the microreactor.

This accumulation may be due to hydrodynamic retention of the enzyme inside the microreactor or adsorption of the enzyme on the walls of the channel.

Hydrodynamic retention is related to the fact that the flow inside the microchannel is laminar and that velocity distribution inside the channel has a parabolic profile. The velocity of the fluid that is in contact with the walls is zero, thus it might be that molecules of enzyme are retained inside the channel because of their proximity to the walls.

It might also be that $\omega-$TAm molecules are adsorbed to the walls of the microchannel determining an increase of the reaction rate until all available sites on the surface are covered (assuming that a monolayer adsorption is taking place).

Both hydrodynamic retention and adsorption depend on the SA:V of the microreactor.

Therefore, in order to test if the SA:V plays a role on the reaction, the outlet concentration at the same residence time in the series of microreactors with different SA:V was compared.

In Figure 5.9 the concentration of APH and the SA:V are both represented as a function of the height of the microreactor.

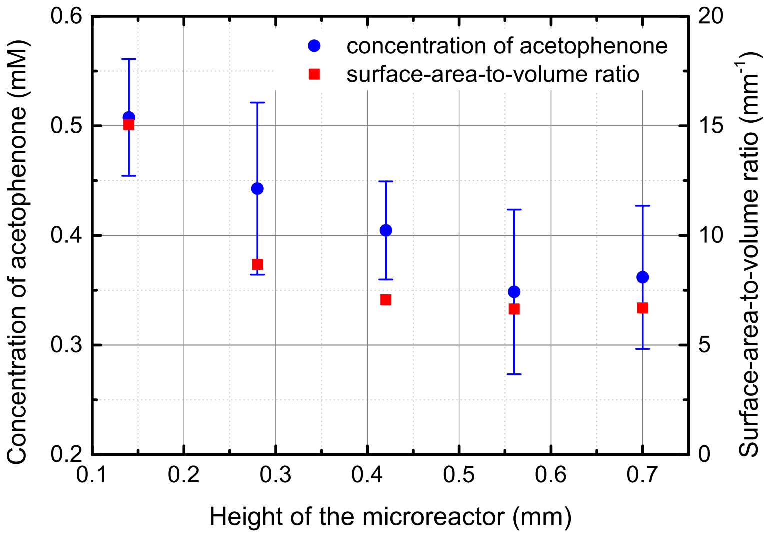

Figure 5.9 *Variation of the outlet concentration of acetophenone and surface-area-to-volume ratio with the height of the microreactor.*

It can be seen that the concentration of APH has the same trend as the SA:V. This means that an enzymatic reaction in microsystems performs differently depending on the SA:V of the reactor. In particular, the concentration of the product is found to be higher in a reactor with a large SA:V. This may be explained by the large surface available where the enzyme can adsorb or be retained.

In conclusion, it seems that in a microreactor the fact that the kinetic model or its parameters are different from a batch reactor is not the only phenomena taking place. The other one may be adsorption of the enzyme on the walls or hydrodynamic retention of the enzyme inside the channel. One of these phenomena could be the explanation for the fact that the reaction rate is faster at a high SA:V of the microreactor since both adsorption and hydrodynamic retention depend on SA:V.

This investigation is continued with GOx, since oxygen concentration can be measured continuously in several points in the microreactor. In this way a more complete understanding of the phenomena taking place can be achieved than only from a comparison of the outlet from the reactor.

5.2 Oxidation

In this Section, the experimental results obtained from the experiment with GOx and the CFD simulation results of the same system are discussed.

5.2.1 Feed of glucose and glucose oxidase

In this Section the results of the experiments done only with GOx and GLU are discussed.

5.2.1.1 Dynamic behaviour of the system

In all experiments, the profiles of oxygen partial pressure present downward peaks; the peaks correspond to the time when the syringes are refilled, determining a temporary condition of stop flow in the microreactor. The stop flow increases the residence time of the fluid in the channel, thus the reaction proceeds at a faster rate because no oxygen is supplied and it is only consumed. The profiles of oxygen partial pressure at the first stop flow at GOx concentration of 0.2 g/l at a flow rate of 1.25 μl/s are shown in Figure 5.10.

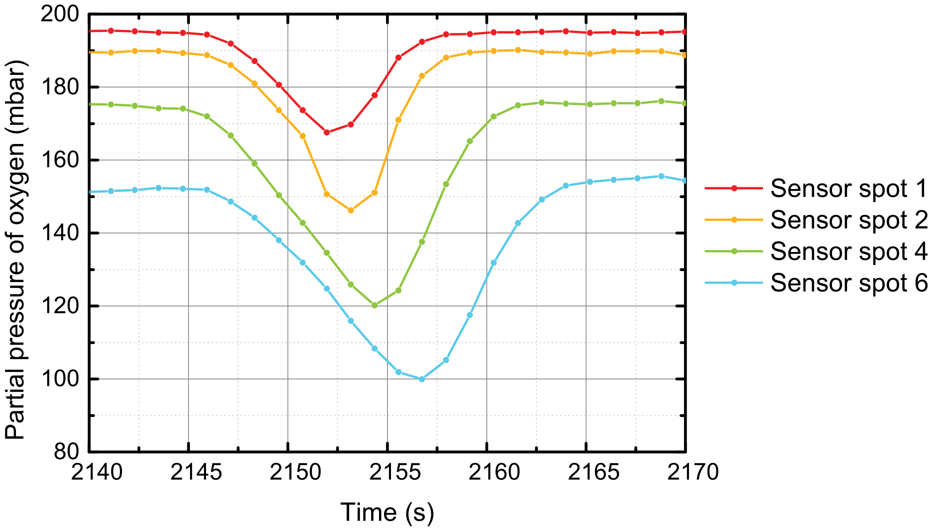

Figure 5.10 *Oxygen profiles at the first stop flow at glucose oxidase concentration of 0.2 g/l and at a flow rate of 1.25 μl/s.*

It is observed that the minimum of the peak of the profile of the first sensor happens earlier in time than for the last sensor. This is due to the fact that, when dissolved oxygen is pumped again in the system, the profiles start to increase again, but the flow reaches sequentially the sensor spots, thus the profiles do not start to increase at the same time.

The profiles in between the peaks corresponds to the continuous flow provided by the syringe pumps. In the interval between two peaks a total volume of 100 μl (corresponding to the total volume of the strokes of the two syringes) flows through the reactor. Thus, since the volume of the reactor is around 10 μl, the fluid volume of the reactor is changed 10 times every time that the syringes are emptied. In general it takes around 5 times the residence time to reach steady state conditions in a reactor; thus, for example, at a flow rate of 0.25 μl/s it should take around 200 seconds to reach steady state conditions. This time is even shorter if it is considered the position of the first sensor spot, which corresponds to a much shorter residence time than the outlet of the reactor. As can be seen from Figure 4.10 and Figure 4.12 steady state is not reached in all the positions in the microreactor after that 500 μl have flowed inside the channel.

In Figure 4.14 it is shown that the steady state is reached approximately at 7000 seconds in all sensor spots, after that 2 ml had flowed through the reactor.

The long time required to reach steady state may be due to the laminar flow in the channel, which limits mass transfer; it may also be due to other dynamics that are taking place in the microchannel, like the adsorption, which takes some time before being completely steady and have a constant effect on the reaction rate.

Negative oxygen partial pressure are maybe due to a not precise calibration of the oxygen meter.

5.2.1.2 Effect of glucose oxidase concentration

The effect of GOx concentration has a strong impact on oxygen partial pressure. Higher GOx concentration means faster reaction rate; this is specially visible from the oxygen profiles in the last sensor spot (Figure 4.10), where the cumulative effects of all dynamics that take place in the previous part of the channel can be seen. Thus, GOx concentration has effects on the reaction rate.

The opposite trend of the profiles in Figure 4.10 and in Figure 4.12, which are downwards and upwards, respectively, is not due to the concentration of GOx but to the initial conditions for the experiment.

On the one hand, oxygen profiles are increasing when the experiment is done with GOx concentration of 0.05 g/l (Figure 4.17); this is due to the initial conditions of oxygen concentration of the experiment, which is lower than the final steady state value of oxygen concentration in the microreactor. On the other hand, oxygen profiles are decreasing when the experiments are performed with GOx concentration of 0.2 g/l beacause the initial condition corresponds to the maximum concentration of oxygen. In Figure 5.11 the oxygen profiles relative to two experiments (first part of the experiment described in § 3.2.7 on page 56 and experiment in § 3.2.3 on page 55 done with the syringes with stroke volume of 250 μl) are compared. The experiments differ only for the initial condition.

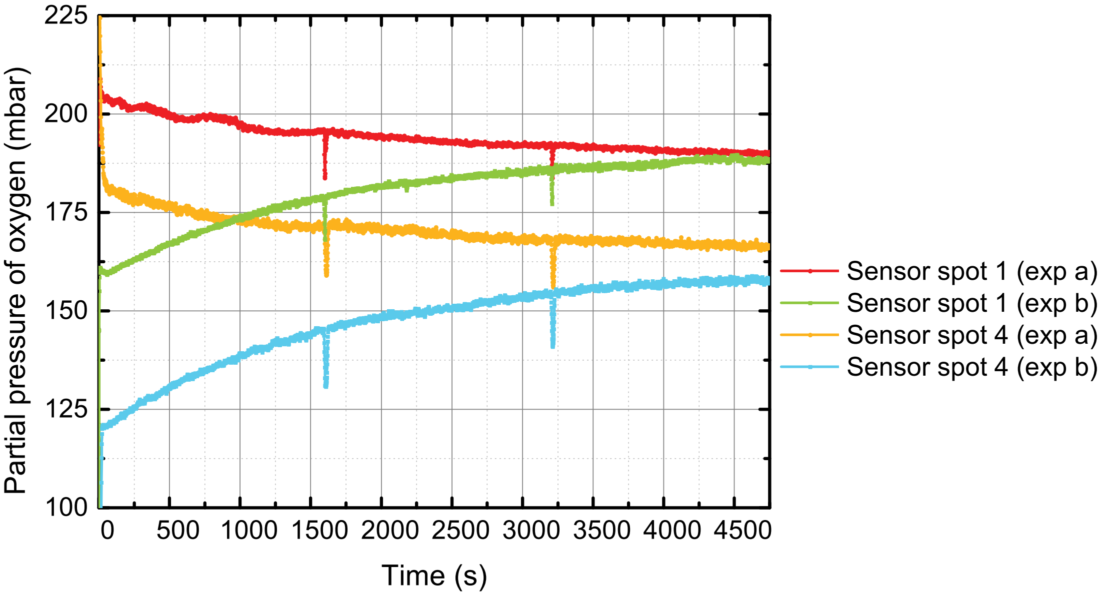

Figure 5.11 *Oxygen profiles in sensor spot 1 and 4 from two experiments at glucose oxidase concentration of 0.05 g/l at a flow rate of 0.313 μl/s. Experiment a corresponds to the first part of the experiment described in § 3.2.7 on page 56 (when glucose and glucose oxidase are fed to the system), while experiment b corresponds to the experiment in § 3.2.3 on page 55 done with the syringes with stroke volume of 250 μl.*

It can be verified in Figure 5.11 that the profiles tend to the same steady state value. The steady state is already reached in correspondence of the first sensor spot and it will be reached later in correspondence of the fourth sensor spot.

5.2.1.3 Effect of the flow rate

When the flow rate is increased, the oxygen partial pressure is higher in all positions than with small flow rates. This is related to the fact that at high flow rate the residence time is shorter than at low flow rate, thus the reaction reaches a smaller extent of conversion. It seems also that at a high flow rate steady state is reached faster than at low flow rate (comparison between Figure 4.10 and Figure 4.16). However, the experiment at high flow rate was done after the one at low flow rate without flushing the reactor in between the experiments. Thus, the fact that the steady state is reached faster can also be due to the fact that other dynamics are already at their steady state.

5.2.1.4 Alternate flow

From Figure 4.21, it is observed that the minimum reached by downward peaks, which corresponds to the moment when GOx starts to be pumped into the system, decreases from one replicate to the next one (with the exception of the profile obtained from the probe in the third sensor spot). This may be due to a progressive accumulation of GOx in the system, which consumes more oxygen every time that fresh GLU is pumped in the system.

5.2.2 Addition of BSA

The purpose of the addition of BSA is to interfere with the dynamics between the wall and the enzyme. When BSA is added before the flow of GLU and GOx it is observed that the profiles have a very similar shape compared to the case when BSA is not added to the system. The only difference is in the value of oxygen partial pressure, which is a bit higher when BSA is added to the system. When GOx has a concentration of 0.2 g/l, the levels that are higher are only the one corresponding to the first and the second sensor spot. When GOx has a concentration of 0.05 g/l the effect of the presence of BSA is visible in all profiles.

The fact that oxygen concentration is in general higher when the microchannel is pretreated with BSA means that the concentration of enzyme inside the microreactor is lower, since all other conditions are exactly the same. This may be due to the fact that

BSA is adsorbed on the walls and when GOx is fed to the system it starts to be adsorbed on the walls by replacing BSA or by being adsorbed to other available sites. This process takes some time, thus the accumulation of GOx inside the channel is not as fast as when only GOx and GLU are fed to the microreactor.

By comparing the profiles obtained at different GOx concentration, it is observed that the concentration of GOx has an impact on the system. In fact, if a high concentration of GOx is used, the difference in the profiles of the fourth and the sixth sensor spots between the experiment performed with and without BSA is not noticeable. This may mean that high concentration of GOx could speed up the adsorption of GOx to the walls to the point that the presence of BSA is completely hidden. On the other hand, when only 0.05 g/l of GOx are use to feed the microreactor, the adsorption seems to be slower, and slowed down by the previous presence of BSA.

The result of the experiment where BSA is fed continuously together with GOx (Figure 4.19) show a very different trend compared to all the others. The oxygen partial pressure is completely constant in all measuring points in the microchannel from the first time when GLU, GOx and BSA are fed to the system.

The results of this experiment look different from all others: in this case all profiles are completely flat from the first time that GOx, GLU and BSA flow inside the microreactor. Thus, it seems that the system can reach steady state faster than in all other cases. It might be that BSA has more affinity with the walls than GOx and that it adsorbs faster than GOx. Since BSA is continuously fed and its concentration is three times GOx concentration, it might be that it is BSA that is only adsorbed to the walls. The molecule of BSA is considerably smaller than the molecule of GOx (BSA has a molecular weight of 66 kDa while GOx has a molecular weight of 160 kDa), thus it can be more mobile and more easily adsorbed, if the adsorption depends on size of the molecules. It is also considered that both GOx and BSA have an isoelectric point around 4, thus, at pH 7, which is the one used for the reaction, they are both negatively charged; thus, if the glass contains metal ions (the type of glass of the microreactor is not known), it is possible that they are attracted by the walls and, since BSA is smaller than GOx, it maybe can migrate faster.

From the comparison of the experimental results presented in Figure 4.22 and in Figure 4.23 it can be concluded that the effect of BSA change the dynamic behaviour of the system in stop flow conditions. In Figure 5.12 and in Figure 5.13 the oxygen profiles relative to the stop flow after the first feed of glucose are compared. The two experiments are identical, they differ only for the addition of BSA in experiment d.

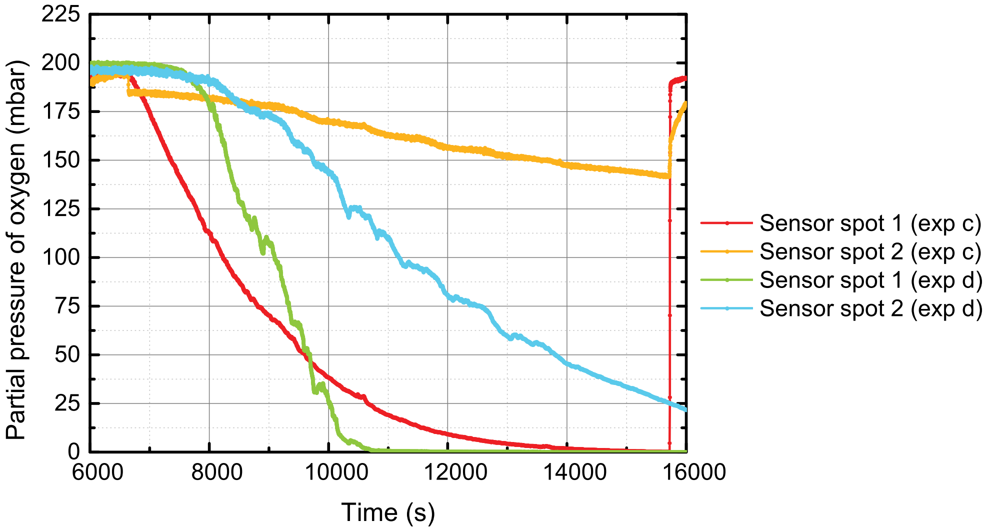

Figure 5.12 *Oxygen profiles in the stop flow condition after the feed of glucose at sensor spot 1 and 2. Experiment c corresponds to the stop flow experiment explained in §3.2.7 (only the stop flow after the first feed of glucose), and experiment d corresponds to the stop flow experiment with the addition of bovine serum albumin explained in §3.2.8 (only the stop flow after the first feed of glucose). The time scale of experiment d is rescaled to the time scale of experiment c in order to compare the profiles.*

From Figure 5.12 and in Figure 5.13 it is observed that the presence of BSA delays the decay of oxygen partial pressure. Moreover, the decay of oxygen partial pressure is slower when BSA is added to the system, meaning that the concentration of GOx is lower than when BSA is not added. This is noticeable specially in Figure 5.13. This could be interpreted considering that the data measured in the last two sensor spots are the results of all dynamics that are taking place in the whole channel. Thus, if it is considered that the phenomena that might be taking place is related to the surface of the walls, it is likely that the effect of it is more visible close to the end of the channel, because the enzyme will have more surface to which it can adsorb.

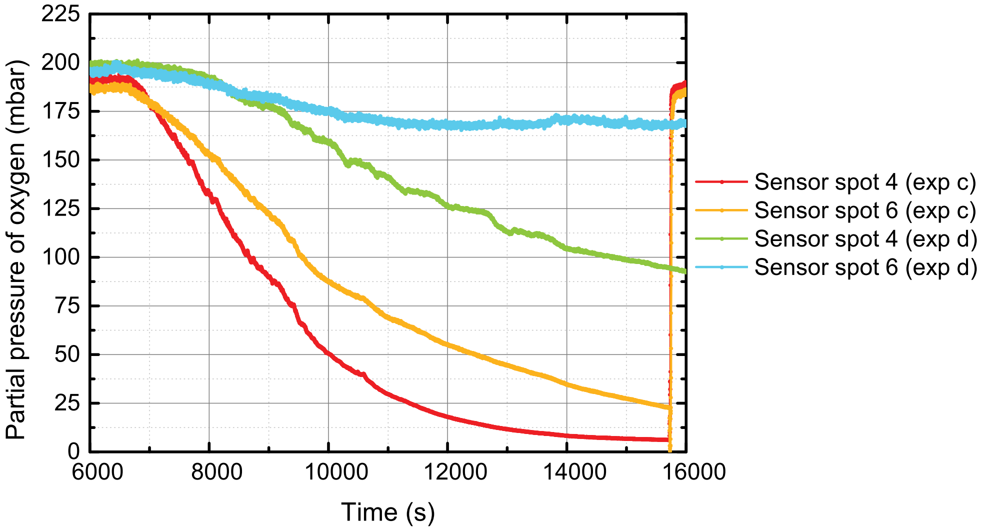

Figure 5.13 *Oxygen profiles in the stop flow condition after the feed of glucose at sensor spot 4 and 6. Experiment c corresponds to the stop flow experiment explained in §3.2.7 (only the stop flow after the first feed of glucose), and experiment d corresponds to the stop flow experiment with the addition of bovine serum albumin explained in §3.2.8 (only the stop flow after the first feed of glucose). The time scale of experiment d is rescaled to the time scale of experiment c in order to compare the profiles.*

In conclusion, from the set of experiments performed with GOx, it can be concluded that adsorption of GOx might take place on the surface of the microreactor walls. This can be seen by comparing the experimental results of the same experiments performed with and without the addition of the protein BSA. It is also possible to conclude that BSA absorbs to the walls of the microreactor since it is observed a faster reaction rate when BSA is not added to the system.

5.2.3 CFD simulations

The oxygen profiles shown in Figure 4.25, Figure 4.27 and Figure 4.28 are to be compared to the profiles in Figure 4.24, which shows the result of the CFD simulations without adsorption. This is done since it is intended to verify if the addition of the adsorption model modifies the oxygen profiles as seen from the experimental results.

It is observed that the addition of the adsorption model does modify the oxygen partial pressure profiles. The shape of the profiles changes a lot depending on the values of the kinetic constants and on the concentration of available sites. Since it is not possible to estimate any of the parameters from the experiments that were performed (and no experimental techniques were available for this type of measurements), some sets of parameters are used and their effect is observed on the system.

On the one hand, it is noticed that c^* influences the final value of the oxygen partial pressure. In fact, it is observed that the profiles reach lower value in Figure 4.27, which corresponds to a system with more available sites than the others. On the other hand, k_{ads} and k_{des} modifies the dynamic part of the profile (the first part); if Figure 4.25, Figure 4.27 and Figure 4.28 are compared, the initial shape of the profiles is completely different.

From the contour plots shown in Figure 4.30, Figure 4.31a and Figure 4.31b it is observed that the adsorption of the enzyme is asymmetric, since the flow is laminar and the enzyme flows parallel to the flow of GLU. It is also observed that the adsorption is mainly taking place in the first part of the channel.

5.2.4 Comparison of CFD simulations and experimental results

None of the performed simulations can completely fit the experimental data, since just by trying combinations of parameters it is not possible to completely describe the complex behaviour of the system. A linear regression of the parameters would be required, as well as experimental investigations for determining the constants. However, in first place it is observed that the model that does not include adsorption reaches steady state faster compared to models that include adsorption (the only exception is represented by the model with very slow adsorption kinetics), and from the experimental data it is observed that the system requires long time to reach steady state. In second place it noticed that the profiles in Figure 4.24 do not represent what is observed experimentally. In Figure 5.14 the profiles of oxygen partial pressure are shown. These experimental data are obtained during the first 30 seconds of measurements after that GOx and GLU are fed simultaneously in the system at a total flow rate of 0.25 μl/s. It is decided to compare these experimental data to the simulations since the initial condition is the same as in the simulation and before collecting these measures, the system was cleaned with ethanol, making sure that no residual enzymatic activity was present.

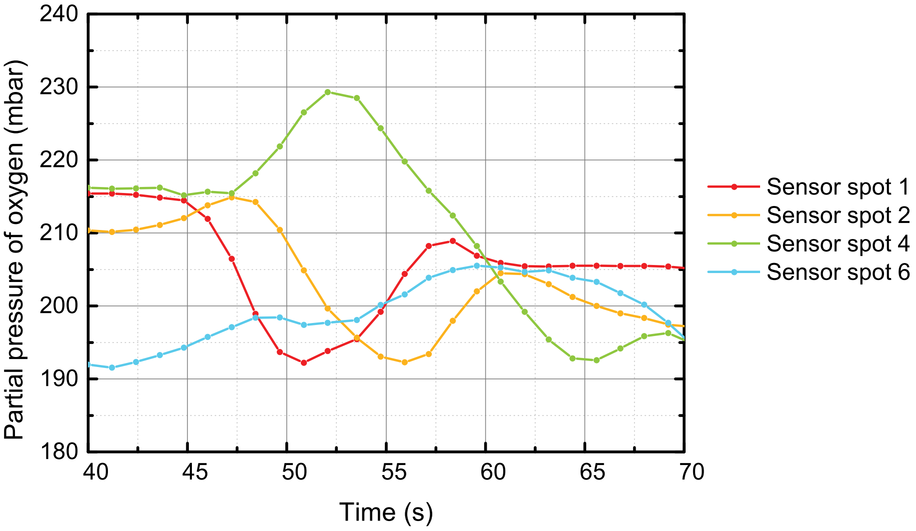

Figure 5.14 *Oxygen partial pressure profiles in sensor spot 1, 2, 4 and 6, immediately after that glucose oxidase and glucose are fed to the system.*

These profiles are close to the one shown in Figure 4.28. In particular, the fast adsorption kinetic model is able to predict the undershoot of the experimental profiles for the first and second measuring points. Therefore, it seems that the CFD simulation that does not include the adsorption model is further from the experimental data than the simulation that includes a relatively fast adsorption model. However, there is still the need to perform linear regression of the parameters, and maybe to include in the model the possibility of multilayer adsorption. The fact that the model that does not include adsorption does not reproduce the dynamics of the experimental data, means that CFD, which solves locally Navier-Stokes equations and the equation of continuity, cannot reproduce only with fluid dynamics the measured data.

Conclusion

The topic of this thesis is the investigation of enzymatic reaction kinetics in microreactors. This has been performed through the experimental study of two enzymatic reactions: transamination with the enzyme $\omega-$TAm and oxidation with the enzyme GOx. The latter has also been studied with CFD simulations. The objective of this work is the investigation of the dependence of the reaction rate of transamination on reactor scale and geometry and the identification of other phenomena occurring in the microreactor that affect the reaction rate.

The effect of the scale of the reactor on the enzymatic activity has been studied experimentally. The activity of the enzyme $\omega-$TAm has been measured both in a batch system and in a microreactor. The results show that the activity of $\omega-$TAm in the microreactor is significantly higher than in the batch reactor, which proves that the reactor scale has an influence on the activity of the studied enzyme and justifies the need for subsequent experiments and simulations at microscale. A possible explanation for this experimental evidence is that the enzyme has a different reaction mechanism depending on the scale of the reactor, or that the reaction mechanism is the same but the parameters in the reaction rate model are different. In this project it has been assumed that the enzyme displays the same kinetic mechanism in both systems, so the kinetic parameters have been determined in both reactor scales.

The apparent kinetic parameters ($K_{M,app}$ and $V_{max,app}$) belong to Michaelis-Menten kinetic model and have been determined for both substrates of the reaction, i.e. $(S)-\alpha-$MBA and PYR. Different values for these parameters have been obtained for the two reactors: both $V_{max,app}$ and $K_{M,app}$ are higher in the microreactor compared to the batch system. Specifically, $V_{max,app}$ in microreactors has been found to be 5 times the measured $V_{max,app}$ in batch systems for both substrates; this result is in agreement with the data obtained by Wang et al. (2013) and Yamashita et al. (2009). Regarding $K_{M,app}$, it is found that it has a higher value in the microreactor than in the batch system for both substrates. However, Wang et al. (2013) and Yamashita et al. (2009) state that K_M in microreactors is smaller than K_M in batch reactors.

The faster reaction rate in the microreactor may not only be due to the reactor scale but also to another phenomena occurring. It has been observed that the reaction rate in a microchannel depends on the SA:V; the larger the SA:V, the higher the product concentration obtained. Therefore, it seems clear that a phenomenon depending on the SA:V happens in the microreactor, which might be hydrodynamic retention of the enzyme on the walls, adsorption of the enzyme on the walls, or both.

More specific experiments and simulations were performed to identify which of these phenomena is taking place. These have been done with a different enzyme (GOx) for two reasons: the possibility of collecting local and dynamic measurements and the availability of a comprehensive and simpler kinetic model. The new enzyme catalyses the oxidation of glucose and is referred as GOx. It has been observed that GOx reaction rate is modified if BSA is added to the system, which may imply that BSA adsorbs to the walls of the channel instead of GOx.

The presence of hydrodynamic retention of the enzyme on the walls and/or adsorption of the enzyme on the walls has been investigated by CFD simulations. The simulation results show that adsorption can explain the experimental observations, while hydrodynamic retention cannot predict them.

In conclusion, the scale of the reactor has an effect on the enzymatic reaction kinetics, as well as the geometry of the reactor. A phenomenon affecting the reaction rate as a function of SA:V in the microreactor has been identified as adsorption of the enzyme on the walls of the channel, based on experimental evidence and validation through CFD simulations.

In future work, more specific experimental techniques can be used to test and quantify the adsorption of the enzyme on the reactor walls. For example, an enzyme assay could be used to measure inlet and outlet concentration of the enzyme (solution depletion technique), or optical or spectroscopic techniques. Radio-isotope labeled enzymes detected by radioisotope counting or autoradiography could also be used. Parameter regression should be employed for the determination of the parameters in the adsorption model from experimental data. Other studies could be conducted on the type of adsorption model to be used, in order to determine if a monolayer or a multilayer adsorption model is required. After the complete determination of the adsorption model, the influence of the material on protein adsorption could be investigated; other types of glass or polymeric materials could be used.

Nomenclature

Roman Symbols

A	Cross-sectional area (m^2)
c^*	Concentration of available sites ($kg \cdot m^{-2}$)
c_i	Concentration of component i (mM)
c_i^*	Concentration of adsorbed compound i ($kg \cdot m^{-2}$)
c_E0	Initial concentration of enzyme ($g \cdot l^{-1}$)
c_I	Concentration of inhibitory compounds (mM)
D_i	Diffusion coefficient of component i ($m^2 \cdot s^{-1}$)
f_j	Fraction of total luminiscence emission for component j (-)
k_{ads}	Rate constant for adsorption ($m^5 \cdot kg^{-2} \cdot s^{-1}$)
$k_\mathrm{cat}^\mathrm{f}$	Turnover rate of the forward reaction (min^{-1})
$k_\mathrm{cat}^\mathrm{r}$	Turnover rate of the reverse reaction (min^{-1})
k_{des}	Rate constant for desorption ($m^2 \cdot kg^{-1} \cdot s^{-1}$)
K_EQ	Equilibrium constant (-)
K_i^i	Competitive inhibition constant of component i (mM)
K_M^i	Michaelis-Menten constant for component i (mM)
K_Si^i	Uncompetitive inhibition constant of substrate i (mM)

K_{SV}^{j}	Stern-Volmer constant for component j ($\mathrm{l} \cdot \mathrm{g}^{-1}$)
m_{E}	Mass of enzyme (mg)
SA:V	Surface-area-to-volume ratio (mm^{-1})
S	Surface of the walls of the channel (m^2)
t	Time (s)
U	Unit of enzyme activity ($\mu\mathrm{mol} \cdot \mathrm{min}^{-1}$)
v_{i}	Reaction rate for component i ($\mathrm{mM} \cdot \mathrm{min}^{-1}$)

Greek Symbols

γ	Binary indicator for the forward reaction (-)
δ	Diffusional length (m)
η	Catalytic efficiency of the enzyme ($\mathrm{mg}^{-1} \cdot \mathrm{min}^{-1}$)
θ	Fractional coverage of the surface (-)
λ	Binary indicator for the reverse reaction (-)
μ	Dynamic viscosity (Pa s)
ρ	Density ($\mathrm{kg} \cdot \mathrm{m}^{-3}$)
τ	Fluorescence lifetime (s)
τ_0	Fluorescence lifetime in absence of oxygen (s)

Abbreviations

ALA	Alanine
APH	Acetophenone
APIs	Active pharmaceutical ingredients
AS	Asymmetric synthesis

AU	Absorbance unit
BSA	Bovine serum albumin
CAL-B	Candida antarctica lipase B
CFD	Computational fluid dynamics
DKR	Dynamic kinetic resolution
ee	Enantiomeric excess
FAD	Flavin adenine dinucleotide
FDA	Food and drug administration
FVM	Finite volume method
GLU	$\beta-\mathrm{D}-\mathrm{glucose}$
GOx	Glucose oxidase
HPLC	High performance liquid chromatography
KR	Kinetic resolution
LAC	$\mathrm{D}-\mathrm{glucono}-1,5-\mathrm{lactone}$
MAO-N	Monoamine oxidase N
NIR	Near infrared
PLP	Pyridoxal-5´-phosphate
PMP	Pyridoxiamine-5-phosphate
PTFE	Polytetrafluoroethylene
PYR	Pyruvic acid
RA	Racemisation agent
$(2R,3R)-(+)-\mathrm{TA}$	$(2R,3R)-(+)-$Tartaric acid

SD	Standard deviation
TAm	Transaminases
α – MBA	α – Methylbenzylamine
ω – TAm	ω–Transaminases

Appendix A

Standard curves

In this Appendix the standard curves are presented. The standard curves were done in order to be able to correlate the measured areas of the absorbance peaks of a compound in the chromatogram to the compound concentration in a solution. The absorbance of a compound is measured in terms of Absorbance Unit (AU). The standard curves were done for APH and $(S)-\alpha-$MBA twice because they are valid only in the range between the smallest and the highest concentration and a wider range was needed.

Standard curves (I)

$$area_{\mathrm{APH}} = 26.0945 \cdot c_{\mathrm{APH}}, \qquad \mathrm{R}^2 = 99.9882$$

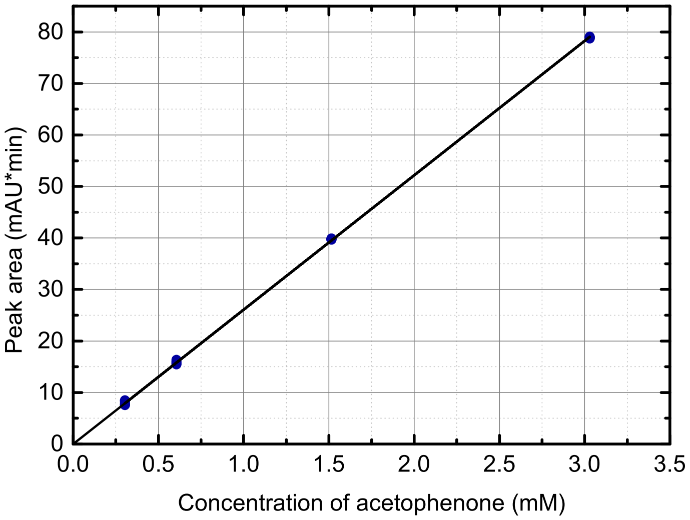

Figure A.1 *Standard curve for APH (used for the experiments regarding activity determination in batch and microreactor).*

$$area_{\mathrm{MBA}} = 0.2958 \cdot c_{\mathrm{MBA}}, \qquad \mathrm{R}^2 = 99.9897$$

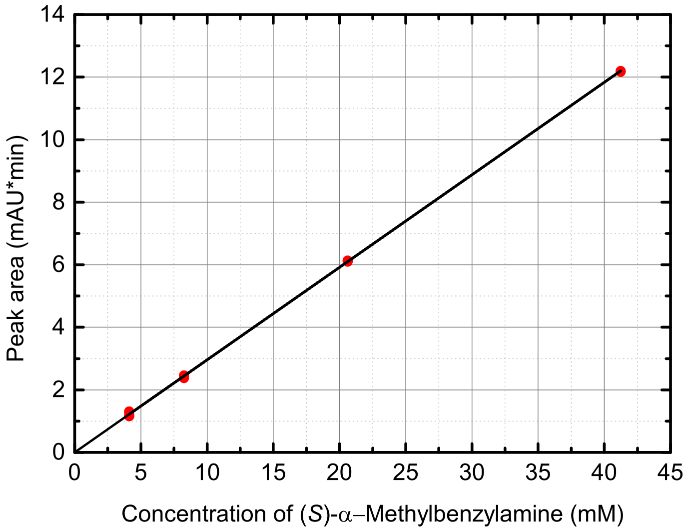

Figure A.2 *Standard curve for MBA (used for the experiments regarding activity determination in batch and microreactor).*

Standard curves (II)

$$area_{\mathrm{APH}} = 24.4606 \cdot c_{\mathrm{APH}}, \qquad \mathrm{R}^2 = 99.9577$$

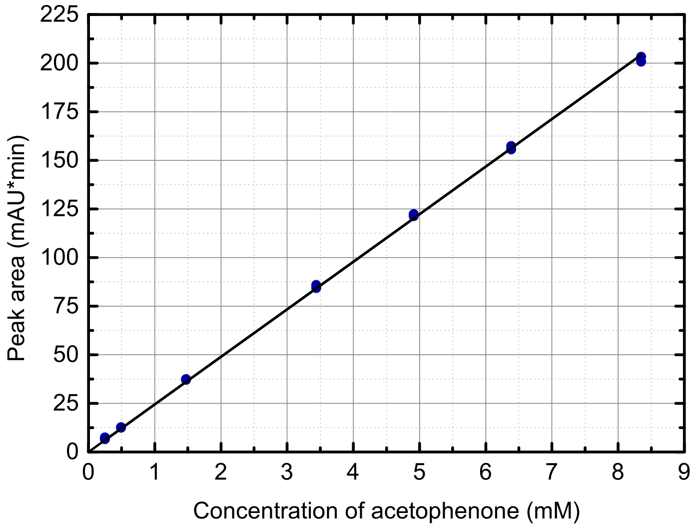

Figure A.3 *Standard curve for APH (used for the experiments regarding kinetic parameters estimation and reaction rate in the series of reactors).*

$$area_{\mathrm{MBA}} = 0.3082 \cdot c_{\mathrm{MBA}}, \qquad \mathrm{R}^2 = 99.9983$$

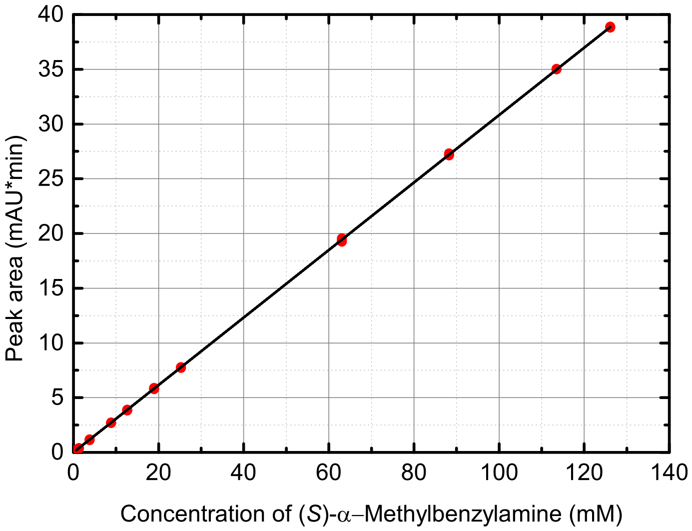

Figure A.4 *Standard curve for MBA (used for the experiments regarding kinetic parameters estimation and reaction rate in the series of reactors).*

Appendix B

Mixing microtube

In this Appendix, the results of the steady state CFD simulation of the microtube placed before the inlet of the microreactors with different geometric dimensions are presented. In the experimental set-up, the inlet of the microtube used for mixing reactant and enzyme is connected with a Y connector to other two microtubes. $\omega-$TAm flows in one of the microtube, while $(S)-\alpha-$MBA, PYR and PLP flow in the other one. This configuration is modeled in the simulation by defining that $\omega-$TAm enters the microtube only from one half of the cross-sectional area of the inlet of the microtube, while the other compounds enter in the microtube from the other half of the cross-sectional area. It is observed that the compounds are completely mixed at the outlet of the microtube that has a length of 7.5 cm. The only species that is not completely mixed is the enzyme $\omega-$TAm.

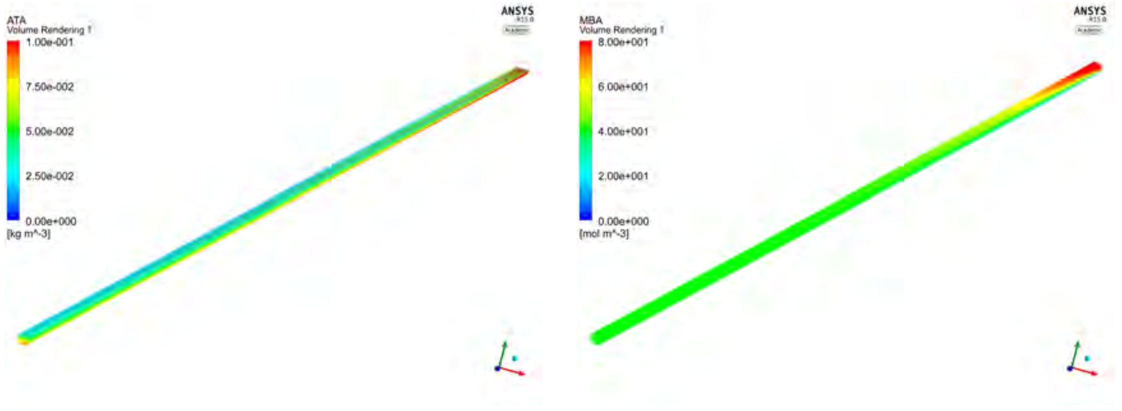

(a) Concentration of $\omega-$TAm.

(b) Concentration of $(S)-\alpha-$MBA.

Figure B.1 *Concentration of $\omega-$TAm and $(S)-\alpha-$MBA in the microtube with diameter 0.17 mm and length 7.5 cm.*

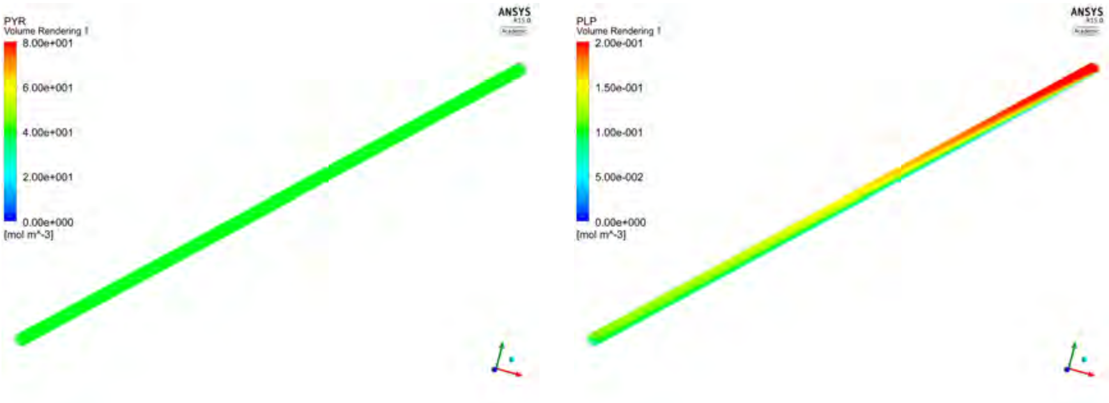

(a) Concentration of PYR.

(b) Concentration of PLP.

Figure B.2 *Concentration of PYR and PLP in the microtube with diameter 0.17 mm and length 7.5 cm.*

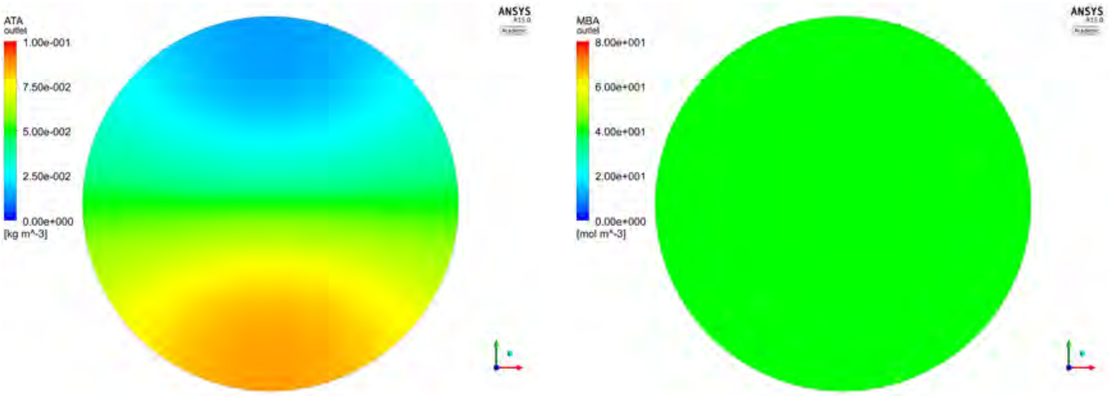

(a) Concentration of $\omega-$TAm.

(b) Concentration of $(S)-\alpha-$MBA.

Figure B.3 *Concentration of $\omega-$TAm and $(S)-\alpha-$MBA on a surface at the outlet of the microtube.*

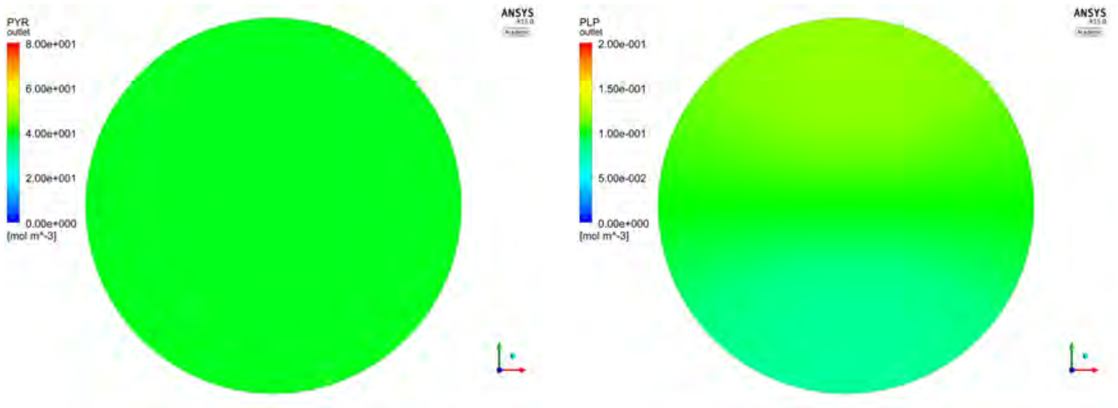

(a) Concentration of PYR.

(b) Concentration of PLP.

Figure B.4 *Concentration of PYR and PLP on a surface at the outlet of the microtube.*

Appendix C

Activity determination

In this Appendix the experimental data relative to the experiment for activity determination are presented. The data refer only to the compound $(S)-\alpha-$MBA.

C.1 Batch system

Table C.1 *Variation of concentration of $(S)-\alpha$-Methylbenzylamine over time in the batch system for activity measurement (first measurement set).*

Time (min)	c_{MBA} (1) (mM)	c_{MBA} (2) (mM)	c_{MBA} (3) (mM)	c_{MBA} (4) (mM)	**Mean (mM)**	**SD (mM)**
0	38.335	37.336	38.519	38.886	38.269	0.663
1	34.870	37.286	36.976	38.246	36.844	1.423
2	38.411	38.715	36.739	37.251	37.779	0.937
4	37.187	37.313	37.045	36.882	37.107	0.186
6	36.228	36.808	36.894	37.067	36.749	0.364
10	35.305	36.674	36.737	36.485	36.300	0.672
60	34.216	33.635	31.576	33.090	33.129	1.133
Slope (mM/min)	0.004	0.038	-0.298	-0.507	-0.191	0.259
R^2	0.000	0.008	0.393	0.893	0.254	

Table C.2 *Variation of concentration of* $(S)-\alpha$*-Methylbenzylamine over time in the batch system for activity measurement (second measurement set).*

Time (min)	c_{MBA} (1) (mM)	c_{MBA} (2) (mM)	c_{MBA} (3) (mM)	c_{MBA} (4) (mM)	**Mean (mM)**	**SD (mM)**
0	37.023	38.251	38.123	37.353	37.687	0.594
1	36.427	36.793	36.232	36.282	36.433	0.254
2	36.376	37.158	35.925	35.958	36.354	0.574
4	36.832	36.609	36.570	35.072	36.271	0.807
6	36.690	36.506	35.742	35.491	36.107	0.581
10	7.266	34.014	35.639	33.868	27.697	13.644
60	32.347	30.926	30.873	29.787	30.983	1.050
Slope (mM/min)	-0.017	-0.328	-0.300	-0.535	-0.295	0.213
$\mathbf{R^2}$	0.008	0.583	0.275	0.939	0.564	

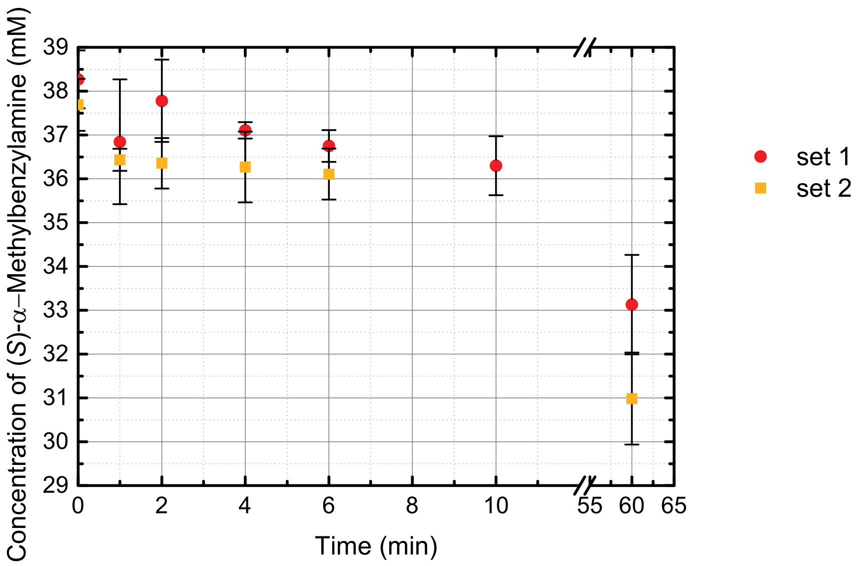

Figure C.1 *Variation of concentration of* $(S)-\alpha$*-Methylbenzylamine over time in the batch system for activity measurement.*

C.2 Microreactor

Table C.3 *Variation of concentration of $(S)-\alpha$-Methylbenzylamine over time in the microreactor for activity measurement (first measurement set).*

Time (**min**)	c_{MBA} (1) (**mM**)	c_{MBA} (2) (**mM**)	c_{MBA} (3) (**mM**)	c_{MBA} (4) (**mM**)	c_{MBA} (5) (**mM**)	**Mean** (**mM**)	**SD** (**mM**)
0	49.503	43.224	39.639	46.169	39.639	43.635	4.271
0.454	36.844	35.557	37.109	37.585	38.949	37.209	1.229
1.067	36.274	38.116	39.119	38.521	39.367	38.279	1.224
2.595	38.123	38.626	38.708	38.427	38.801	38.537	0.269
3.632	38.779	38.377	38.840	38.662	38.347	38.601	0.228
Slope (mM/min)	-1.508	-0.435	0.042	-1.148	-0.289	-1.168	0.697
R^2	0.177	0.057	0.004	0.243	0.767	0.212	

Table C.4 *Variation of concentration of $(S)-\alpha$-Methylbenzylamine over time in the microreactor for activity measurement (second measurement set).*

Time (**min**)	c_{MBA} (1) (**mM**)	c_{MBA} (2) (**mM**)	c_{MBA} (3) (**mM**)	c_{MBA} (4) (**mM**)	c_{MBA} (5) (**mM**)	**Mean** (**mM**)	**SD** (**mM**)
0	42.633	41.779	41.834	43.037	41.340	42.124	0.691
0.454	40.301	38.292	34.575	37.320	39.155	37.929	2.173
1.067	27.401	34.543	37.234	37.792	39.349	35.264	4.725
2.595	39.489	39.275	39.264	39.218	39.148	39.279	0.128
3.632	39.362	38.939	38.880	39.275	39.042	39.100	0.210
Slope (mM/min)	-0.021	-0.131	0.144	-0.327	-0.402	-0.599	0.198
R^2	0.000	0.006	0.007	0.049	0.393	0.056	

Table C.5 *Variation of concentration of* $(S)-\alpha$*-Methylbenzylamine over time in the microreactor for activity measurement (third measurement set).*

Time (min)	c_{MBA} (1) (mM)	c_{MBA} (2) (mM)	c_{MBA} (3) (mM)	c_{MBA} (4) (mM)	c_{MBA} (5) (mM)	**Mean (mM)**	**SD (mM)**
0	35.362	37.052	37.520	37.887	38.271	37.219	1.131
0.454	26.838	30.851	33.605	35.449	36.373	32.623	3.860
1.067	36.510	36.489	36.593	36.617	37.271	36.696	0.326
2.595	35.953	36.384	36.460	36.451	36.301	36.310	0.209
3.632	36.599	36.525	34.924	36.463	35.869	36.076	0.706
Slope (mM/min)	1.293	0.569	-0.192	-0.128	-0.486	0.312	0.696
R^2	0.222	0.112	0.036	0.050	0.593	0.028	0.085

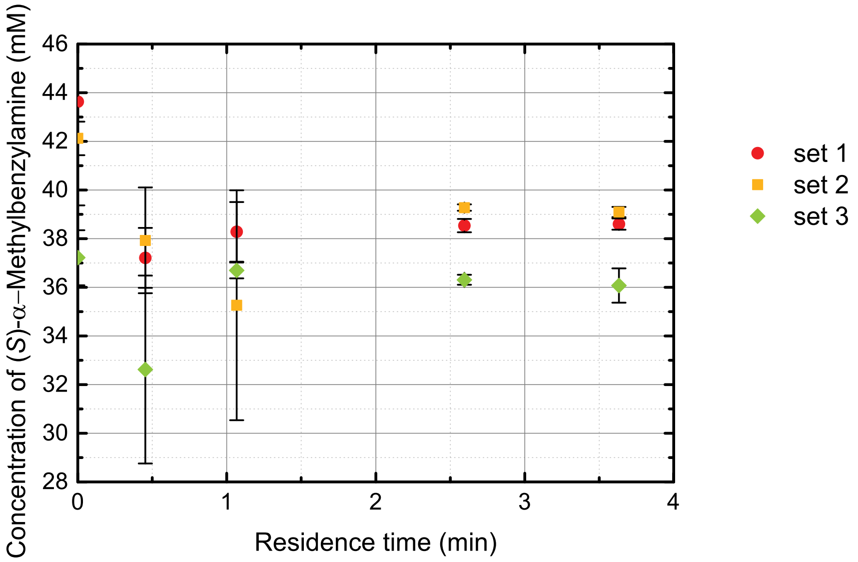

Figure C.2 *Variation of concentration of* $(S)-\alpha$*-Methylbenzylamine over time in the microreactor for activity measurement.*

Appendix D

Kinetic parameter determination

In this Appendix all experimental data obtained for the determination of the kinetic parameters are presented. From each experiment the initial reaction rate was calculated and used for the estimation of the parameters.

D.1 Constant pyruvic acid concentration, variable $(S)-\alpha-$MBA concentration

D.1.1 Batch system

Table D.1 *Variation of the concentration of α-Methylbenzylamine over time with initial reactant composition A.1 in the batch system.*

Time (min)	**c_{MBA} (1) (mM)**	**c_{MBA} (2) (mM)**	**c_{MBA} (3) (mM)**	**Mean (mM)**	**SD (mM)**
0	0.354	0.386	0.388	0.376	0.019
1	0.291	0.303	0.315	0.303	0.012
2	0.251	0.275	0.268	0.265	0.012
4	0.176	0.188	0.189	0.184	0.007
6	0.119	0.131	0.135	0.128	0.008
10	0.050	0.050	0.057	0.052	0.004
Slope (mM/min)	-0.043	-0.047	-0.048	-0.046	0.003
R^2	0.984	0.966	0.978	0.977	

Table D.2 *Variation of concentration of acetophenone over time with initial reactant composition A.1 in the batch system.*

Time (min)	**c_{APH} (1) (mM)**	**c_{APH} (2) (mM)**	**c_{APH} (3) (mM)**	**Mean (mM)**	**SD (mM)**
0	0.000	0.000	0.000	0.000	0.000
1	0.049	0.054	0.059	0.054	0.005
2	0.110	0.113	0.114	0.112	0.002
4	0.199	0.201	0.201	0.200	0.001
6	0.277	0.274	0.272	0.274	0.003
10	0.382	0.368	0.369	0.373	0.008
Slope (mM/min)	0.050	0.050	0.050	0.050	0.000
R^2	0.996	0.995	0.994	0.995	

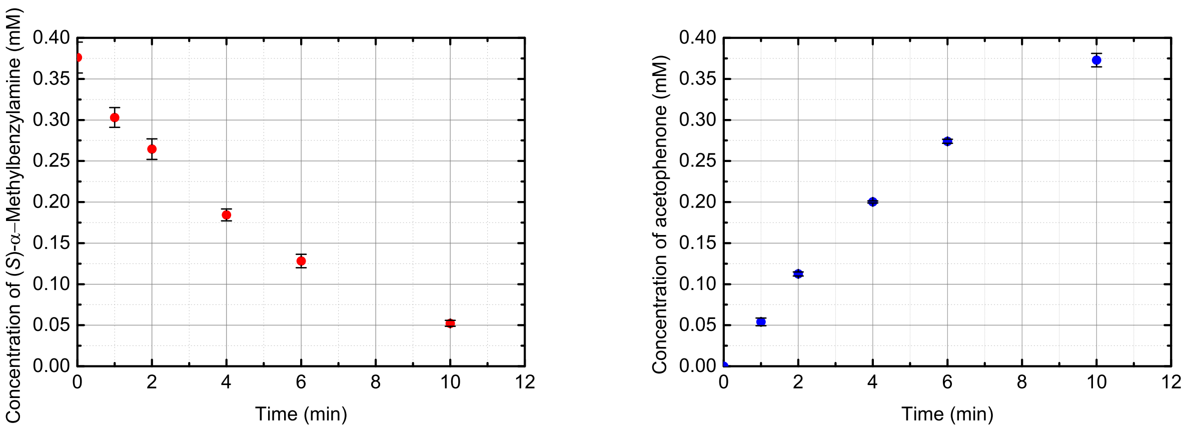

(a) Plot of the variation of concentration of α-Methylbenzylamine over time with initial reactant composition A.1.

(b) Plot of the variation of concentration of acetophenone over time with initial reactant composition A.1.

Figure D.1 *Plots of the variation of concentration of α-Methylbenzylamine and acetophenone over time with reactant composition A.1 in the batch system.*

Table D.3 *Variation of concentration of* α*-Methylbenzylamine over time with initial reactant composition B.1 in the batch system.*

Time (min)	c_{MBA} (1) (mM)	c_{MBA} (2) (mM)	c_{MBA} (3) (mM)	**Mean** (mM)	**SD** (mM)
0	1.701	1.725	1.753	1.726	0.026
1	1.568	1.530	1.565	1.554	0.021
2	1.473	1.474	1.496	1.481	0.013
4	1.300	1.298	1.387	1.328	0.051
6	1.126	1.141	1.144	1.137	0.010
10	0.867	0.877	0.891	0.878	0.012
Slope (mM/min)	-0.098	-0.100	-0.085	-0.095	0.008
R^2	0.990	0.948	0.897	0.955	

Table D.4 *Variation of concentration of acetophenone over time with initial reactant composition B.1 in the batch system.*

Time (min)	c_{APH} (1) (mM)	c_{APH} (2) (mM)	c_{APH} (3) (mM)	**Mean** (mM)	**SD** (mM)
0	0.000	0.000	0.000	0.000	0.000
1	0.104	0.112	0.107	0.108	0.004
2	0.194	0.206	0.209	0.203	0.008
4	0.386	0.393	0.423	0.401	0.019
6	0.555	0.560	0.546	0.553	0.007
10	0.840	0.841	0.854	0.845	0.008
Slope (mM/min)	0.096	0.097	0.105	0.100	0.005
R^2	1.000	0.998	1.000	1.000	

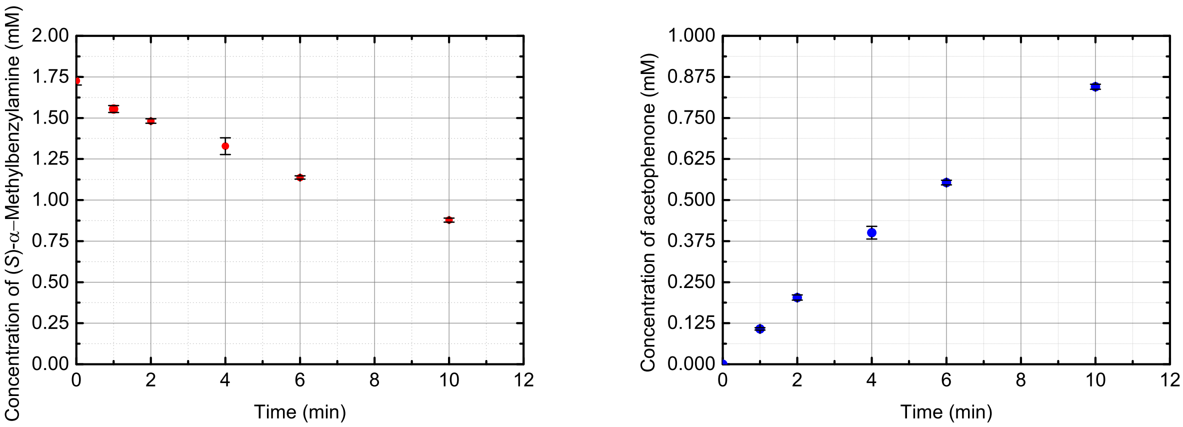

(a) Plot of the variation of concentration of α-Methylbenzylamine over time with initial reactant composition B.1.

(b) Plot of the variation of concentration of acetophenone over time with initial reactant composition B.1.

Figure D.2 *Plots of the variation of concentration of* α*-Methylbenzylamine and acetophenone over time with reactant composition B.1 in the batch system.*

Table D.5 *Variation of concentration of α-Methylbenzylamine over time with initial reactant composition C.1 in the batch system.*

Time (min)	c_{MBA} (1) (mM)	c_{MBA} (2) (mM)	c_{MBA} (3) (mM)	**Mean (mM)**	**SD (mM)**
0	4.745	4.716	4.851	4.771	0.071
1	4.398	4.388	4.426	4.404	0.020
2	4.255	4.320	4.322	4.299	0.038
4	4.050	4.021	4.058	4.043	0.020
6	3.907	3.799	3.857	3.854	0.054
10	3.420	3.399	3.469	3.429	0.036
Slope (mM/min)	-0.163	-0.162	-0.183	-0.169	0.012
R^2	0.905	0.940	0.894	0.913	

Table D.6 *Variation of concentration of acetophenone over time with intial reactant composition C.1 in the batch system.*

Time (min)	c_{APH} (1) (mM)	c_{APH} (2) (mM)	c_{APH} (3) (mM)	**Mean (mM)**	**SD (mM)**
0	0.000	0.000	0.000	0.000	0.000
1	0.125	0.129	0.173	0.142	0.027
2	0.260	0.245	0.252	0.252	0.007
4	0.475	0.472	0.493	0.480	0.011
6	0.703	0.709	0.734	0.715	0.017
10	1.147	1.148	1.156	1.151	0.005
Slope (mM/min)	0.119	0.117	0.119	0.118	0.001
R^2	0.997	0.999	0.987	0.997	

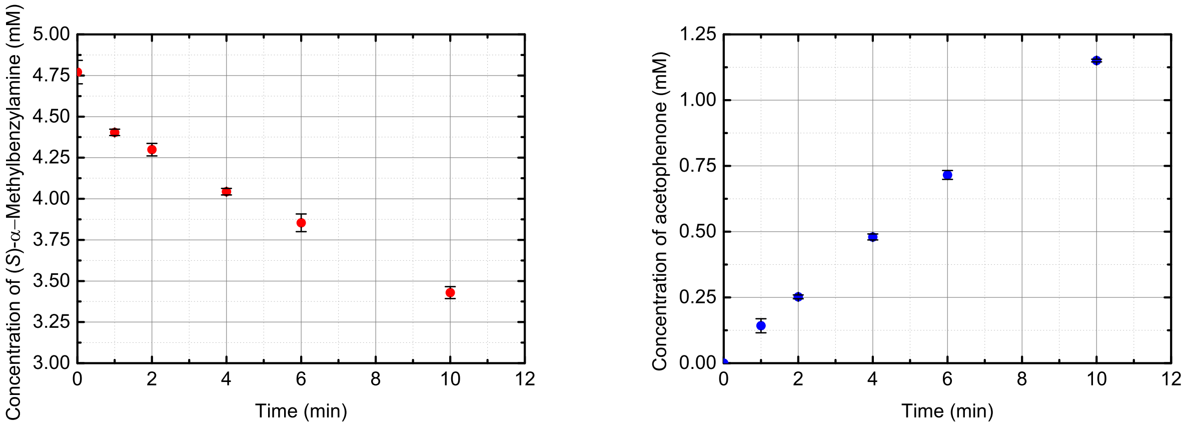

(a) Plot of the variation of concentration of α-Methylbenzylamine over time with initial reactant composition C.1.

(b) Plot of the variation of concentration of acetophenone over time with initial reactant composition C.1.

Figure D.3 *Plots of the variation of concentration of α-Methylbenzylamine and acetophenone over time with reactant composition C.1 in the batch system.*

Table D.7 *Variation of concentration of α-Methylbenzylamine over time with initial reactant composition D.1 in the batch system.*

Time (min)	c_{MBA} (1) (mM)	c_{MBA} (2) (mM)	c_{MBA} (3) (mM)	**Mean (mM)**	**SD (mM)**
0	8.878	9.035	9.130	9.014	0.127
1	8.476	8.550	8.536	8.520	0.040
2	8.386	8.481	8.383	8.417	0.056
4	8.042	8.108	8.031	8.060	0.042
6	8.424	7.874	7.878	8.059	0.316
10	7.388	7.435	7.443	7.422	0.029
Slope (mM/min)	-0.195	-0.213	-0.253	-0.220	0.030
R^2	0.935	0.909	0.889	0.911	

Table D.8 *Variation of concentration of acetophenone over time with initial reactant composition D.1 in the batch system.*

Time (min)	c_{APH} (1) (mM)	c_{APH} (2) (mM)	c_{APH} (3) (mM)	**Mean (mM)**	**SD (mM)**
0	0.000	0.024	0.000	0.008	0.014
1	0.150	0.158	0.157	0.155	0.004
2	0.280	0.290	0.290	0.286	0.006
4	0.536	0.534	0.533	0.534	0.002
6	0.839	0.778	0.783	0.800	0.034
10	1.245	1.274	1.263	1.261	0.015
Slope (mM/min)	0.133	0.127	0.132	0.131	0.003
R^2	0.999	0.999	0.997	0.998	

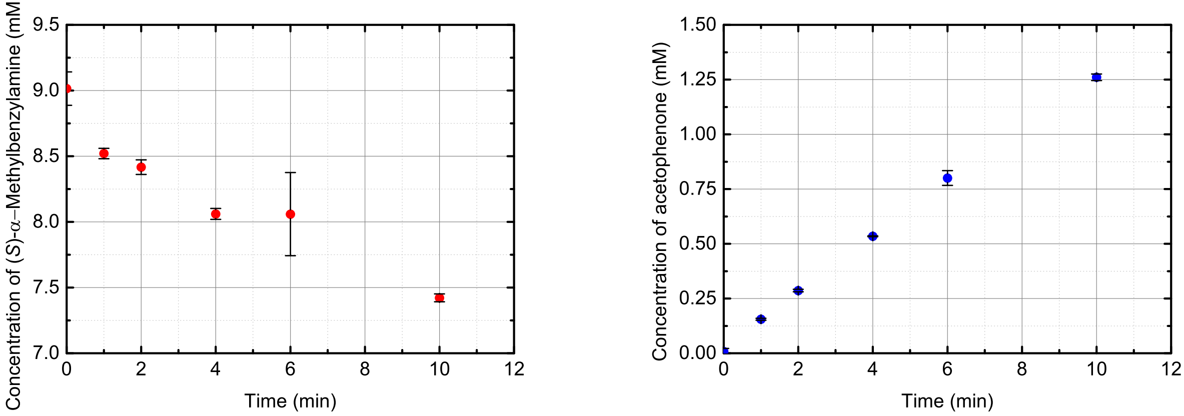

(a) Plot of the variation of concentration of α-Methylbenzylamine over time with initial reactant composition D.1.

(b) Plot of the variation of concentration of acetophenone over time with initial reactant composition D.1.

Figure D.4 *Plots of the variation of concentration of α-Methylbenzylamine and acetophenone over time with reactant composition D.1 in the batch system.*

Table D.9 *Variation of concentration of α-Methylbenzylamine over time with initial reactant composition E.1 in the batch system.*

Time (min)	c_{MBA} (1) (mM)	c_{MBA} (2) (mM)	c_{MBA} (3) (mM)	**Mean (mM)**	**SD (mM)**
0	55.932	58.157	58.287	57.459	1.324
1	55.723	56.113	55.013	55.616	0.558
2	56.123	56.193	55.579	55.965	0.336
4	55.895	55.984	54.770	55.549	0.677
6	55.305	54.621	54.386	54.771	0.477
10	55.034	53.668	54.289	54.330	0.684
Slope (mM/min)	0.014	-0.440	-0.701	-0.376	0.362
R^2	0.021	0.528	0.547	0.365	

Table D.10 *Variation of concentration of acetophenone over time with initial reactant composition E.1 in the batch system.*

Time (min)	c_{APH} (1) (mM)	c_{APH} (2) (mM)	c_{APH} (3) (mM)	**Mean (mM)**	**SD (mM)**
0	0.038	0.037	0.039	0.038	0.001
1	0.185	0.180	0.183	0.183	0.003
2	0.306	0.298	0.298	0.301	0.005
4	0.566	0.553	0.545	0.554	0.011
6	0.800	0.787	0.782	0.790	0.009
10	1.283	1.239	1.271	1.264	0.023
Slope (mM/min)	0.131	0.128	0.125	0.128	0.003
R^2	0.999	0.999	0.999	0.999	

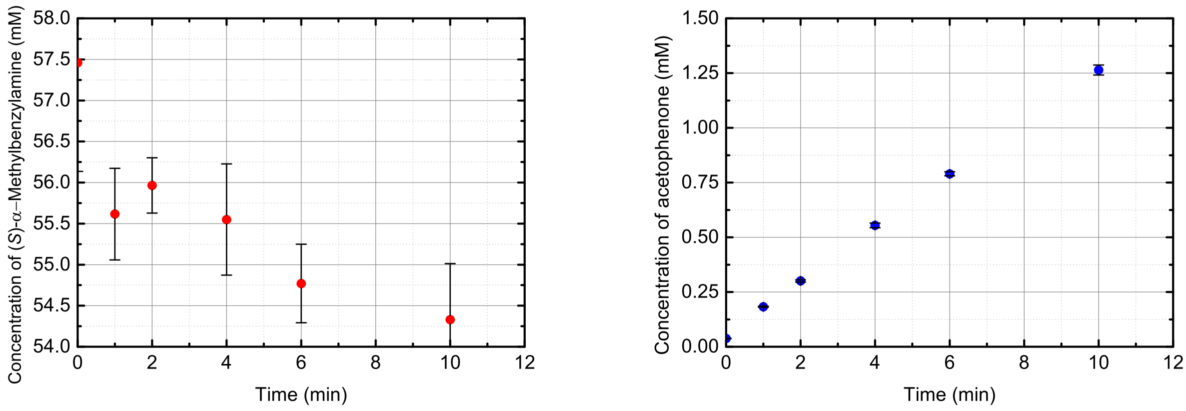

(a) Plot of the variation of concentration of α-Methylbenzylamine over time with initial reactant composition E.1.

(b) Plot of the variation of concentration of acetophenone over time with initial reactant composition E.1.

Figure D.5 *Plots of the variation of concentration of α-Methylbenzylamine and acetophenone over time with reactant composition E.1 in the batch system.*

Table D.11 *Variation of concentration of α-Methylbenzylamine over time with initial reactant composition F.1 in the batch system.*

Time (min)	c_{MBA} (1) (**mM**)	c_{MBA} (2) (**mM**)	c_{MBA} (3) (**mM**)	**Mean** (**mM**)	**SD** (**mM**)
0	100.759	100.673	100.145	100.526	0.332
1	97.127	96.033	97.113	96.758	0.628
2	96.944	98.527	97.123	97.532	0.867
4	96.296	96.176	96.347	96.273	0.088
6	96.274	96.165	95.768	96.069	0.266
10	96.306	95.796	96.609	96.237	0.411
Slope (mM/min)	-0.945	-0.820	-0.803	-0.856	0.078
R^2	0.641	0.405	0.665	0.570	

Table D.12 *Variation of concentration of acetophenone over time with initial reactant composition F.1 in the batch system.*

Time (min)	c_{APH} (1) (**mM**)	c_{APH} (2) (**mM**)	c_{APH} (3) (**mM**)	**Mean** (**mM**)	**SD** (**mM**)
0	0.074	0.063	0.066	0.068	0.006
1	0.207	0.197	0.198	0.200	0.005
2	0.305	0.317	0.315	0.313	0.006
4	0.537	0.546	0.546	0.543	0.005
6	0.771	0.777	0.776	0.775	0.003
10	1.219	1.220	1.238	1.225	0.010
Slope (mM/min)	0.114	0.120	0.119	0.118	0.003
R^2	0.998	0.999	0.999	0.999	

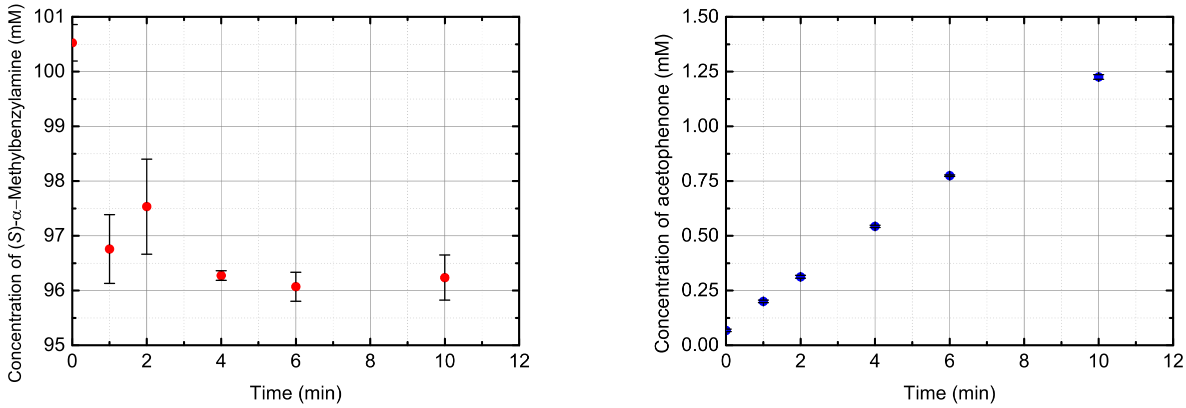

(a) Plot of the variation of concentration of α-Methylbenzylamine over time with initial reactant composition F.1.

(b) Plot of the variation of concentration of acetophenone over time with initial reactant composition F.1.

Figure D.6 *Plots of the variation of concentration of α-Methylbenzylamine and acetophenone over time with reactant composition F.1 in the batch system.*

D.1.2 Microreactor

Table D.13 *Variation of concentration of α-Methylbenzylamine over time with initial reactant composition A.1 in the microreactor.*

Time (min)	c_{MBA} (1) (mM)	c_{MBA} (2) (mM)	c_{MBA} (3) (mM)	**Mean** (mM)	**SD** (mM)
0.000	0.390	0.395	0.393	0.393	0.003
0.454	0.380	0.366	0.370	0.372	0.007
1.067	0.339	0.335	0.325	0.333	0.007
2.595	0.266	0.236	0.219	0.240	0.024
3.632	0.149	0.155	0.197	0.167	0.026
Slope (mM/min)	-0.049	-0.061	-0.068	-0.060	0.010
R^2	0.991	0.998	0.998	0.999	

Table D.14 *Variation of concentration of acetophenone over time with initial reactant composition A.1 in the microreactor.*

Time (min)	c_{APH} (1) (mM)	c_{APH} (2) (mM)	c_{APH} (3) (mM)	**Mean** (mM)	**SD** (mM)
0.000	0.000	0.000	0.000	0.000	0.000
0.454	0.036	0.040	0.040	0.039	0.002
1.067	0.071	0.077	0.079	0.076	0.004
2.595	0.142	0.162	0.168	0.158	0.014
3.632	0.093	0.103	0.132	0.109	0.020
Slope (mM/min)	0.053	0.061	0.063	0.059	0.005
R^2	0.988	0.992	0.994	0.991	

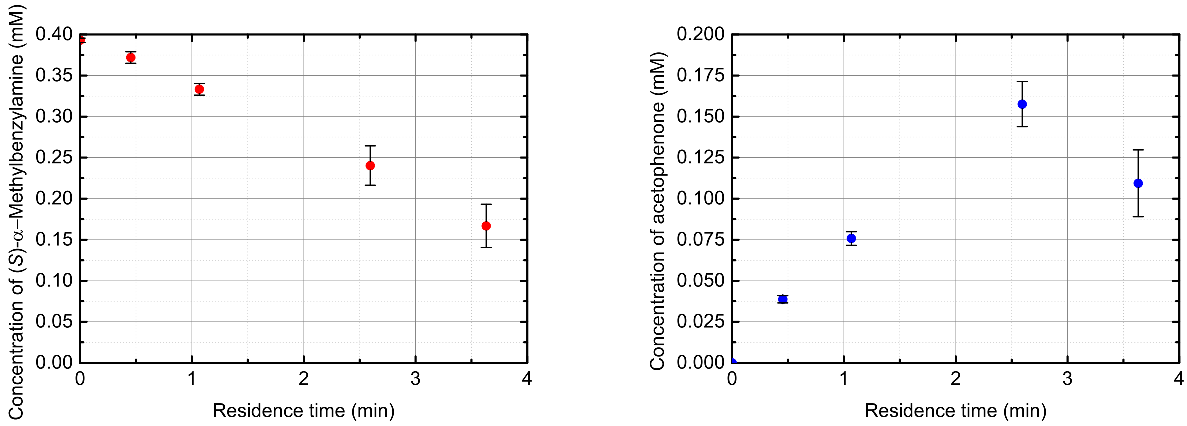

(a) Plot of the variation of concentration of α-Methylbenzylamine over time with initial reactant composition A.1.

(b) Plot of the variation of concentration of acetophenone over time with initial reactant composition A.1.

Figure D.7 *Plots of the variation of concentration of α-Methylbenzylamine and acetophenone over time with reactant composition A.1 in the microreactor.*

Table D.15 *Variation of concentration of* α*-Methylbenzylamine over time with initial reactant composition B.1 in the microreactor.*

Time (min)	c_{MBA} (1) (mM)	c_{MBA} (2) (mM)	c_{MBA} (3) (mM)	**Mean (mM)**	**SD (mM)**
0.000	1.726	1.752	1.748	1.742	0.014
0.454	1.620	1.638	1.639	1.632	0.011
1.067	1.639	1.526	1.503	1.556	0.073
2.595	1.331	1.269	1.280	1.293	0.033
3.632	0.906	1.164	1.145	1.072	0.144
Slope (mM/min)	-0.146	-0.182	-0.177	-0.168	0.019
R^2	0.926	0.994	0.985	0.994	

Table D.16 *Variation of concentration of acetophenone over time with initial reactant composition B.1 in the microreactor.*

Time (min)	c_{APH} (1) (mM)	c_{APH} (2) (mM)	c_{APH} (3) (mM)	**Mean (mM)**	**SD (mM)**
0.000	0.000	0.000	0.000	0.000	0.000
0.454	0.072	0.081	0.079	0.077	0.004
1.067	0.154	0.173	0.177	0.168	0.012
2.595	0.355	0.405	0.406	0.389	0.029
3.632	0.287	n.a.	0.384	0.336	0.069
Slope (mM/min)	0.135	0.154	0.155	0.148	0.011
R^2	0.999	0.999	0.999	0.999	

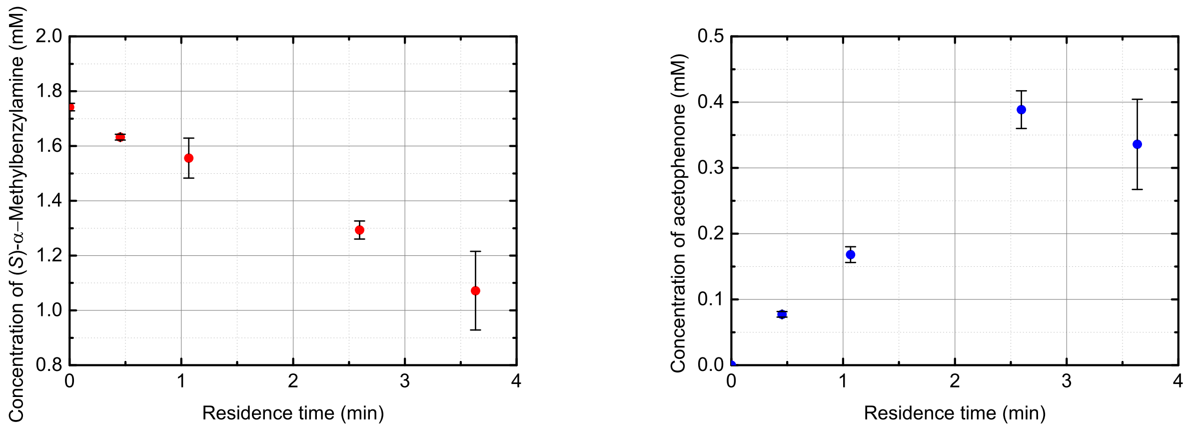

(a) Plot of the variation of concentration of α-Methylbenzylamine over time with initial reactant composition B.1.

(b) Plot of the variation of concentration of acetophenone over time with initial reactant composition B.1.

Figure D.8 *Plots of the variation of concentration of* α*-Methylbenzylamine and acetophenone over time with reactant composition B.1 in the microreactor.*

Table D.17 *Variation of concentration of α-Methylbenzylamine over time with initial reactant composition C.1 in the microreactor.*

Time (min)	c_{MBA} (1) (mM)	c_{MBA} (2) (mM)	c_{MBA} (3) (mM)	**Mean (mM)**	**SD (mM)**
0.000	4.755	4.971	4.850	4.859	0.108
0.454	4.799	4.739	4.831	4.790	0.046
1.067	4.449	4.490	4.549	4.496	0.050
2.595	4.370	4.388	4.347	4.368	0.021
3.632	4.135	3.952	4.117	4.068	0.101
Slope (mM/min)	-0.172	-0.242	-0.204	-0.206	0.035
R^2	0.894	0.920	0.967	0.947	

Table D.18 *Variation of concentration of acetophenone over time with initial reactant composition C.1 in the microreactor.*

Time (min)	c_{APH} (1) (mM)	c_{APH} (2) (mM)	c_{APH} (3) (mM)	**Mean (mM)**	**SD (mM)**
0.000	0.000	0.000	0.000	0.000	0.000
0.454	0.094	0.101	0.104	0.100	0.005
1.067	0.125	0.175	0.194	0.165	0.036
2.595	0.462	0.500	0.484	0.482	0.019
3.632	0.607	0.703	0.676	0.662	0.049
Slope (mM/min)	0.171	0.193	0.184	0.183	0.011
R^2	0.986	0.997	0.999	0.996	

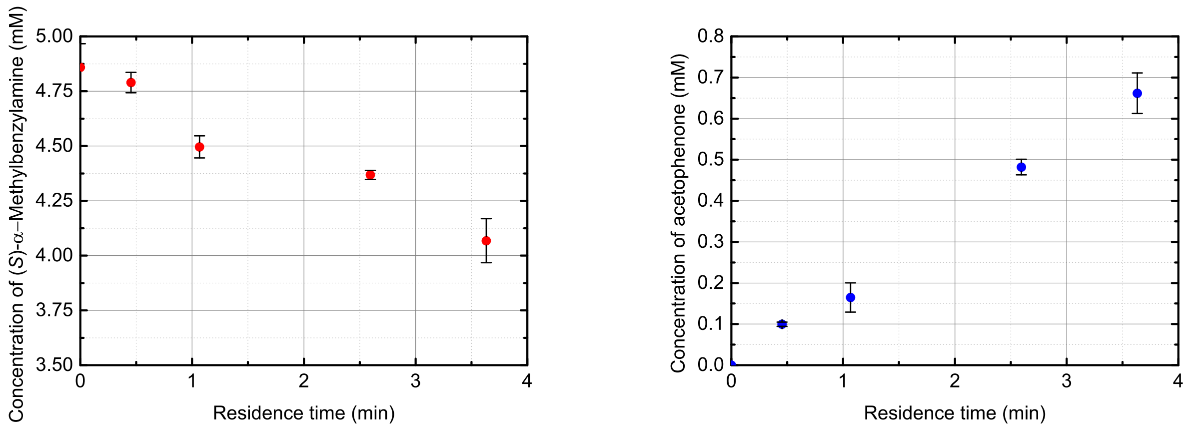

(a) Plot of the variation of concentration of α-Methylbenzylamine over time with initial reactant composition C.1.

(b) Plot of the variation of concentration of acetophenone over time with initial reactant composition C.1.

Figure D.9 *Plots of the variation of concentration of α-Methylbenzylamine and acetophenone over time with reactant composition C.1 in the microreactor.*

Table D.19 *Variation of concentration of* α*-Methylbenzylamine over time with initial reactant composition D.1 in the microreactor.*

Time (min)	c_{MBA} **(1) (mM)**	c_{MBA} **(2) (mM)**	c_{MBA} **(3) (mM)**	**Mean (mM)**	**SD (mM)**
0.000	9.123	9.326	9.151	9.200	0.110
0.454	8.208	8.852	9.125	8.728	0.471
1.067	9.283	9.048	9.340	9.224	0.155
2.595	9.033	8.911	8.918	8.954	0.069
3.632	8.830	8.684	8.648	8.721	0.097
Slope (mM/min)	0.024	-0.121	-0.146	-0.081	0.092
$\mathbf{R}^2$	0.008	0.581	0.712	0.255	

Table D.20 *Variation of concentration of acetophenone over time with initial reactant composition D.1 in the microreactor.*

Time (min)	c_{APH} **(1) (mM)**	c_{APH} **(2) (mM)**	c_{APH} **(3) (mM)**	**Mean (mM)**	**SD (mM)**
0.000	0.000	0.000	0.000	0.000	0.000
0.454	0.103	0.114	0.118	0.112	0.008
1.067	0.232	0.267	0.270	0.256	0.021
2.595	0.541	0.635	0.650	0.609	0.059
3.632	0.758	0.900	0.896	0.852	0.081
Slope (mM/min)	0.207	0.247	0.247	0.234	0.023
$\mathbf{R}^2$	1.000	1.000	1.000	1.000	

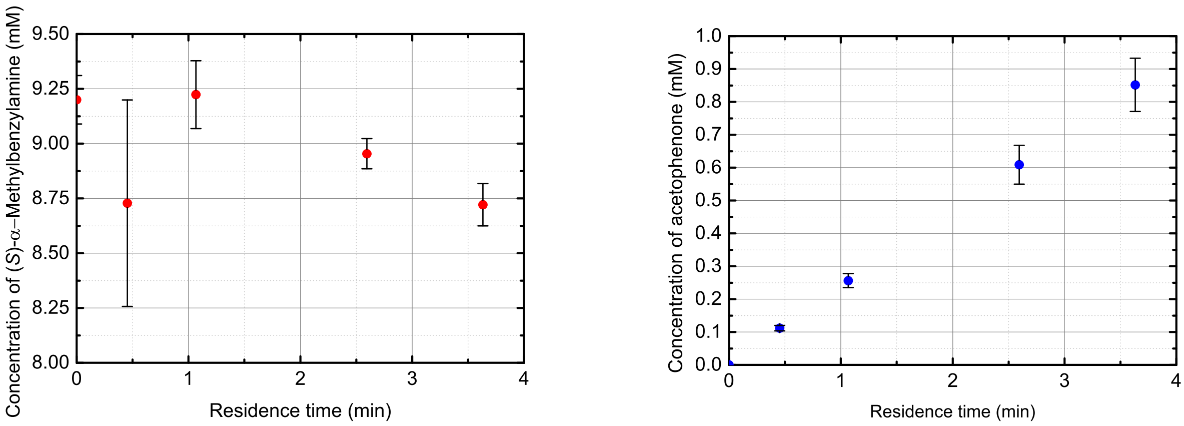

(a) Plot of the variation of concentration of α-Methylbenzylamine over time with initial reactant composition D.1.

(b) Plot of the variation of concentration of acetophenone over time with initial reactant composition D.1.

Figure D.10 *Plots of the variation of concentration of* α*-Methylbenzylamine and acetophenone over time with reactant composition D.1 in the microreactor.*

Table D.21 *Variation of concentration of α-Methylbenzylamine over time with initial reactant composition E.1 in the microreactor.*

Time (min)	c_{MBA} (1) (mM)	c_{MBA} (2) (mM)	c_{MBA} (3) (mM)	**Mean (mM)**	**SD (mM)**
0.000	60.927	61.055	60.840	60.941	0.108
0.454	59.778	59.350	59.164	59.431	0.315
1.067	59.292	59.333	61.165	59.930	1.070
2.595	60.511	60.251	58.092	59.618	1.328
3.632	59.317	58.591	58.680	58.863	0.396
Slope (mM/min)	-0.188	-0.353	-0.614	-0.385	0.215
R^2	0.153	0.319	0.479	0.583	

Table D.22 *Variation of concentration of acetophenone over time with initial reactant composition E.1 in the microreactor.*

Time (min)	c_{APH} (1) (mM)	c_{APH} (2) (mM)	c_{APH} (3) (mM)	**Mean (mM)**	**SD (mM)**
0.000	0.041	0.042	0.038	0.041	0.002
0.454	0.294	0.330	0.325	0.316	0.020
1.067	0.571	0.686	0.725	0.661	0.080
2.595	1.149	1.416	1.552	1.372	0.205
3.632	1.573	1.946	1.955	1.825	0.218
Slope (mM/min)	0.412	0.515	0.532	0.486	0.065
R^2	0.997	0.998	0.993	0.997	

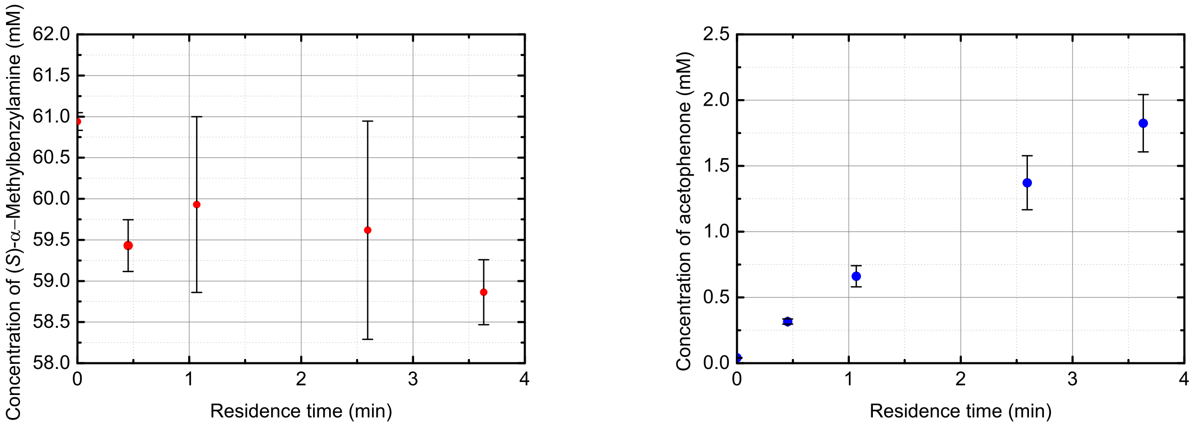

(a) Plot of the variation of concentration of α-Methylbenzylamine over time with initial reactant composition E.1.

(b) Plot of the variation of concentration of acetophenone over time with initial reactant composition E.1.

Figure D.11 *Plots of the variation of concentration of α-Methylbenzylamine and acetophenone over time with reactant composition E.1 in the microreactor.*

Table D.23 *Variation of concentration of α-Methylbenzylamine over time with initial reactant composition F.1 in the microreactor.*

Time (min)	c_{MBA} (1) (mM)	c_{MBA} (2) (mM)	c_{MBA} (3) (mM)	**Mean (mM)**	**SD (mM)**
0.000	n.a.	101.678	101.579	101.629	0.070
0.454	86.384	92.786	96.883	92.018	5.292
1.067	97.892	100.389	100.294	99.525	1.415
2.595	99.314	99.279	99.609	99.401	0.181
3.632	98.055	97.407	97.882	97.781	0.336
Slope (mM/min)	2.919	-0.112	-0.431	0.130	1.849
R^2	0.486	0.002	0.122	0.003	

Table D.24 *Variation of concentration of acetophenone over time with initial reactant composition F.1 in the microreactor.*

Time (min)	c_{APH} (1) (mM)	c_{APH} (2) (mM)	c_{APH} (3) (mM)	**Mean (mM)**	**SD (mM)**
0.000	n.a.	0.067	0.118	0.092	0.036
0.454	0.284	0.329	0.345	0.319	0.031
1.067	0.620	0.744	0.742	0.702	0.071
2.595	1.349	1.554	1.600	1.501	0.133
3.632	2.111	2.450	2.508	2.357	0.214
Slope (mM/min)	0.560	0.637	0.645	0.609	0.047
R^2	0.991	0.992	0.992	0.992	

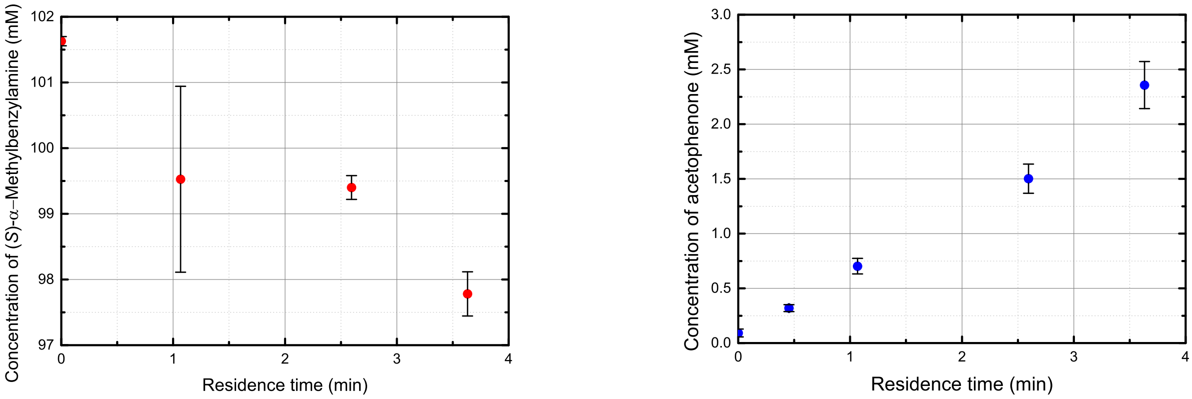

(a) Plot of the variation of concentration of α-Methylbenzylamine over time with initial reactant composition F.1.

(b) Plot of the variation of concentration of acetophenone over time with initial reactant composition F.1.

Figure D.12 *Plots of the variation of concentration of α-Methylbenzylamine and acetophenone over time with reactant composition F.1 in the microreactor.*

D.2 Constant $(S)-\alpha-$MBA concentration, variable pyruvic acid concentration

D.2.1 Batch system

Table D.25 *Variation of concentration of α-Methylbenzylamine over time with initial reactant composition L.1 in the batch system.*

Time (min)	c_{MBA} **(1) (mM)**	c_{MBA} **(2) (mM)**	c_{MBA} **(3) (mM)**	**Mean (mM)**	**SD (mM)**
0	37.944	38.572	39.410	38.642	0.736
1	37.132	37.077	37.537	37.249	0.251
2	37.111	37.255	37.675	37.347	0.293
4	37.054	37.044	36.805	36.968	0.141
6	37.228	36.824	37.663	37.238	0.420
10	36.525	36.542	38.094	37.054	0.901
Slope (mM/min)	-0.183	-0.302	-0.559	-0.348	0.192
R^2	0.544	0.502	0.748	0.598	

Table D.26 *Variation of concentration of acetophenone over time with initial reactant composition L.1 in the batch system.*

Time (min)	c_{APH} **(1) (mM)**	c_{APH} **(2) (mM)**	c_{APH} **(3) (mM)**	**Mean (mM)**	**SD (mM)**
0	0.027	0.028	0.029	0.028	0.001
1	0.136	0.126	0.132	0.132	0.005
2	0.218	0.219	0.231	0.222	0.007
4	0.376	0.381	0.380	0.379	0.003
6	0.543	0.538	0.532	0.537	0.005
10	0.816	0.818	0.802	0.812	0.008
Slope (mM/min)	0.086	0.088	0.087	0.087	0.001
R^2	0.994	0.998	0.993	0.995	

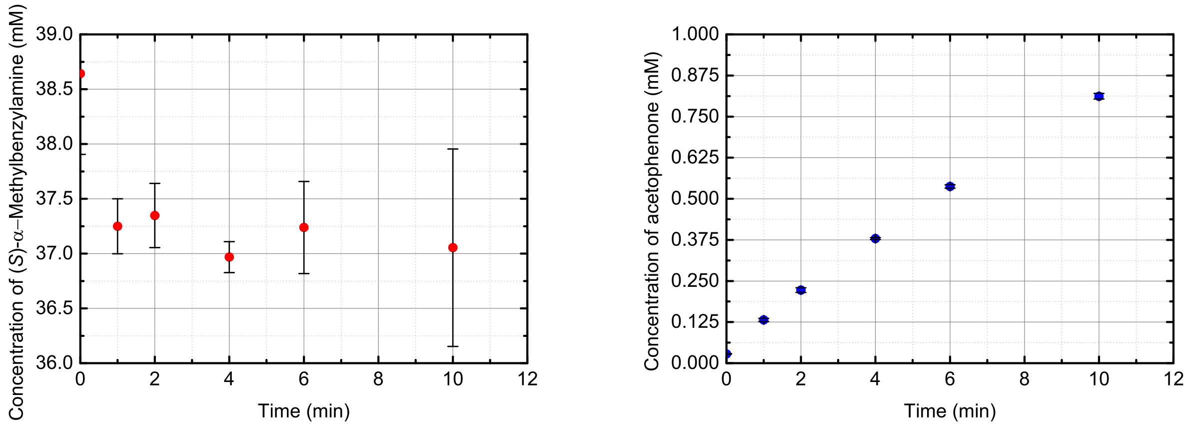

(a) Plot of the variation of concentration of α-Methylbenzylamine over time with initial reactant composition L.1.

(b) Plot of the variation of concentration of acetophenone over time with initial reactant composition L.1.

Figure D.13 *Plots of the variation of concentration of α-Methylbenzylamine and acetophenone over time with reactant composition L.1 in the batch system.*

Table D.27 *Variation of concentration of α-Methylbenzylamine over time with initial reactant composition M.1 in the batch system.*

Time (min)	c_{MBA} (1) (mM)	c_{MBA} (2) (mM)	c_{MBA} (3) (mM)	**Mean (mM)**	**SD (mM)**
0	40.554	40.342	41.037	40.644	0.357
1	38.563	39.880	39.830	39.424	0.746
2	38.075	36.878	39.721	38.224	1.427
4	38.845	38.794	39.226	38.955	0.236
6	38.015	39.048	38.657	38.573	0.522
10	38.108	38.848	38.120	38.359	0.424
Slope (mM/min)	-0.340	-0.457	-0.400	-0.399	0.059
R^2	0.290	0.257	0.789	0.450	

Table D.28 *Variation of concentration of acetophenone over time with initial reactant composition M.1 in the batch system.*

Time (min)	c_{APH} (1) (mM)	c_{APH} (2) (mM)	c_{APH} (3) (mM)	**Mean (mM)**	**SD (mM)**
0	0.030	0.030	0.033	0.031	0.002
1	0.163	0.161	0.159	0.161	0.002
2	0.260	0.246	0.270	0.258	0.012
4	0.473	0.458	0.469	0.467	0.008
6	0.670	0.689	0.662	0.674	0.014
10	1.064	1.044	1.024	1.044	0.020
Slope (mM/min)	0.109	0.105	0.108	0.107	0.002
R^2	0.997	0.996	0.997	0.997	

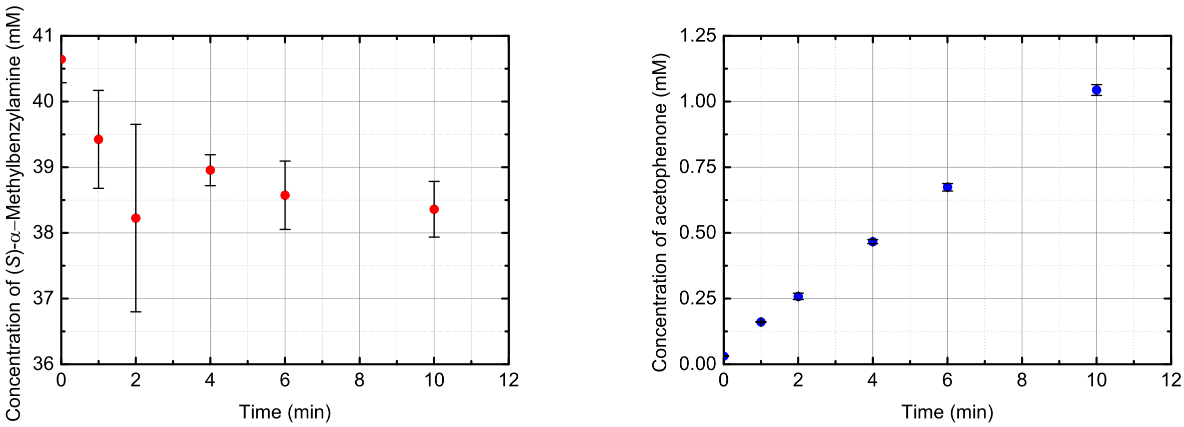

(a) Plot of the variation of concentration of α-Methylbenzylamine over time with initial reactant composition M.1.

(b) Plot of the variation of concentration of acetophenone over time with initial reactant composition M.1.

Figure D.14 *Plots of the variation of concentration of α-Methylbenzylamine and acetophenone over time with reactant composition M.1 in the batch system.*

Table D.29 *Variation of concentration of α-Methylbenzylamine over time with initial reactant composition N.1 in the batch system.*

Time (min)	c_{MBA} (1) (**mM**)	c_{MBA} (2) (**mM**)	c_{MBA} (3) (**mM**)	**Mean** (**mM**)	**SD** (**mM**)
0	39.695	39.166	41.141	40.001	1.022
1	38.567	38.911	38.024	38.501	0.447
2	38.613	38.287	38.118	38.339	0.251
4	38.267	37.851	38.121	38.080	0.211
6	38.286	37.127	37.826	37.746	0.583
10	37.772	37.430	37.614	37.605	0.171
Slope (mM/min)	-0.301	-0.342	-0.596	-0.413	0.160
R^2	0.677	0.955	0.444	0.692	

Table D.30 *Variation of concentration of acetophenone over time with initial reactant composition N.1 in the batch system.*

Time (min)	c_{APH} (1) (**mM**)	c_{APH} (2) (**mM**)	c_{APH} (3) (**mM**)	**Mean** (**mM**)	**SD** (**mM**)
0	0.028	0.028	0.030	0.029	0.001
1	0.151	0.162	0.155	0.156	0.006
2	0.271	0.271	0.271	0.271	0.000
4	0.477	0.483	0.479	0.480	0.003
6	0.683	0.683	0.686	0.684	0.002
10	1.067	1.069	1.064	1.066	0.003
Slope (mM/min)	0.112	0.112	0.112	0.112	0.000
R^2	0.998	0.997	0.998	0.998	

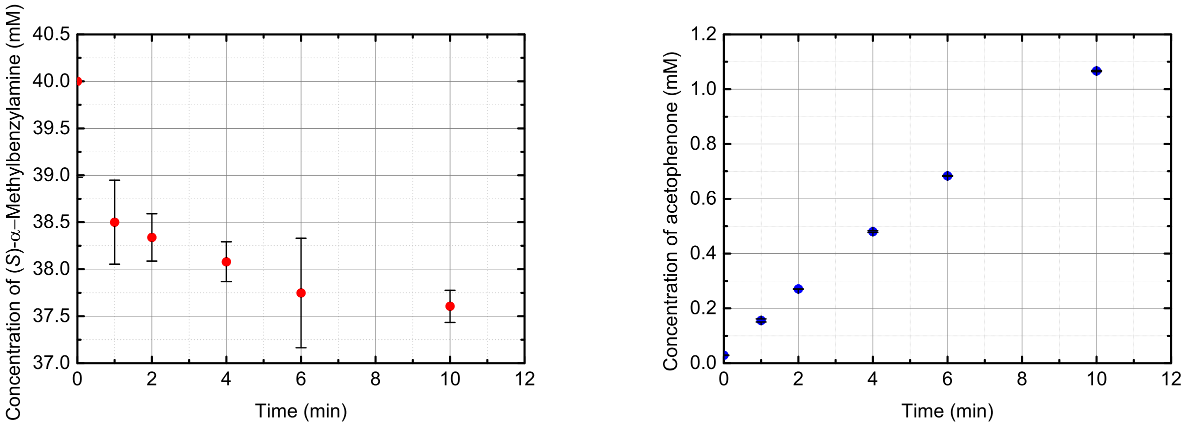

(a) Plot of the variation of concentration of α-Methylbenzylamine over time with initial reactant composition N.1.

(b) Plot of the variation of concentration of acetophenone over time with initial reactant composition N.1.

Figure D.15 *Plots of the variation of concentration of α-Methylbenzylamine and acetophenone over time with reactant composition N.1 in the batch system.*

Table D.31 *Variation of concentration of α-Methylbenzylamine over time with initial reactant composition O.1 in the batch system.*

Time (min)	c_{MBA} (1) (mM)	c_{MBA} (2) (mM)	c_{MBA} (3) (mM)	**Mean (mM)**	**SD (mM)**
0	38.554	37.655	39.271	38.493	0.810
1	35.753	36.501	36.184	36.146	0.375
2	35.814	36.637	36.142	36.198	0.414
4	35.300	36.280	35.651	35.744	0.496
6	35.146	35.809	35.223	35.393	0.362
10	34.132	35.077	35.035	34.748	0.534
Slope (mM/min)	-0.497	-0.284	-0.756	-0.512	0.236
R^2	0.524	0.633	0.607	0.588	

Table D.32 *Variation of concentration of acetophenone over time with initial reactant composition O.1 in the batch system.*

Time (min)	c_{APH} (1) (mM)	c_{APH} (2) (mM)	c_{APH} (3) (mM)	**Mean (mM)**	**SD (mM)**
0	0.020	0.023	0.024	0.022	0.002
1	0.181	0.172	0.176	0.177	0.005
2	0.336	0.326	0.333	0.331	0.005
4	0.749	0.606	0.637	0.664	0.075
6	0.917	0.919	0.913	0.916	0.003
10	1.455	1.481	1.493	1.476	0.019
Slope (mM/min)	0.145	0.146	0.153	0.148	0.005
R^2	0.999	1.000	1.000	0.999	

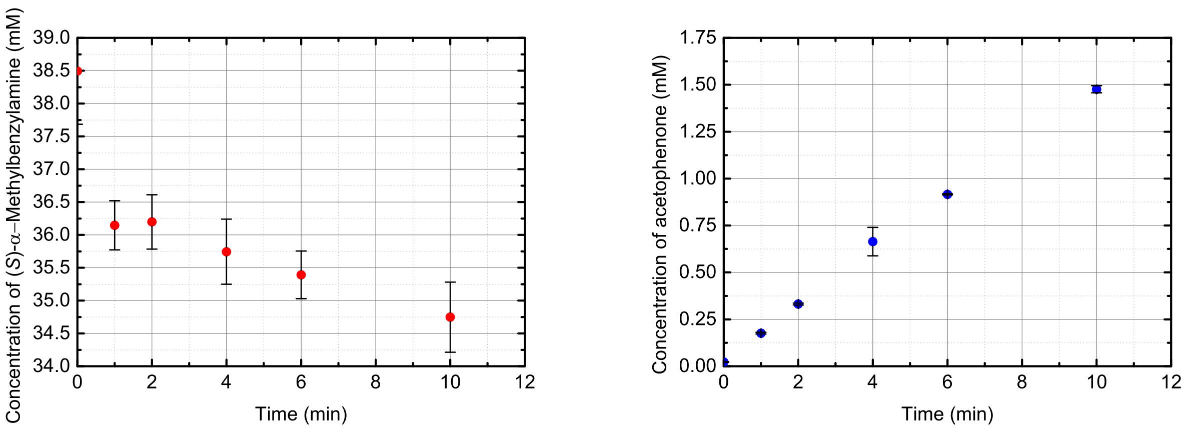

(a) Plot of the variation of concentration of α-Methylbenzylamine over time with initial reactant composition O.1.

(b) Plot of the variation of concentration of acetophenone over time with initial reactant composition O.1.

Figure D.16 *Plots of the variation of concentration of α-Methylbenzylamine and acetophenone over time with reactant composition O.1 in the batch system.*

Table D.33 *Variation of concentration of α-Methylbenzylamine over time with initial reactant composition P.1 in the batch system.*

Time (min)	c_{MBA} **(1) (mM)**	c_{MBA} **(2) (mM)**	c_{MBA} **(3) (mM)**	**Mean (mM)**	**SD (mM)**
0	37.486	38.464	38.575	38.175	0.599
1	35.858	35.572	36.501	35.977	0.476
2	35.599	35.887	36.360	35.949	0.384
4	35.330	35.060	36.177	35.522	0.583
6	0.267	34.908	36.133	23.769	20.363
10	34.257	34.301	34.518	34.359	0.140
Slope (mM/min)	-0.469	-0.701	-0.502	-0.557	0.126
R^2	0.682	0.622	0.584	0.629	

Table D.34 *Variation of concentration of acetophenone over time with initial reactant composition P.1 in the batch system.*

Time (min)	c_{APH} **(1) (mM)**	c_{APH} **(2) (mM)**	c_{APH} **(3) (mM)**	**Mean (mM)**	**SD (mM)**
0	0.018	0.026	0.025	0.023	0.004
1	0.174	0.185	0.171	0.177	0.008
2	0.316	0.328	0.313	0.319	0.008
4	0.608	0.628	0.582	0.606	0.023
6	0.007	0.901	0.884	0.597	0.512
10	1.485	1.470	1.417	1.457	0.036
Slope (mM/min)	0.147	0.150	0.139	0.145	0.006
R^2	1.000	1.000	1.000	1.000	

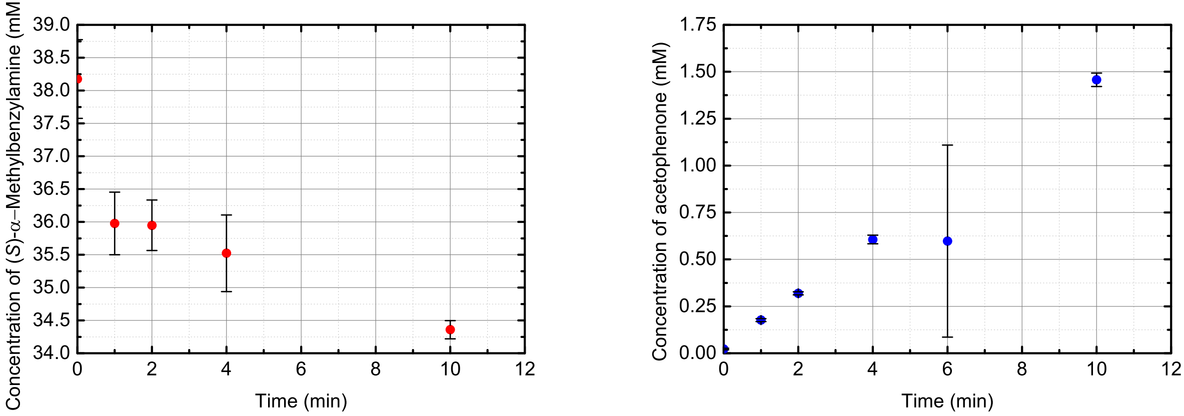

(a) Plot of the variation of concentration of α-Methylbenzylamine over time with initial reactant composition P.1.

(b) Plot of the variation of concentration of acetophenone over time with initial reactant composition P.1.

Figure D.17 *Plots of the variation of concentration of α-Methylbenzylamine and acetophenone over time with reactant composition P.1 in the batch system.*

Table D.35 *Variation of concentration of α-Methylbenzylamine over time with initial reactant composition Q.1 in the batch system.*

Time (min)	c_{MBA} (1) (mM)	c_{MBA} (2) (mM)	c_{MBA} (3) (mM)	**Mean (mM)**	**SD (mM)**
0	35.069	36.653	35.711	35.811	0.797
1	34.480	33.768	33.683	33.977	0.437
2	34.179	34.033	33.494	33.902	0.361
4	33.734	33.766	32.921	33.474	0.479
6	33.123	33.252	32.856	33.077	0.202
10	32.962	32.264	32.344	32.523	0.382
Slope (mM/min)	-0.318	-0.570	-0.607	-0.498	0.157
R^2	0.941	0.480	0.726	0.716	

Table D.36 *Variation of concentration of acetophenone over time with initial reactant composition Q.1 in the batch system.*

Time (min)	c_{APH} (1) (mM)	c_{APH} (2) (mM)	c_{APH} (3) (mM)	**Mean (mM)**	**SD (mM)**
0	0.017	0.027	0.027	0.024	0.005
1	0.154	0.158	0.163	0.159	0.005
2	0.276	0.274	0.291	0.280	0.009
4	0.512	0.543	0.552	0.536	0.021
6	0.786	0.781	0.800	0.789	0.010
10	1.297	1.300	1.263	1.287	0.021
Slope (mM/min)	0.123	0.128	0.131	0.127	0.004
R^2	0.999	0.999	1.000	0.999	

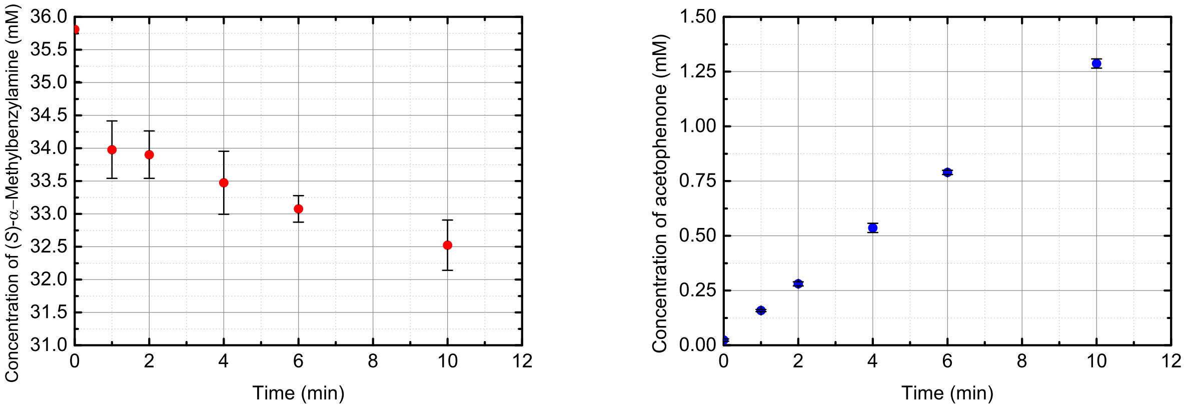

(a) Plot of the variation of concentration of α-Methylbenzylamine over time with initial reactant composition Q.1.

(b) Plot of the variation of concentration of acetophenone over time with initial reactant composition Q.1.

Figure D.18 *Plots of the variation of concentration of α-Methylbenzylamine and acetophenone over time with reactant composition Q.1 in the batch system.*

D.2.2 Microreactor

Table D.37 *Variation of concentration of α-Methylbenzylamine over time with initial reactant composition L.1 in the microreactor.*

Time (min)	$\mathbf{c_{MBA}}$ (1) (**mM**)	$\mathbf{c_{MBA}}$ (2) (**mM**)	$\mathbf{c_{MBA}}$ (3) (**mM**)	**Mean** (**mM**)	**SD** (**mM**)
0.000	38.800	40.266	41.231	40.099	1.224
0.454	40.022	40.298	40.535	40.285	0.256
1.067	39.094	39.630	40.315	39.680	0.612
2.595	40.122	39.873	39.832	39.942	0.157
3.632	27.112	39.299	38.951	35.121	6.938
Slope (mM/min)	0.359	-0.171	-0.475	-0.096	0.422
R^2	0.376	0.362	0.855	0.179	

Table D.38 *Variation of concentration of acetophenone over time with initial reactant composition L.1 in the microreactor.*

Time (min)	$\mathbf{c_{APH}}$ (1) (**mM**)	$\mathbf{c_{APH}}$ (2) (**mM**)	$\mathbf{c_{APH}}$ (3) (**mM**)	**Mean** (**mM**)	**SD** (**mM**)
0.000	0.034	0.031	0.031	0.032	0.002
0.454	0.119	0.134	0.135	0.129	0.009
1.067	0.213	0.249	0.259	0.240	0.024
2.595	0.416	0.493	0.507	0.472	0.049
3.632	0.265	0.474	0.561	0.433	0.152
Slope (mM/min)	0.145	0.175	0.181	0.167	0.019
R^2	0.995	0.995	0.994	0.995	

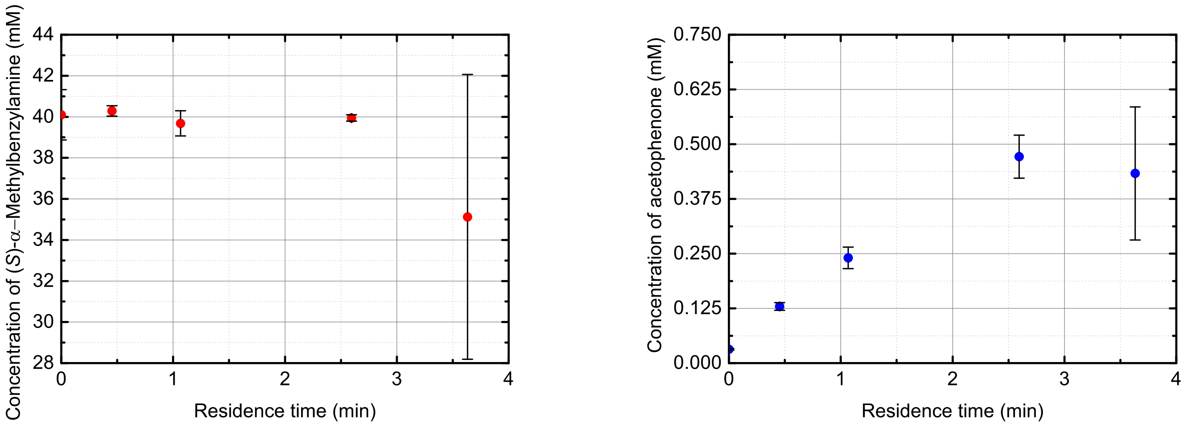

(a) Plot of the variation of concentration of α-Methylbenzylamine over time with initial reactant composition L.1.

(b) Plot of the variation of concentration of acetophenone over time with initial reactant composition L.1.

Figure D.19 *Plots of the variation of concentration of α-Methylbenzylamine and acetophenone over time with reactant composition L.1 in the microreactor.*

Table D.39 *Variation of concentration of α-Methylbenzylamine over time with initial reactant composition M.1 in the microreactor.*

Time (min)	c_{MBA} **(1) (mM)**	c_{MBA} **(2) (mM)**	c_{MBA} **(3) (mM)**	**Mean (mM)**	**SD (mM)**
0.000	41.461	41.053	41.909	41.474	0.428
0.454	39.995	40.848	40.700	40.514	0.456
1.067	40.308	41.337	40.825	40.823	0.514
2.595	40.804	40.213	40.461	40.493	0.297
3.632	29.783	34.549	37.333	33.888	3.818
Slope (mM/min)	-0.060	-0.309	-0.420	-0.263	0.184
R^2	0.011	0.536	0.549	0.422	

Table D.40 *Variation of concentration of acetophenone over time with initial reactant composition M.1 in the microreactor.*

Time (min)	c_{APH} **(1) (mM)**	c_{APH} **(2) (mM)**	c_{APH} **(3) (mM)**	**Mean (mM)**	**SD (mM)**
0.000	0.029	0.030	0.029	0.029	0.001
0.454	0.167	0.192	0.193	0.184	0.014
1.067	0.291	0.351	0.356	0.333	0.036
2.595	0.523	0.639	0.669	0.610	0.077
3.632	0.279	0.422	0.560	0.420	0.141
Slope (mM/min)	0.183	0.227	0.240	0.217	0.030
R^2	0.978	0.981	0.986	0.981	

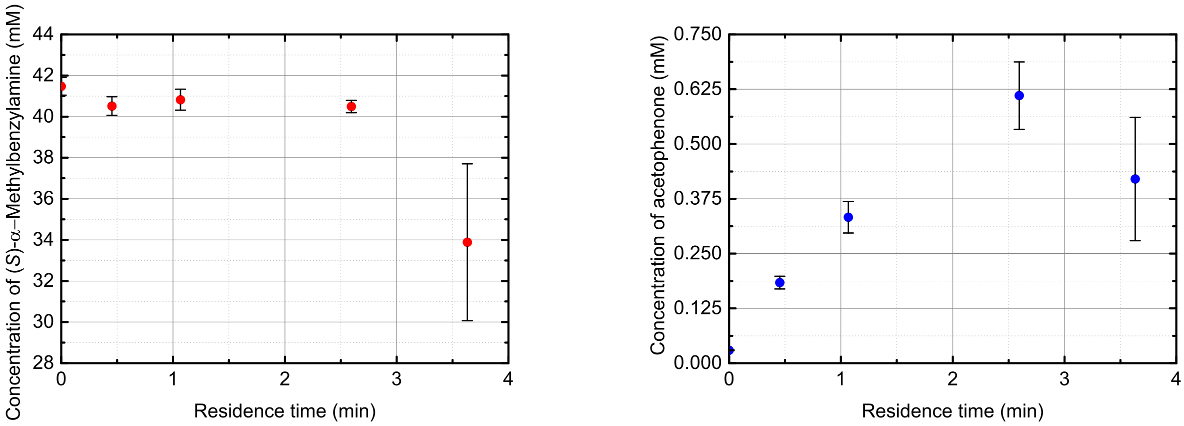

(a) Plot of the variation of concentration of α-Methylbenzylamine over time with initial reactant composition M.1.

(b) Plot of the variation of concentration of acetophenone over time with initial reactant composition M.1

Figure D.20 *Plots of the variation of concentration of α-Methylbenzylamine and acetophenone over time with reactant composition M.1 in the microreactor.*

Table D.41 *Variation of concentration of α-Methylbenzylamine over time with initial reactant composition N.1 in the microreactor.*

Time (min)	c_{MBA} (1) (mM)	c_{MBA} (2) (mM)	c_{MBA} (3) (mM)	**Mean (mM)**	**SD (mM)**
0.000	41.203	41.673	41.889	41.588	0.350
0.454	40.165	40.638	40.946	40.583	0.393
1.067	40.910	40.934	40.478	40.774	0.257
2.595	38.866	38.583	39.281	38.910	0.351
3.632	40.434	40.405	40.289	40.376	0.077
Slope (mM/min)	-0.299	-0.473	-0.469	-0.413	0.099
R^2	0.252	0.394	0.562	0.417	

Table D.42 *Variation of concentration of acetophenone over time with initial reactant composition N.1 in the microreactor.*

Time (min)	c_{APH} (1) (mM)	c_{APH} (2) (mM)	c_{APH} (3) (mM)	**Mean (mM)**	**SD (mM)**
0.000	0.029	0.033	0.034	0.032	0.003
0.454	0.177	0.201	0.204	0.194	0.015
1.067	0.387	0.461	0.456	0.435	0.042
2.595	0.887	1.055	1.079	1.007	0.104
3.632	1.179	1.430	1.431	1.347	0.145
Slope (mM/min)	0.319	0.387	0.390	0.365	0.040
R^2	0.999	1.000	0.999	0.999	

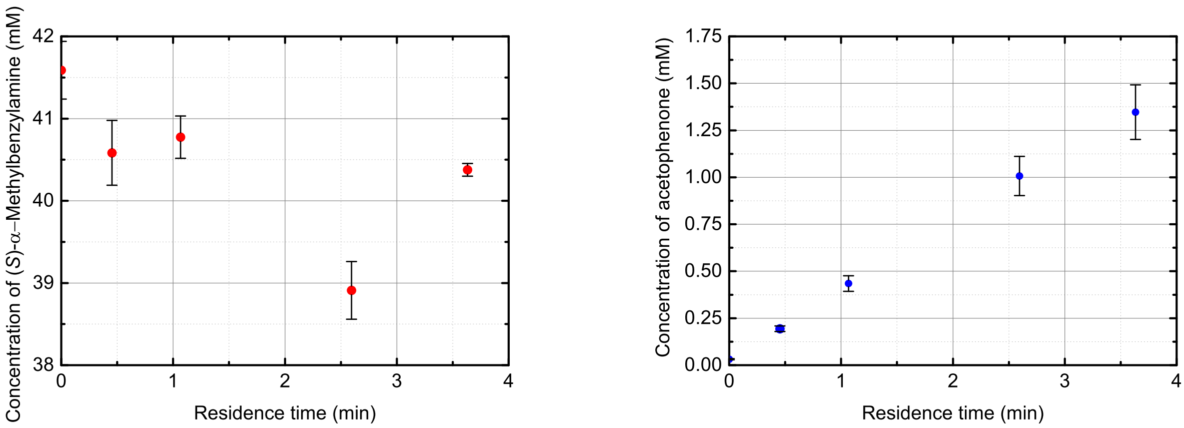

(a) Plot of the variation of concentration of α-Methylbenzylamine over time with initial reactant composition N.1.

(b) Plot of the variation of concentration of acetophenone over time with initial reactant composition N.1.

Figure D.21 *Plots of the variation of concentration of α-Methylbenzylamine and acetophenone over time with reactant composition N.1 in the microreactor.*

Table D.43 *Variation of concentration of α-Methylbenzylamine over time with initial reactant composition O.1 in the microreactor.*

Time (min)	c_{MBA} (1) (mM)	c_{MBA} (2) (mM)	c_{MBA} (3) (mM)	**Mean (mM)**	**SD (mM)**
0.000	39.823	39.995	39.933	39.917	0.088
0.454	39.095	38.656	39.509	39.087	0.427
1.067	39.012	38.596	38.620	38.743	0.234
2.595	38.193	37.463	37.558	37.738	0.397
3.632	28.266	32.916	35.947	32.377	3.869
Slope (mM/min)	-2.653	-1.646	-1.045	-1.781	0.812
R^2	0.694	0.843	0.981	0.812	

Table D.44 *Variation of concentration of acetophenone over time with initial reactant composition O.1 in the microreactor.*

Time (min)	c_{APH} (1) (mM)	c_{APH} (2) (mM)	c_{APH} (3) (mM)	**Mean (mM)**	**SD (mM)**
0.000	0.021	0.025	0.027	0.024	0.003
0.454	0.284	0.326	0.332	0.314	0.026
1.067	0.583	0.683	0.690	0.652	0.060
2.595	1.214	1.501	1.525	1.413	0.173
3.632	1.266	1.697	1.905	1.623	0.326
Slope (mM/min)	0.354	0.473	0.521	0.449	0.086
R^2	0.945	0.974	0.993	0.977	

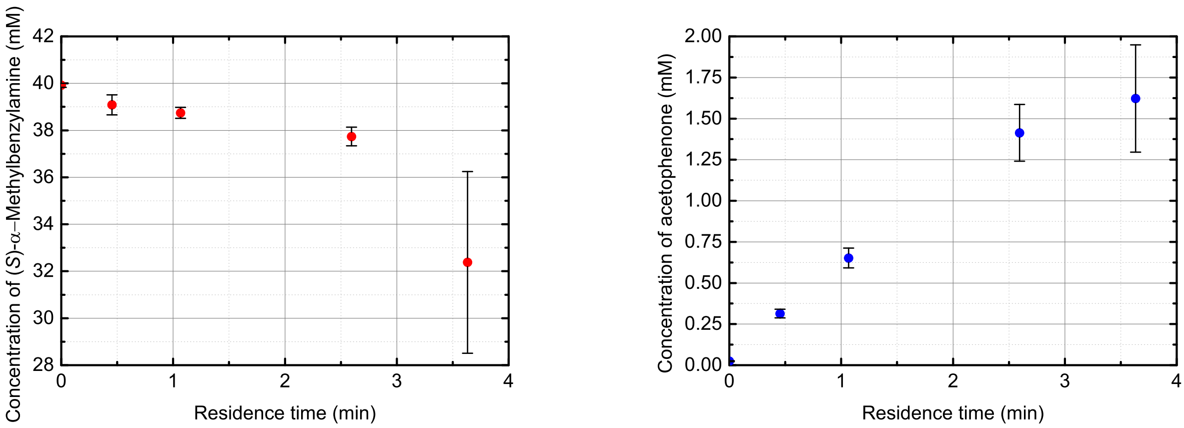

(a) Plot of the variation of concentration of α-Methylbenzylamine over time with initial reactant composition O.1.

(b) Plot of the variation of concentration of acetophenone over time with initial reactant composition O.1.

Figure D.22 *Plots of the variation of concentration of α-Methylbenzylamine and acetophenone over time with reactant composition O.1 in the microreactor.*

Table D.45 *Variation of concentration of α-Methylbenzylamine over time with initial reactant composition P.1 in the microreactor.*

Time (min)	c_{MBA} (1) (mM)	c_{MBA} (2) (mM)	c_{MBA} (3) (mM)	**Mean (mM)**	**SD (mM)**
0.000	37.895	39.318	40.422	39.212	1.267
0.454	36.925	37.779	37.807	37.504	0.501
1.067	38.367	37.850	37.795	38.004	0.315
2.595	37.657	37.220	37.277	37.385	0.238
3.632	38.283	37.070	37.025	37.459	0.714
Slope (mM/min)	0.150	-0.484	-0.673	-0.335	0.431
R^2	0.156	0.685	0.566	0.443	

Table D.46 *Variation of concentration of acetophenone over time with initial reactant composition P.1 in the microreactor.*

Time (min)	c_{APH} (1) (mM)	c_{APH} (2) (mM)	c_{APH} (3) (mM)	**Mean (mM)**	**SD (mM)**
0.000	0.022	0.021	0.032	0.025	0.006
0.454	0.285	0.319	0.322	0.309	0.021
1.067	0.637	0.736	0.739	0.704	0.058
2.595	1.523	1.832	1.815	1.723	0.174
3.632	2.049	2.491	2.490	2.344	0.255
Slope (mM/min)	0.562	0.687	0.683	0.644	0.071
R^2	0.999	1.000	1.000	1.000	

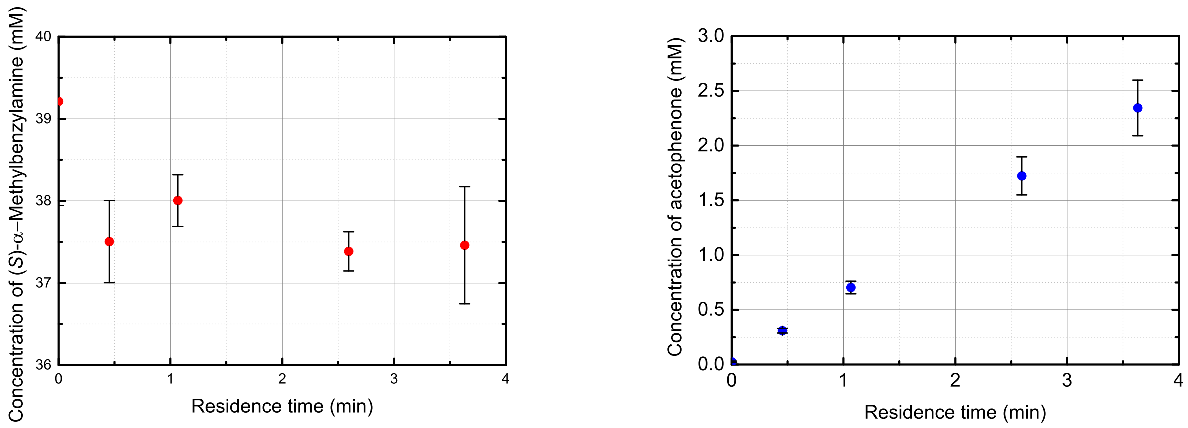

(a) Plot of the variation of concentration of α-Methylbenzylamine over time with initial reactant composition P.1.

(b) Plot of the variation of concentration of acetophenone over time with initial reactant composition P.1.

Figure D.23 *Plots of the variation of concentration of α-Methylbenzylamine and acetophenone over time with reactant composition P.1 in the microreactor.*

Table D.47 *Variation of concentration of α-Methylbenzylamine over time with initial reactant composition Q.1 in the microreactor.*

Time (min)	c_{MBA} (1) (mM)	c_{MBA} (2) (mM)	c_{MBA} (3) (mM)	**Mean (mM)**	**SD (mM)**
0.000	38.142	38.633	37.226	38.000	0.714
0.454	37.778	37.064	37.733	37.525	0.400
1.067	37.490	37.336	36.777	37.201	0.375
2.595	36.523	36.103	35.966	36.197	0.290
3.632	35.758	35.049	35.159	35.322	0.382
Slope (mM/min)	-0.642	-0.838	-0.643	-0.708	0.113
R^2	0.997	0.896	0.917	0.995	

Table D.48 *Variation of concentration of acetophenone over time with initial reactant composition Q.1 in the microreactor.*

Time (min)	c_{APH} (1) (mM)	c_{APH} (2) (mM)	c_{APH} (3) (mM)	**Mean (mM)**	**SD (mM)**
0.000	0.027	0.027	0.027	0.027	0.000
0.454	0.290	0.330	0.321	0.314	0.021
1.067	0.617	0.719	0.724	0.687	0.061
2.595	1.400	1.720	1.730	1.617	0.188
3.632	1.934	2.407	2.345	2.229	0.257
Slope (mM/min)	0.522	0.654	0.642	0.606	0.073
R^2	1.000	1.000	1.000	1.000	

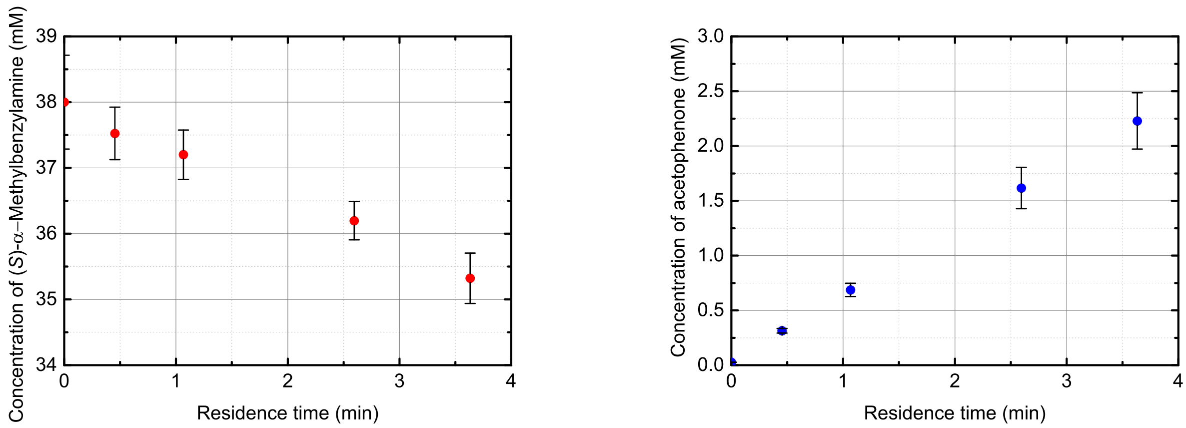

(a) Plot of the variation of concentration of α-Methylbenzylamine over time with initial reactant composition Q.1.

(b) Plot of the variation of concentration of acetophenone over time with initial reactant composition Q.1.

Figure D.24 *Plots of the variation of concentration of α-Methylbenzylamine and acetophenone over time with reactant composition Q.1 in the microreactor.*

Appendix E

Test of adsorption model

In this Appendix the simple model used for the test of the kinetic model in the CFD simulations is described. The geometry, the conditions for the simulation and the results of the simulations with different parameters in the adsorption model are presented.

E.1 Geometry and mesh

The channel has a length of 100 mm, width of 0.2 mm and height of 0.1 mm. The SA:V of this geometry is 30 mm^{-1}. The mesh contains 160,000 elements; the mesh is not uniform because it has smaller elements close to the walls (Figure E.1).

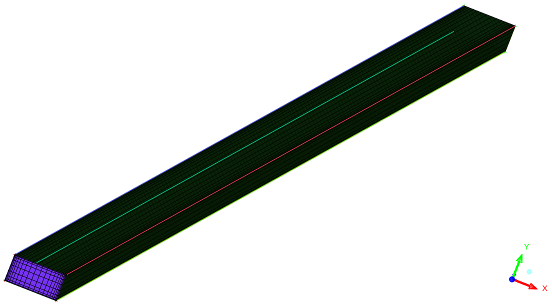

Figure E.1 *Geometry of the channel used for the testing the adsorption model.*

E.2 Boundary conditions

The inlet mass flow rate is $1.994 \cdot 10^{-6}$ $\mathrm{kg \cdot s^{-1}}$ with composition 0.05 $\mathrm{g \cdot l^{-1}}$ of GOx, 50 $\mathrm{g \cdot l^{-1}}$ of GLU and 0.258 mM of O_2. The kinetic model, its parameters and the adsorption model are the same as in § 3.2.9.3 on page 58.

E.3 Without adsorption

Variable	**Value**
$< c_{O_2} >= \frac{\int_{\bar{A}} c_{O_2} dA}{\int_{\bar{A}} dA}$ (at 50 s)	0.2266 mM
$< c_{O_2} >$ vs. time	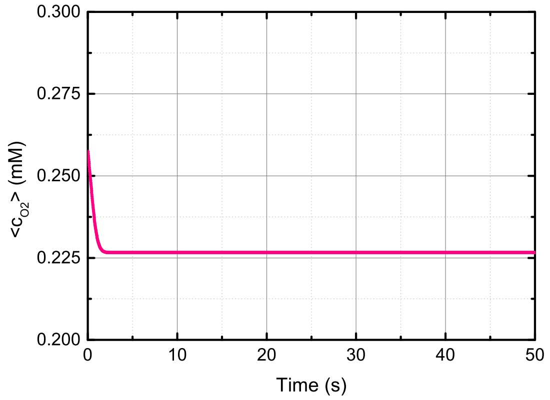

E.4 With adsorption

In Table E.1 the results of the CFD simulations in the geometry in Figure E.1 are summarized. The adsorption model is as in the set of equations from equation (3.4) to equation (3.7). The results of each set of parameters are presented after the Table in the same Section.

Table E.1 *Summary of the results of some combinations of parameters.*

Parameter set	$\mathbf{k_{ads}}$	$\mathbf{k_{des}}$	$\mathbf{c^*}$	$< \mathbf{c_{O_2}} >$ **(at 50 s)**	$< \mathbf{c_E^*} >$ **(at 50 s)**
	$\left(m^5 \cdot kg^{-1} \cdot s^{-1}\right)$	$\left(kg \cdot s^{-1}\right)$	$\left(kg \cdot m^{-2}\right)$	**(mM)**	$\left(kg \cdot m^{-2}\right)$
0	-	-	-	0.2266	0
1	$1 \cdot 10^{-8}$	$1 \cdot 10^{-12}$	$5 \cdot 10^{-3}$	0.0362	$3.9799 \cdot 10^{-5}$
2	$1 \cdot 10^{-4}$	$1 \cdot 10^{-5}$	$5 \cdot 10^{-7}$	0.2199	$1.6665 \cdot 10^{-7}$
3	$1 \cdot 10^{-4}$	$1 \cdot 10^{-5}$	$5 \cdot 10^{-6}$	0.1699	$1.6661 \cdot 10^{-6}$
4	$1 \cdot 10^{-8}$	$1 \cdot 10^{-12}$	$5 \cdot 10^{-5}$	0.2061	$5.5059 \cdot 10^{-7}$
5	$1 \cdot 10^{-8}$	$1 \cdot 10^{-10}$	$5 \cdot 10^{-3}$	0.0362	$3.9766 \cdot 10^{-5}$
6	$1 \cdot 10^{-8}$	$1 \cdot 10^{-12}$	$5 \cdot 10^{-7}$	0.2264	$5.5275 \cdot 10^{-9}$

E.4.1 Parameter set 1

Parameter	**Value**
k_{ads}	$1 \cdot 10^{-8}\ \mathrm{m^5 \cdot kg^{-1} \cdot s^{-1}}$
k_{des}	$1 \cdot 10^{-12}\ \mathrm{kg \cdot s^{-1}}$
c^*	$5 \cdot 10^{-3}\ \mathrm{kg \cdot m^{-2}}$

Variable	**Value**
$< c_E^* >= \dfrac{\int_{\bar{S}} c_{E^*}\, dS}{\int_{\bar{S}} dS}$ (at 50 s)	$3.9799 \cdot 10^{-5}\ \mathrm{kg \cdot m^{-2}}$
$< c_{O_2} >= \dfrac{\int_{\bar{A}} c_{O_2}\, dA}{\int_{\bar{A}} dA}$ (at 50 s)	0.0362 mM
$< c_E^* >$ vs. time	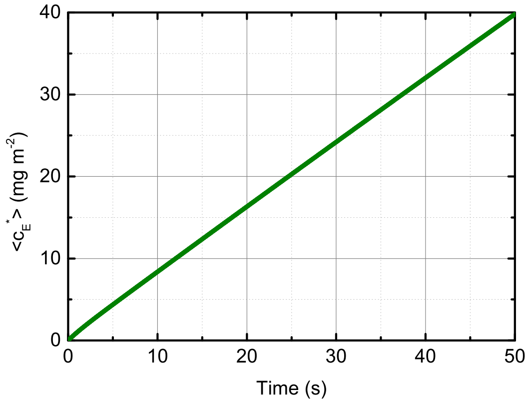
$< c_{O_2} >$ vs. time	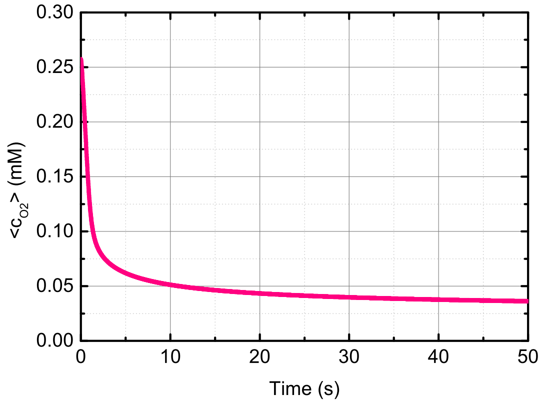

E.4.2 Parameter set 2

Parameter	**Value**
k_{ads}	$1 \cdot 10^{-4}\ \mathrm{m^5 \cdot kg^{-1} \cdot s^{-1}}$
k_{des}	$1 \cdot 10^{-5}\ \mathrm{kg \cdot s^{-1}}$
c^*	$5 \cdot 10^{-7}\ \mathrm{kg \cdot m^{-2}}$

Variable	**Value**
$< c_E^* >= \dfrac{\int_{\bar{S}} c_{E^*}\, dS}{\int_{\bar{S}} dS}$ (at 50 s)	$1.6665 \cdot 10^{-7}\ \mathrm{kg \cdot m^{-2}}$
$< c_{O_2} >= \dfrac{\int_{\bar{A}} c_{O_2}\, dA}{\int_{\bar{A}} dA}$ (at 50 s)	0.2199 mM

$< c_E^* >$ vs. time

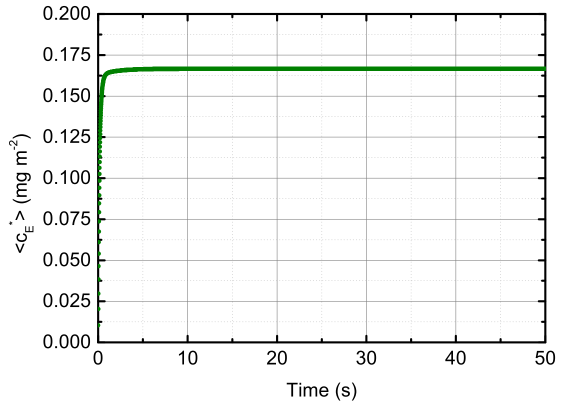

$< c_{O_2} >$ vs. time

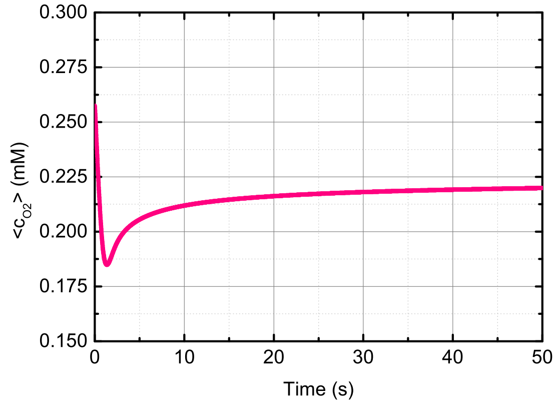

E.4.3 Parameter set 3

Parameter	**Value**
k_{ads}	$1 \cdot 10^{-4}\ \mathrm{m}^5 \cdot \mathrm{kg}^{-1} \cdot \mathrm{s}^{-1}$
k_{des}	$1 \cdot 10^{-5}\ \mathrm{kg} \cdot \mathrm{s}^{-1}$
c^*	$5 \cdot 10^{-6}\ \mathrm{kg} \cdot \mathrm{m}^{-2}$

Variable	**Value**
$< c_{\mathrm{E}}^* > = \dfrac{\int_{\bar{S}} c_{\mathrm{E}^*}\, dS}{\int_{\bar{S}} dS}$ (at 50 s)	$1.6661 \cdot 10^{-6}\ \mathrm{kg} \cdot \mathrm{m}^{-2}$
$< c_{\mathrm{O}_2} > = \dfrac{\int_{\bar{A}} c_{\mathrm{O}_2}\, dA}{\int_{\bar{A}} dA}$ (at 50 s)	0.1699 mM
$< c_{\mathrm{E}}^* >$ vs. time	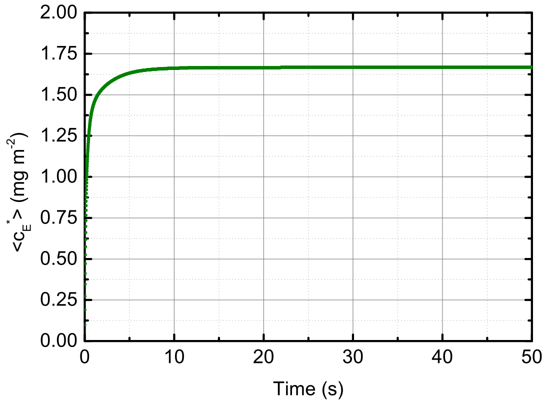
$< c_{\mathrm{O}_2} >$ vs. time	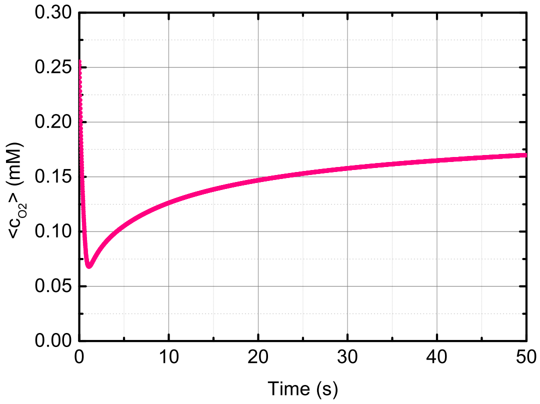

E.4.4 Parameter set 4

Parameter	**Value**
k_{ads}	$1 \cdot 10^{-8}\ \mathrm{m}^5 \cdot \mathrm{kg}^{-1} \cdot \mathrm{s}^{-1}$
k_{des}	$1 \cdot 10^{-12}\ \mathrm{kg} \cdot \mathrm{s}^{-1}$
c^*	$5 \cdot 10^{-5}\ \mathrm{kg} \cdot \mathrm{m}^{-2}$

Variable	**Value**
$< c_E^* > = \dfrac{\int_{\bar{S}} c_{E^*}\, dS}{\int_{\bar{S}} dS}$ (at 50 s)	$5.5059 \cdot 10^{-7}\ \mathrm{kg} \cdot \mathrm{m}^{-2}$
$< c_{O_2} > = \dfrac{\int_{\bar{A}} c_{O_2}\, dA}{\int_{\bar{A}} dA}$ (at 50 s)	0.2061 mM
$< c_E^* >$ vs. time	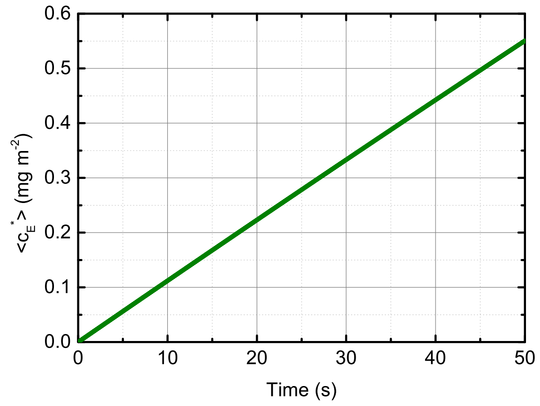
$< c_{O_2} >$ vs. time	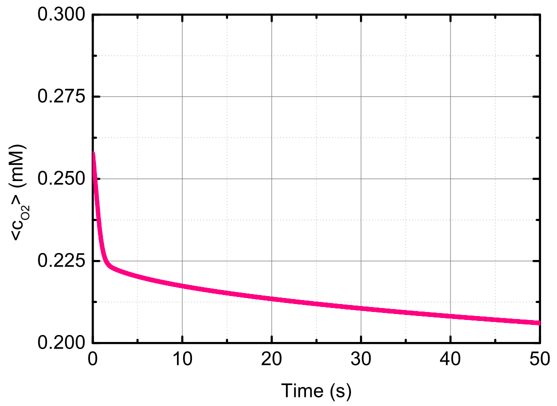

E.4.5 Parameter set 5

Parameter	**Value**
k_{ads}	$1 \cdot 10^{-8}\ \mathrm{m^5 \cdot kg^{-1} \cdot s^{-1}}$
k_{des}	$1 \cdot 10^{-10}\ \mathrm{kg \cdot s^{-1}}$
c^*	$5 \cdot 10^{-3}\ \mathrm{kg \cdot m^{-2}}$

Variable	**Value**
$< c_E^* > = \dfrac{\int_{\bar{S}} c_{E^*}\, dS}{\int_{\bar{S}} dS}$ (at 50 s)	$3.9766 \cdot 10^{-5}\ \mathrm{kg \cdot m^{-2}}$
$< c_{O_2} > = \dfrac{\int_{\bar{A}} c_{O_2}\, dA}{\int_{\bar{A}} dA}$ (at 50 s)	0.0362 mM
$< c_E^* >$ vs. time	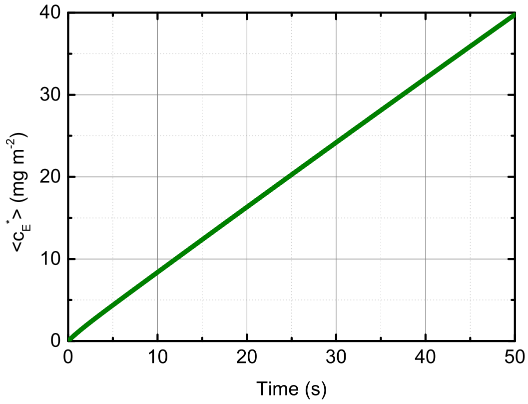
$< c_{O_2} >$ vs. time	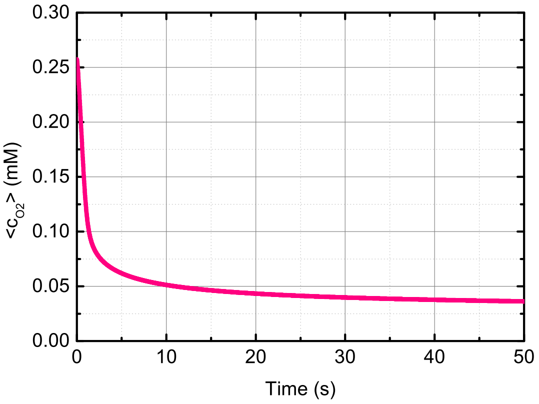

E.4.6 Parameter set 6

Parameter	**Value**
k_{ads}	$1 \cdot 10^{-8}\ \mathrm{m}^5 \cdot \mathrm{kg}^{-1} \cdot \mathrm{s}^{-1}$
k_{des}	$1 \cdot 10^{-12}\ \mathrm{kg} \cdot \mathrm{s}^{-1}$
c^*	$5 \cdot 10^{-7}\ \mathrm{kg} \cdot \mathrm{m}^{-2}$

Variable	**Value**
$< c_{\mathrm{E}}^* > = \frac{\int_{\bar{S}} c_{\mathrm{E}^*}\, dS}{\int_{\bar{S}} dS}$ (at 50 s)	$5.5275 \cdot 10^{-9}\ \mathrm{kg} \cdot \mathrm{m}^{-2}$
$< c_{\mathrm{O}_2} > = \frac{\int_{\bar{A}} c_{\mathrm{O}_2}\, dA}{\int_{\bar{A}} dA}$ (at 50 s)	0.2264 mM
$< c_{\mathrm{E}}^* >$ vs. time	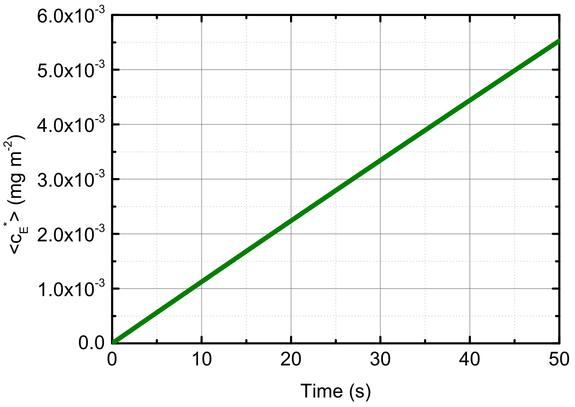
$< c_{\mathrm{O}_2} >$ vs. time	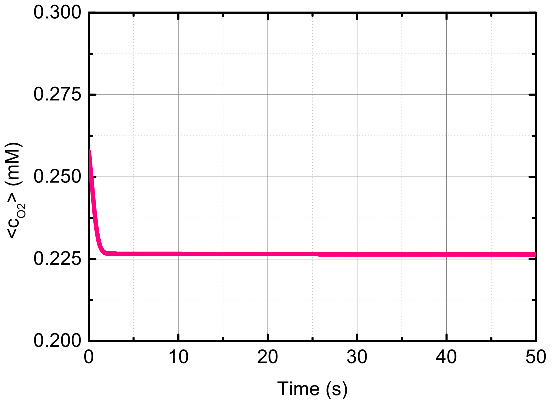

Appendix F

Glucose oxidase experimental results

In this Appendix the experimental results obtained in the experiments with GOx are presented.

F.1 Continuous feed of glucose and glucose oxidase

F.1.1 Glucose oxidase concentration of 0.2 $\mathrm{g \cdot l^{-1}}$

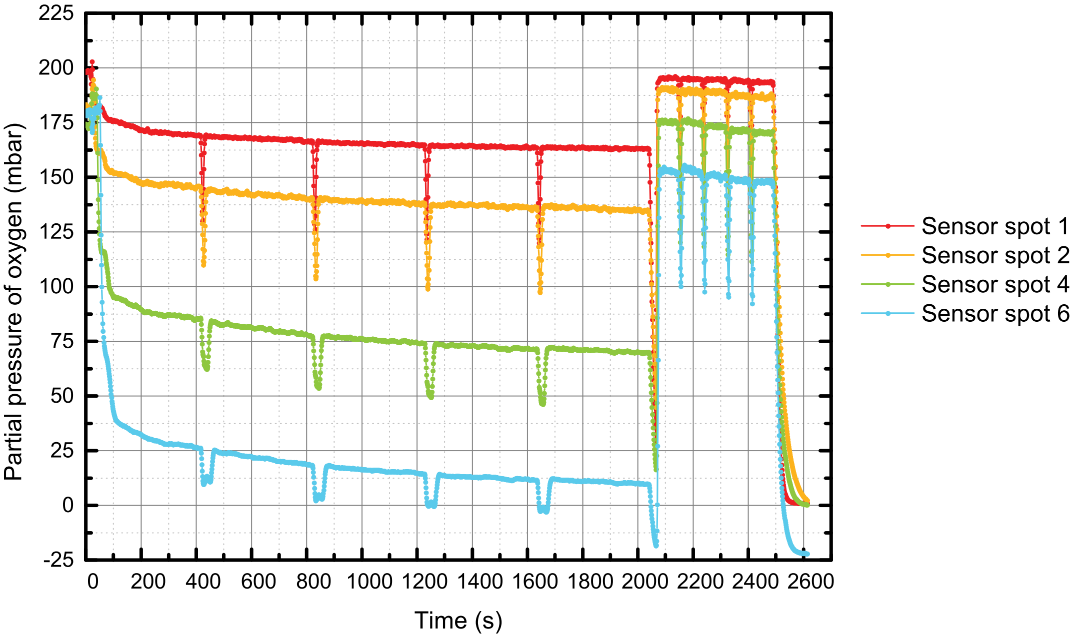

Figure F.1 *Profiles of oxygen partial pressure over time in the sensor spots 1, 2, 4 and 6 for the entire experiment at concentration of GOx solution of 0.2* $\mathrm{g \cdot l^{-1}}$.

F.1.2 Glucose oxidase concentration of 0.05 $\mathrm{g \cdot l^{-1}}$

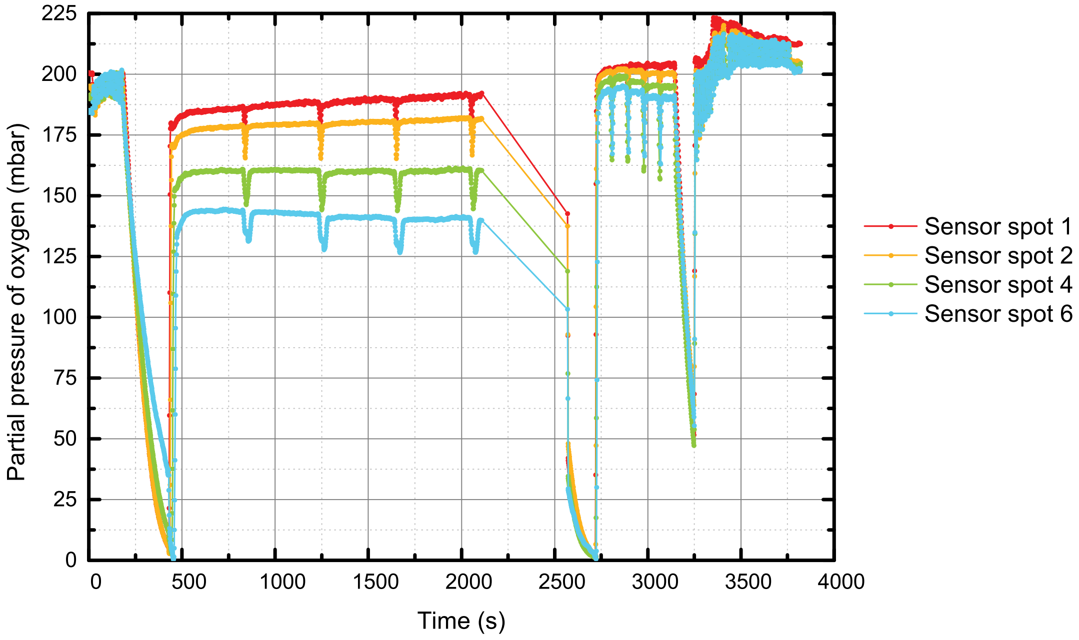

Figure F.2 *Profiles of oxygen partial pressure over time in the sensor spots 1, 2, 4 and 6 for the entire experiment at concentration of GOx solution of 0.05* $\mathrm{g \cdot l^{-1}}$.

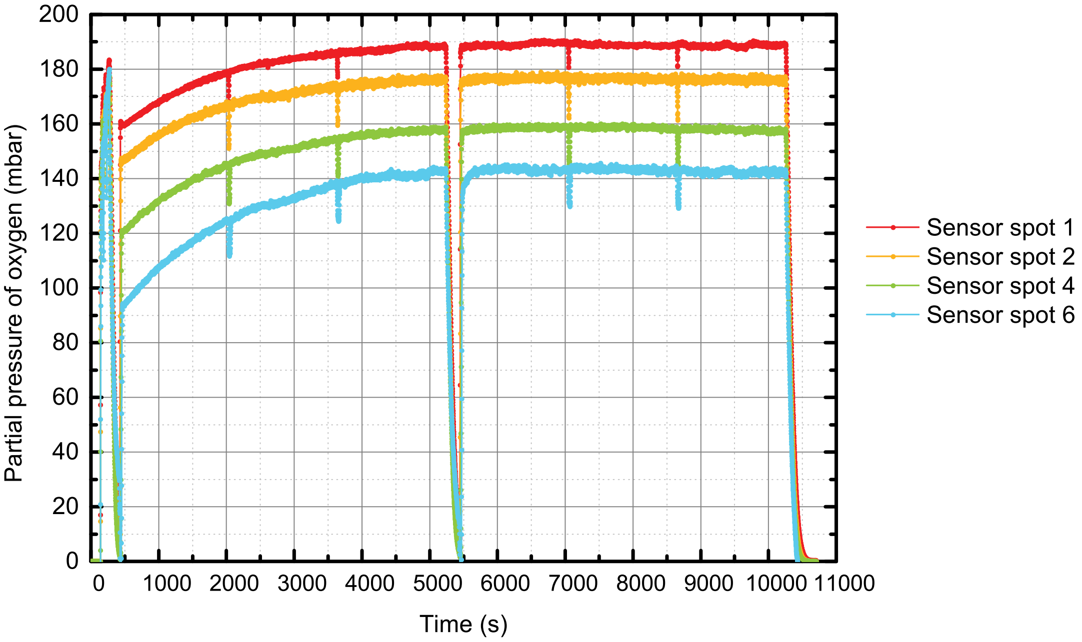

Figure F.3 *Profiles of oxygen partial pressure over time in the sensor spots 1, 2, 4 and 6 for the entire experiment at concentration of GOx solution of 0.05* $\mathrm{g \cdot l^{-1}}$*, with syringes with strokes of 250* μ*l each.*

F.2 Continuous feed of glucose and glucose oxidase after feeding bovine serum albumin

F.2.1 Glucose oxidase concentration of 0.2 $\mathrm{g \cdot l^{-1}}$

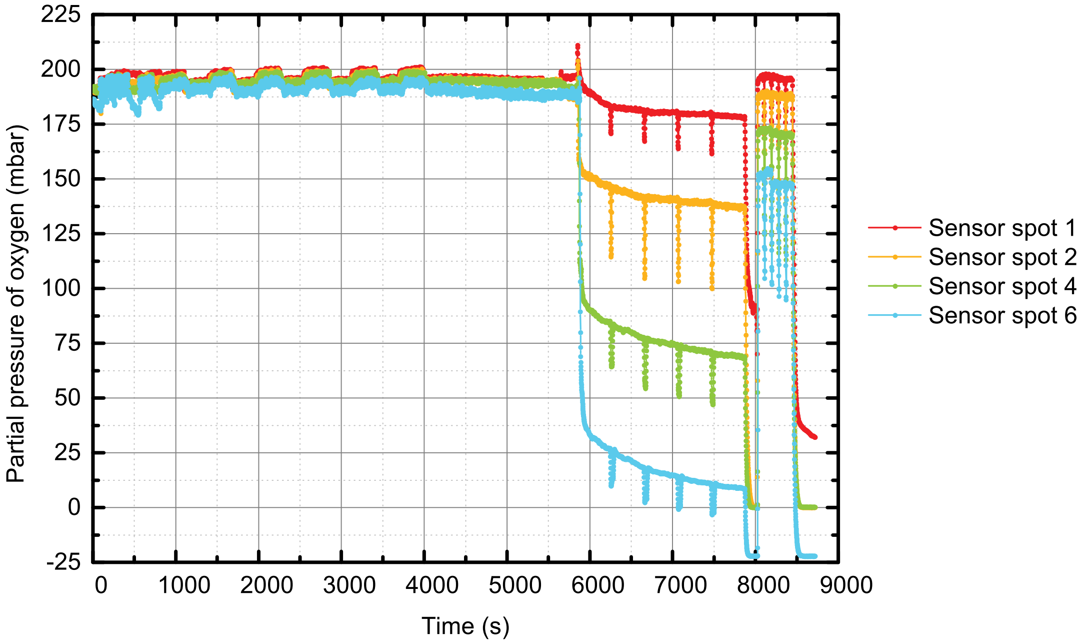

Figure F.4 *Profiles of oxygen partial pressure over time in the sensor spots 1, 2, 4 and 6 for the entire experiment at concentration of GOx solution of 0.2* $\mathrm{g \cdot l^{-1}}$*, with an initial feed of BSA only.*

F.2.2 Glucose oxidase concentration of 0.05 $\mathrm{g \cdot l^{-1}}$

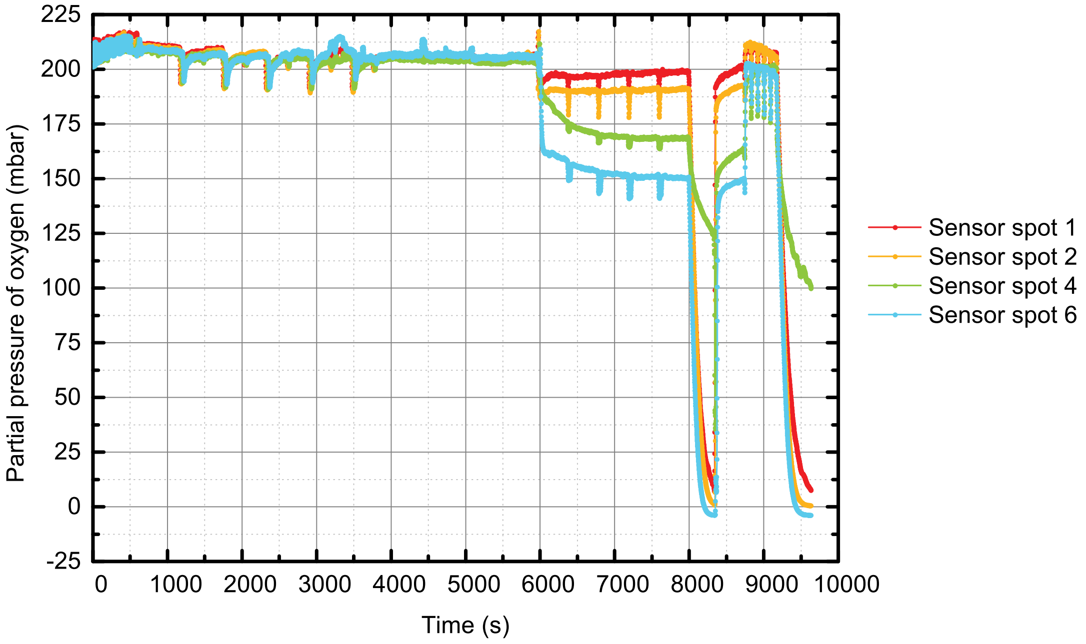

Figure F.5 *Profiles of oxygen partial pressure over time in the sensor spots 1, 2, 4 and 6 for the entire experiment at concentration of GOx solution of 0.05* $\mathrm{g \cdot l^{-1}}$*, with an initial feed of BSA only.*

F.3 Continuous feed of glucose and glucose oxidase mixed with bovine serum albumin

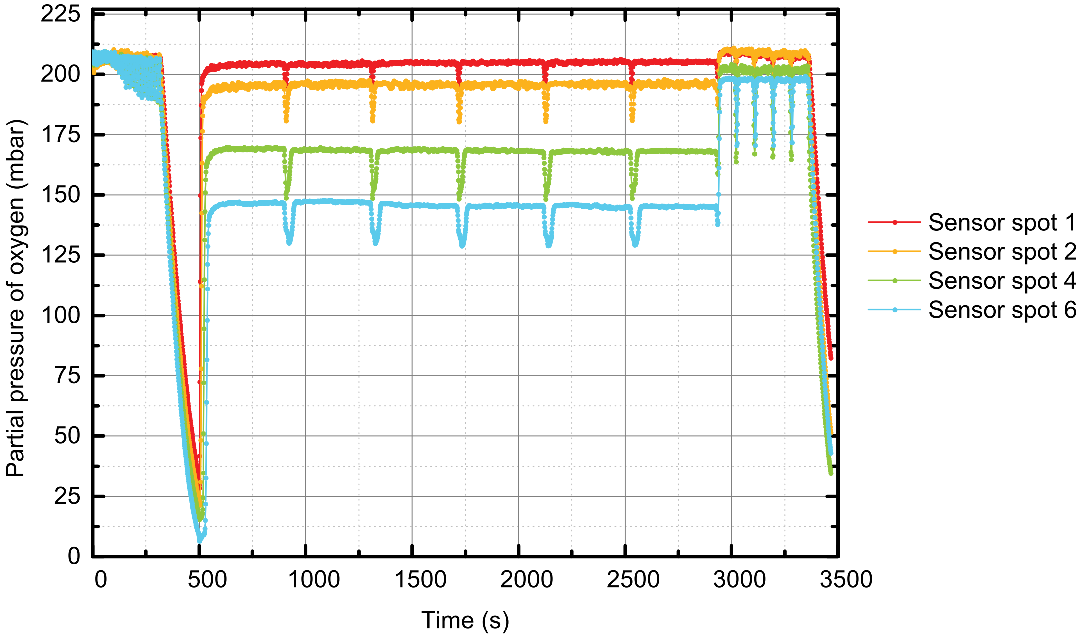

Figure F.6 *Profiles of oxygen partial pressure over time in the sensor spots 1, 2, 4 and 6 for the entire experiment with a simultaneous feed of GOx and BSA.*

F.4 Alternate flow of glucose oxidase and glucose

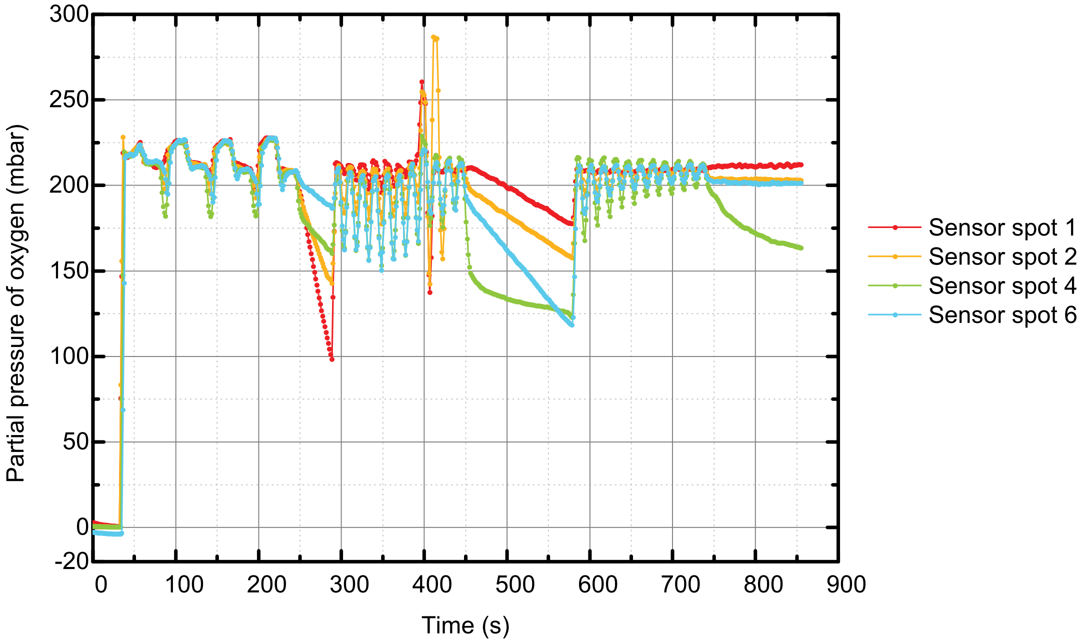

Figure F.7 *Profiles of oxygen partial pressure over time in the sensor spots 1, 2, 4 and 6 for the entire experiment with flow of GOx followed by a flow of GLU.*

F.5 Flow of glucose and stop flow after continuous feed of glucose and glucose oxidase

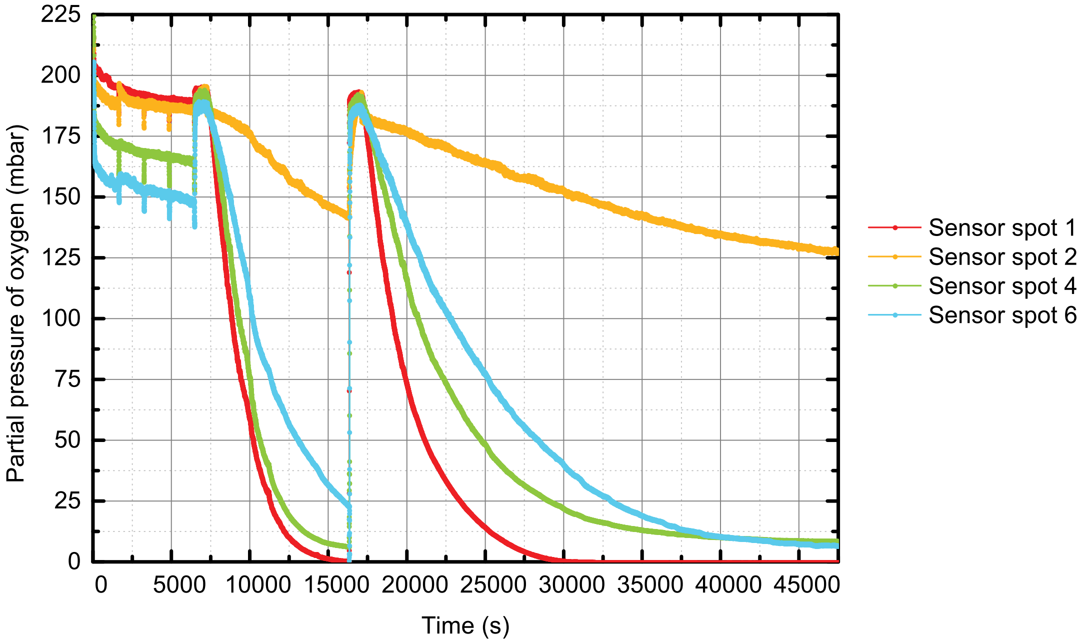

Figure F.8 *Profiles of oxygen partial pressure over time in the sensor spots 1, 2, 4 and 6 for the entire experiment with flow of GLU followed by stop flow, after a continuos feed of GLU, GOX and BSA.*

F.6 Flow of glucose and stop flow after continuous feed of glucose, glucose oxidase and bovine serum albumin

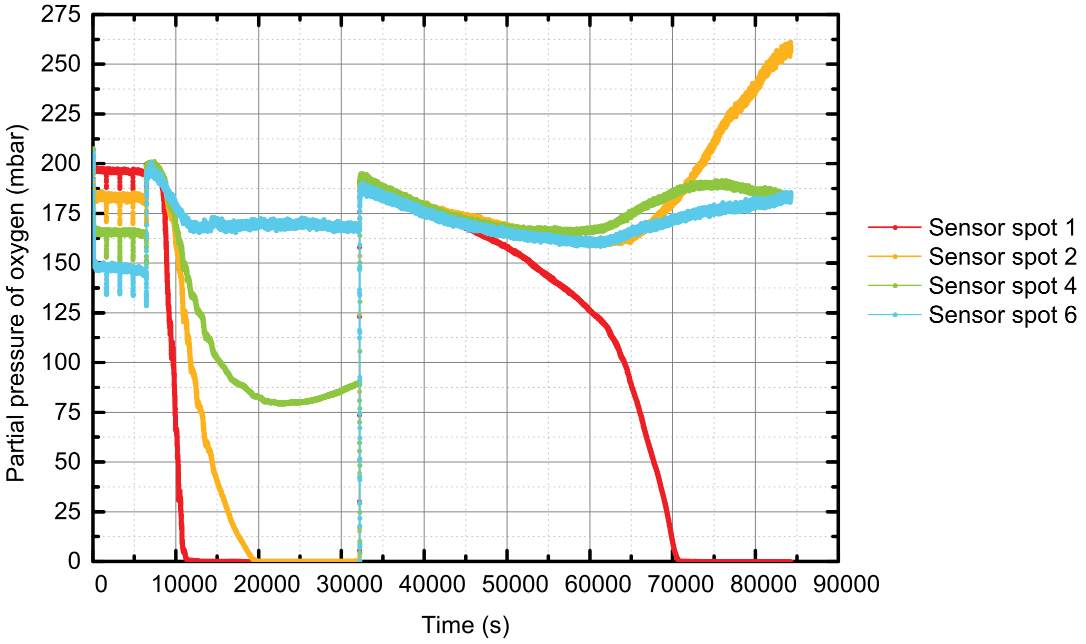

Figure F.9 *Profiles of oxygen partial pressure over time in the sensor spots 1, 2, 4 and 6 for the entire experiment with flow of GLU followed by stop flow, after a continuous feed of GLU, GOX and BSA.*

Bibliography

Al-Haque, N. (2012). Integrating Porous Resins in Enzymatic Processes. *Ph.D. Thesis*, Technical University of Denmark (Denmark).

Al-Haque, N., P. A. Santacoloma, W. Neto, P. Tufvesson, R. Gani, and J. M. Woodley (2012). A Robust Methodology for Kinetic Model Parameter Estimation for Biocatalytic Reactions. *Biotechnol. Prog.*, **28** (5), 1186–1196.

Atkins, P. and J. De Paula (2010). *Atkins' Physical Chemistry* (6th ed.). Oxford University Press, Oxford (United Kingdom).

Ault, A. (1965). Resolution of D, L -α-Phenylethylamine. *J. Chem. Educ.*, **42** (5), 269.

Baleizão, C., S. Nagl, M. Schäferling, M. N. Berberan-Santos and O. S. Wolfbeis (2008). Dual Fluorescence Sensor for Trace Oxygen and Temperature with Unmatched Range and Sensitivity. *Anal. Chem.*, **80** (16), 6449–6457.

Bodla, V. K., R. Seerup, U. Krühne, J. M. Woodley and K. V. Gernaey (2013). Microreactors and CFD as Tools for Biocatalysis Reactor Design: a Case Study. *Chem. Eng. Technol.*, **36** (6), 1017–1026.

Breuer, M., K. Ditrich, T. Habicher, B. Hauer, M. Kesseler, R. Stürmer and T. Zelinski (2004). Industrial Methods for the Production of Optically Active Intermediates. *Angew. Chem., Int. Ed. Engl.*, **43** (7), 788–824.

Bull, H. B. (1956). Adsorption of bovine serum albumin on glass. *Biochim. Biophys. Acta*, **19**, 464–471.

Cassimjee, K. E. (2012). ω-Transaminase in Biocatalysis Methods, Reactions and Engineering. *Ph.D. Thesis*, KTH Royal Institute of Technology (Sweden).

El Gihani, M. T. and J. M. J. Williams (1999). Dynamic kinetic resolution. *Curr. Opin. Chem. Biol.*, **3** (1), 11–15.

Hlady, V., J. Buijs and H. P. Jennissen (1999). Methods for Studying Protein Adsorption. *Methods Enzymol.*, **309** (26), 402–429.

Höhne, M. and U. T. Bornscheuer (2009). Biocatalytic Routes to Optically Active Amines. *ChemCatChem*, **1** (1), 42–51.

Kagan, H. B. and J. C. Fiaud (1988). Kinetic Resolution. *Top. Stereochem.*, **18**, 249–330.

Koszelewski, D., K. Tauber, K. Faber and W. Kroutil (2010). ω-Transaminases for the Synthesis of Non-Racemic α-chiral Primary Amines. *Trends Biotechnol.*, **28** (6), 324–32.

Leskovac, V., S. Trivic, G. Wohlfahrt, J. Kandrac and D. Pericin (2005). Glucose Oxidase from *Aspergillus niger*: the Mechanism of Action with Molecular Oxygen, Quinones, and One-Electron Acceptors. *Int. J. Biochem. Cell Biol.*, **37** (4), 731–750.

Moore, J. S. and K. F. Jensen (2014). "Batch" Kinetics in Flow: Online IR Analysis and Continuous Control. *Angew. Chem., Int. Ed. Engl.*, **53** (2), 470– 473.

Neto, W. (2013). Process Considerations for the Asymmetric Synthesis of Chiral Amines using ω-Transaminases. *Ph.D. Thesis*, Technical University of Denmark (Denmark).

Nugent, T. C. and M. El-Shazly (2010). Chiral Amine Synthesis - Recent Developments and Trends for Enamide Reduction, Reductive Amination, and Imine Reduction. *Adv. Synth. Catal.*, **352** (5), 753–819.

O’Reilly, E., C. Iglesias and N. J. Turner (2014). Monoamine Oxidase-ω-Transaminase Cascade for the Deracemisation and Dealkylation of Amines. *ChemCatChem*, **6** (4), 992–995.

D. L. Purich (2010). *Enzyme Kinetics: Catalysis & Control. A Reference of Theory and Best-Practice Methods*. Academic press, Waltham, Massachusetts (USA).

Shin, J. S. and B. G. Kim (1998). Kinetic Modeling of ω-transamination for Enzymatic Kinetic Resolution of α-Methylbenzylamine. *Biotechnol. Bioeng.*, **60** (5), 534–540.

Shin, J. S. and B. G. Kim (2002). Substrate Inhibition Mode of ω-Transaminase from Vibrio fluvialis JS17 Is Dependent on the Chirality of Substrate. *Biotechnol. Bioeng.*,

77 (7), 832–837.

Suelter, C. H. and M. DeLuca (1983). How to Prevent Losses of Protein by Adsorption to Glass and Plastic. *Anal. Biochem.*, **135**, 112–119.

Tufvesson, P., J. Lima-Ramos, J. S. Jensen, N. Al-Haque, W. Neto and J. M. Woodley (2011). Process Considerations for the Asymmetric Synthesis of Chiral Amines using ω-Transaminase. *Biotechnol. Bioeng.*, **108** (7), 1479–1493.

Turner, N. J. and M. D. Truppo (2010). Biocatalytic Routes to Nonracemic Chiral Amines. In: *Chiral Amine Synthesis* (T. C. Nugent, Ed., 1st ed.), Wiley-VCH Verlag GmbH & Co. KGaA, Weinheim, Germany.

Van Stroe-Biezen, S. A. M., A. P. M. Janssen and L. J. J. Janssen (1994). A Kinetic Study of Soluble Glucose Oxidase Using a Rotating-Disc Electrode. *Bioelectroch. and Bioener.*, **33** (1), 55–60.

Wang, C., D. K. Ye, Y. Y. Wang, T. Lu and X. H. Xia (2013). Insights into the "Free State" Enzyme Reaction Kinetics in Nanoconfinement. *Lab on a chip*, **13** (8), 1546–1553.

Wohlfahrt, G., S. Trivic, J. Zeremski, D. Pericin and V. Leskovac (2004). The Chemical Mechanism of Action of Glucose Oxidase from *Aspergillus niger*. *Mol. Cell. Biochem.*, **260**, 69–83.

Yamashita, K., M. Miyazaki, H. Nakamura and H. Maeda (2009). Non-immobilized Enzyme Kinetics That Rely on Laminar Flow. *J. Phys. Chem. A*, **113** (1), 165–169.

Web sites

`http://www.in-pharmatechnologist.com/Ingredients/Amine-goldmine-BASF-commits-to-new-plant-citing-growing-demand` (accessed: 4th July 2014)

`http://www.fda.gov/ucm/groups/fdagov-public/@fdagov-foods-gen/documents/document/ucm267044.pdf` (accessed: 4th July 2014)